Falin Chen

The Kuroshio Power Plant

Springer

Lecture Notes in Energy 15

Falin Chen

The Kuroshio Power Plant

Falin Chen
Institute of Applied Mechanics
National Taiwan University
Taipei
Taiwan, Republic of China (ROC)

Preface

The earth's three great oceans feature many perennial and stable currents encompassing tremendous amounts of kinetic energy. This energy, if properly captured, could make an important contribution to human civilization and sustainable development. The Kuroshio, a branch of the North Pacific Gyre, shows particular promise in this regard. It flows particularly strong along the eastern coast of Taiwan and then follows a stable course to pass the Ryukyu Islands and Japan. From the perspective of energy development, the Kuroshio is a high-quality ocean current, able to provide a steady and high-volume power output needed to achieve economies of scale and commercial value. The Kuroshio power plant has many competitive advantages. It has environmental advantages in that it causes no carbon emissions, pollution, or waste. It is completely renewable requiring no fuel. It offers a continuous power supply with a capacity factor greater than 0.7, considerably superior to most currently available renewable energy sources. In terms of technical advantage, the power plant construction can be accomplished with existing technologies and mature engineering processes, thus avoiding potential technological bottlenecks. In terms of cost advantages, it is estimated that, once technical development costs are accounted for, construction and operation costs will be competitive with offshore wind power.

Over the past 30 years, research institutions in Europe, the USA, Japan, and other developed countries have investigated ocean-based energy sources and developed over 70 projects to explore various kinds of ocean energy. In facilities off the coast of Europe and North America, long-term testing and operation have focused on the development of wave, tidal, and ocean-thermal energy. Among these projects, the principles of tidal energy generation are similar to that proposed for the Kuroshio, but the former is designed to be implemented in shallow waters no more than 30-m deep, while the latter requires construction in waters several hundred meters in depth, thus requiring different engineering designs. The key differences lie in the design of the turbine generators and the anchorage system.

This book presents a new design for the Kuroshio power plant. The deployment of hundreds of turbines in deep waters, anchored in a stable formation to the seabed hundreds of meters below is an unprecedented engineering feat, entailing new

approaches to turbine design, anchorage system planning, deep-sea marine engineering, and power plant operations and maintenance. In addition, the large-scale deployment of such turbines will inevitably have an impact on the local environment and ecology. Power plant operations may also be subject to impacts from earthquakes, typhoons, climate change, and other natural factors. Consequently, a careful assessment for the environmental impact, both on the plant and from the plant, is absolutely required for such a power plant project.

The six chapters of this book explore each of these challenges in detail. Chapter 1 reviews the available literatures to survey the ocean current characteristics, seabed geology, ecology, and environment of the Kuroshio's waters. In Chap. 2, we propose a conceptual design for the Kuroshio power plant while focusing on the power plant's core technologies—the turbine, the replay platform, and the marine engineering at deep sea. Chapter 3 establishes the analysis logic for the design of the turbine. We first select the Gulf Stream Turbine for computational fluid dynamic analysis to investigate the dynamic reaction of each turbine component under the action of the Kuroshio. Results provide information for the designs of the tail–wing stabilizer, a mechanism needed to ensure the turbine's autonomous balance and the single-cable anchorage system. In Chap. 4, the relay platform design follows another logic. We first analyze the rigidity of the unit platform and then analyze the stability of the test platform (composed of six unit platforms) under the actions of the designed anchorage system and the Kuroshio. Finally, we analyze the complete relay platform (composed of 66 unit platforms) to examine the power plant's structural integrity. These two chapters provide a complete Kuroshio power plant analysis and design logic, based on which the design engineer could set out the complete construction specifications for the detailed design of power plant. Chapter 5 attempts to elucidate potential environmental and ecological impacts from the construction and operation of the Kuroshio power plant, while also explores the potential impact of natural events, such as earthquakes, typhoons, and climate change on power plant operations. Finally, Chap. 6 presents a plan to build a 30-MW pilot power plant.

As explained in Chap. 2, the Kuroshio power plant design has many advantages. Mainly, the single cable used to anchor the turbine to the platform is short, thus minimizing the amplitude of the fuselage's drift with the current. In addition, the multi-cable anchorage design for the relay platform can protect from earthquake damage, and the power plant's flexible structure can effectively prevent damage from high-frequency fatigue. However, the design also includes some drawbacks: The new design increases uncertainty, the structure flexibility reduces overall turbine efficiency, and deep-sea construction is extremely challenging.

The technologies proposed here can also be applied to generate power in other waters, such as the Gulf Stream east of Florida, the East Australian Current, the Humboldt Current west of South America, the East Africa Coastal Current, and so on. All these areas feature strong currents and deep waters, similar to those found in the Kuroshio. For application in other areas, the environmental and ecological impact assessments presented in Chap. 5 would need another comprehensive study and, if a different type of turbine (Chap. 3) or relay platform structure

(Chap. 4) is used, the relevant computational analyses would also have to be redone. However, the analysis logic and sequence presented in this book would still apply.

Finally, since the proposed Kuroshio power plant is a new design and requires deep-sea construction, it entails high research costs and construction risks during the development stage. Therefore, initial development and construction must be conducted with extreme caution to methodically explore and resolve all potential problems. Once all potential issues are resolved, the machinery can be committed and underwater construction be commenced.

Taipei, Taiwan, Republic of China   Falin Chen

Acknowledgments

This book touches on many fields outside the author's field of expertise. Without the valuable assistance by the following scholars, this book could have never been finished. First, the author is particularly indebted to Professor Chao Shenn-Yu of the University of Maryland and Dr. Ko Dong-Shan of the US Naval Research Institute. Without their computational results for the Kuroshio shown in Chaps. 1, 5, and 6, it would have been very difficult to illustrate the flow characteristics of the Kuroshio, let alone to establish the legitimacy of the construction of the Kuroshio power plant. I am also very grateful to Professor Tang Tsun-Yong of the Institute of Oceanography at National Taiwan University for his generous providing of a wealth of research results and graphics presented in Chap. 6, which are critical to the conception of the pilot power plant. I would also like to express particular thanks to Professor Pai Shu-Chen also of the IOO-NTU for his patience in explaining his meticulous research results. The unique insights resulting from his long-term investment in research of the source of the Kuroshio was critical to the introduction of the Kuroshio's hydrological environment presented in Chap. 1.

In the preparation of this book, many of my colleagues of the Department of Geology at NTU were very generous with their time and expertise, offering valuable input and feedback which greatly improved the book's content. Professor Chen Cheng-Hong provided valuable insights into the geological evolution of the waters off eastern Taiwan. Professor Wei Kuo-Yan provided key information on the ancient Kuroshio. Professor Chen Hong-Yu provided precise explanations for the mechanical properties of the rock forming the Kuroshio's seabed. Professor Yang Tsan-Yao provided the massive information about the geological structure under the Kuroshio waters. Moreover, Professor Liu Char-Shine of IOO-NTU shared the results of his long-term research into underwater earthquakes in the Kuroshio, Professor Chiu Feng-Chen of the Department of Engineering Science and Ocean Engineering provided insights into the possible impact of typhoons, and Professor Liu Chi-Wen of the Department of Electrical Engineering offered the valuable information about power transmission schemes which are also gratefully appreciated. Finally, I would also like to thank Dr. Ko Chia-Hao of Houston, Texas

for providing information about Kuroshio engineering which helped me better understand construction cost estimates.

In addition, many of the researchers, students, and assistants in the author's research lab made contributions to analyses and organization for this book. Among them, I am particularly grateful to Dr. Chen Chi-Hao for analyzing the relay platform dynamics and the tail–wing stabilizer of the turbine, Mr. Wang Rui-Shian for conducting analysis on the turbine dynamics, Dr. Cheng Kuo-Dong for reviewing the Kuroshio-related literatures, Dr. Chung Jia-Lu for organizing the literature on the Kuroshio ecology and environment, and Dr. Fan Cheng-Wen for cataloging the underwater turbine models. I would also like to thank the following students Mr. Chang Sen-Chun, Miss Tsai Chia-Shuan, and Mr. Luo Wen-Fu for their contributions to this book through preparing figures, tables, and compiling relevant literatures.

Finally, I would especially like to thank the president of National Taiwan University, Professor Lee Si-Chen, who has unstintingly provided support for my research into the Kuroshio power plant. Without his steadfast encouragement and support, this book would not have been completed. The funding needed to complete this book was mainly offered by Delta Electronics, Inc., through a project implemented in National Taiwan University. Part of the funding was provided by The National Science Council of Taiwan through the operation project of the program office for the National Science and Technology Program for Energy.

Taipei, Republic of China   Falin Chen
1 February 2013

Contents

Chapter 1
Hydrology, Ecology, and Environment of Kuroshio Waters

Taiwan's Kuroshio and Florida's Gulf Stream are both referred to as Western Intensified Flows because they both increase in velocity as they progress westward, which, as indicated by Stommel [1], is caused by variation of the Coriolis force with latitude. In both cases, the atmospheric circulation is recognized as the major driving force behind this increase. In both the Atlantic (for the Gulf Stream) and the Pacific (for the Kuroshio), the atmospheric circulation is established through a western wind (i.e., blowing from west to east) between 30°N and 45°N and an eastern wind between 15°N and 30°N. This clockwise vortex (or gyre) extrudes to the west to enhance the strength of the current along the western shores, thus creating the current. These two circulatory currents in the northern Hemisphere are referred to as Geostrophic Currents [2, p. 193], striking a balance among three forces: flow momentum of the current, the Coriolis force, and static pressure due to sea level difference. The Coriolis force and static pressure are both induced by the reaction to the flow momentum, which accordingly must be sufficiently large to support these two forces. This indicates that the force to drive Kuroshio shall be extraordinary large to maintain the large momentum required to not only balance the other two forces but also to counter act the friction loss occurred in such a large-scale current. This also explains why the mass flow rate of Gulf Stream increases significantly (up to three times larger) when it reaches its northern boundary [2, p. 513].

Kuroshio is Japanese for "black current." According to Professor Pai Shu-Chen (private communication, 2012), the name is given due to the fact that the Kuroshio water is transparent and reflects less sunlight. From above, one easily notices a difference in appearance of Kuroshio from the surrounding waters. The Kuroshio is about 400 km long and 100 km wide, flowing north along the east coast of Taiwan. While the Kuroshio primarily originate in the south, it also receives another inflow from the east. These two inflows provide the thrust to push the current north towards Japan, overcoming the frictional resistance resulting from the interaction between the current and dry land or the seabed, as well as the friction from internal turbulence and the interaction with the atmosphere at surface. The Kuroshio flow is also subject to corrections due to coastal and seabed topographies (for example, the Kuroshio accelerates as it passes through the channel between Tai-Dong and
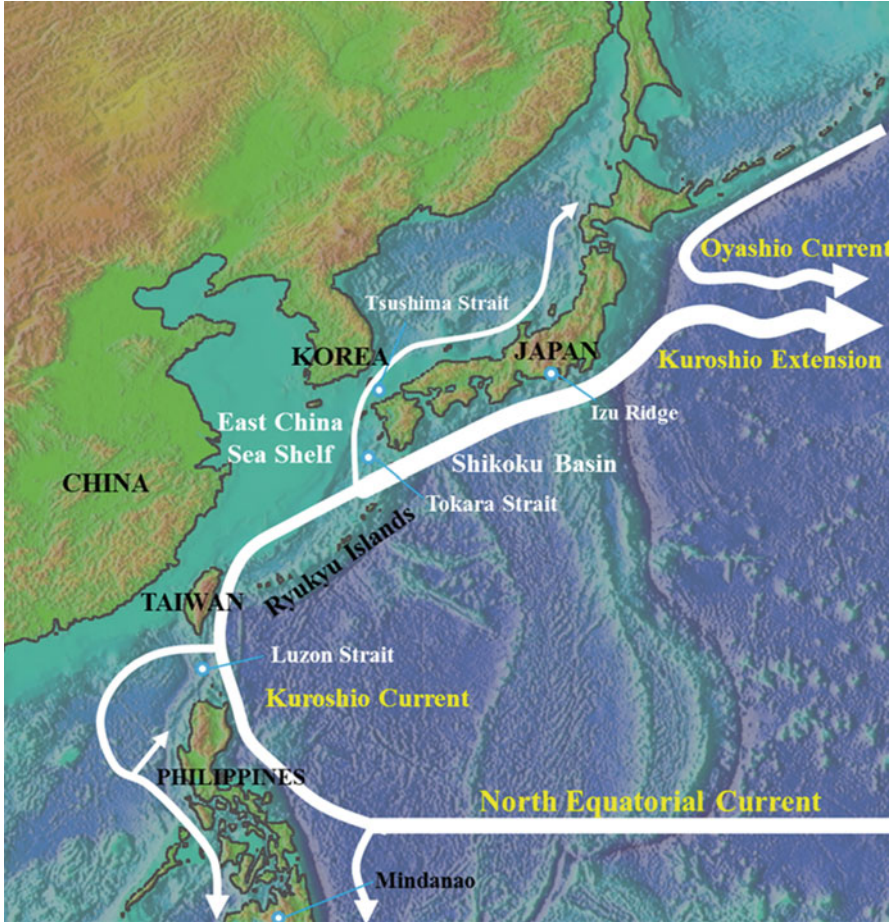
Fig. 1.1 Schematic of currents in the western Pacific. At the north of the equator, Pacific current runs from east to west, splitting at the Philippines into northern and southern currents. The northern current passes Taiwan's east coast as the Kuroshio, extending up past the Ryukyu Islands and Japan before merging with the cold water of Oyashio to form the Kuroshio Extension

Lu-Dao, see Fig. 1.1), to the seasonal correction due to monsoons (for example, in winter the northeast wind significantly reduces the current's flow rate, see Fig. 1.4), and to the short-term corrections caused by other factors such as the turbulence generated by typhoons, the change in salinity of the seawater, and the change in atmospheric pressure resulting in the change of sea level, ..., etc. [3–6].

According to Kawaii's [3] definition, on the other hand, the Kuroshio is a current in the north Pacific stretching from the waters around Taiwan to the Sea of Japan, inextricably linked with the North Pacific Gyre. This chapter reviews previous researches related to the North Pacific Gyre to discuss how the characteristics of gyre circulation are related to the change of Kuroshio. In addition, because the

construction and operation of the Kuroshio power plant are also closely linked to the geology of the seabed and the ecology of the Kuroshio's waters, the environmental and ecological issues will also be discussed.

1.1   Kuroshio: A Branch of the North Pacific Gyre

Currents in the north Pacific circulate with atmospheric flows to form a gyre. The current flows west at about 100 km north to the equator, turns to north as it runs into the Philippine plate, and then flows along the east coast of Taiwan to the north. It then passes the Ryukyu Islands and Honshu, reaching to the southeast point of Hokkaido where it merges with Oyashio, a southward current from the Arctic Ocean, to form an easterly flow. When this flow runs into the North American plate, it turns south to the equator before turning west towards the Philippines, forming the North Pacific Gyre (see Fig. 1.1).

We begin our discussion of the Kuroshio with the water at east Mindanao, an island of the Philippines, where the Kuroshio originates. The westward current approaches Mindanao flowing between 12 and 13°N (though sometimes reaching as far north as 14.5°N or as far south as 11°N) and splits into two currents after run into Mindanao. One current flows northwest as the Kuroshio, the other flows south as the Mindanao Current. In winter, the monsoon will push the Kuroshio westward through the Luzon Strait [7] to 117°E where it stops after hitting the shallower water near the continental shelf. Without monsoon effect, the Kuroshio will flow northeast and move along the east coast of Taiwan. When it reaches Lan-Yu, an island at east Taiwan, the current splits again, but remerges at the north of Lan-Yu to continue north.

At approximately 22–25°N, in general, under the influence of various vortices from Pacific, the flux as well as the path of Kuroshio vary periodically with a cycle of approximately 100 days [8], causing a greater eddy variability at east Taiwan than that found at east Philippine. At 24°N, the Kuroshio splits again. The main current flows northeast along the continental shelf of the East China Sea, while the secondary current flows southeast and then northeast after passing the Ryukyu Islands. At 30°N and 128–129°E, after getting through the constrain due to the submarine terrain, the main current flows through the Tokara Strait with a flux exceeding 30 sv (30×10^6 m^3/s), and then merges with the secondary flow to continue flowing towards the north Pacific [8].

Part of the Kuroshio near the Tokara Strait intrudes intermittently into the Tsushima Strait between Japan and Korea with a flux of about 2 sv, causing the mix between the colder water from the continental shelf and the warmer water from East China Sea. After passing through the Tokara Strait, the Kuroshio enters the relatively deeper Shikoku Basin and, at 139°E, is forced by submarine terrain obstacles to flow over the Izu Ridge. Near 140°E and 35°N, the Kuroshio leaves the coast of Japan and enters the north Pacific, forming the Kuroshio extension [8]. Because of the absence of continents, this eastward winding inertial flow generates many large-scale eddies.

At 159°E, the Kuroshio splits again, with the primary stream flowing north to 40°N to merge with the Subarctic Current. The Kuroshio extension features the largest wind-driven variation of eddy, raising the Kuroshio flux in this area to 130 sv [8], which is about three times or more of the Kuroshio near the equator. This area of the ocean sees large-scale changes in surface altitude over the course of the year, with the Kuroshio offset amplitude exceeding 120 km.

The flux of Kuroshio near Taiwan is generally estimated to be between 20 and 30 sv, or approximately 100 times the flow of the Brazilian Amazon, or 1,000 times the flow of the Yangtze or Mississippi Rivers [9]. From 1960 to 1975, the flux of the Kuroshio off of Taiwan's east coast averaged 22.5 sv, but this average increased to 27 sv by the late 1990s. This long-term change in the average flux was primarily due to changes in the subtropical north Pacific ocean currents. As it moves northeast, the Kuroshio continues to grow in volume, exceeding 42 sv in the Tokara Strait and 55 sv in the Shikoku Basin. This increase in volume is primarily due to the clockwise eddies to the south of the Kuroshio, which contribute about 12 sv to the total volume. Since the 1960s, the Kuroshio's flow volume has fluctuated annually as it passes northwest of the Ryukyu Islands, from a low of 17.5 sv in 1974–1975 to a high of 28 sv in 1986 [8].

1.2 Factors Influencing the Kuroshio

It is generally believed that the primary force driving the Kuroshio is the atmospheric circulation over the Pacific (circulating over a scale of thousands of kilometers) [1, 10]. This clockwise circulation is formed by the west wind between 30°N and 45°N and the east wind between 15°N and 30°N. At deeper waters, however, the circulation is mainly driven by the variation of sea water density and modified by the effect of Coriolis force. In the waters close to continent, such as the Kuroshio at east Taiwan, the static pressure due to sea level difference also plays a major role to influence the current motion. To the Kuroshio at Taiwan's waters, as a whole, the Kuroshio motion is a result balanced among the atmospheric circulation wind force, the Coriolis force, and the static pressure due to the sea level difference, and is modified by various kinds of influential factors [11]. This is referred to as the so-called geostrophic flow.

Although the Kuroshio is primarily a balance among the above-mentioned forces, it may nevertheless flow in an unstable way called meandering in the waters away from coast. As early as 1943, Suda [12] suggested that typhoons shall be the main cause for the meandering assumed by the Kuroshio near Japan. However, in 1949 after examined the meandering phenomenon from 1934 to 1943, Uda [11] speculated that the meandering of Kuroshio extension is a result due to the intrusion of the cold Oyashio from north of a velocity about 3 cm/s. Ten years later, Yosida and Moriyasu [13] studied the meandering of the Kuroshio in March 1959 at south Japan and found that as the Kuroshio passed Kyushu, it detoured away from the coast, traveling east with a small-scale meandering at a flow speed of approximately 5 km/day. This conclusion prompted Nan'niti [14, 15] to suggest that changes of the

seawater flow of the central north Pacific are closely related to changes of the Kuroshio. Despite a plethora of research, no strong consensus has been reached. Only recently have various factors affecting the flow of the Kuroshio been verified. The physical characteristics of these factors are discussed below.

1.2.1   Seasonal Effect

The Kuroshio's flow rate, flow path, flow area, and velocity distribution are all subject to seasonal variation. For example, as the Kuroshio flows through Luzon Strait, its main stream flows directly north while a tributary flows west into South China Sea, see Fig. 1.1. This westward intrusion flows at a speed reaching 0.5 m/s in fall and winter, but slows to about 0.1 m/s in spring and summer [16]. This speed variation is a reaction to wind stress applied on the sea surface, and is related to westward movement of eddies along the equator and the relative strength of the Kuroshio's northward flow [17]. Near the Ryukyu Islands, the Kuroshio's main axis moves eastward in summer to form an upwelling and reduces the sea surface temperature. As a result, one can see from the vertical velocity distribution at Kuroshio cross-section that the Kuroshio moves with a bimodal motion [18]. At the waters off of Taiwan's northeast coast, the vertical speed of the upwelling at 30 m deep is larger in winter than in summer, while is opposite at 100 m deep.

1.2.2   Seabed Effect

To study the influence of the seabed on the Kuroshio, Chen and Yan [18] used a quasi-spectrum primitive equation model to calculate changes of the Kuroshio under various seabed topographical conditions. In their analyses, two cases of different seabed conditions were considered. In case A, the Kuroshio was bounded by land on the left and by sea on the right. Both boundaries were straight and parallel south-north lines, with a seabed depth of 75 m on the left, gradually increasing to 475 m by 16 increments to the right. In case B, depth changes were identical to case A, but the left and right boundaries were changed into two parallel curves. In case A, results show that the initial south-north velocity (excluding the vertical velocity) causes the sea surface to tend to flow towards the landward boundary even in the absence of wind. In case B, the Kuroshio moves along the isobaths and turns under the influence of curved isobaths, resulting in a higher flow velocity than case A. The velocity distribution on the cross-section of Kuroshio clearly shows that, because of the curve terrain, the flow velocity reduces from south to north while increases from east to west, a phenomenon known as the Kuroshio meandering. Aside from the effect of changing terrain on the Kuroshio, the seawater impacting the shore results in changes in sea level, which has emerged as the primary driving force behind the Kuroshio, and is also closely related to the Kuroshio's path.

Above simulations conducted by Chen and Yan [18] clearly indicated that as the upwelling caused by the Kuroshio occurs closer to land, a greater change in vertical velocity is resulted due to the secondary flow (i.e., a stream-wise vortex) generated in the curved area. The upwelling can not only produce variation in water properties but may also increase the flow rate of river into ocean by a factor of 10–30, thus producing a tremendous impact on the water of Kuroshio. Although in general the upwelling velocity is very small, about 1 m per day, it carries nitrogen rich and colder water from a depth of several 100 m to the surface and creates a cold dome [19] with a temperature about 3 °C below that of the surrounding waters, thus creating important fishing grounds.

Sudden changes in the seabed depth also have a huge impact on the Kuroshio. In their investigation of Tokara Strait, Feng et al. [20] found that, when crossing the strait from east to west, the depth of the strait increases from 500 m to 4,000 m from east to west, and decreases from 2,000 m to 600 m from south to north. When Kuroshio moves across Tokara Strait from south to north, the current speed in this area assumed a double core formation, with the flow on the shallow side accounting for only 29 % of the total flow volume through the Tokara Strait, while the rest was concentrated in the deep water area over 500 m in depth. In fact, in these waters, the change of speed was not only abrupt, but the direction of flow also experienced a bigger change every 3–4 months and a smaller change approximately every 10–12 days or 20 days.

1.2.3   Wind Effect

The impact of wind stress not only affects the sea surface but, due to viscous forces, also drives the lower layer of seawater in the same direction. On the other hand, the Coriolis effect causes water to pull to the right, and the impact of this effect increases with depth resulting in the formation of Ekmann Layer. Changes to the flow rate also impact the path of Kuroshio [17]. Generally speaking, lower speeds tend to occur near a coastline while higher speeds often occur in the open ocean with its axis deviating to the east. This result explains why the Kuroshio veers to the right as it passes Japan into the northern Pacific.

To explore the effect of wind stress, Chen and Yan [18] assumed the previously mentioned boundary conditions of case A and case B and added a north wind. Compared with the results from the case without wind, they found the seawater's flowing away from land is enhanced due to the impact of the north wind and the Coriolis force as well. Under the impact of the north wind, the speed of the upwelling increases, while the flow rate of the surface water decreases, allowing some seawater to flow towards land.

Wind stress not only directly affects the speed and direction of the surface flow but also causes variation of the height of the sea surface and produces variations in lateral static pressure, thus determining the flow direction of Kuroshio [21]. For example, when the Kuroshio passes the sea close to south Japan, the flow path is clearly affected by the pressure difference caused by wind stress between Kyushu

and the Bōsō peninsula. When the pressure difference increases beyond the critical range, the Kuroshio flows along the coastline; if the pressure difference falls within the critical range, the Kuroshio turns smoothly to move from west to east following the rotation of the North Pacific Gyre. Qiu and Miao [22] also discovered that, as passing the south tip of Japan, the change of the path of the Kuroshio is closely related to Kuroshio's flow volume. Given large volumes, Kuroshio flows in a curved path away from shore, but at times of low volume it flows along the coastline.

1.2.4   Temperature Effect

Deser [23] conducted a study seeking for long-term effects on the flow volume of the Kuroshio and found similar trends of change between the pressure at surface and the temperatures at 50 m deep, and further noted that the volume variation for the Kuroshio and the temperature variation at depths from 0 to 450 m were highly correlated. Within this depth range, when the seawater temperature drops by 0.6 °C, the Kuroshio volume falls by 2 sv and, when the temperature drops by 1.2 °C, the volume falls by 6 sv. As the temperature rises by 0.3–0.9 °C, the Kuroshio volume increases by about 6 sv. The correlation between temperature and flow volume is related to latitude: Negative change occurs in 36–42°N and positive change occurs in 28–32°N. The largest change, both positive and negative, occurs near 35°N.

1.2.5   Surface Level Effect

The Kuroshio's path is closely related to variations of sea level. Naeije and Ambrosius [24] analyzed the relationship between sea level and temperature in the western Pacific, finding that variations in sea level often follow changes in temperature and that changes in one factor are followed by changes in the other about a month later. Kawabe [25] performed a long-term measurement of the waters south of Japan, finding that variation in sea level is positively correlated with the flow rate of the Kuroshio, with larger differences in sea level associated with faster flow rates. When the axis of the Kuroshio moves north, the sea level of the surrounding waters rises significantly, but the rise is not correlated with the vertical water flows.

In another study, Kawabe [26] found that when the Kuroshio in north Pacific flows to 134°E, it curves southward with an increased flow rate and volume, and with a surface higher than that of the surrounding waters. The greatest rise in sea level is found in the waters between Naze (in Okinawa Prefecture) and Nishinoomote (south of Kyushu's Kagoshima Prefecture), coinciding with another increase in the flow rate of the Kuroshio. He also found that as the Kuroshio flows through the Tokara Strait, its sea level, flow rate, and curvature depends on whether the current tends to the north or south, with the northern track exhibiting increased sea level, flow rate, and curvature, while the southern track shows reduction in all three parameters.

1.2.6 Depth Effect

In the area of the Kuroshio extension in north Pacific, the cause of the Kuroshio meandering and its curved path are found to be related to deep water activity. In the 1950s, researchers investigating the Kuroshio south of Japan indicated that the path curvature is inversely proportional to the flow rate, but this conclusion was later refuted due to their failure to account for how the flow calculations might be affected by the movement of waters below the Kuroshio [27]. Robinson and Niiler [28] indicated further that deep water movement can cause the Kuroshio to flow in a straight path along the slope of the continental shelf, but, nevertheless, when the deep water motion stops, the Kuroshio behaves as a Rossby inertial wave flowing along the meandering curve path. Later, White and McCreary [29] used vorticity conservation equations to investigate Kuroshio path variability and shown that the Kuroshio meandering is caused by a Rossby lee wave from the shelf slopes of Kyushu, and the wavelength of meandering is related to the velocity of the Kuroshio.

1.2.7 Typhoon Effect

The typhoon-driven wave might have a complex impact on the Kuroshio, which can be generally categorized as follows:

1. Variations of path and volume
   Sun et al. [30] conducted a numerical analysis for the impact of typhoons on the Kuroshio's path south of Japan, finding that violent disturbances on the sea surface caused by a typhoon produces a strong upwelling, further strengthening the counterclockwise eddy and causing the Kuroshio to deviate southward from original path by about $2°$ of latitude. In terms of flow volume, Chen et al. [31] suggested that, in the sea as east Taiwan, typhoons with a diameter exceeding 200 km (a large counterclockwise eddy) can reduce significantly the Kuroshio's flow volume and cause a $180°$ change of the Kuroshio flow direction.

2. Upwelling enhancement
   Because of the low pressure at the sea surface induced by the typhoon, a significant upwelling of deep sea water can be generated, increasing the concentration of surface nitrates and chlorophyll, and doubling the volume of particulate organic carbon flux. Plankton can be brought to the surface by the upwelling, reducing the sunlight penetration and luminosity of the water [31].

3. Reduction of surface temperature
   Due to the upwelling caused by typhoon, the temperature of the Kuroshio water at surface at east Taiwan, for example, is normally 28 °C in average, which can drop to 25 °C before and after the impact of typhoon, though the temperature will recover to 28 °C about 10 days after the typhoon passed. The presence of a typhoon can also cause a rapid expansion of the low-temperature sea area (usually lower than 27 °C) to 15,000 km^2 or more, which will also gradually disappear after the typhoon passed [32].

4. Variation of algae species

   Again, due to the upwelling caused by typhoon, the change of algae species in the Kuroshio can be significant. Before a typhoon hits, algae populations of the Kuroshio water are mostly comprised of smaller dinoflagellates (Gymnodinium, Trichodesmium, etc.), indicating the water is of oligotrophic. Three days after a typhoon hits, however, the algae in this area is found to be dominated by diatoms (Pseudo-nitzschia and Nitzschia). Changes occur further 7 days after the typhoon hit; algae populations are then dominated by larger cell colony formation of diatoms (*Chaetoceros muelleri*, etc.), indicating a large-scale introduction of nutrient-rich seawater into the Kuroshio [32].

   Later in Sect. 5.4.1, the impact of the typhoon named Morack, which attacked Taiwan in August 2008, will be discussed. The research results made by both measurements and computations will be examined to discuss various influences on the Kuroshio caused by typhoon's attack.

1.3   Power Reserve of the Kuroshio

Figure 1.2 shows the annual-averaged energy density distribution of the Kuroshio, which was computed by Chao (Exploring Kuroshio's energetic cores with an ocean nowcast/forecast system. Private communication, University of Maryland, 2008) using a computer code simulating global ocean motion under the boundary conditions such as the sea level, the temperature, and the salinity at sea surface detected by satellites. The power density distribution of the Kuroshio of Fig. 1.2a shows that, after the Kuroshio enters the area off of Taiwan's east coast, it immediately hits Lan-Yu and splits into two streams flowing around the island. The eastern stream is quickly dissipated in the Pacific due to viscous friction, while the western stream is driven strongly north due to the aforementioned three-force-balance relationship. The highest energy density is found in the waters between Lu-Dao and Tai-Dong. This is because, when the western stream from Lan-Yu enters the channel between Lu-Dao and Tai-Dong, it is compressed and accelerated by the rising seabed. This acceleration extends over several tens of kilometers to the area off the coast of Hua-Lien where it finally slows down but is of a larger flow area, with the overall flow volume remaining unchanged.

Figure 1.2b shows the Kuroshio's velocity distribution on a vertical cross-section between Lu-Dao and Tai-Dong. It is found the maximum velocity of the Kuroshio occurs at the surface due to the fact that the majority of the driving force is derived by atmospheric circulation. In the water closer to the land (Tai-Dong on the left and Lu-Dao on the right), the flow velocity drops due to the friction caused by the coast. As a result, there are over 50 % of the Kuroshio's kinetic energy being concentrated in the current's central part and within a depth of 100 m. Consequently and ideally, the turbines of the Kuroshio power plant should be deployed close to the surface and away from the coast. However, the turbines may have to be positioned several tens of meters below the surface to prevent the potential damages caused by, for example, typhoon-driven waves, interference with shipping or
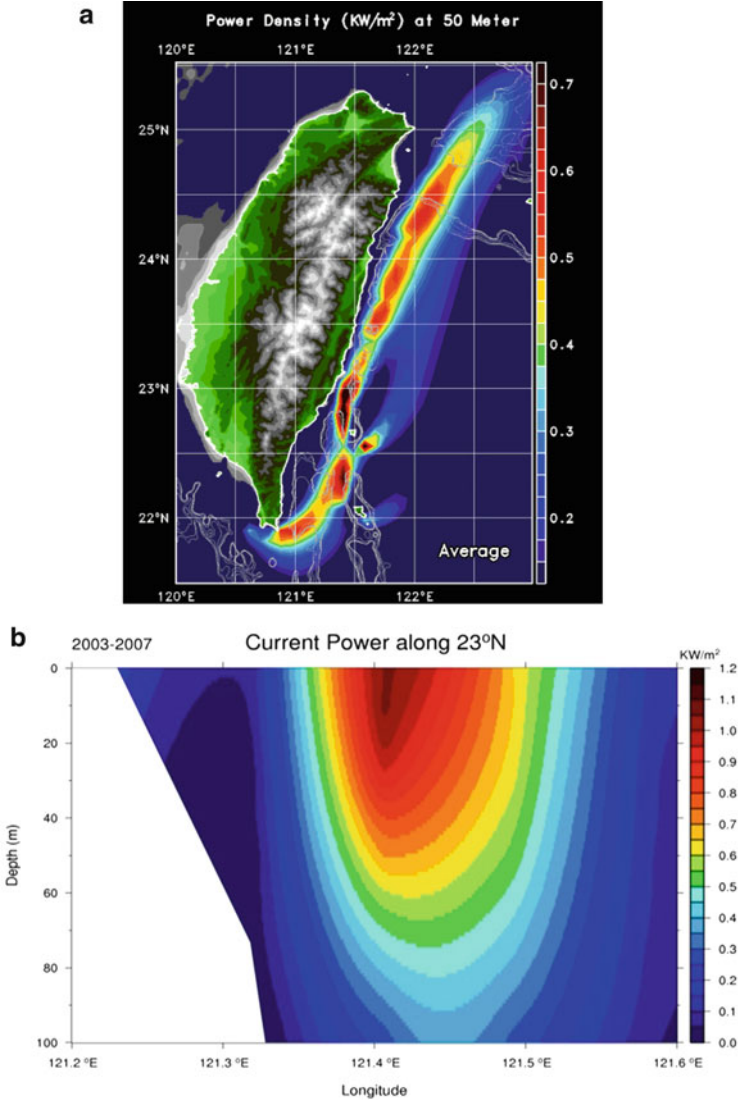
Fig. 1.2 (**a**) Annual averaged energy density distribution along the Kuroshio for 2007 at a depth of 50 m. When the Kuroshio enters the waters east of Taiwan, the current is very strong before corrections due to seabed variation in the area between Lan-Yu, Lu-Dao, and Taiwan, after which it flows north along the east coast towards Ryukyu islands. (**b**) The vertical sectional view of the velocity distribution of the Kuroshio at 23°N. Tai-Dong County, on the east coast of Taiwan, is to the left, while Lu-Dao is on the right at a distance of about 32 km. The velocity distribution shows that the Kuroshio is a surface current, with more than 50 % of its energy concentrated near the surface while far from the coast, with the maximum velocity occurring at the sea surface [*Source*: [10]; Courtesy of Professor Shenn-Yu Chao (Exploring Kuroshio's energetic cores with an ocean nowcast/forecast system. Private communication, University of Maryland, 2008)]

fishing, and the cavitation occurred on the surface of turbine blade. Therefore, the energy that can actually be harvested from the Kuroshio will be less than the current's theoretical reserve. We shall discuss the strategy of the turbine deployment and the criteria of the power plant site selection in Chap. 6, where a conceptual design of a 30 MW pilot plan is discussed based on the flow and geological data measured in the area between Lu-Dao and Tai-Dong.

The Kuroshio's annual-averaged flow rate can be calculated from the data used to make Fig. 1.2. Both the ocean current simulation [16] and the on-site single point test [33, 34] estimated that the maximum flow rate of the Taiwan Kuroshio is around 20–30 sv, equivalent to about 100 times the flow rate of the Brazilian Amazon River or 1,000 times the Yangtze River or Mississippi River. Given that the average velocity of the Kuroshio is 1 m/s, the average power of each cross-section of the Kuroshio can be as high as 5.5 GW. This estimation is confirmed by the data shown in Fig. 1.3, in which the variations of average power at three different cross-sections in 2005 are shown. The data show that the average power of a cross-section is about 6 GW, but this energy is subject to variation due to many factors. As discussed in previous section, these factors are closely related to many different factors such as the frequency and intensity of typhoons or the appearance and intensity of El Niño, while the factor due to seasonal change influences most significantly and constantly, pulling the Kuroshio power down to as low as 4 GW in winter and pushing it up to as high as 10 GW in summer.

To further understand the Kuroshio's seasonal variations, the 5-year-average power density distribution of each month during 2003–2007 are plotted in Fig. 1.4. Results show that the Kuroshio's energy density and drainage area begin to increase in February and reach its peak in July before falling off again in autumn and winter. Generally speaking, the Kuroshio slows down considerably under the influence of northeastern monsoon in winter, while its power density and drainage area expand considerably in spring and summer. On the other hand, however, the Kuroshio's path is not affected by seasonal changes, and the current mostly flows north straight along Taiwan's east coast without the meandering seen in the sea at south Japan. It is also seen from Fig. 1.4 that the previous-mentioned factors that influence the Kuroshio's path do not have a significant effect in the waters at east Taiwan. This shall be a result due to the strict balance among the three forces: the flow momentum, the Coriolis force, and the sea level difference. And this balance is well maintained due to the presence of the Taiwan mainland on the left of the Kuroshio, which acts as a boundary to the Kuroshio guiding the flow path and offering a reacting force to level up the sea surface.

At last, we shall emphasize that special attention should be paid to the impact of typhoon and El Niño. In the north Pacific, typhoons mostly occur in summer and fall, coinciding with the Kuroshio's maximum power season, which may cause the decrease of the power output or, more seriously, the temporary shutdown of the power plant. Since its critical influence period is relatively short, typhoon's influence can be hardly seen from the 5-year-average power distribution depicted in Fig. 1.4. On the other hand, El Niño occurs on average once every 7 years. Once occurs, it can
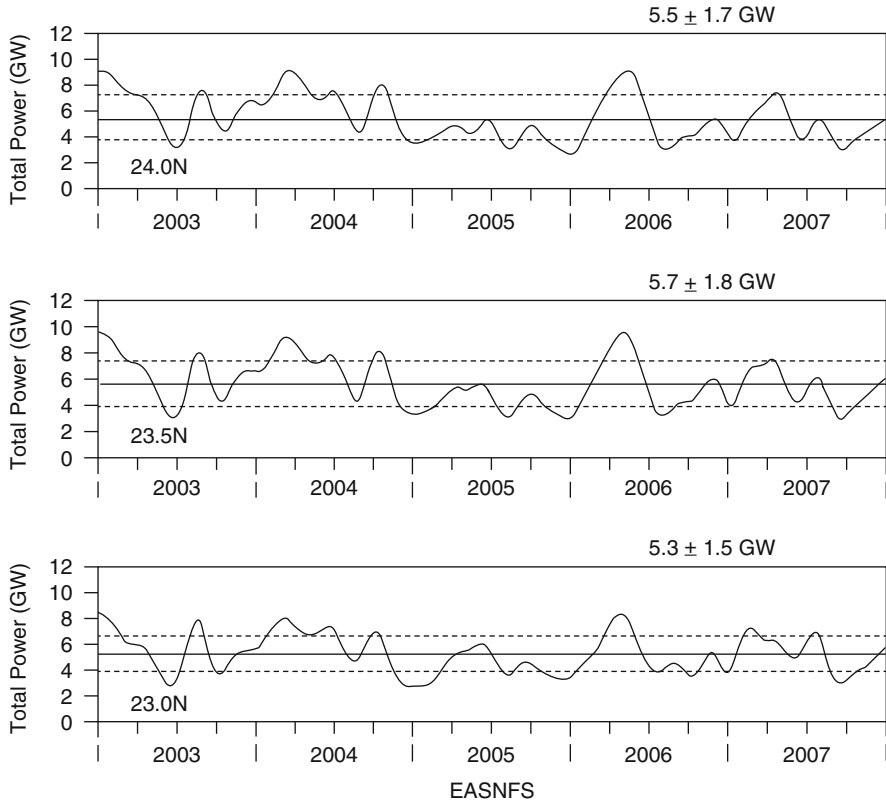
Fig. 1.3 Kuroshio energy variation over time in three sections. The three sections are, respectively, located at 23°N (near Tai-Dong and Lu-Dao), 23.5°N (near Hua-Lian), and 24°N (near Su-Aou). The figure shows the following phenomena: (1) energy variations in the three sections are practically synchronous, (2) the energy increases as the current flows north, and (3) the energy in the three sections ranges from a maximum of 10 GW to a minimum of 4 GW [*Source*: [10]; Courtesy of Professor Shenn-Yu Chao (Exploring Kuroshio's energetic cores with an ocean nowcast/forecast system. Private communication, University of Maryland, 2008)]

cause extreme climate change in the western Pacific, disrupting monsoon winds and rains with seasonal variations, which in turn will lead to a dramatic change of the driving force of the Kuroshio.

1.4   Topography and Geology of the Seabed

About 60 million years ago, the island of Taiwan was formed by the collision between the Philippine Sea Plate and the Eurasian Continental Plate. Over the years, the collision widened and rose, and through countless changes in the crust surface, volcanic eruptions, and plate impacts to form the region's current topography, structure, rock formation, and terrain [35]. The Luzon island arc at southeast Taiwan
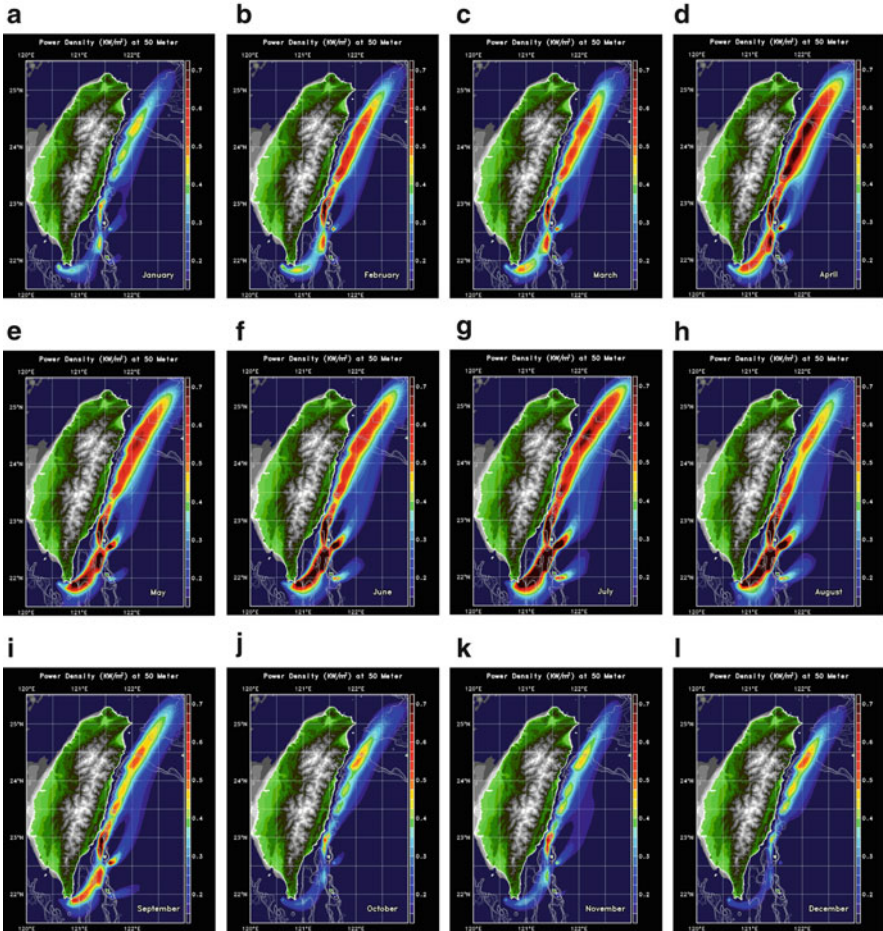
Fig. 1.4 Average monthly flow power density (KW/m^2) of the Kuroshio at a depth of 50 m. (**a**) January, (**b**) February, (**c**) March, (**d**) April, (**e**) May, (**f**) June, (**g**) July, (**h**) August, (**i**) September, (**j**) October, (**k**) November, (**l**) December [Source: [10]; Courtesy of Professor Shenn-Yu Chao (Exploring Kuroshio's energetic cores with an ocean nowcast/forecast system. Private communication, University of Maryland, 2008)]

is still moving northwest towards the Eurasian Continental Plate at a rate of 6–8 cm per year [36, 37]. This force generated by plat extrusion continues to lift the crust of Taiwan island from east to west, forming the eastern coastal mountains, the Central Mountain Range, and the western foothills and coastal plains [35].

The tectonic activity of the Taiwan Plate causes an intensive distribution of undersea fault under the Kuroshio water. The seabed is divided into densely packed strata to form a rugged seabed, which is covered by a thick and rapidly accumulating layer of sediment eroded from Taiwan's mountains and the Luzon Arc. Due to the frequent seismic activity, the sediment may end up with ubiquity of
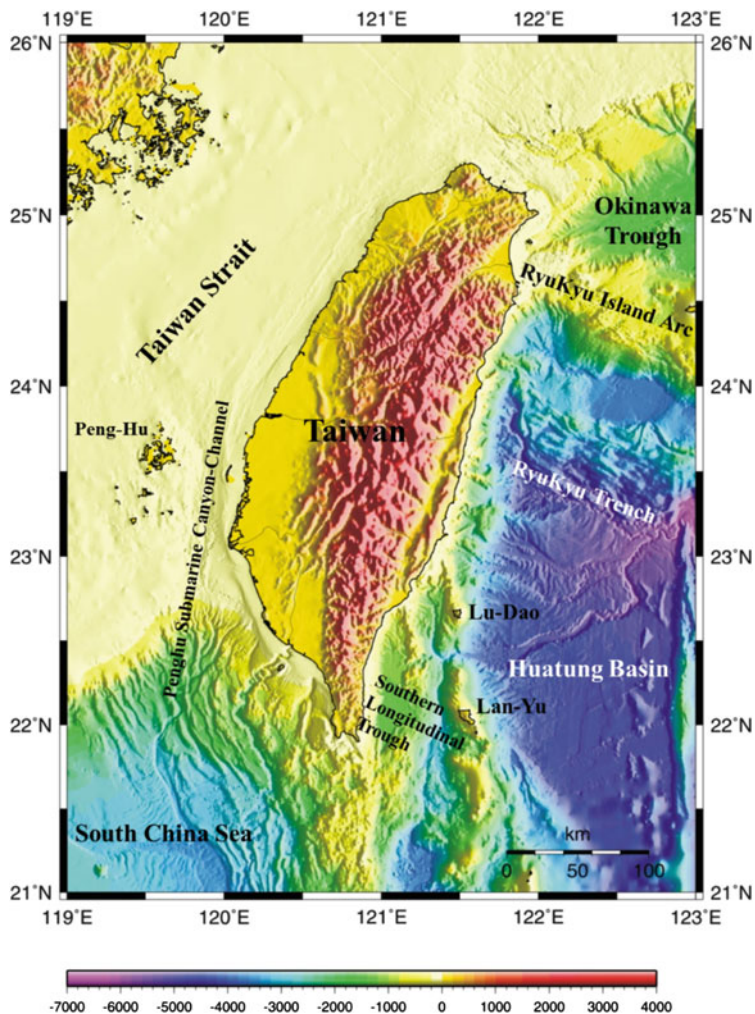
Fig. 1.5 Topographic map of the waters around Taiwan. Taiwan's Central Mountain Range stretches from north to south. The Coastal Range lies along Taiwan's east coast, with the Hua-Dong Valley lying between the two ranges. The sea off the east coast varies greatly in depth, exceeding 1,000 m within 3 km off the coastline. An arc of volcanic islands between Taiwan and Luzon (including Lu-Dao and Lan-Yu) provides an area of shallow water (Courtesy of Professor Char-Shine Liu, 2012)

undersea landslides [38–41]. The Kuroshio flows through a water under which a steep terrain rapidly increases in depth to 3,000 m within a range of 10 km off of Taiwan's east coast (see Fig. 1.5). Shallower waters are only found in four areas: in the south along the Heng-Chun Peninsula at Taiwan's southern tip, in the southeast at the waters between Taiwan and Lan-Yu and between Taiwan and Lu-Dao, in the northeast at the waters between Yi-Lan continental shelf and Ryukyu island arc, and in the far north along East China Sea continental shelf and Okinawa Trough.

Table 1.1 The physical properties of the andesite found from Lu-Dao

Sample	Density (tons/m^3)	Moisture content (%)	Porosity (%)	Compression strength (MPa)	Strength grade [Note]
1	2.14	4.26	4.84	42.78 − 60.68	Strong rock
2	2.34	7.51	17.6	81.95	Strong rock
3	2.60	5.92	15.4	28.60	Mid-strength rock
4	2.28	0.62	3.28	157.0–192.3	Very strong rock
5	2.06	2.24	11.3	142.0–171.3	Very strong rock
6	2.98	3.67	3.60	118.2	Very strong rock
7	2.72	6.11	4.38	86.25–157.3	Very strong rock
8	2.63	4.18	6.81	84.56–104.0	Strong rock

A total of eight core samples were subject to physical and mechanical property tests including natural physical property tests, point loading tests, and compaction tests [42, 43]
Note: Weak rock <25 MPa; Mid-strength rock 25–50 MPa; Strong rock 50–100 MPa; Very strong rock 100–250 MPa

Figure 1.5 shows an underwater volcanic ridge stretching from south to north between Luzon arc and Taiwan's east coast, dotted by several volcanic islands with Lu-Dao in the north and the Babuyan Island group in the south. The so-called Lu-Dao-Babuyan Ridge also includes Lan-Yu of Taiwan and Batan and other islands of the Philippines. These volcanic islands are formed of andesite, which is a result by magmatic activity caused by the subduction of the South China Sea Plate [41]. The seabed surrounding Lu-Dao is also formed of andesite, and the granularity of the sediment varies with depth, with an average size of about 20 μm (10^{-6} m) [42, 43]. The physical properties of andesite are summarized in Table 1.1. As the volcanic magma solidified to form the andesite, the rock becomes light and porous with a compressive strength of 28.6–192 MPa (106 Pa). The andesite under Kuroshio is classified to be of mid or high strength, making it suitable for the anchorage engineering for the relay platform. Even so, still, a careful survey shall be completed prior to the construction to ensure that the anchors are not sunk into loose or broken rock.

1.5 Hydrological and Chemical Environments

Generally speaking, the hydrological environment refers to the movement, the distribution, and the quality of a body of water. These features include the circulation of the body of water, the water source, and the flow continuity. The movement of a body of water, such as the ocean current, is generated primarily by atmospheric circulation and modified by the earth's spinning. The flow direction and distribution is also affected by local terrain and water's quality. To understand flow distribution and water quality requires well-defined parameters for the body of water, which in general are temperature, salinity, and density. Each body of water has its own combination of temperature and salinity, and these parameters are commonly measured to determine

the properties of the body of water and to determine how the body of water will interact with others.

Oceanic chemistry primarily focuses on changes in the distribution and behavior of chemical elements in the ocean. The chemical environment refers to the concentration, classification, and reaction of these elements in the sea water, including biological reactions and concentrations resulting from the presence and activity of biological organisms. Generally speaking, the type of chemical elements present in sea water is determined by salinity and pH value. Therefore, understanding the composition of a given body of water may provide insights into the interaction between these elements and sea water and its impact on the environment.

As it runs along Taiwan's east coast, the Kuroshio interacts with other bodies of water in the western Pacific, including arctic sinking water, north Pacific intermediate water, north Pacific central water, and the water injected from rivers. Among these, the north Pacific central water has the greatest impact. Because the waters off of Taiwan's east coast are often thousands of meters in depth, its water structure is similar to that of the western Pacific except for the fact that the Kuroshio pushes the surface water northward, resulting in differences in the hydrological and chemical environment from the Pacific. Since the movement of the Kuroshio has been illustrated in previous sections, the following discussion shall focus on the seawater composition and the distribution and change of chemical elements.

1.5.1   Hydrological Environment

The wide variety of solutes found in the seawater can be broadly categorized as inorganic salts, organic compounds, and gasses, of which inorganic salts account for the largest volume. Inorganic salts are mostly derived from thawed soil. Dissolved in seawater, more than 95 % of inorganic salts are made up of Na^+ and Cl^- ions, with the remainder composed of sulfates, magnesium ion, potassium ion, and calcium ion. The total weight of these ions is commonly referred to as S (salinity) or psu (practical salinity unit, with 1 psu = 1 g salt per kg seawater).

In ocean, the salinity varies generally from 33 to 37 psu, and the average value is about 35 psu. The salinity is influenced by precipitation and evaporation, resulting in a higher salinity in tropical and subtropical waters and a lower salinity in temperate and boreal waters. On the other hand, the seawater density changes with temperature and salinity. As temperature is fixed, the density is proportional to the salinity; as salinity is fixed, the density is inversely proportional to the temperature as it is higher than 4 °C. In addition, the water at larger depth is of higher density due to increasing pressure. In general, the seawater belongs to the same body of water having the same relation among temperature, salinity, and density. The following example explains well the scenario.

According to the analysis made by Professor Pai Shu-Chen (private communication, 2012), the surface water of the sea off of Taiwan's east coast basically comes from the south and is transported rapidly north by the Kuroshio. As seen in Fig. 1.6, the
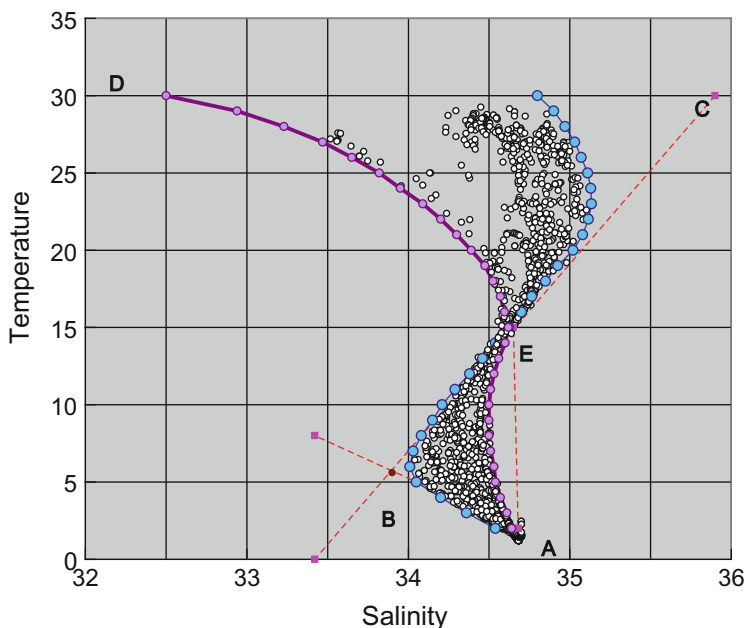
Fig. 1.6 Temperature and salinity in the western Pacific, the Philippines Sea, the Luzon Strait, and the northern South China Sea. A–B, B–C, and A–E are connections between various seawater layers. Increased mixing of the water masses creates two interlaced smooth S-curves. The *circled-line* from the *upper right* to the *lower left* represents the Philippine Sea water mass, while the *circled-line* from the *upper left* to the *lower right* is typical of the South China Sea water mass. The temperature and salinity for the water layers from the western Pacific to the South China Sea all fall within the two S-curves (*Source*: Indopac survey, Sea Research 1, voyages 257, 266, 287, 300; courtesy of Professor Shu-Chen Pai, 2012)

temperature and salinity of the waters of the western Pacific, the Luzon Strait, and the northern reaches of the South China Sea clearly result in a mixing of water column originating from different sources, or called end members, labeled A through D, with the following characteristics:

- A: Arctic and Antarctic sinking water typically features a temperature of 2 °C and salinity of 34.68 psu.
- B: North Pacific intermediate water features a temperature of 5.6 °C and a salinity of 33.9 psu. This water mass originates in the Sea of Okhotsk and the Bearing Sea, and is the only sinking water area in the north Pacific, stretching south through a gap in the Kuril Islands to arrive near Taiwan at a depth of around 600 m.
- C: North Pacific central water is characterized by a temperature of 30 °C and a salinity of 34.9 psu. It originates in the open ocean west of Hawaii, being about at the center of the North Pacific Gyre. The surface is exposed to evaporation, thus being of higher salinity and density. As it sinks into the surrounding waters especially the southern waters, it will be transported with the Pacific North Equatorial Current

moving west towards Luzon and Taiwan. Equatorial rainfall and freshwater runoff from islands marginally dilutes the salinity to 35 psu near the surface, but the temperature remains around 30 °C. As it approaches Taiwan's east coast, this body of water becomes the main axis of salinity of the Kuroshio, which locates at a depth of about 150 m.

- D: Uncertain sources, including low-latitude rainfall and river outflows from Indonesia, the Philippines, and lands surrounding South China Sea (including the Pearl River, Mekong River, Red River, and Chao Phraya River), can substantially dilute the salinity but has little effect on the water temperature.

In Fig. 1.6, the body of water can move freely along the surface of constant density while mixes vertically with other waters through molecular diffusion. Most interestingly, the intersection point E between the two curves represents a point of equal density for all the waters at subsurface, with a temperature of 15 °C and a salinity of 34.65 psu. In the waters around Taiwan, this point appears at depths greater than 200 m. In the waters between Tai-Dong and Lan-Yu, the body of water within a depth of 400 m mostly comes from the North Pacific intermediate waters (close to the CE line), while those deeper than 400 m come from South China Sea (close to the EA line).

Inorganic salts not only can affect the salinity of seawater but also have effects of various level on their ionic strength, ionic affinity and pH value. For example, CO_2 dissolves in seawater as CO_3^{-2}, which can easily combine with calcium to form $CaCO_3$, which plays an important role in the formation of coral reefs and shells of some mollusks. A high carbonate content indicates a low pH value, causing the continued release of carbonates in the water, which shall affect the growth of coral and flowstone algae. In addition, the sea itself provides a good buffer solution, limiting the damage to biological organisms from non-drastic changes in pH value. Usually, the pH value of the ocean remains to be eight.

Light penetration in the body of water is related to the volume of suspended particulates which reflect and refract light in high concentrations. Accordingly, increased light penetration indicates reduced levels of suspended particles, while decreased light penetration indicates increased levels of particulates. Generally, the light penetration of open ocean is higher than that in estuarine coastal areas because runoff and rivers carry a large volume of mud and sand, increasing the particulate loading of the water. Because of its warm temperature and high flow rate, the Kuroshio water have low particulate loadings and high light penetration, resulting in a high illuminating water where biological activity can be relatively high at deep water.

Seawater contains copious amounts of dissolved gasses, with dissolved oxygen primarily coming from interaction between seawater and air at the surface, and those released through the photosynthesis of phytoplankton, which usually occurs in water layers with ample light. On the other hand, both the respiration and decomposition of biological organisms consume more oxygen in deeper water. Consequently, the dissolved oxygen is larger in the shallow water of more light than in the deeper water of less light; as depth increases, the dissolved oxygen increases again because of lower temperature and less biological activity.

Table 1.2 The hydrological data of the Kuroshio seawater at various depths [42]

Depth (m)	Temperature (°C)	Salinity (psu)	Density (kg/m^3)	Dissolved oxygen (μM)	Light penetration (l/m)
0	30	33.6	21	200	2.6
100	28	33.8	23	180	1.4
200	22	34.8	24	160	0.4
300	14	34.4	26	140	0.2
400	10	34.2	27	120	0.2
500	8	34.0	27	110	0.2

The vertical variation of the level of dissolved oxygen in the Kuroshio is similar to that found in general seawater, ranging from 75 to 210 μM (10^{-6} mol) [44, 45]. On the other hand, regarding the CO_2 of the Kuroshio water, since it is not only dissolved in the air-sea exchange, but also is related to the respiration and decomposition of marine organisms. The CO_2 concentration increases with depth in the Kuroshio, changing within a range of 1.80–2.34 mM/kg (10^{-3} mol/kg) [44]. Table 1.2 summarizes changes in hydrological conditions at various depths in the Kuroshio.

1.5.2   Chemical Environment

Nutrient salts refer to substances required for biological growth, generally nitrates, phosphates, and silicates in the ocean. Ocean nitrates mainly take the form of NO_3^{-2} from river outflows, rainfall, and biological nitrogen fixation, while phosphate comes from rocks and bird droppings, and silicates are dissolved from rocks. Thus, nutrient silicates exist in higher concentrations near coastal river mouths. Concentrations of nutrient salts in the ocean generally increase with depth due to, first, the biological absorption and utilization in illuminated shallow layers and the fact that, second, in deep waters nutrient particles sink and dissolve without being utilized or absorbed, resulting in a higher concentration at deep water than near the surface.

In the illuminated layer above, the concentration of nutrient salts is influenced by not only the terrestrial inputs but also the mixing of the lower non-illuminated water mass with the layers above. In colder seasons, the temperature differential of the upper and lower water layers decreases, blurring the distinction between the layers. However, in warmer seasons, the temperature differential increases, resulting in a clear thermocline and a clear delineation between the upper and lower layers. In addition, in summer phytoplankton absorb vast amounts of nutrient salts, resulting in an extreme low concentration of nutrient salt as external sources are absent, while the reverse is true in winter. In the Kuroshio, because of the high light-penetration rate, the concentrations of nitrates, phosphate, and silicates, respectively, range between 0–28 μM, 0–2 μM, and 1–66 μM [44], which is relatively low comparing with the surrounding water.

Trace elements refer to rarer elements in the ocean, including copper, tweezer, cadmium, and iron. These elements can be classified into essential elements and

Table 1.3 Marine nutrient concentrations and heavy metal content of the Kuroshio at various depths [42]

Depth (m)	Phosphates (μM)	Nitrates (μM)	Silicates (μM)	Cadmium (nM)	Silver (pM)
0	0	0	1.0	0	0
100	0.5	8.0	12	0.18	2.5
200	1.0	15	26	0.30	5.0
300	1.3	20	38	0.40	6.5
400	1.6	25	45	0.52	10
500	2.0	28	66	0.57	13

μM $= 10^{-6}$ mol, nM $= 10^{-9}$ mol, pM $= 10^{-12}$ mol

nonessential elements for biological life. For example, copper is an essential and important element in serotonin in crustaceans, while cadmium is a nonessential element because it can cause metal poisoning in biological organisms. Trace elements in the ocean come from the same sources as nutrient salts, and are similarly distributed.

Nutrient salts and essential elements become concentrated within biological organisms as they are actively absorbed. However, some nonessential elements are also absorbed along with the nutrient salts into the biological organisms. Some of them can be toxic and cannot be precluded, so that the biological organisms react in a way either by producing a coating protein to isolate the toxic element. These ingested nonessential elements are accumulated in the organism. When the concentration of nonessential elements exceeds that of essential elements by several times (a phenomenon known as bio-magnification), the organism may be poisoned, which may in turn influence the chemical ingredients in the seawater.

In the surface water of the Kuroshio, copper concentration varies from 7.0 to 11.0 nM/kg (10^{-9} mol/kg) and shows significant seasonal fluctuation. Cadmium concentration does not fluctuate seasonally and stays within a range of 0.36–0.53 nM/kg [46]. Concentrations of cobalt and nickel, respectively, range between 1.2–2.4 nM/kg and 1.9–3.7 nM/kg. In addition, studies of particle and element concentrations in organisms indicate that the average concentration of copper in suspended particles is 142 gg^{-1} (element weight normalized by sampling weight), while the concentrations of cadmium, nickel, and zinc are 2.80, 84.1, and 818 gg^{-1}, respectively, and increase with depth [47]. Concentrations in zooplankton for cooper, cadmium, nickel, and zinc were found to be about 30–60, 3–16, 100–300, and 75–250 gg^{-1}, respectively [48]. Table 1.3 shows the vertical variations of nutrient salts and nonessential elements (cadmium and silver) in the Kuroshio.

Aggregated studies of the hydrological and chemical environment show that temperature and salinity remain mostly in a high level in the Kuroshio and their variations stay within a limited range. Given the nutrient salts and essential elements contributed from land-based sources stay mostly in the illuminated layer, they will be "reserved" in vivo in the organisms which ingest them, resulting in that the surrounding waters will stay in a state lacking in nutrient salts. In addition, some types of algae in the Kuroshio, such as tricodesmium, will engage in nitrogen fixing (or denitrification), producing more nitrogen salts for their own growth,

with the excess released into the water, increasing the concentration of nutrition salts to be used by other organisms. In conclusion, biological organisms have a significant influence on changes in the Kuroshio's chemical environment, and the survival mechanisms of biological organisms can be considered to be a type of chemical change. Therefore, biology and chemistry are inextricably linked, particularly in the illuminated layer of the Kuroshio which has the highest level of biological activity.

The discussion above leads to a question: How can the Kuroshio, a water being clear and lacking for nutrient salts, offer the nutrient salts to form a bioaccumulation? Professor Pai Shu-Chen (private communication, 2012) noted that the nutrient chain does not completely rely on the apparent amount of nutrient salt concentrations but on the supply of nutrient (or the nutrient flux). In other words, the Kuroshio itself does not contain high concentration of nutrients, but the volume of nutrient flux is surprisingly high. Moreover, the ocean current winds through sea sills, bringing nutrient-rich water up from the bottom, while on both the left and right sides of the Kuroshio small eddies are created to contribute to the expansion of the biological food chain. Therefore, despite the low nutrient concentrations in the water, the high volume nutrient flux in the Kuroshio behaves like a nutrient highway for biological organisms, with many migratory organisms (ranging in size from eel fry to swordfish) following the current for long distances and contributing to the fishing catch off of Taiwan's eastern coast.

1.6 Ecological Environment

The north Pacific is a vast, complex ecosystem. With its high temperatures and lack of phytoplankton, the Kuroshio basin features less ecological activity than neighboring bodies of water which feature relatively rich ecosystems. Below we describe the Kuroshio's ecological structure in terms of the marine food chain, starting from the bottom with phytoplankton, continuing up through common larval fish populations and ending with marine mammals.

1.6.1 Phytoplankton Populations

Phytoplankton refers to a group of photosynthesizing single-celled organisms between 2 and 200 μm in size. Some species, such as Tricodsium, often appear in the summer in the Kuroshio waters. These organisms bundle together to raise their chances of survival. Phytoplankton are the primary producers of the oceans, using photosynthesis to convert CO_2 into required nutrients, and releasing O_2 for use by other organisms. Phytoplankton is also a food source for other plankton which is, in turn, a source of nutrition for seaborne bacteria [49]. Phytoplankton absorb CO_2; then, when they die, they sink to the bottom depositing their CO_2 at the seabed in a process known as biological pumping, which plays a key role in mitigating global warming. Thus, phytoplankton is not only a source of organic carbon for marine

Table 1.4 Phytoplankton chlorophyll concentrations on Taiwan's continental shelf, upwelling zone, and the Kuroshio area as a basis of productivity and species dominance

	Continental shelf[a] or upwelling zone[b]	Kuroshio area	Reference
Chlorophyll *a* concentration (mg/m^3)	0.1–1.1[b]	0.1–0.5	Chen [51]
	0.2–3.1[ab]	0.2–1.0	Gong et al. [54]
	3.93[a]	0.11	Shiah et al. [55]
	0.89[a]	0.10	Chang et al. [52]
	NA	0.06–0.08	Chen et al. [53]
Base productivity (mg C/m^3/day)	207.15[b]	11.30	Chen [51]
	20–140[ab]	20–110	Gong et al. [54]
	160.7 [a]	3.2	Shiah et al. [55]
	NA	8	Chen et al. [53]
Dominant species	*Tricodesium* spp. [ab] *Thalassionema nitzschioides*[ab] *Nitzschia* spp.[ab]	*Tricodesium* spp.	Chen [51]
	Synechococcus spp.[a] *Skeletonema costatum*[a]	*Synechococcus* spp.	Chang et al. [52]
	NA	*Prochlorococcus* spp. *Synechococcus* spp.	Chen et al. [53]

[a]In continental shelf
[b]At upwelling zone
NA indicates no measurements available

ecosystems but also helps sequester carbon on a global scale, thus playing a key role in maintaining marine ecological environments and mitigating climate change.

Takahashi et al. [50] found that phytoplankton species along the south coast of Japan and in the Kuroshio basin are made up mostly of small types of blue-green algae, in some places accounting for more than 50 % of the total biomass, and that small algae species frequently are the dominant species in oligotrophic salt regions. Chen [51] studied differences in phytoplankton species and volumes in the upwelling area and the Kuroshio basin on the continental shelf off of Taiwan's eastern coast. Results showed that *Tricodesmium* ssp. accounted for the vast majority of phytoplankton (nearly 88 %), with *Thalassioneme nitzschioides* and *Nitzschia* spp. featured as other dominant species. Other studies [52, 53] also found a predominance of *Prochlorococcus* ssp. and *Synechococcus* ssp. (see Table 1.4). After surveying the Kuroshio basin and the Philippine Sea, Yang et al. [56] found 24 types of Coccolithophora—a kind of small phytoplankton—as opposed to only 19 types in Taiwan's coastal waters, indicating this is the dominant phytoplankton species in the Kuroshio basin. Due to its nitrogen fixation capacity, *Tricodesmium* ssp. can turn N_2 into NO_3 for its own use, thus making it the dominant species in the nutrient-poor Kuroshio.

From Table 1.4 that summarizes research results regarding the surface phytoplankton biomass found in the Kuroshio, one can see that Chlorophyll concentrations are low, mostly around 0.1 mg/m^3 and making out at 1.0 mg/m^3 [53, 54, 56], levels which are 3–8 times lower than the coastal upwelling area. In addition that the

continental shelf zone has a more abundant supply of nutrients; the upwelling at Taiwan's northeast tip also carries nutrient salts from deep waters into the Kuroshio, resulting in higher concentrations of nutrient and biomass in the upwelling area.

Regarding the productivity, aside from Gong et al.'s [54] measured productivity levels of 110 mg C/m^3/day, other measurements were found to be within 3–11 mg C/m^3/day, being about 20 times lower than those at coastal or upwelling areas. Since productivity refers to the capacity of organic carbon of the local ecosystem provided by phytoplankton, it is therefore seen as a criteria to justify whether there is sufficient nutrients to support higher-order food chain organisms such as fishes or mammals. As a result, in the Kuroshio these higher-order organisms shall be quite scarce.

1.6.2   Chlorophyll

Zooplankton swim weakly and generally follow the flow of the ocean. Micro-zooplankton measures from 20 to 200 μm in size and is primarily single-celled flagellates and ciliates. Meso-zooplankton measures from 200 to 2,000 μm and includes Copepoda, Chaetognatha, Pteropoda, and appendicularia. Finally, macro-zooplankton is over 2,000 μm long and includes jellyfish, larval fish, Euphausia, and Salp.

Zooplankton exists in a wide variety, is mostly heterotrophic, and is the food source for other organisms such as phytoplankton and micro-zooplankton. Some species (known as mixotrophic) also feature internal chloroplasts, allowing the zooplankton to produce its own energy. Zooplankton forms the ecosystem's primary consumer and also serves as a primary food source for higher-order organisms. From the standpoint of fishery resources, it is a basic source of nutrition for commercial fish. Zooplankton eats vast amounts of phytoplankton, producing fecal pellet sediments which contribute to biological pumping.

Three factors affect the distribution of planktonic populations: (1) temperature mainly affects the growth rate and maturation of zooplankton and, in conditions of food scarcity, group concentrations change in proportion to changes in temperature, (2) food supply affects zooplankton growth and population sizes, and (3) the number of predators affects zooplankton populations, with zooplankton engaging in nocturnal vertical migrations to escape predators. Among these three factors, food supply has the most significant effect because, even with high temperatures, zooplankton can't grow without adequate food supplies, and predators do not have a dominant effect on population sizes [57]. Below, we itemize the three most populous zooplankton types, copepods, larval fish, and krill, and illustrate their characteristic role played in the Kuroshio basin.

(a) Copepods
   Copepods are the most dominant species of zooplankton. These are a soft crustacean subclass living in salt and fresh water, with nearly 10,000 different types worldwide [58], and nearly 200 types in the ocean at vicinity of Taiwan (Shih, Key to the copepod genera occurring in the adjacent water of Taiwan.

Unpublished, 2001). Because they are primary food organisms, their volume and growth are very important to fisheries. In addition, copepods feed on phytoplankton and are often used as a benchmark for secondary production. Thus, copepods play a very important role in both the global carbon cycle and fishery resource management.

Considerable research has been devoted to Kuroshio copepods [59–63], but finding no significant difference in terms of varieties and abundance within the Kuroshio water. The dominant species are *Paraalanus aculeatus*, *Clausocalanus furcatus*, and *Temora discaudata*, all featuring significant population changes from day to night at depths reaching to about 250 m, but are significantly less abundant in the waters between Lan-Yang river estuary and the Kuroshio. Other dominant species include *Cosmocalanus darwini*, *Clausocalanus minor*, *Oithona plumifera*, and *Oncaea venusta*, all of which are more predominant near Lan-Yang river estuary, and less so in the Kuroshio water.

In addition to the indicator species mentioned above, the Kuroshio also features copepods brought in from other ocean currents and seasonal winds, such as *Calanus Sinicus*, which is the dominant species in East China Sea and is transported to the waters near Taiwan and the Kuroshio basin by northeast monsoon in winter. In fact, the Kuroshio's unique hydrological environment results in it sharing only 16 % of copepod species with other neighboring waters.

In summary, the Kuroshio region's copepods are significantly different from those nearer to Taiwan, and their populations undergo significant seasonal variation in addition to daily vertical migration. Copepod types and volume are subject to the influence of food availability and interaction with other currents. Copepods in the Kuroshio are also an important source of secondary productivity and are a key source of nutrition for oligotrophic phytoplankton in the area lacking for nutrient salt.

(b) Larval fish

In the Kuroshio and upwelling area in the northeast corner of Tawain's continental shelf, zooplankton and fish larvae experience significant seasonal variation. Between 1989 and 1991, stocks of larval fish dropped significantly [64]. While 158 types of Scombridae, Myctophidae, and Myctophidae are found in the Kuroshio in summer, this drops to 136 in winter, but without a significant change in general abundance between the two seasons. However, populations of the dominant species vary significantly with the season, with *Encrasicholina punctifer*, *Engraulis japonicas*, and *Encrasicholina heteroloba* dominant in summer and *Sigmops gracilis*, *Sigmops gracilis*, *Maurolicus* sp., and *Myctophum asperum* dominant in winter [65]. In spring, *Cyclothone alba*, *Vinciguerria nimbaria*, *Scomber* sp., and *Neoscopelus* sp. are dominant, while *Sigmops gracilis*, *Diaphus* sp., *Maurolicus* sp., and *Vinciguernia nimbaria* are dominant in winter. All indicate significant seasonal variation [66].

The regional distribution of larval fish in the Kuroshio shows relative less abundance than that of the water off of Taiwan's east coast or in Taiwan Strait. A total of ten dominant species are found in the Pacific and the Kuroshio basin, comprising 93 % of the total, with *Engraulis japonicas* forming the majority,

followed by *Neoscopelus microchir* and *Cyclothone alba* [67]. A total of 19 dominant species are found in Taiwan Strait and other coastal areas, accounting for 90 % of the total, with *Auxis* sp. forming the majority, followed by *Encrasicholina punctifer*及*Gunnellichthys* sp. Populations in Taiwan Strait and coastal areas are six times that found in the Kuroshio basin, and analysis results show that chlorophyll concentrations and zooplankton levels are proportional to each other, indicating that the population and distribution of larval fish near Taiwan are primarily impacted by the availability of food.

These aggregated research findings indicate the presence of many types of larval fish in the Kuroshio basin is subject to significant seasonal fluctuations. The spatial variation of abundance is similar to that of copepods, with lower numbers in the Kuroshio, and is highly correlated to concentrations of chlorophyll and zooplankton. We accordingly may imply that the number of larval fish is primarily subject to bottom-up control through the food availability and the characteristics of hydrology as well.

(c) Krill

Krill is one of the main food sources for larval fish and fry. Although copepods are more abundant, the dominant species of krill, *Euphausia pacifica*, has 160 times as much biomass [68]. Common carnivorous plankton, such as Chaetognatha, exhibit no significant vertical variation [69], and the vertical distribution among species is almost nonoverlapping, which is believed to be a function of salinity and species characteristics.

The above aggregated studies indicate that zooplankton populations in the Kuroshio area are primarily impacted by food availability. In seas with high level of nutrient salts, food is plentiful and abundant copepods can supply a greater population of larval fish, resulting in greater fish populations, making it a critical factor in the development and distribution of large fish and migratory fish.

1.6.3   Fish and Marine Mammal

Fish are better swimmers (i.e., are nektons) than zooplankton, their movement is thus not necessarily determined by ocean currents. Global fish species exceed over 36,000 types and can be broadly categorized as Chondrichthyes (i.e., cartilaginous fish such as sharks) and Osteichthyes (i.e., bony fish). The key differences between these two categories are that (1) the teeth of Chondrichthyes can be replaced throughout the life of the fish, unlike those of Osteichthyes, (2) Chondrichthyes have 5–7 pairs of gill slits, while Osteichthyes have one on each side, (3) the scales of Chondrichthyes are mostly small and structured similar to shields (known as placoid scales), while those of Osteichthyes are mostly flat and larger, (4) Chondrichthyes do not possess a buoyancy bladder, but achieve buoyancy through the high fat content of the liver and continuous swimming, whereas most Osteichthyes use a bladder to maintain buoyancy, and (5) the tails of Chondrichthyes are large on

top and small on the bottom to increase swimming efficiency, while those of Osteichthyes are more uniform.

The habitat behavior of fish can be broadly divided into two categories: sedentary and migratory. For example, Canadian salmon spend most of their lives in the ocean but migrate back to upstream river to mate and spawn. Fish are also categorized by the area of the ocean they inhabit, including (1) pelagic fish (e.g., mackerel) which stay close to the surface, (2) demersal fish (e.g., flounder and stingrays) which stay on the bottom, (3) oceanic fish (e.g., tuna or swordfish) which mostly stay far out at sea, (4) neritic fish (e.g., shrimp and tiger fish) which stay in the coastal area around estuary, and (5) deep-water fish such as monkfish.

There are 128 types of marine mammals, falling into four categories: Cetaceans, Pinnipeds, Fissipeds, and Sirenians. The most commonly seen cetaceans are dolphins and whales, while pinnipeds include sea lions and seals, fissipeds include sea otters and polar bears, and sirenians include manatees. These are similar to land-based mammals in that they all breathe using lungs, feed on mother's milk, and are viviparous. While cetaceans live fully in the water, they retain traces of mammalian characteristics. For example, in the area of the anus, dolphins have a vestigial limb which corresponds to the hind legs of land-based mammals. Aside from dolphins and carnivorous sea otters, most marine mammals are concentrated in the Polar regions, and some dolphin species engage in long-distance migrations.

The populations of both fish and marine mammals are restricted by food availability. Since fish and dolphin are high up on the marine food chain, they are thus susceptible to the accumulation of heavy metals or toxins which become more heavily concentrated as they move up the food chain. This process is known as bio-magnification and can result in the death or stranding of fish and dolphin. In addition, commercial fish populations may suffer from overfishing and habitat destruction.

At east Taiwan the Kuroshio passes Lu-Dao and Lan-Yu, both islands are featured with coral reefs which support hundreds of fish species (665 species in Lu-Dao and about 620 species in Lan-Yu) [70–72]. The reefs near Lu-Dao are dominated by 103 types of Labridae and 63 types of Pomacentridae, while other dominant species include *Pseudanthias squamipinnis*, *Cirrhidabrus cyanopleura*, *Hemitaurichthys polylepis*, *Naso hexacanthus*, *C. rubrimaraginatus*, *C. exquisitus*, and *Hemiochus acuminatus*, all of which are diurnal and swim in schools. Long-term monitoring has also reported appearances of *Plectroglyphidodon imparipennis*, *Thalassoma amblycephalus*, *T. hardwickii*, and *Pterleotris evides*.

For Lan-Yu, the most common species are Labridae (71 types) and Pomacentridae (43 types), with the most common types being *Chromis chrysurus*, *C. margaritifer*, *Pseudanthias squamipinnis*, *Dascyllus reticulatus*, and *Pterocaesio digramma*, which are of similar characteristics to those of Lu-Dao being diurnal and appear in schools. Such fish cluster in stronger ocean currents which funnel a greater volume of zooplankton, such as the area between the two islands where the Kuroshio, is particularly strong.

As for migratory and commercial fish, bluefin tuna spawn in large numbers in the Kuroshio off of Taiwan's east coast before migrating north at maturity. They exhibit a clear tendency towards nocturnal vertical migration, possibly due to the

temperature distribution of the water [73, 74]. Albacore is distributed in the Kurioshio basin at north Pacific and migrate in large numbers from March to July in a direction against the Kuroshio to arrive in the water at vicinity of Taiwan [75]. Once black skipjack mature, they follow the Kuroshio from the Philippines to the seas near Taiwan for forage [76], a pattern also found among skipback tuna. Swordfish follow the Kuroshio in spring and summer; once they're sexually mature in fall and winter, they return south against the Kuroshio to spawn [77].

The seas off of Taiwan's east coast are a popular place for whale watching, with sightings of about 28 types [78] including *Grampus griseus*, *Stenella longirostris*, *Stenella attenuata*, *Tursiops truncatus*, *Lagenodelphis hosei*, and *Pseudorca crassidens*. Most whales appear in spring and summer, including *Megaptera novaeangliae*, *Physeter macrocephalus*, *Orcinus orca*, and *Globicephala macrorhynchus* [79]. Of particularly, *Balaenoptera* migrate north in winter and spend spring and summer in lower latitudes such as in the Sea of Japan. This migration is related to the distribution of food, as they follow the migration of sardines (their staple food), while eating mostly krill at higher latitudes [80]. The whale shark is the largest creature to appear in the Kuroshio as they follow thermo fronts and upwellings. Surveys of fish populations show that the Kuroshio has abundant fishery resources, and Taiwan is a key relay point for migratory fish.

References

1. Stommel H (1948) The westward intensification of wind-driven ocean currents. Am Geophys Union Trans 29(2):202–206
2. Gill AE (1982) Atmosphere-ocean dynamics. Academic, New York
3. Kawai H (1998) A brief history of recognition of the Kuroshio. Prog Oceanogr 41:505–578. doi:10.1016/S0079-6611(98)00024-X
4. Nakano H, Tsujino H, Furue R (2008) The Kuroshio current system as a jet and twin relative recirculation gyres embedded in the sverdrup circulation. Dyn Atmos Oceans 45:135–164. doi:10.1016/j.dynatmoce.2007.09.002
5. Kurogi M, Akitomo K (2006) Effects of stratification on the stable paths of the Kuroshio and on their variation. Deep Sea Res 53:1564–1577. doi:10.1016/j.dsr.2006.07.003
6. Tang TY, Tai JH, Yang YJ (2000) The flow pattern north of Taiwan and the migration of the Kuroshio. Cont Shelf Res 10:349–371. doi:10.1016/S0278-4343(99)00076-X
7. Wang J, Chern C-S (1988) On the Kuroshio branch in the Taiwan strait during winter time. Prog Oceanogr 21:469–491. doi:10.1016/0079-6611(88)90022-5
8. Qiu B (2001) Kuroshio and Oyashio currents. In: Thorpe S, Steve A, Turekian K, Karl K (eds) Encyclopedia of ocean sciences. Academic, New York, pp 1413–1425
9. Chen F (2010) Kuroshio power plant development plan. Renew Sust Energy Rev 14:2655–2668. doi:10.1016/j.rser.2010.07.070
10. Munk WH (1950) On the wind-driven ocean circulation. J Meteorol 7(2):79–93
11. Uda M (1949) On the correlated fluctuation of the Kuroshio current and the cold water mass. J Oceanogr Mag 1:1–12
12. Suda K (1943) Kaiyo-Kagaku (in Japanese). Kokin Shoin, Tokyo, p 726
13. Yosida S (1960) On the short period variation of the Kuroshio in the adjacent sea of Izu islands. J Hydrogr Bull 65:1–18 (in Japanese)
14. Nan'niti T (1958) A theory of the mechanism of the generation of the cold water region in the offing of Enshu-nada. Pap Meteorol Geophys 8:317–331

15. Nan'niti T (1960) Long-period fluctuations in the Kuroshio. Pap Meteorol Geophys 11:339–347
16. Hsin YC, Wu CR, Shaw PT (2008) Spatial and temporal variations of the Kuroshio east of Taiwan, 1982–2005: a numerical study. J Geophys Res 113, C04002. doi:10.1029/2007JC004485
17. Sheu WJ, Wu CR, Oey LY (2010) Blocking and westward passage of Eddies in the Luzon strait. J Deep Sea Res Part II 57:1783–1791. doi:10.1016/j.dsr2.2010.04.004
18. Chen HT, Yan XH (1996) A numerical simulation of wind stress and topographic effects on the Kuroshio current path near Taiwan. J Phys Oceanogr 26:1769–1802. doi:10.1175/1520-0485(1996)026<1769:ANSOWS>2.0.CO;2
19. Sekine Y (1990) A numerical experiment on the path dynamics of the Kuroshio with reference to the formation of the large meander path south of Japan. J Deep Sea Res 37(3):359–380. doi:10.1016/0198-0149(90)90014-M
20. Feng M, Mitsudera H, Yoshikawa Y (2000) Structure and variability of the Kuroshio current in Tokara strait. J Phys Oceanogr 30:2257–2276
21. Akitomo K (2008) Effects of stratification and mesoscale eddies on Kuroshio path variation south of Japan. J Deep Sea Res Part I 55:997–1008. doi:10.1016/j.dsr.2008.03.013
22. Qiu B, Miao WF (2000) Kuroshio path variations south of Japan: bimodality as a self-sustained internal oscillation. J Phys Oceanogr 30:2124–2137
23. Deser C (1999) Evidence for a wind-driven intensification of the Kuroshio current extension from the 1970s to the 1980s. J Climate 12:1697–1706. doi:10.1175/1520-0442(1999)012<1697:EFAWDI>2.0.CO;2
24. Naeije MC, Ambrosius BAC (2000) Seasonal cycle and inter-annual variability of the Kuroshio/Oyashio current system using multi-channel sea surface temperature and altimetry sea level data. J Adv Space Res 25(5):1103–1106. doi:10.1016/S0273-1177(99)00870-4
25. Kawabe M (1985) Sea level variations at the Izu islands and typical stable paths of the Kuroshio. J Oceanogr Soc Japan 41:307–326. doi:10.1007/BF02109238
26. Kawabe M (1995) Variation of current path, velocity, and volume transport of the Kuroshio in relation with the large meander. J Phys Oceanogr 25:3103–3117. doi:10.1175/1520-0485(1995)025<3103:VOCPVA>2.0.CO;2
27. Taft B (1972) Characteristics of the flow of the Kuroshio South of Japan. In: Stommel H, Yoshida K (eds) Kuroshio: its physical aspects. University of Tokyo Press, Tokyo, pp 165–216
28. Robinson AR, Niiler PP (1967) The theory of free inertial currents I. Path and structure. Tellus 19:269–291. doi:10.1111/j.2153-3490.1967.tb01482.x
29. White WB, McCreary JP (1976) On the formation of the Kuroshio meander and its relationship to the large-scale ocean circulation. Deep Sea Res 23:33–47. doi:10.1016/0011-7471(76)90806-8
30. Sun L, Yang YJ, Gu YF (2009) Impacts of typhoons on the Kuroshio large meander: observation evidences. J Atmos Ocean Sci Lett 2:45–50
31. Chen CT, Liu CT, Chuang WS, Yang YJ, Shiah FK, Tang TY, Chung SW (2003) Enhanced buoyancy and hence upwelling of subsurface Kuroshio waters after a typhoon in the southern east China sea. J Mar Syst 42:65–79. doi:10.1016/S0924-7963(03)00065-4
32. Hung CC, Gong GC, Chou W-C, Chung CC, Lee MA, Chang Y, Chen HY, Huang SJ, Yang Y, Yang WR, Chung WC, Li SL, Laws E (2010) The effect of typhoon on particulate organic carbon flux in the southern east China sea. J Biogeosci discuss 7:3521–3550. doi:10.5194/bgd-7-3521-2010
33. Andres M, Park J-H, Wimbush M, Zhu XH, Chang KI, Ichikawa H (2008) Study of the Kuroshio/Ryukyu current system based on satellite-altimeter and in situ measurements. J Oceanogr 64:937–950. doi:10.1007/s10872-008-0077-2
34. Johns WE, Lee TN, Zhang D, Zantopp R (2001) The Kuroshio east of Taiwan: moored transport observations from WOCE PCM-1 array. Am Meteorol Soc 31:1031–1053. doi:10.1175/1520-0485(2001)031<1031:TKEOTM>2.0.CO;2
35. Chen WS (2002) The rocks in Taiwan. In: 2002 Taiwan rock engineering symposium, pp 17–23

36. Kao H, Huang GC, Liu CS (2000) Transition from oblique subduction to collision in the northern Luzon arc-Taiwan region: constraints from bathymetry and seismic observations. J Geophys Res 105:3059–3079. doi:10.1029/1999JB900357

37. Liu CS, Liu SY, Lallemand SE, Lundberg N, Reed D (1998) Digital elevation model offshore Taiwan and its tectonic implications. Terr Atmos Ocean Sci 9:705–738

38. Chen WS (2005) The geology of the coastal range—the coastal range—deep tourism of longitudinal valley—an introduction. Translated from http://ashan.gl.ntu.edu.tw/chinese/GeoPark/SeacoastSierraGeology/SeacoastSierraGeology01/print/SeacoastSierraGeology01.pdf. Accessed 19 Mar 2013

39. Hsu SK, Liu CS, Shyu CT, Liu SY, Sibuet JC, Lallemand SE, Wang C, Reed D (1998) New gravity and magnetic anomaly maps in the Taiwan-Luzon region and their preliminary interpretation. Terr Atmos Ocean Sci 9:509–532

40. Liu KK, Gong GC, Shyu CZ, Pai SC, Wei CL, Chao SY (1992) Response of Kuroshio upwelling to the onset of the northeast monsoon in the sea north of Taiwan: observations and a numerical simulation. J Geophys Res 97:12511–12526. doi:10.1029/92JC01179

41. Juang WS, Chen JC, Chang JG (2005) The topographic landscapes of volcanic necks in the Coastal Range, Lutao, and Lanyu, eastern Taiwan (in Chinese). Bull Central Geol Surv 14:108–148

42. Tang TY, He CR, Wang YH, Jan S, Hsu SK, Wen LS, Yang TY, Song SR, Chen HY, Song GS, Chang TY, Chiao LY (2008–2010) Comprehensive research on the natural resources of the east waters of Taiwan: a precisely topographic, geological, hydrological, and ecological surveys of the waters around Green Island. A research report of the project sponsored by National Science Council

43. Sinotech Engineering Consultants (2006) Metropolitan area and the periphery sloping integrated environmental and geological databases to build a sloping rock engineering survey study (5/5) The final report of the eastern region of Taiwan (in Chinese). Bulletin of the Central Geological Survey, vol 95–21, project number: 5226902000-03-95-21

44. Chen CTA, Liu CT, Pai SC (1995) Variations in oxygen, nutrient and carbonate fluxes of the Kuroshio current. La Mer 33:161–176

45. Dai CF (1993) The ocean of Taiwan (in Chinese). Walkers Cultural Corporation, Taipei, Taiwan. ISBN 986-7630-00-9

46. Wang ZF, Gong M, Lu Y, Ruan Z, Qiu HY, Wang H (1992) Analysis of Cu, Cd, Co, and Ni in surface water of the Kuroshio area in the east China sea. Chin J Oceanogr Limnol 10:223–230. doi:10.1007/BF02843823

47. Hung JJ, Chan CL (1998) Distribution and enrichment of particulate trace metals in the southern east China sea. Geochem J 32:189–203

48. Hsiao SH, Hwang JS, Fang TH (2011) Copepod species and their trace metal contents in coastal northern Taiwan. J Mar Syst 88:232–238. doi:10.1016/j.jmarsys.2011.04.009

49. Azam F, Fenchel T, Field JG, Grey JS, Meyer-Reil LA, Thingstad F (1983) The ecological role of water-column microbes in the sea. Mar Ecol Prog Ser 10:257–263. doi:10.3354/meps010257

50. Takahashi M, Kikuchi K, Hara Y (1985) Importance of picocyanobacteria biomass (unicellular, blue-green algae) in the phytoplankton population of the coastal waters off Japan. Mar Biol 89:63–69. doi:10.1007/BF00392878

51. Chen LYL (1995) Phytoplankton composition and productivity in response to the upwelling off northeastern Taiwan. Proc Natl Sci Counc Repub China B 19:66–72

52. Chang J, Shiah FK, Gong GC, Chiang KP (2003) Cross-shelf variation in carbon-to-chlorophyll a ratios in the east China sea, summer 1998. Deep Sea Res Part II 50:1237–1247. doi:10.1016/S0967-0645(03)00020-1

53. Chen LYL, Chen HY, Jan S, Tuo SH (2009) Phytoplankton productivity enhancement and assemblage change in the upstream Kuroshio after typhoons. Mar Ecol Prog Ser 385:111–126. doi:10.3354/meps08053

54. Gong GC, Shiah FK, Liu KK, Wen YH, Liang MH (2000) Spatial and temporal variation of chlorophyll a, primary productivity and chemical hydrography in the southern east China Sea. Cont Shelf Res 20:411–436

55. Shiah FK, Chen TY, Gong GC, Chen CC, Chiang KP, Hung JJ (2001) Differential coupling of bacterial and primary production in mesotrophic and oligotrophic systems of the east China Sea. Aquat Microb Ecol 23:273–282

56. Yang TN, Wei KY, Gong GC (2001) Distribution of coccolithophorids and coccoliths in surface ocean off northeastern Taiwan. Bot Bull Acad Sini 42:287–302

57. Chung JL, Shiah FK, Gong GC, Chiang KP (2009) Trophic cascading of medusae on the relationship between copepods and diatoms in a subtropical coastal ecosystem. Terr Atmos Ocean Sci 20:547–556. doi:10.3319/TAO.2008.05.23.01(Oc)

58. Huys R, Boxshall G (1991) Copepod evolution. The Royal Society, London. ISBN 0903874210

59. Shih CT, Chiu TS (1998) Copepod diversity in the water masses of the southern east China sea north of Taiwan. J Mar Syst 15:533–542. doi:10.1016/S0924-7963(97)00053-5

60. Lee CY, Liu DC, Su WC (2009) Seasonal spatial variations in the planktonic copepod community of Ilan Bay and adjacent Kuroshio water off northeastern Taiwan. Zool Stud 48:151–161

61. Hwang JS, Dahms HU, Tseng LC, Chen QC (2007) Intrusions of the Kuroshio current in the northern south China sea affect copepod assemblages of the Luzon strait. J Exp Mar Biol Ecol 352:12–27. doi:10.1016/j.jembe.2007.06.034

62. Hsiao SH, Fang TH, Shih CT, Hwang JS (2011) Effects of the Kuroshio current on copepod assemblages in Taiwan. Zool Stud 50:475–490

63. Lo WT, Shih CT, Hwang JS (2004) Diel vertical migration of the planktonic copepods at an upwelling station north of Taiwan, Western North Pacific. J Plankton Res 26:89–97. doi:10.1093/plankt/fbh004

64. Chiu TS, Hsyu YH (1994) Interannual variation of ichthyoplankton density and species composition in the waters off northeastern Taiwan. Mar Biol 119:441–448. doi:10.1007/BF00347541

65. Su WC, Lo WS, Liu DC, Wu LJ, Hsieh HY (2011) Larval fish assemblages in the Kuroshio water east of Taiwan during two distinct monsoon seasons. Bull Mar Sci 87:13–29. doi:10.5343/bms.2010.1010

66. Lo WT, Hsieh HY, Wu LJ, Jian HB, Liu DC, Su WC (2010) Comparison of larval fish assemblages between during and after northeasterly monsoon in the waters around Taiwan, west north Pacific. J Plankton Res 32:1079–1095

67. Hsieh HY, Lo WT, Liu DC, Hsu PK, Su WC (2007) Winter spatial distribution of fish larvae assemblages relative to the hydrography of the waters surrounding Taiwan. Environ Biol Fishes 78:333–346

68. Nishikawa J, Tsuda A, Ishigaki T, Terazaki M (1995) Distribution of euphausiids in the Kuroshio front and warm water tongue with special reference to the surface aggregation of *Euphausia pacifica*. J Plankton Res 17:611–629

69. Terazaki M (1992) Horizontal and vertical distribution of chaetognaths in a Kuroshio warm-core ring. Deep-Sea Res 39(suppl 1):S231–S245. doi:10.1016/S0198-0149(11)80014-2

70. Chen JP, Jan RQ, Kuo JW, Huang CH, Chen CY (2009) Fish fauna around green island. J Natl Park 19:23–45

71. Chang KH, Jan RQ, Shao KT (1983) Community ecology of the marine fishes on LuTao Island, Taiwan. Bull Inst Zool, Acad Sini 22:141–155

72. National museum of marine biology and aquarium: beauty and sadness of Lan-Yu. http://210.243.41.4/activity/tao/. Accessed 19 Mar 2013

73. Kimura S, Kato Y, Kitagawa T, Yamaoka N (2010) Impact of environmental variability and global warming scenario on Pacific Bluefin tuna (*Thunnus orientalis*) spawning grounds and recruitment habitat. Prog Oceanogr 86:39–44

74. Kitagawa T, Nakata H, Kimura S, Itoh T, Tsuji S, Nitta A (2000) Effect of ambient temperature on the vertical distribution and movement of Pacific Bluefin tuna *Thunnus orientalis*. Mar Ecol Prog Ser 206:251–260. doi:10.3354/meps206251
75. Kimura S, Nakai M, Sugimoto T (1997) Migration of albacore, *Thunnus alalunga*, in the North Pacific Ocean in relation to large oceanic phenomena. Fish Oceanogr 6:51–57
76. Chiou WD, Lee LK (2004) Migration of kawakawa *Euthynnus affinis* in the waters near Taiwan. Fish Sci 70:746–757. doi:10.1111/j.1444-2906.2004.00867.x
77. Watanabe H, Kubodera T, Yokawa K (2009) Feeding ecology of the swordfish *Xiphias gladius* in the subtropical region and transition zone of the western North Pacific. Mar Ecol Prog Ser 396:111–122. doi:10.3354/meps08330
78. Chou LS (2004) History of the marine mammals study in Taiwan. Natl Sci Mus Monogr 24:129–138
79. Hsu HH, Joung SJ, Liao YY, Liu KM (2007) Satellite tracking of juvenile whale shark, *Rhincodon typus*, in the Northwestern Pacific. Fish Res 84:25–31. doi:10.1016/j.fishres.2006.11.030
80. Gong GC, Liu KK, Pai SC (1995) Prediction of nitrate concentration from two end member mixing in the east China sea. Cont Shelf Res 15:827–842. doi:10.1016/0278-4343(94)00039-P

Chapter 2
Conceptual Design of Kuroshio Power Plant

The design of a Kuroshio power plant begins with the selection of turbine. Once the turbine is chosen, the turbine anchoring system will be designed accordingly, followed by the designs of construction procedure and relevant equipments. Figure 2.1 shows the conceptual design of the Kuroshio power plant, which was made under a major concern that the design must securely anchor hundreds of turbines in deep ocean under the action of a dynamical force of hundreds of thousands of Newton. This is an unprecedented challenge stemming mainly from the design of an effective anchorage system.

Figure 2.1 shows a power plant being composed of tens of horizontal-axis turbines. As different types of turbine are chosen, such as those given in Appendix A, one may result in a different design in the anchorage system of the power plant. In the figure, a relay platform is used to anchor dozens of turbines. The platform consists of hundreds of hollow floats connected by ball joints, being allowed to deform under the dynamical force applied on the turbines by the Kuroshio. To prevent typhoon-driven waves from damaging the turbines and the platform, the axis of the turbines should be submerged at least 30 m below the surface, and the platform can be submerged to a depth of up to 70 m.

The relay platform serves as an artificial seabed, raising the level of the actual seabed from hundreds of meters deep. The turbine is anchored to the relay platform by a single cable of a length about 20–30 m, allowing the turbines to drift with the ocean current within a limited domain. The platform is anchored to the seabed hundreds of meters deep by tens or hundreds of cables, and the direction of the cables shall be in accordance with the ocean current, so that the whole relay platform will not suffer significant displacement or deformation under the action of the strong current. This approach, simultaneously anchoring the platform by hundreds of cables, can prevent collapse of the platform due to seabed slumping caused by undersea earthquakes. Moreover, not needing to secure the anchors in predetermined positions helps keep overall construction costs down.

However, on the other hand, the anchorage of the turbine to the platform cannot be random, as the anchor position and the platform structure robustness are closely related. One must consider that, with tens of turbines simultaneously operating in
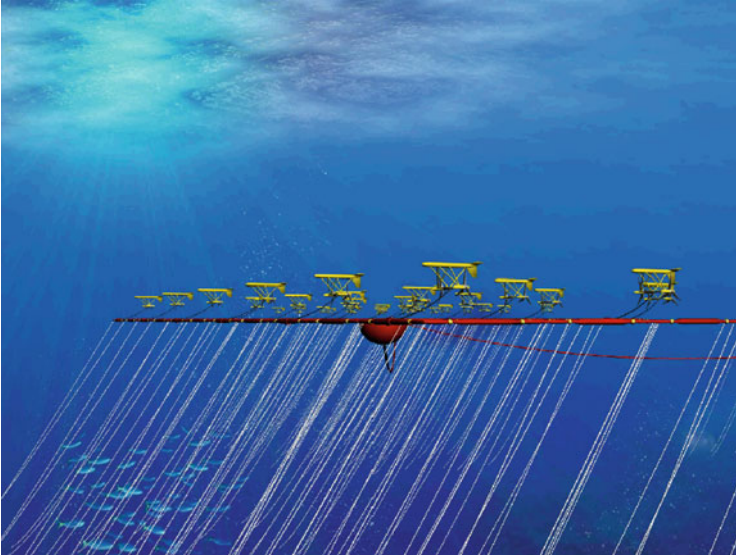
Fig. 2.1 Schematic of a Kuroshio power plant, which shows a so-called turbine cluster having 25 turbines simultaneously anchored to the floating relay platform. Power transmission cables connect different clusters, with each cluster equipped with its own transformer. The floating relay platform is anchored to the seabed by hundreds of cables

the ocean, the entire platform's static tolerance must be kept within a safe range while, at the same time, the overall dynamic reaction of the platform and the turbines must not create a structural fatigue or damage.

On the center of the relay platform, a set of power conversion equipment is deployed, allowing the platform to modulate the power to be transmitted to the land-based grid. To prevent the damage caused by earthquake, the power cable should hang from one platform to the other before finally connecting to power station on land. Without the need to lower the cable to the seabed, the length of the cable can be reduced significantly and the earthquake-caused cable damage can be prevented. The distance between platforms is relevant to the current characteristics and turbine performance. By deploying platforms in different depth, the distance between platforms can be shortened.

Preliminary estimates of construction feasibility, ease of maintenance, cost-effectiveness, and other optimization considerations indicate that a platform should accommodate 25–35 turbines to achieve optimal performance, covering an area of approximately $400 \times 700 \, \text{m}^2$. With this set up, the movement of the entire turbine cluster is coordinated with that of the floating platform; thus, the reaction force between ocean current and the turbines, and the deformation and displacement of the platform as well, can all be effectively controlled within a safe range.

All of the technologies needed to build a Kuroshio power plant are traditional and mature, but integrating these technologies together to build a Kuroshio power plant is a new endeavor. Currently, tidal power plants have been built in a lot of

shallow waters around the world, which is not necessarily applicable to the east coast of Taiwan where the waters are usually of several hundred meters deep, and goes as deep as 3,000 m within a few kilometers from the coast. Deep sea engineering poses very different problems from shallow water engineering. Although the needed technologies are not new (for example, the oil-drilling engineering in the Gulf of Mexico often takes place in depths of over 1,000 m), stably anchoring thousands of turbines to an earthquake-prone sea floor poses various severe engineering challenges.

Based on the deep-sea engineering characteristics discussed above, the engineering design of Kuroshio power plant can be classified into three major categories: the turbine design, the relay platform design, and the construction engineering design. Two more important designs, although may not be so significant as previous ones, are respectively the so-called anchored pile driver design and the site selection of the power plant. The characteristics of these five designs are illustrated in the following.

2.1 The Turbine Design

The principles of ocean turbine to convert current momentum into electric power are similar to those of wind turbine. Both are designed to convert kinetic energy of fluid flow into rotational torque to drive the power generator. But, since the density of seawater is 832 times that of air, the ocean turbine can produce the same amount of electricity by using smaller blades at a slower rate of rotation. Besides, since ocean current flows at a steadier rate than wind, it therefore makes generating capacity larger and more predictable.

Although the energy conversion principle for both ocean and wind is nearly identical, ocean current electrical generation equipment is used in a more extreme underwater environment, requiring more complex construction technology. Also, a higher degree of reliability is needed for ocean turbines, and operations and maintenance costs are higher, thus the costs associated with the early development of ocean current power generation equipment were high, making it hard to compete with other renewable energies or traditional fossil fuels. Recently, however, increased emphasis on upgrading technology for ocean power generation in various countries has reduced the cost, prompting the development of several large-scale underwater turbines in the commercial power generation supply chain [1–3].

In nowadays, most of the commercially available underwater turbines were developed in Europe or the USA, and most models were developed for use in tidal power generation in shallow waters. These turbines can be broadly classified into four types: horizontal axis, vertical axis, reciprocating, and Venturi tube. Online searches found 63 different types of turbines covered by more than 320 patents. The design principles and characteristics of these turbines, along with their development profiles, manufacturers, origin, and relevant patents are organized in Appendix A.

The structure of ocean current turbines can be divided into three large areas (1) the turbine: converts linear kinetic energy into rotational kinetic energy, (2) the generator: converts rotational kinetic energy into electrical energy, (3) the gear assembly: the interface between the turbine and the generator, adjusts the rotation speed and absorbs the axial impact force. Of course, additional gear is needed as well, including electrical power conversion equipment, submarine cables, anchoring devices, etc. In this three-part design, detailed research and development of the following key technologies requires particular attention:

1. Dynamical design of turbine: Turbine performance is determined by the hydrodynamic performance of the turbine body and rotor blades, wherein the average velocity, characteristic velocity of the water, short- and long-term flow velocity fluctuations, typhoon-induced velocity change, and other environmental factors are all important considerations in the design of blade performance. The design of the body of turbine not only must consider the shell shape and structural strength but also the selection of the anchorage point and the design of the cable connector, all of these shall affect turbine performance and safety [4–8].

2. Design of turbine body structure and material selection: Generally speaking, the structure of an ocean turbine is not complex. The key components include the generator, the rotor blades, and the support structure of the frame. The ocean current imposes dynamic stress and strain on the entire turbine structure, requiring the 3D structural mechanical analysis to ensure that the rigidity of the selected materials meets the requirement to survive the dynamic stress imposed by strong current. Regarding component materials, special alloys should be considered for the bearings and brackets, and composite materials for others, such as floats for the body. Fabricating the body from composites in large quantities can reduce the cost but requires mold design and processing techniques, coupled with a production line designed for the designed processing procedures.

3. Generator design: Ocean turbine generators, designed to operate in a low-speed ocean current such as the Kuroshio, should be featured by a large radius and long shaft to output a large torque at a low rotational speed. To maintain optimal efficiency in response to changes of the Kuroshio, the rotational speed of the turbine (and the generator) shall be precisely adjusted through the electronic control circuits.

4. Gear assembly design: Ocean turbines operating at low speed currents is subject to large high torque and axial thrust. These static and dynamic forces are absorbed by the gear assembly which transfers this force from rotor to the generator. Achieving this requires key technologies for variable speed transmissions, force characteristics analysis, anticorrosion, and waterproofing. At the design stage, one needs to consider problems related to maintenance, lubrication, and heat dissipation.

5. Anticorrosion design: The turbines for the Kuroshio power plant will be submerged tens of meters beneath the ocean surface and are thus less prone to oxidation corrosion than shallow-water turbines, but deep water organisms may

adhere to turbines creating the so-called biofouling problem. Previously, bio-fouling can be prevented by using toxic paints to smear on the turbine. But, nevertheless, this kind of toxic paint is strictly prohibited under marine environmental laws. Therefore, one may need to develop a new type of environmentally friendly paint through a suitable synthesis of chemistry and pharmacology. In addition, some metal parts may require plating and lubrication. The design of anticorrosion process design should take maintenance periods and procedures into account, which will affect operating costs.

6. Maintenance design: All aspects of maintenance contribute to operating costs, and the specific maintenance procedures are closely related to the design of the turbine. Therefore, in the beginning of the design stage of turbine, maintenance procedures and content, such as specific maintenance procedures, frequency, time, replacement parts, and lubrication, must be set out clearly. Ideally, the maintenance shall be done once in a few years. Whether it should be done underwater or above water must be carefully specified.

7. Depreciation: According to the author's understanding after talking with many turbine companies worldwide, the standard can be designed as that no maintenance is required during the first 5 years of service, and the life span can be designed for 25 years. After the first 5 years, the turbine should be able to operate at full load for 10 months out of a year.

As shown in Appendix A, there are over 60 different types of ocean current turbine, covered by more than 320 patents. In which, 20 types have been subjected to long-term full-scale model testing at sea, but only a few have been anchored in deep water to produce electricity. After taking the reliability of anchorage systems and construction procedures, as well as the low construction and operating costs into account, we selected the Gulf Stream Turbine (GST) for use in the Kuroshio power plant. The GST features an auto-stabilizing design, allowing it to be securely anchored on the relay platform by a single anchor. We follow the original design of GST to reproduce the turbine body structure diagram as shown in Fig. 2.2, while detailed specific descriptions can be found in Appendix A, product no. A-1.26.

This turbine was first demonstrated by Robson in 2003 (see Appendix B) and is mainly used for ocean current power generation. The device consists of two sets of counter-rotation rotors, a triangular structure supporting a main pontoon made of carbon or fiberglass to strengthen the fuselage structure and prevent corrosion. The two multiblade rotors are positioned at the rear of two watertight nacelles, generating rotational torque in opposite directions. The generators are contained within the watertight nacelles, and the weight of the generators acts as ballast for the triangular structure. The upper middle part of the body features a torpedo-shaped main pontoon with a tail stabilizer to maintain the turbine to face against the ocean current, keeping it level and aligned with the flow. The main pontoon and the watertight nacelles are connected by numerous linkages. The bulk and shape of the linkages are designed to not affect turbine performance. The cable anchor is connected through a ball joint onto the connecting rod below the main pontoon.
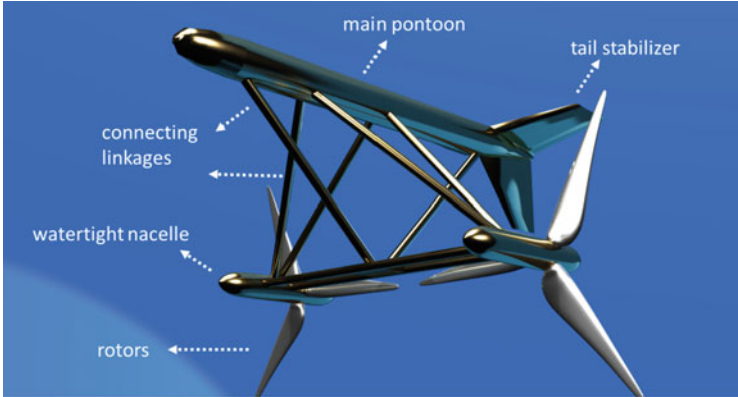
Fig. 2.2 Schematic of the Gulf Stream Turbine (GST), which has been modified by present study in line with the purpose of the dynamic analysis

The GST design features four mechanical stability mechanisms to keep the fuselage level and aligned with the current, while balancing the fuselage against sudden impacts:

(a) Tail stabilizer:
   The tail stabilizer features two horizontal tail wings and a vertical rudder. The tail wings ensure that, during yawing, the fuselage can quickly regain its current-facing alignment. The rudder acts to restore the fuselage's horizontal posture when the pitching angle changes.
(b) Resistance center located behind the anchor point:
   This works like an arrow's fletching; when the fuselage pitches or yaws, it acts to quickly produce a corrective torque, thus restoring the original attitude and keeping the turbines faced against the current.
(c) The center of gravity located below the center of buoyancy:
   This works on the same principle as "Weeble" toys in that, when the fuselage pitches or rolls, immediate compensation restores the turbine to its original attitude.
(d) Symmetrical design:
   The design contains a pair of counter rotating rotors and generators, mutually offsetting the force and torque under the flow action on the turbine. However, the operation of the blades of the two rotors is not necessarily in the same phase (commonly referred to as the dual-rotor effect), which will be discussed in greater detail in Sect. 3.5.3.

With these stability mechanisms, the GST design does not require additional balance control systems, thus reducing to some extent the maintenance difficulty and the construction cost. In Sect. 3.7, we discuss the functions of these four stabilization mechanisms, based on the design of the tail stabilizer of the GST.

The dynamic reaction force on the fuselage of GST will be analyzed in Chap. 3, based on which viable anchorage system and components are designed. Of course, some other turbine models are also operable in the Kuroshio. But the dynamic behavior is highly likely to be different from GST, which requires another analysis to be done as shown in Chap. 3.

2.2   The Relay Platform Design

The design of the relay platform is done with a single purpose in mind that one shall deploy the GST at a predetermined position in deep waters and ensure it to stably operate under the action of the Kuroshio. With the relay platform, dozens of turbines can be deployed as a cluster to simplify the engineering procedure to construct the power plant in deep waters. Besides, the relay platform can also comply with the rationality of construction, operation, and maintenance costs. Conceptually, in brief, the relay platform is composed of hundreds of buoyant pontoons connected by universal joints. Above the platform, there are dozens of turbines anchored stably on the platform. Below the platform, hundreds of cables serve to anchor the platform unto the seabed at a depth of several hundred meters.

After tried with several different designs, an assembly for the relay platform (Fig. 2.3a) made up of 66 individual unit platforms (Fig. 2.3b) is developed. Each unit platform measured 70×70 m^2, with each side made of three components: a primary linkage (30 m) in the middle, an auxiliary linkage (15 m) on each side, and a cross (or a cruciform) joint (10 m). The side facing against the current has a width of 11 unit platforms, while the side being parallel with the current is six unit platforms wide, giving the relay platform an overall area of 770×420 m^2. The turbines above the platform are arranged in a form of staggered grid, anchored by cables of about 50 m long. Each relay platform is able to support a total of 39 turbines. The installed capacity of each GST turbine is 0.5 MW, giving each relay platform a total installed capacity of 19.5 MW.

To ensure sufficient buoyancy to support the platform in the Kuroshio, the primary linkage and the auxiliary linkage are made of hollow floats, with dimensions dictated by the size of the platform. These floats can be made of composite materials or rust-proof metal. All floats are connected by universal joints, giving the platform a flexible structure. The turbine anchor point can be rotated with a hollow sleeve jacketing on the primary linkage. This sleeve is installed at the middle of the primary linkage and can move around the primary linkage, but its lateral movement along the linkage is prohibited. The platform's cable anchor point is located on the bottom of the cross joint, which is connected to the cable by a ball joint. To prevent significant drift in the current, the anchor point of each cross joint is attached to two cables anchored to the seabed, thus restricting the platform's displacement. One cable drops vertically to restrict the platform's vertical displacement, while the other falls diagonally to restrict downstream displacement (Fig. 2.3c).
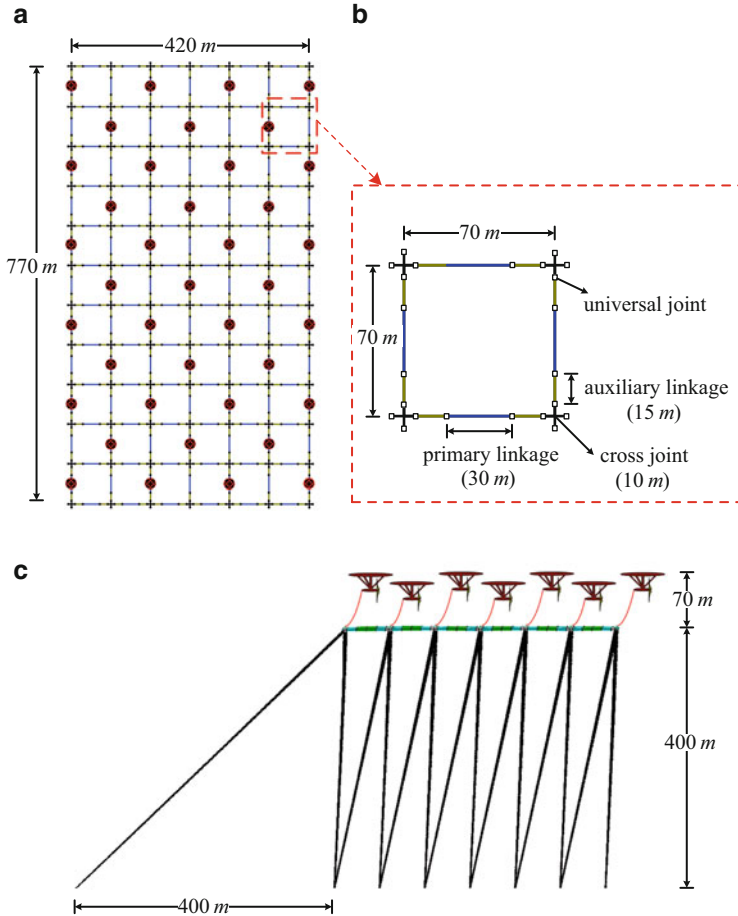
Fig. 2.3 Schematic of relay platform components and overall structure. (**a**) The complete platform is made up of 66 unit platforms, with a total of 39 turbines arranged in a staggered formation and anchored to the upstream primary linkage of the unit platforms. (**b**) The unit platform—a square structure with each side constituted by one 30-m-long primary linkage, two 15-m-long auxiliary linkages, and two cross joints, with each component connected by universal joints. (**c**) Side view of the complete Kuroshio power plant, with the platform secured to the seabed by two sets of cables (vertical and inclined) and the turbines anchored to the relay platform with the central axis of the rotors positioned 30 m above the platform. Note: the current moves from left to right, with the left-most cable at a 45° angle. The turbines are not drawn to scale, and the second, fourth, and sixth turbines in (**c**) appear lower to indicate the staggered configuration

The universal joint connecting the primary and auxiliary linkages is the key design focus of the relay platform. This universal joint not only controls the deformation of the entire platform but also absorbs high frequency vibrations caused by the current, thus reducing the risk of damage to the power plant's structure from deformation strain or fatigue. At the same time, both the level of

platform deformation and the degree of linkage rotation can be controlled by selecting a proper stiffness of the rotating spring of the universal joint.

The relay platform has four major elements: the floats that make up the main structure of the platform, the universal joints which connect the floats, the cross joints that bear the cable anchors, and the anchors and the cables. The key technologies involved include the mechanical design and material selection of the floats, the force specifications and deformation limitations of the universal joint, the stress and strain analysis of the cable and the anchor, and the force distribution, the deformation and displacement analysis of the platform in the Kuroshio. Other technologies required include the design of the anticorrosion treatment, warranty, and maintenance of the aforementioned elements, along with depreciation estimates. The work content of the above mentioned is as follows:

1. Platform dynamic design: The relay platform, supporting tens of turbines, is anchored to the seabed by hundreds of cables. The operation of the overall structure reflects complex and dynamic changes in the Kuroshio current, leading to deformation and displacement of the platform. These forces and their action on the platform components are the key focus of analysis and technology application for power plant design. This work begins from establishing a theoretical model for use in conducting reliable numerical computations to analyze the stress and strain on the overall structure.

   Only in this way can we determine the required mechanical strength for the platform components, effectively select appropriate materials, and properly predict the structural rigidity and apparent stability of the overall power plant structure. The selection of materials for the platform's buoyant linkages requires combining material mechanics analysis and structural analysis with other mature techniques in assembly and manufacturing [9–12]. The platform can be made of composite or plastic steel materials. Assembly shall be completed on land before installation at sea.

2. Cable material: Traditional anchor chains are typically made of steel, which is heavy and prone to corrosion and is possibly unsuitable for use in anchoring the turbines to the relay platform. There are cables made of composite materials or polymer compounds, which is light and strong and their bristly surface capable of helping to reduce low-frequency swinging or high-frequency vibration caused by the current [13, 14] and is optimally suitable for use in Kuroshio power plant. In particular, the sea off the coast of Tai-Dong in southeast Taiwan is hundreds of meters deep, requiring cables as long as 1 km. As such the weight and strength of the cable are key engineering concerns.

3. Anchor specifications: There is a wide selection of existing anchors [15, 16] including caissons, pilings, screws, etc. The choice of anchor is directly influenced by the local seabed geological conditions. As discussed in Chap. 1, the geology of the seabed at Taiwan's east coast is generally made up of solid igneous rock, covered by a layer of sediment up to several meters in depth. Using caisson anchors under these conditions would require the weight of the caissons to be highly large, and its shape also requires special consideration given the

adhesiveness of the sediment layer. Using piling anchors requires detailed mechanical data for the geology below the sediment layer, which show that the seabed geology of eastern Taiwan is primarily made up of igneous rocks in a compact structure, so permanently anchoring the cables by screws would be a more viable approach. Finally, the depth to which the anchor should be set and the required tension resistance are important issues that shall be clarified during the design phase.

4. Anchor system: The overall anchoring system consists of the anchors, the cables and the relay platform. The movement of each component influences the others, and the ocean current will cause the overall structure to vibration and deformation [17–19], potentially affecting the overall safety, lifespan, the efficiency, and performance of the turbine. Therefore, the structural design of the anchoring system is essential to the power plant design, along with static equilibrium calculations and dynamic vibration analysis [20]. However, in terms of mechanical analysis, these processes all draw on mature technologies, and assembly techniques are existent in engineering market.

5. Anti-biofouling: Similar to the turbine, the three major components of the anchoring system above are subject to biofouling. Special attention shall be paid to the universal joints, since sever biofouling on the joints will make them broken, leading to the disintegration of the platform. The biofouling on the pontoons and the cables shall also be prohibited, since the weight of the platform will increase gradually. The overall buoyancy of the power plant is then reduced and, if no attention is paid, the platform will sink to the deep sea eventually.

6. Maintenance: One maintenance run per year is taken as a rough standard, primarily for removing biofouling and inspecting the structure robustness. Maintenance and repair work would primarily occur on site, but the design needs also to consider the difficulty of maintenance work at deep sea. Specialized submersibles (ideally remote controlled) will be required. Key technologies will be required for clearing biofouling and repairing structural damage.

2.3 The Construction Engineering Design

Construction engineering for the Kuroshio power plant is divided into four major stages: anchoring the platform, deploying the turbines, laying submarine cables and installing power transmission equipment, and power transmission and distribution on land. The first two tasks are highly complex, but the key challenge lies in the deep sea engineering required. The last two tasks involve mature undersea technology, and engineers can reference many previous projects; thus this discussion shall focus on the first two stages. The work content of these two tasks is explained in the following (illustrated in Fig. 2.4).
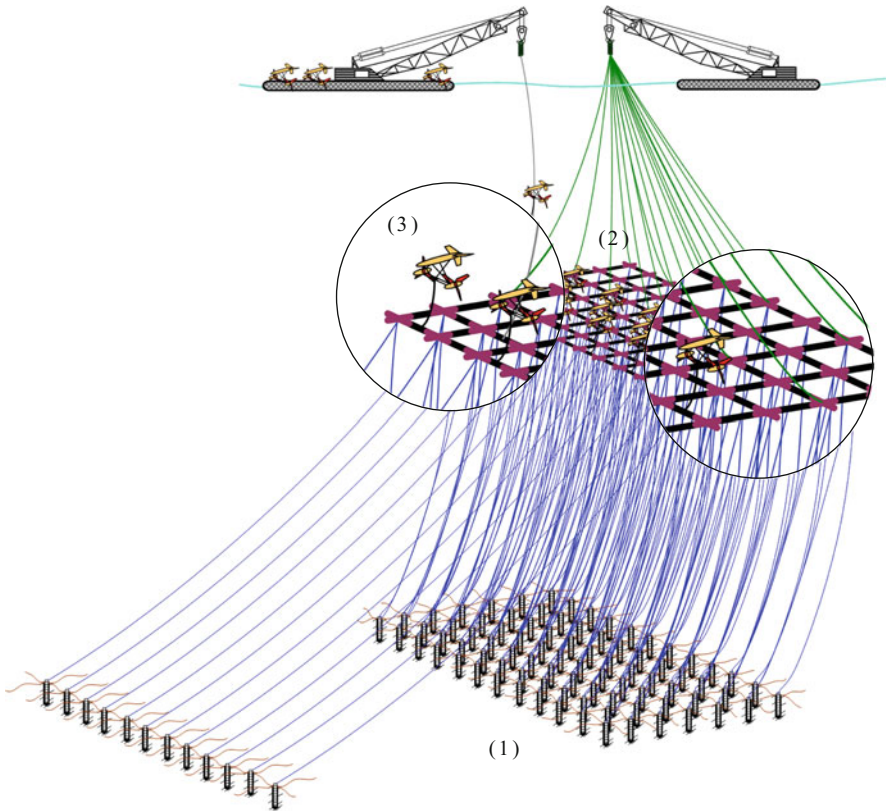
Fig. 2.4 Schematic of Kuroshio power plant construction. The construction procedure is designed to be three steps (1) anchoring the cables to the seabed, (2) anchoring the relay platform in place, and (3) installing the turbines on the relay platform. Each turbine is anchored to the platform by a single cable, while the platform is anchored to the seabed by two sets of cables: vertical and inclined

1. Anchoring the cables to the seabed: The seabed geology off of Taiwan's east coast consists primarily of igneous rock, covered by several meters of sediment. Combining screw-type anchors with pilings provides a more suitable means of anchoring the cables to the seabed [21, 22]. Installation will require the design of a deep sea piling device (see Sect. 2.4), which is remotely controlled by engineers on the barge at sea surface. This installation does not require exact precision in placing each anchor in advance, providing additional flexibility in terms of anchor type, number of required anchors, and the extension angle of the cables, thus significantly reducing installation complexity.
2. Anchor the relay platform to the sea bed: Once several hundred cables have been anchored to the sea bed, the cables are attached to their corresponding anchor points on the relay platform. The relay platform initially floats on the surface but,

as the cables are attached, it gradually sinks until the platform assumes a horizontal attitude at a predetermined depth. Finally, the tension of each cable is individually adjusted to compensate for the buoyancy of the platform, ensuring the platforms stable positioning. The area of the relay platform may cover tens of thousands of square meters, supporting dozens of turbines, each of which is exposed to hundreds of thousands of Newtons (see Chap. 3 for analysis).

Given the large size of the platform, its dynamical variations of stress and strain will be quite intense. Thus, the number of cables securing the platform to the seabed should include a suitably broad margin to enhance the overall safety of the structure [23]. The relay platform is constructed of many floats of varying sizes, shapes, and hollowness which can be used to adjust the structural strength and buoyancy. Each float should be able to swing freely, but the platform's overall deformation should be restricted within a small range to prevent the turbine groups from swinging excessively. This can be accomplished through the designing rigidity of the universal joints.

3. Anchor the turbine to the relay platform: One should not underestimate the difficulty and complexity of installing dozens of turbines safely in the ocean, which shall float stably at a distance of 50 m or more above a relay platform covering tens of thousands of square meters. The turbines can only be installed once the relay platform has been erected. Given that the side of the relay platform facing the current is subject to the greatest force of the current, the components of this side requires the greatest structural stiffness. Therefore, turbine installation should begin at the upstream side of the platform and gradually shift towards downstream. Once the turbines are fully deployed, the buoyancy and tensile strength of the anchor cable for each turbine needs to be adjusted to ensure the turbine will float at the predetermined depth and will not swift out of position due to the turbulence in current flow.

Although not shown in Fig. 2.4, submarine cables and electrical transmission engineering are still key technologies for power plant engineering [24]. The decision regarding whether AC or DC power is transmitted should be made first. Additionally, evaluations on what voltage level suits the Kuroshio power plant, how to maintain the voltage level of the power collection system in the event of malfunction or momentary power outages, and locations of the offshore and onshore power substations are also crucial issues for the power plant engineering. In fact, the location of the substations affects the costs for power generation and construction, and thus must be determined in the early planning stages. The choice of AC and DC power transmission entails a tradeoff between increased construction costs and increased transmission capacity. Cost estimates must be based on the scale of the ocean current's generating capacity and the transmission distance. Data for AC and DC power transmission must be collected and analyzed to establish a reference for future AC and DC transmission designs.

Regardless AC or DC, the output needs to be collected together to one or several locations and then transmitted through a system of AC or DC parallel submarine

cables to shore. The power collection system can be used as a power bus function for each generator, thus collecting together the power output to the interconnecting point for the power system. In addition to collecting power, the system should also be able to control the switching equipment for each turbine group, allowing for easy isolation of malfunctions to prevent damages from overload and short-circuit. Moreover, the possibility of system-wide failure should be reduced, and equipment failures that could potentially affect other facilities should be prevented.

Finally, the seismic-related risk such as the possibility of severe underwater landslides in off Taiwan's east coast shall be investigated. On this account, recommendations are made that power conversion be completed on the relay platform before transmission to the land substation by cable to improve safety and efficiency, and to lower installation costs.

2.4   The Anchor Pile Driver Design

Due to the geology makeup of hard andesite off Taiwan's east coast, screw-type anchors are recommended to secure the Kuroshio power plant. Initial estimates show a 0.5 m diameter steel screw anchor embedded 5 m into the rock would withstand a force several times that it needs to stably hold the platform (see Sect. 4.3.1 for analysis). In addition, to adapt to the rugged seabed geomorphology and reduce the cost of the anchor engineering for hundreds of buried anchor points, we have designed an unmanned deep sea anchor installation device, referred to as the Anchor Deployment Machine (ADM). The ADM allows for the remote installation of anchors through a simple and quick procedure with little environmental damage and well suited to the installation of a large number of anchors.

As shown in Fig. 2.5, the body of the ADM consists of three main parts: the housing, the anchor carrying plate (in the center), and the pressurized gear set (on the right). The housing supports the other two parts and is hold by a cable to connect to the surface barge, while using another cable to transmit power and signal between ADM and the surface barge.

Figure 2.5 also shows a sequence of nine images illustrating the anchor installation process. Once the housing is stably positioned on the seabed (Fig. 2.5a, b), the burial engineering at the heart of the ADM design uses the anchor carrying plate and the pressure gear set to individually install each screw anchor. The gear set engages the anchor and the motor drives the anchor's rotation under pressure to screw the anchor into the seabed (Fig. 2.5c–f). Once the anchor is completely buried, the ADM moves to another anchor point and repeats the process until all anchors are installed. It is then raised to the surface to be loaded with another set of anchors (Fig. 2.5g–i). The operation of the ADM is remote controlled by technicians on the barge.
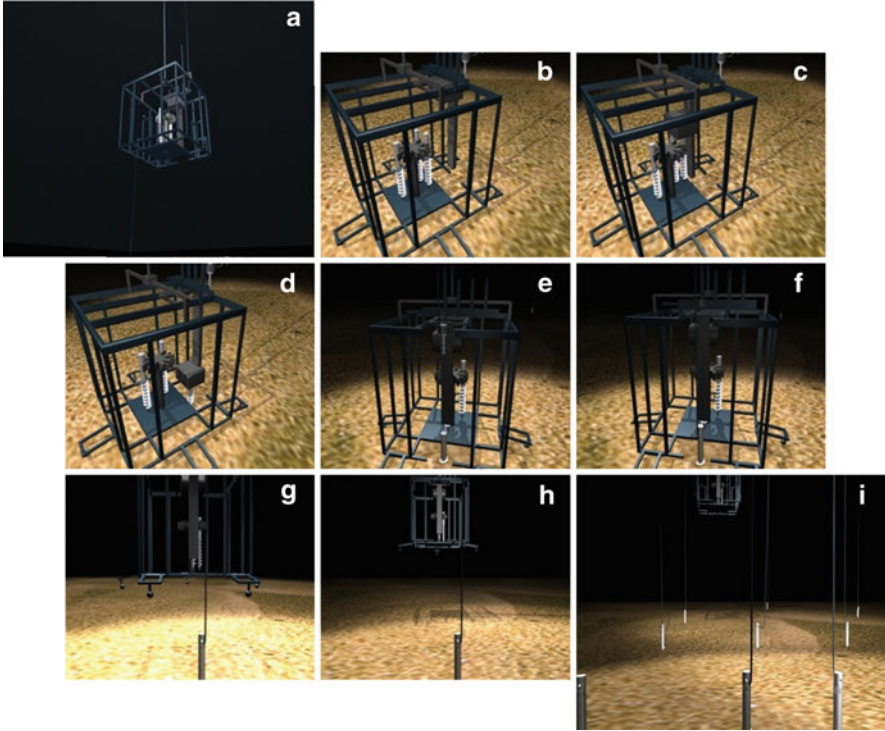
Fig. 2.5 Schematic of ADM construction procedure. (**a**) ADM hanging from the operations platform into water. (**b**) When ADM reaches the seabed, four legs extend to support the device. (**c**) The gear set on the right moves to the left to combine with the anchor set. (**d**) The gear set with the anchor moves laterally to the right to a position rotatable with pressure, where the anchor is screwed into a seabed. (**e**) Connecting the cable to the top of the anchor. (**f**) The gear set is removed after the cable is connected. (**g**) The ADM is removed, leaving the anchor and cable. (**h**) The ADM is moved to the next anchor position and repeats the aforementioned process. (**i**) With eight anchors installed, the ninth anchor is being fixed.

In brief, the ADM has three special features:

1. The body is capable of simultaneously carrying multiple anchors and cables, allowing it to complete multiple anchor installations without surfacing.
2. When the system approaches the seabed, landing brackets around open out, each supported by spherical contact points, thus allowing it to cope with uneven seabed conditions.
3. How anchors connect cables are specially designed: The end of the cable is fitted to a key-shaped retainer ring on shore. Once the anchor is secured to the seabed, the retainer ring is fixed to the anchor.

2.5   Site Selection for the Power Plant

The site selection of Kuroshio power plant is crucial. Location conditions for deep sea Kuroshio power plants are different from those for shallow water ones. Existing marine and geological data shall be used to evaluate the quality of the proposed location, wherein the type of plant—commercial or pilot—shall also be taken into account.

For a commercial power plant, there are five conditions to be considered (1) the current is strong and stable, (2) the depth of seabed shall not be large, (3) the seabed geology shall be stable and of high strength, (4) the location shall be close to coast, (5) turbine deployment shall not influence the robustness of the Kuroshio.

For a pilot plant, a sea area with various geological and marine features should be selected, so that several test units can be deployed in areas of different features, in order to carry out tests for different functions of the power plant at the same time. However, criteria for the two types of plants are not necessarily exclusive.

Figure 2.6 shows the average energy density of Taiwan's Kuroshio current at a depth of 50 m in summer 2003, which shows the Kuroshio flowing strongly northward from the Philippines to Taiwan's east coast, producing a high level of energy density as it passes Lan-Yu and Lu-Dao.

As the current passes the seas off Hua-Lien, it slows down a little bit, but then picks up again as it turns northeast towards Okinawa. An overall assessment of the current strength indicates three sites worth considering:

1. The sea between Lan-Yu and Lu-Dao: As the Kuroshio flows north from the Philippines, the current is fast and stable, but the far offshore location and deep seabed entails higher construction costs and more difficult maintenance.
2. The sea between Lu-Dao and Taiwan: As the Kuroshio passes between Lu-Dao and Taiwan, both the width and the depth of the current diminish. Squeezed by land and lifted seabed, the Kuroshio current accelerates, resulting in a strong and stable flow. Besides, the "proximity to land" and "the shallow seabed" characteristics make construction and maintenance easy, hence lowering cost. However, the forces that keep the Geostrophic Current in balance are likely to be influenced by Lu-Dao, making it difficult for the Kuroshio current to restore the kinetic energy lost. In addition, the deployment density of turbines should not be over-high to prevent a possible turn-away of the Kuroshio towards the east of Lu-Dao.
3. The sea between Hua-Lien and Yi-Lan: Here, the current is strong and wide, with a clear balance among the three balance forces to maintain the strength of the geostrophic current. However, the location is far offshore with a deep seabed, and is in an area where the current is often weakened by northeast winds.

Based on the discussion above, the optimal layouts of the site selection are prioritized as follows:

1. The sea between Lu-Dao and Taiwan
2. The sea between Lan-Yu and Lu-Dao
3. The sea off the east coast of Hua-Lien and Yi-Lan

Fig. 2.6 Average energy
density of the Kuroshio in
July 2003 at a depth of 50 m.
The highest (*darkest*) energy
density is found in three
areas: between Lan-Yu and
Lu-Dao, between Lu-Dao
and Taiwan, and between
Hua-Lien and Yi-Lan
(courtesy of Professor
Shenn-Yu Chao [Exploring
Kuroshio's energetic cores
with an ocean nowcast/
forecast system. Private
communication, University
of Maryland, 2008])
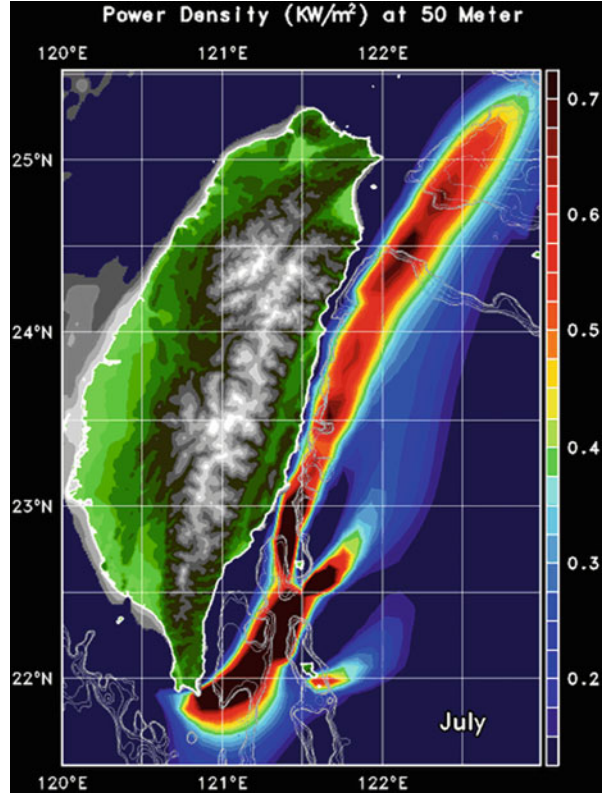
The seabed in these three areas is largely formed of hard igneous rock, covered
by a layer of sediment of varying thickness. The seabed topography near Lu-Dao
and Lan-Yu changes more drastically. To their west the seabed becomes shallower
as getting closer to Taiwan, making it be suitable for the Kuroshio power plant. To
their right the depth of seabed drops to 3,000 m, making it more difficult to
construct the Kuroshio power plant. The seabed of the third candidate, the sea
near Hua-Lien and Yi-Lan, often falls below 1,000 m, leading to difficult installa-
tion and high costs. In terms of seabed conditions, the said order of priority can be
justified.

The Kuroshio at Taiwan is wide and broad; harnessing the Kuroshio power in
such a wide area requires a systematic assessment, whereby an overall strategy for
long-term stability shall be formulated. Four key points for this purpose are as
follows:

• A detailed investigation of the economic value and technical feasibility of plant
  development within the Kuroshio waters, including the current's fluid dynamical
  characteristics, seabed engineering characteristics, and sea (and seabed) ecolog-
  ical and environmental characteristics.

- Estimation of the installation and generation capacity of the potential sites.
- Estimation of the development costs and cost of electricity for the proposed sites and the lease value for each site as well.
- Development priorities of potential sites based on the above-mentioned characteristics for each site.

2.6   The Design Features of the KPP

This chapter presents a novel and unprecedented design for a Kuroshio power plant: a group of 39 GSTs, each having an installation power of 0.5 MW, is anchored on a $770 \times 420 \text{ m}^2$ relay platform, which is a flexible marine structure stably anchored by hundreds of vertical and inclined cables to the seabed hundreds of meters below.

Conceptually speaking, the relay platform serves as an artificial seabed on which tens of turbines can be anchored safely and stably in the deep ocean. In engineering terms, it can help eliminate the high frequency forces caused by the interaction among the Kuroshio, the turbines, and the platform, providing the power plant structure with significant advantages in combating fatigue and failure.

Overall, the current design offers the following advantages:

1. Anchoring the turbine to the relay platform by a single cable of a length less than 50 m can significantly reduce the lateral drift of the turbine.
2. The relay platform is anchored to the seabed by hundreds of cables. As a result, the position where the cable is anchored is not required to be preciously accurate comparing with the predetermined one. Moreover, this design also offers significant flexibility in several parameters including anchor type, number of anchors, and angle of cable extension.
3. Taiwan's east coast experiences frequent earthquakes and undersea landslides which could easily loosen the anchors. To cope with this potential situation, the design calls for hundreds of cables, providing sufficient redundancy that allows some unexpected anchoring damages, enhancing the safety and reliability of the power plant.
4. The flexible relay platform structure, combined with the features of using a single cable to anchor each turbine, allows the overall power plant structure to effectively eliminate the high-frequency forces caused by the impact of the current, significantly reducing the likelihood of component fatigue and damage.
5. The design of the relay platform ensures the accurate positioning of the turbines in deep water, increasing the reliability of the power plant engineering. It also eliminates the need of anchoring the turbine directly in the seabed, which reduces overall costs for construction, operations, and maintenance, and increases the power plant's life span as well.
6. The turbines and platform feature simple mechanical and structural designs by making use of mature technologies. The anchoring system for the relay platform is simple and does not require a high degree of positioning accuracy on the

seabed. The single-cable anchoring for turbines offers accurate positioning and simple engineering of turbine deployment. These factors all result in a significant reduction in costs for construction, operations, and maintenance.

7. Although each sub-construction employs mature technologies, these are combined into new products and a brand new design. This is a new form of marine engineering, represents a significant change in human energy development and marine engineering technology, and should have an inspiring and enlightening influence.

However, there are also some drawbacks:

1. It is a novel and unprecedented design, leaving much to be explored and higher R&D costs.
2. The flexible structure reduces turbine efficiency; the degree of reduction needs a reassessment.
3. The construction is complex, including setting the anchors in the seabed, erecting the cables, installing the platform, anchoring the turbines, testing and starting the power plant, and so on. This entails many procedures, each of which requires careful planning and design.
4. Many construction procedures are unprecedented; the construction equipment and rigging may require a new design.
5. Finally, the novelty of the engineering design and the nature of deep sea engineering entail high costs and considerable risk. In early development stages, one needs to proceed cautiously, wherein each likely problem should be investigated and solved step by step. The turbines should not be installed underwater until all engineering procedures are well designed and clarified.

Recently, the engineering design for the harness of ocean power has been ascendant [25], but that for deep ocean is indeed rarely seen. There are three cases that can be representative: the case for the Gulf Stream at east Florida, the case for the Agulhas Current at southeast Africa, and the case for the Kuroshio at south Japan. All cases had created new designs for the power plant in deep ocean. For the Gulf Stream [7, 8, 26], they design a twin-rotor turbine to be anchored directly onto the seabed. For the Agulhas Current, Wright et al. [27] studied the feasibility of employing the SeaGen developed by MCT company of Scotland. For the Kuroshio [28], the Industrial Technology Development Organization (or NEDO) has proposed to build a 850 MW Kuroshio power plant in the Kuroshio waters at south Shikoku and the Kii Peninsula. The power plant is composed of hundreds of turbines; each turbine has two counter-rotating rotors of 40 m in diameter and is anchored to the seabed at 100 m deep by a single cable.

Similar to the present KPP design, because of the deep water, all cases use flexible cables to anchor turbines in the ocean. The major difference stems from that they did not consider a design like the relay platform to create an artificial seabed closer to the surface. Accordingly, it is implied that the length of anchoring cable of the turbine of these three cases shall be much longer than the present one, so will the drift of the turbine be of a larger amplitude, causing great difficulties for power plant operation and maintenance.

References

1. Khan J, Bhuyan GS (2009) Ocean energy: global technology development status. Report prepared by Powertech Labs Inc. for the IEA-OES
2. Ben Elghali SE, Balme R, Le Saux K, Benbouzid MEH, Charpentier JF, Hauville F (2007) A simulation model for the evaluation of the electrical power potential harnessed by a marine current turbine. IEEE J Oceanic Eng 32(4):786–797. doi:10.1109/JOE.2007.906381
3. Thake J (2005) Development, installation and testing of a large-scale tidal current turbine. IT Power, http://webarchive.nationalarchives.gov.uk/+/, http://www.berr.gov.uk/files/file18130.pdf. Accessed 29 Jun 2013
4. Coiro DP, Nicolosi F, De Marco A, Melone S, Montella F (2005) Dynamic behavior of novel vertical axis tidal current turbine: numerical and experimental investigations. In: Chung JS, Hong SW, Koo J, Komai T, Koterayama W (eds) The proceedings of 15th international offshore and polar engineering conference, Seoul, Korea, 19–24 June 2005
5. Zanette J, Imbault D, Tourabi A (2010) A design methodology for cross flow water turbines. Renew Energy 35(5):997–1009. doi:10.1016/j.renene.2009.09.014
6. Bahaj AS, Molland AF, Chaplin JR, Batten WMJ (2007) Power and thrust measurements of marine current turbines under various hydrodynamic flow conditions in a cavitation tunnel and a towing tank. Renew Energy 32(3):407–426. doi:10.1016/j.renene.2006.01.012
7. VanZwieten J, Driscoll FR, Leonessa A, Deane G (2006) Design of a prototype ocean current turbine – part I: mathematical modeling and dynamics simulation. Ocean Eng 33:1485–1521. doi:10.1016/j.oceaneng.2005.10.005
8. VanZwieten J, Driscoll FR, Leonessa A, Deane G (2006) Design of a prototype ocean current turbine – part II: flight control system. Ocean Eng 33:1522–1551. doi:10.1016/j.oceaneng.2005.10.006
9. Hermans AJ (2003) The ray method for the deflection of a floating flexible platform in short waves. J Fluids Struct 17(4):593–602. doi:10.1016/S0889-9746(02)00148-2
10. Garrett DL (2005) Coupled analysis of floating production systems. Ocean Eng 32:802–816. doi:10.1016/j.oceaneng.2004.10.010
11. Shafieefar M, Rezvani A (2007) Mooring optimization of floating platforms using a genetic algorithm. Ocean Eng 34:1413–1421. doi:10.1016/j.oceaneng.2006.10.005
12. Chakrabarti S (2009) State of offshore structure development and design challenges. In: Kim YC (ed) Handbook of coastal and ocean engineering. World Scientific, Singapore, pp 667–694
13. Brown DT, Lyons GJ, Lin HM (1997) Large scale testing for mooring line hydrodynamic damping contributions at combined wave and drift frequencies. In: Proceedings of BOSS, vol 2. Oxford, Pergamon, pp 397–406
14. Brown DT, Mavrakos S (1999) Comparative study of mooring line dynamic loading. J Mar Struct 12(3):131–151. doi:10.1016/S0951-8339(99)00011-8
15. Hinz ER (2001) The complete book of anchoring and mooring, 2nd revised edn. Cornell Maritime, Centreville, MA
16. Poiraud A, Ginsberg-Klemmt A, Ginsberg-Klemmt E (2007) The complete anchoring handbook: stay put on any bottom in any weather. International Marine/Ragged Mountain (McGraw-Hill)
17. Bungartz H-J, Schäfer M (eds) (2006) Fluid–structure interaction: modelling, simulation, optimization. Springer, Berlin
18. Paidoussis MP (1998) Fluid–structure interactions: slender structures and axial flow. Academic, San Diego, CA
19. Ablow CM, Schechter S (1983) Numerical simulation of undersea cable dynamics. Ocean Eng 10(6):443–457. doi:10.1016/0029-8018(83)90046-X
20. Kim YC (2010) Handbook of coastal and ocean engineering. World Scientific, Singapore
21. Kutt LM, Pifko AB, Nardiello JA, Papazian JM (1998) Slow-dynamic finite element simulation of manufacturing processes. Comput Struct 66(1):1–17. doi:10.1016/S0045-7949(97)00069-2

22. Lewis WJ (2003) Tension structures: form and behaviour. Thomas Telford, London
23. Hallam MG, Heaf NJ, Wooton JR (1997) Dynamics of marine structures. Report UR8 CIRA Underwater Engineering Group, London
24. Liu CS (2008) Geological physical survey, earthquake monitoring and disaster assessment. A proposal submitted to National Science Council, Taiwan
25. Hardisty J (2009) The analysis of tidal stream power. Wiley-Blackwell, Chichester
26. Finkl CW, Charlier R (2009) Electrical power generation from ocean currents in the Straits of Florida: some environmental considerations. Renew Sustain Energy Rev 13:2597–2604. doi:10.1016/j.rser.2009.03.005
27. Wright SH, Chowdhury SP, Chowdhury S (2011) A feasibility study for marine energy extraction from the Agulhas Current. In: 2011 I.E. Power and Energy Society general meeting, p 9. doi:10.1109/PES.2011.6039896
28. http://www.monoist.atmarkit.co.jp/mn/articles/1111/29/news007.html (in Japanese). Accessed 20 Mar 2013

Chapter 3
Dynamic Analysis and Design of Turbine

Under the action of the Kuroshio, the turbine anchored by a single cable on the relay platform shall experience complicated reaction to the strong current, among which the displacement of the turbine swift with the current, the deformation of the turbine body due to the forces applied by the current, and the vibration of the turbine due to the dynamic effects in various respects are all important problems to be solved to make a turbine of great power efficiency. On the other hand, the power efficiency of turbine correlates closely with its structure stiffness. To analyze the stiffness of the turbine, one shall investigate the reaction force applied on each component of the turbine, the dynamical effects due to the vortex shedding generated from rotor, the high-frequency force variation due to the turbulence, the impact due to the phase difference between rotors, and the cavitation possibly occurring on the rotor blade so that the design of turbine can be carried out. In this chapter, we employ the computational fluid dynamic to explore the time-dependent dynamic forces applied on the turbine under the action of the Kuroshio, and the results are compared with those obtained by blade element momentum (BEM) theory to confirm the accuracy of the CFD results.

As mentioned in Chap. 2, the reasons to choose GST to deploy in the Kuroshio are that it has a tail-wing stabilizer to autonomously adjust the turbine altitude to face against the current, and it can be anchored on the relay platform with a single cable. Two reversely rotating rotors are installed at the nose of watertight nacelles, which are connected with the main pontoon by several connecting linkages. The front view of the turbine looks like a triangular configuration, as shown in Fig. 3.1. Given the characteristics of the Kuroshio and the power generation requirements in mind, we made some minor changes to the original GST design [1]. For example, the length of the axial ratio for the main pontoon and the two watertight nacelles was changed to 3:1 for elliptical streamlining, the cross section of the connecting linkage with the anchor joint was changed to an aspect ratio of 2:1, a NACA4415 airfoil is chosen to be the blade of the rotors, and so on.

As one can see from Fig. 3.1, we decided to use two three-blade rotors for the turbine because, in general, increasing the number of the blades will end up with a lower rotational speed, but will enlarge the bearing torque and increase the costs of
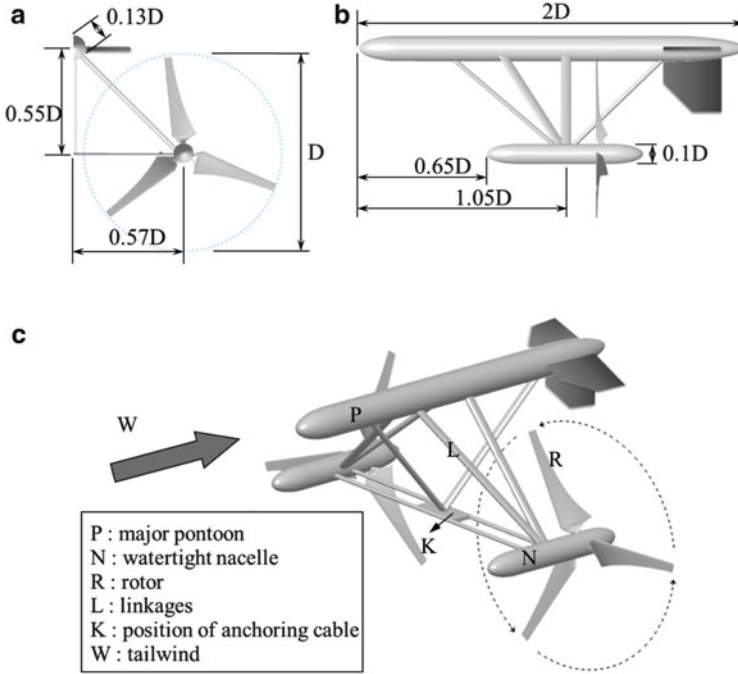
Fig. 3.1 The schematic drawing of the GST (modified after [1]). (**a**) Front view (half-symmetry model). The GST has two sets of three-bladed rotors connected with a pontoon in a *triangular* configuration. (**b**) Side view. A 2D length main pontoon and two 1D length watertight nacelles are connected by the connecting linkages. Note that D is the diameter of the rotor. (**c**) Perspective view. The main pontoon is at the *top center* of the turbine, the two nacelles are placed on the two sides of the turbine, and the anchoring point is at the *bottom center*. The linkages connect the pontoon and the watertight nacelles. Note that in the computation the tail-wing stabilizer is not taken into account

manufacture and maintenance as well. On the other hand, decreasing the number of the blades increases the rotational speed, resulting in higher noise and vibration. Consequently, as concluded by numerous studies from different perspectives, a three-blade rotor shall reach an optimizing situation of reasonable rotation speed with a higher power output without producing annoying noise or vibration [1, 2].

The optimized design for the blade is to ensure that the torque applied on the blade shall be constant in the radial direction. As a result, the pitch angle, the twist angle, and the chord length of the blade shall vary in the radial direction so that the interaction between the blade and the current can be done under the most efficient angle of attack and a maximum contact area. To meet the requirements above, the airfoil NACA4415 is selected. A special attention is paid to the design for the base of the blade, which locates within $r/R < 0.1$, where r is the distance from the blade to the rotor center and R is the rotational radius. The base serves to hook the blade on the hub of the rotor and is designed to change the shape from the airfoil to a circular cylinder, so that the blade can be strong enough to cope with the largest

Fig. 3.2 The schematic drawing of the cross section of the blade. Based on the NACA4415 airfoil data, the pitch angle, the twist angle, and the chord length are varied along the radial direction of the blade. The cross section of the blade base is changed from an airfoil at the blade tip to a cylinder at the blade root
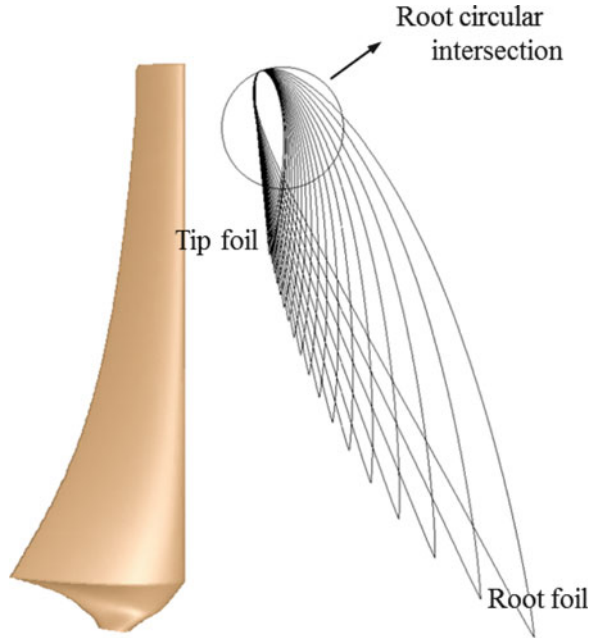
torque ever occurring at the turbine. In addition, an optimal tip speed ratio (TSR) with the number of blade, the size, and the cross-sectional shape is also prerequisite for the analysis. We referred to the design of SeaGen of MCT company [2] and determined the following design parameters: A three-blade rotor with blade length of 10 m, a hub of a diameter 2.3 m, and a rated TSR of 5. Consequently, the schematic drawing of the blade shape is shown in Fig. 3.2.

3.1 Physical Models and Numerical Schemes

As shown in Fig. 3.1, the turbine can be divided into the fuselage (including the main pontoon and the watertight nacelles), the connecting linkages, and the rotors. Given the right–left symmetry of the body, the computational effort can be saved significantly by only considering the right half of the turbine in the analysis. Besides, given this symmetry, the tail stabilizer can be excluded from the computation momentarily. We accordingly assume that the turbine shall remain the designed altitude facing against the current without being disturbed by flow turbulence. Finally, the design of the tail-wing stabilizer will be taken into account based on the forces applied on the turbine's components obtained by previous computations.

In present computational work, a computer-aided design (CAD) software is used to build a geometric model of the turbine. We then computed the grid division and demarcation and ended up with a computational grid, which is then used as an input to the CFD code named ANSYS Fluent [3] to discretize the governing equations and boundary conditions. The governing equations are conservation equations of mass and momentum [4, 5]. The Reynolds-averaged Navier–Stokes equations (RANS) are employed to take the turbulent effect into account. As a result, the eddy viscosity is generated in the equation and is simulated by using the so-called $k - \omega$ model [6, 7], where k is the turbulence kinetic energy and ω is the specific dissipation rate.

To discretize the governing equations, we select a second-order upwind difference scheme and employ the slow-converging pressure-based segregated algorithm to reduce the size of memory required for efficient computations. The pressure correction equation is solved by using the semi-implicit method for pressure-linked equations (SIMPLE) proposed by Patankar and Spalding [8]. Transient phenomena are dealt with a sliding mesh (SM) which is based on implicit time discretization to derive unconditional stability for all time steps.

Figure 3.3 shows the final computational grid. The computational domain is enclosed by a half cylinder (symmetrical model) where the diameter of the cylinder is ten times the diameter of the rotor (i.e., $10D$). The gravity center of turbine locates at the center of the computational domain and is at a distance of $5D$ from the left boundary and $12D$ from the right boundary of the computational domain. Consequently, the total number of nodes is about 1.5 million (or 1.5 M). Special attention shall be paid to the grid surrounding the rotor. To simulate the rotation of the rotor, the grid surrounding the rotor is separated with the remaining grid to form a domain of a circular plate; see the yellow grid in Fig. 3.3. The computation moves forwards with a proper speed so that the circular-plate grid will rotate in the same phase with the rotor. Consequently, the nodes inside and outside the circular plate shall coincide with each other at each time step.

Before carrying out the entire analysis, we conducted a grid independency test by considering three different grids, which have, respectively, 1.5 M, 3.3 M, and 7.0 M nodes. Results show that, for the three cases considered, the difference between the results lies within a range from 0.57 % to 5.32 %, implying that a larger number of grid nodes do not mean to get a more accurate result, while the computational effort for 7.0 M case is many folds larger than the 1.5 M case. Accordingly, the grid of 1.5 M nodes will be used for the cases considered in this study.

3.2 Typical Flow Field

In the computation, the incoming flow is assumed to be a laminar flow of a velocity 1.4 m/s. While the flow passes through the turbine, complicated and unstable variations will be generated under the action of the rotor blades. A typical flow
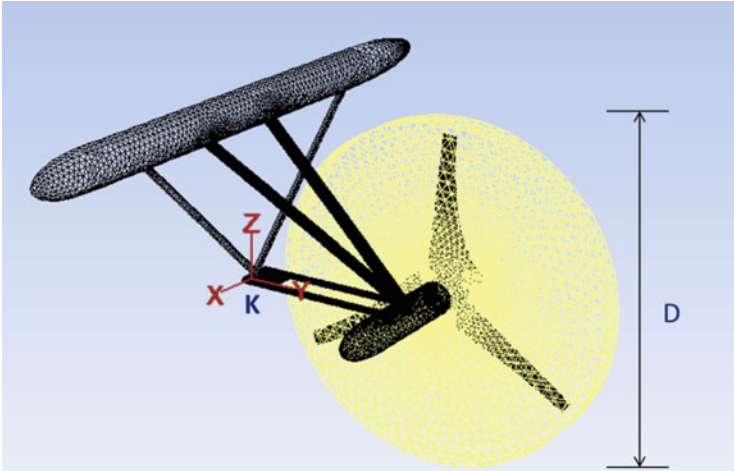
Fig. 3.3 The half-symmetrical computation domain and grid are shown. The total number of the grid nodes is about 1.5 M. A cylindrical offset rotating domain rotates with the three-blade rotor. In the calculation, the half-symmetrical model is employed without considering the tail-wing

for the case of rotor's angular speed being 6 rpm is shown in Fig. 3.4, where the flow animation illustrates the position change of a row of flow particles (white balls) perpendicular to the rotor axis passing through the turbine. As shown in Fig. 3.4a–f, the particles behind the rotor experience a serious lag behind those away from the rotor, implying that the flow momentum behind the rotor is decreased and the wakes are generated behind the rotor. The flow far away from the rotors retains most of the momentum of the inflow, virtually not affected by the rotor. The loss of linear momentum is converted to angular momentum by the rotor to drive the power generator. As a result, a higher loss of momentum in the wake leads to a higher efficiency and better performance of the turbine. As shown in Fig. 3.4, the momentum loss in the wake accounts for a large portion of the total momentum of the incoming flow, implying that the present design of the rotor is of high efficiency and the turbine is of good performance, which will be confirmed by the discussions in the following sections.

According to the conceptual design shown in Chap. 2 (see Fig. 2.1), the Kuroshio power plant is assembled by dozens of turbines arranged in a way of staggered matrix. The space between turbines is determined based on the principle that the adjoining turbines cannot interfere with each other and the wake generated by the turbine at front cannot affect the performance of the turbine at behind [9–14]. As a result, in the direction perpendicular with the flow, the distance between turbines can be arranged to be 2D–3D. In the direction parallel to the flow, the distance between turbines shall be as large as 5D–10D, depending on the flow velocity and the rotor's angular speed [15].
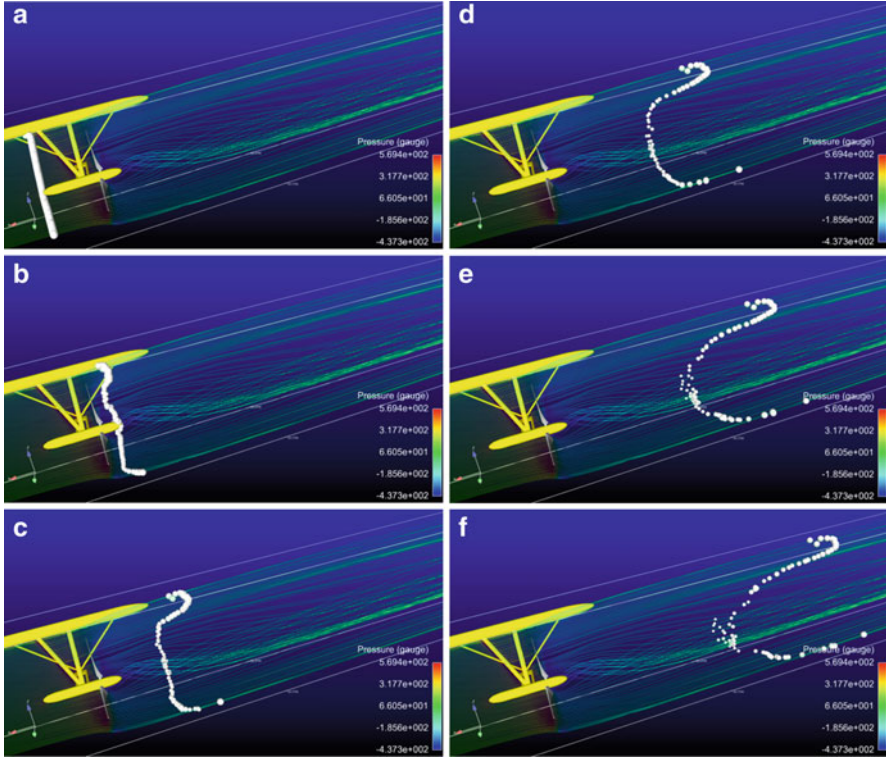
Fig. 3.4 The flow field animation of the current running through the turbine. The row of flow particles (*white balls*) shows (**a**) the flow precedent to the turbine; (**b**) the flow is passing the rotor; (**c–f**) the flow behind the rotor moves much slower than that far away from the rotor

3.3 Reaction Force on the Turbine

After referred to the parameter analyses and results of previous studies [15–19], we consider for the following cases the flow velocity to be 1.4 m/s and the blade rotation speed to be 6 rpm to fit the optimal operating condition of GST. Figure 3.5 shows the reaction forces of the GST in three axial directions, which vary with the phase angle of the blades. As shown in Fig. 3.3, we set the origin of the Cartesian coordinate system at the center of based connection linkage, noted as the anchor point K on which the cable is fixed. The flow moves along the X-axis, the Z-axis stands for the vertical axis perpendicular with the flow, and the Y-axis stands for the horizontal axis perpendicular with the flow. The three curves depicted in Fig. 3.5 show the force changes three times in the Y-direction and six times in both the X- and Z-directions, while all vary periodically with the blade rotation. In the direction of the flow (i.e., the X-axis), the force is 365 ± 10 kN (1 KN means $10^{**}3$ Newton), while the respective forces in the Y- and Z-axes are 5 ± 3 kN and 7 ± 2 kN. The force in the X-axis is considerably larger than those in the other two
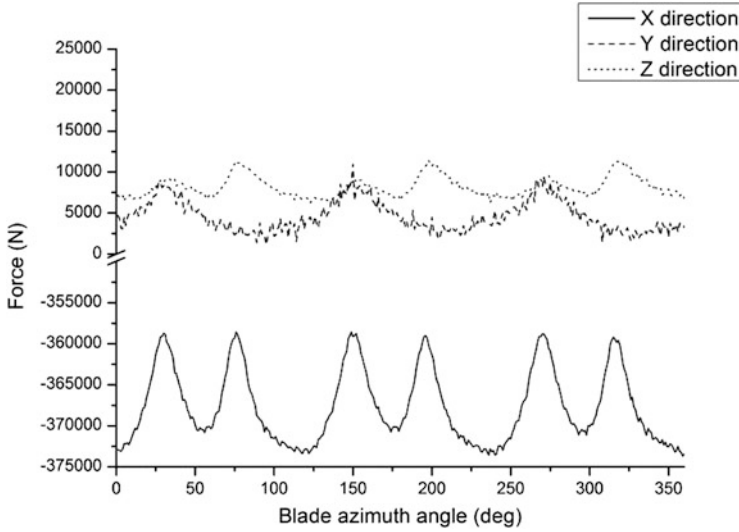
Fig. 3.5 The forces in three axial directions exerted on the single-rotor turbine with different blade azimuthal angles. Force is largest in the *X*-direction (*bottom curve*), about 40–50 times the force in the *Y*- and *Z*-directions (*top two curves*). For the normal twin-rotor turbine, the actual forces shall be twice as large as the ones shown in the figure

axes due to the fact that the blades absorb the vast majority of the flow's kinetic energy, implying that the present GST is a good design of high efficiency. Note please that the present computation is done for a single-rotor turbine due to the symmetric situation considered. As soon as the normal twin-rotor turbine is considered, the forces shown in Fig. 3.3 shall be multiplied by two to account for the overall force exerted on the turbine.

The periodical variation of the force exerted on the turbine is a result from the fact that the forces exerted on the three blades vary periodically with time. As shown in Fig. 3.6, the force exerted on blade 1, for example, exceeds 118 kN when the blade passes through the angle at 150° and then drops to 105 kN twice before the blade returns to 150°. This is because the blade passes consecutively through the wakes generated behind the connecting linkage 3 (and linkage 4) and the base linkage (see Fig. 3.1), resulting in a periodic reduction of power output of turbine which is referred to as the so-called tower shadow effect. Similar results are also found for the other blades. The reduction of the exerted force on each blade due to the tower shadow effect is about 12 % of the force in *X*-direction, which may cause structure damage and power reduction. This, however, cannot be prevented as long as the rotor is set behind the connecting linkages.

The time variations of the force exerted on the other turbine components are plotted in Fig. 3.7. It shows that the maximum forces occur on linkages 1 and 2, and then the forces on linkage 3, the base linkage, linkage 4, and finally the minimum
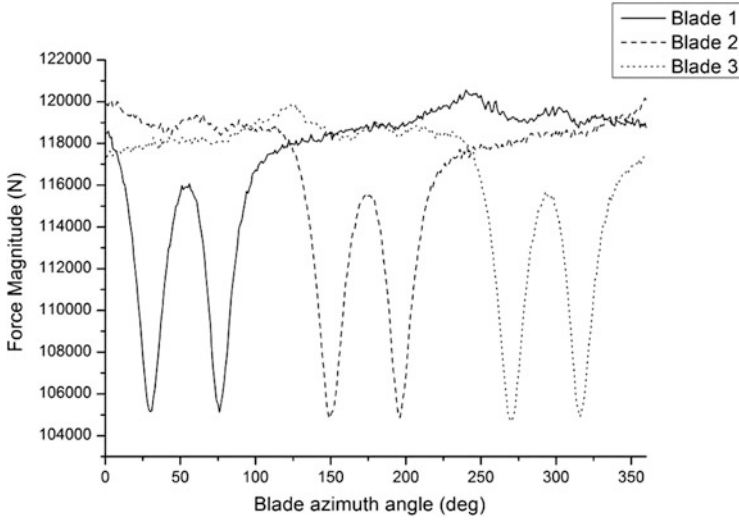
Fig. 3.6 The cyclic variations of the force exerted on each blade. On each blade, the force experiences twice the force reduction because the blade passes through two wakes behind the two linkages
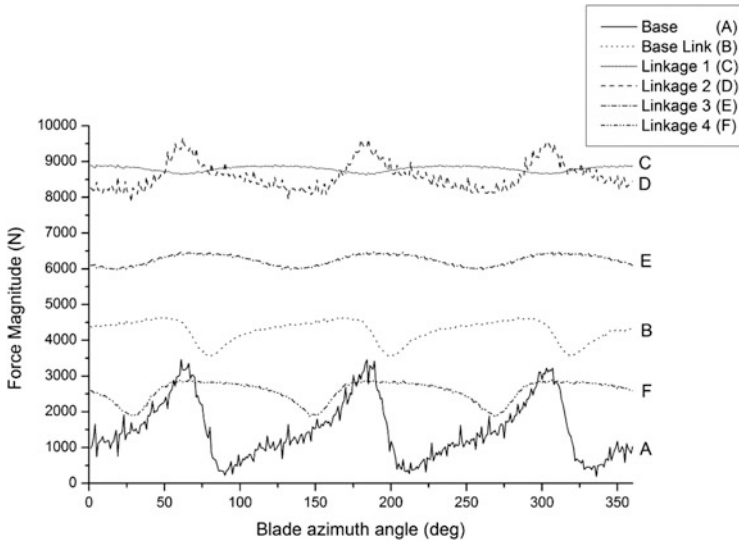
Fig. 3.7 The cyclic variations of the force exerted on each linkage

force occurs on the base. The periodical variation of the force exerted on linkage 2 is apparently due to that it sits within the wake generated by linkage 1. Similar reason can be applied for that the force exerted on linkage 3 is greater than that on linkage 4. That the force exerted on linkages 1 and 2 is greater than that of linkages
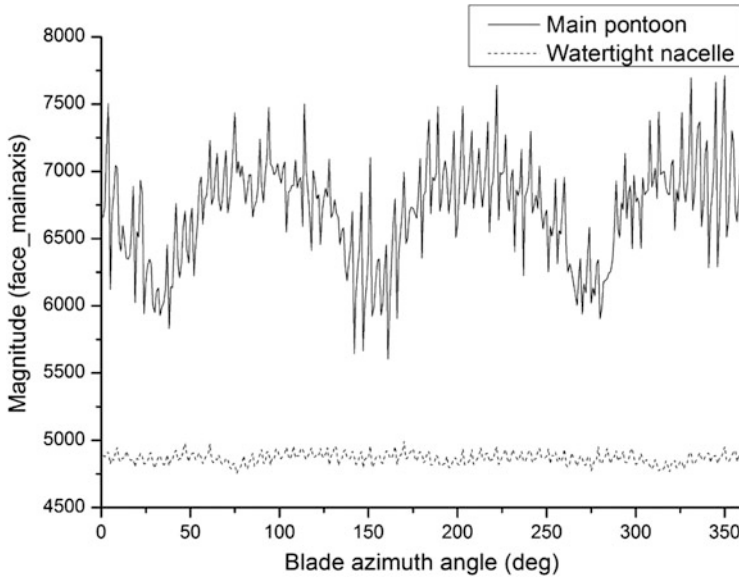
Fig. 3.8 The cyclic variations of the force exerted on the main pontoon and the watertight nacelle

3 and 4 is because the flow velocity is larger when passing through the region between two rotors than when flowing into the rotor regimes. The force exerted on the base point is the smallest because the cross area facing the flow is the smallest, resulting in a smallest resistance force to the flow. Nevertheless, the reaction forces on these linkages are only about 3 % of those on the blades in the X-direction, showing that the streamline shape of the cross section of these linkages has successfully reduced the resistance to the flow.

Also shown in Fig. 3.8 are the force variations on the main pontoon and the watertight nacelle. It is seen that the averaged forces on pontoon and nacelle are about 6.7 kN and 4.8 kN, respectively, being about the same magnitude with those on the linkage. Although the size of pontoon or nacelle is much larger than that of linkage, the forces exerted on these components are virtually of the same magnitude, implying that the streamline shape of pontoon and nacelles works successfully to reduce the resistance on the flow. On the other hand, because both the diameter and length of the main pontoon are larger than those of watertight nacelle, a larger reaction force and a greater wake-induced force fluctuation occur on the pontoon. But, after all, this high-frequency force fluctuation of both pontoon and nacelle is negligible comparing with those on the blade.

We categorize the components of the turbine into blade, linkage, and hull and sum up the forces on each of them, and the results are shown in Fig. 3.9. It is seen that in the X-direction the force on the blade accounts for more than 93 % of the total force on the turbine. The other parts of turbine, i.e., the five linkages, one pontoon, and two nacelles, are loaded with less than 7 % of the total force. Similar results are found in the other two directions, although the percentage of the total

Hydrodynamic force distribution			
	X-direction	**Y-direction**	**Z-direction**
Blade (A)	344135.06 (93.62%)	42615.85 (82.78%)	41937.91 (72.36%)
Linkage (B)	16535.64 (4.5%)	5570.14 (10.82%)	13163.44 (22.71%)
Hull (C)	6910.34 (1.88%)	3295.20 (6.40%)	2858.41 (4.93%)

unit: N
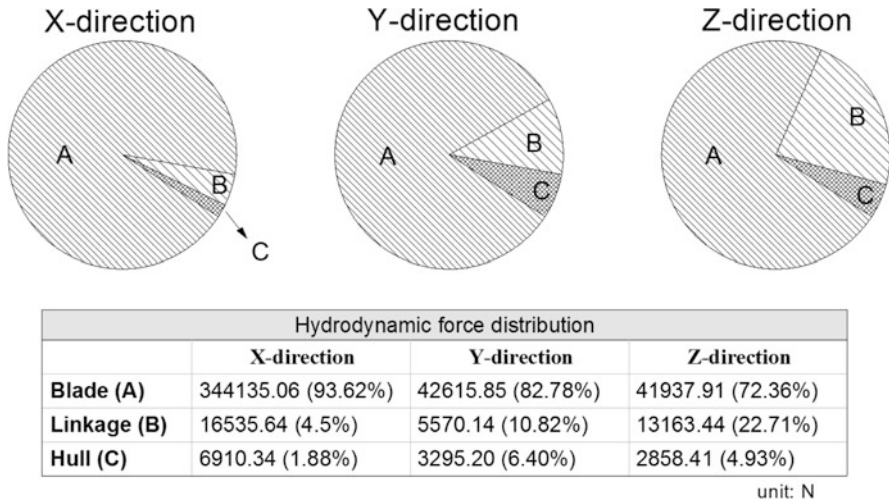
Fig. 3.9 Force exerted on each GST component. The force on blades accounts for a great majority of force exerted on GST in all directions. The proportion of the force on the connecting linkages and fuselage increases slightly in the Y- and Z-directions

force on the turbine body is larger due to the smaller magnitude of the forces on the blade than that in the X-direction. It is also seen that, in all three directions, the forces exerted on linkages and hull are much smaller than those on the blades, showing that the present design of turbine body meets the requirement to reach a high efficiency. On the other hand, the forces on the blades are dominated by that in the X-direction, which is about eight times larger than those in the other two directions, also showing how a good design of turbine shall be. The forces on linkages and hull, nevertheless, are of the similar magnitude in all three directions, showing that the present design has no directional preference with respect to the incoming flow.

3.4 Turbine Performance

The performance of turbine is evaluated through three aspects, i.e., the power output, the shaft torque, and the thrust. By and large, the power output directly reflects the amount of kinetic energy captured by the rotor, the shaft torque directly impacts the power output, and the thrust influences the magnitude of shaft torque. Their values are interdependent and vary with the velocity of the incoming flow [20]. In this section, we discuss on the influence of the flow velocity on the turbine performance.
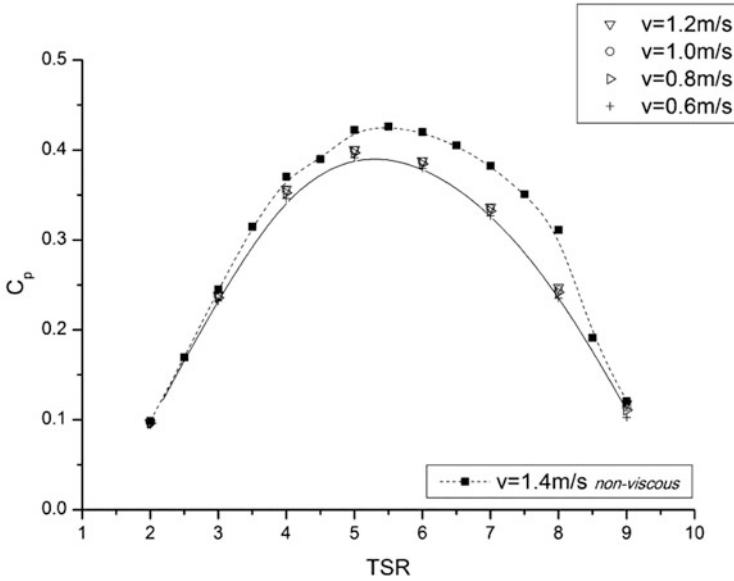
Fig. 3.10 The relation between TSR and C_p for the rotor of GST under four different inflow velocities U and a constant shaft angular velocity Ω

To investigate the dependence of the turbine performance on the flow velocity, the relation between the TSR and the power output coefficient C_p of the rotor shall be illustrated. The TSR is the ratio of the tangential velocity at the blade tip to the inflow velocity, defined as TSR $= \Omega R/U$, where Ω is the shaft angular velocity, $R = D/2$ is the distance between the blade tip and the center of the shaft (or the radius of the rotor), and U is the inflow velocity. If P is the power output, then the power coefficient is defined as $C_p = 2P/\rho U^3 A_{\text{eff}}$, where ρ is the seawater density, and A_{eff} is the effective area of the rotor. Accordingly, TSR can represent the variation of C_p in different values of U (or Ω) for a constant Ω (or U).

In Fig. 3.10, we show the TSR–C_p curve for the rotor of GST, in which four different flow velocities, $U = 0.6$, 0.8, 1.0, and 1.2 m/s with a constant shaft angular velocity Ω are considered. Interestingly, all these four curves show that the maximum C_p occurs at TSR $\doteqdot$ 5, implying that the rotation speed of rotor shall change with inflow velocity to maintain TSR $\doteqdot$ 5, which is by no means an easy job because, in reality, the velocity of the Kuroshio fluctuates with time. Accordingly, a powerful electronic control unit shall be installed within the generator to control the rotation speed of the rotor to achieve the design value of TSR $\doteqdot$ 5 under varying inflow velocity.

Figure 3.11 shows the power output of the GST rotor under the conditions $U = 1.4$ m/s, $\Omega = 6$ rpm, and $R = 11.15$ m. Results show the power output varies periodically because of the tower shadow effect explained in Sect. 3.3. The maximum power output can be as high as 245 kW and the minimum is about 225 kW, giving an average value of power output about 235 kW, which is for a single rotor.
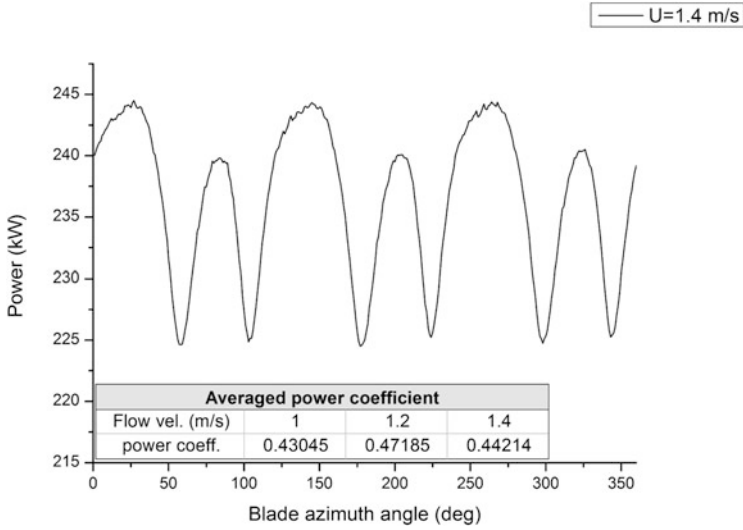
Fig. 3.11   Turbine output power fluctuates with the blade azimuthal angle

For GST a turbine of two rotors, the average power output can be 470 kW, and the maximum power output can be as high as 490 kW.

The results of Fig. 3.10 obtained by CFD can be verified by the cubic relation between the power output and the flow velocity. For TSR = 5 with $U = 1$ m/s and $\Omega = 4.28$ rpm, the single rotor average P is about 88.83 kW, which is about 0.38 times that of $U = 1.4$ m/s, fitting well with the theoretical relationship that $P \sim U^3$.

3.5   Dynamic Effects

The design of GST is endowed with several dynamical phenomena which may influence significantly the performance of the turbine. They are, for example, the tower shadow effect due to the wake impinging on the rotor, the turbulence effect due to the flow fluctuation, the dual-rotor effect due to rotors operated in different phase, the cavitation effect due to the exceeding rotor speed, and so on. We shall discuss these effects on the turbine performance in the following.

3.5.1   Tower Shadow Effect

As shown in Figs. 3.5, 3.6, 3.7, and 3.8, the forces exerted on GST components vary periodically with time, resulting in the fluctuation of the power output as shown in Fig. 3.11. As explained in Sect. 3.3, this is clearly a result from that
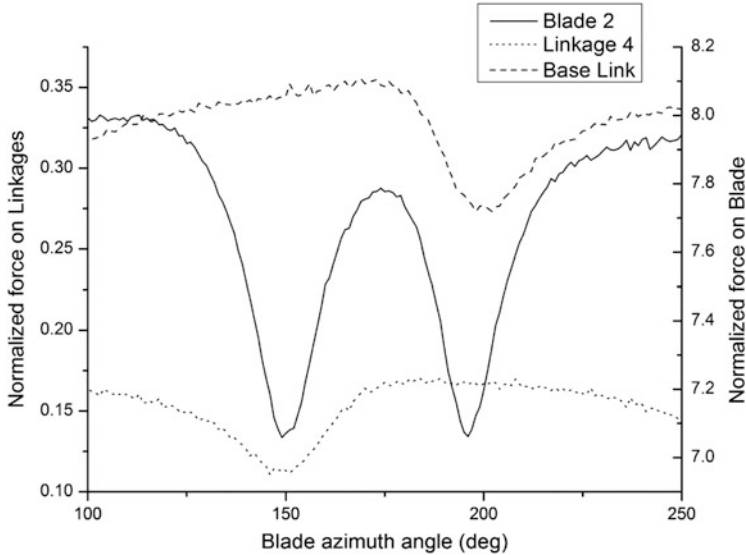
Fig. 3.12 The normalized force exerted on the blade and linkages changes periodically with blade azimuthal angles

the wakes generated by the two sets of connecting linkages impinge on the rotor, commonly known as the tower shadow effect. Figure 3.5 shows that the force in X-direction experiences six undulations of an amplitude about ± 3 % of the total force in one revolution of rotation. The force in Z-direction also experiences six undulations. But the force in Y-direction experiences only three undulations because the wake effects on the two rotors are offset due to the right–left symmetry.

To illustrate the tower shadow effect on GST, the variations of the normalized forces, defined as $C_{Fi} = 2F_i/\rho U^2 A_{\mathrm{effi}}$, exerted on blade 2, linkage 4, and the base linkage are shown in Fig. 3.12, where F_i and A_{effi} are the force and effective area of the turbine component. Results show that the normalized force on base linkage is about twice as large as that on linkage 4, which is because the cross-sectional area of base linkage is larger. The force on linkage 4 experiences a drop at the blade azimuthal angle at $149°$ when the blade is passing behind the linkage. This is because the impedance on the flow due to the rotor at behind reduces the force exerted on the linkage. Similarly, the force on base linkage experiences a drop at the angle of $196°$ under the same reason. On the other hand, a combination of above two force-drops leads to that the blade 2 experiences two force-drops at respectively $149°$ and $196°$ due to the wakes generated by the base linkage and the linkage 4 [13, 14].

3.5.2 Turbulence Effect

Figure 3.5 shows the turbine is not only subject to the low-frequency force variations due to the tower shadow effect, but also subject to the high-frequency force variation of smaller amplitude caused by the turbulence effect. It is seen that, although the turbulence effect is seen at almost every blade angle, the effect is more obvious when it rotates to the downstream of linkage 4 and base linkage. The variation due to turbulence effect is largest in the Y-direction (about $\pm 1,500$ N). In the X-direction, the turbulence effect creates a variation of about $\pm 1,000$ N, but this variation is only noticeable when the blade is affected by the wake behind the connecting linkage. In the Z-direction, the turbulence effect is negligible. Overall, the turbulence effect accounts for only 0.3 % of the overall change in force, being negligible in the design of turbine [5, 6].

3.5.3 Dual-Rotor Effect

The GST has two rotors of the same geometric dimension that rotate in opposite directions to balance the torques generated by the rotors. However, when the rotors rotate in difference phases, the force fluctuations caused by tower shadow effect cannot be offset. As a result, the power output and the turbine performance will be influenced by the phase difference between two rotors.

To examine this so-called dual-rotor effect, we examine the variation of the force exerted on the turbine under different phase shift between two rotors. Since in the present analysis only half of the turbine is considered due to its geometric symmetry, we shall use the data of Fig. 3.5 and superpose two sets of data of different phases. Given that the rotors have three blades, the force variation will repeat in every 120°. Furthermore, due to the symmetry between two blades, for example, the result under a 50° phase difference shall be the same as the result under a 70° phase difference, we need only to consider the phase difference ranging from 0° to 60° to account for an entire cycle of force variation.

Figure 3.13 presents the force variations for six phase differences ranging from 0° to 60°. Results show that, in terms of the force fluctuation, the greatest fluctuation occurs at the case of zero phase difference, and the smallest fluctuation occurs when the phase difference is 20°. In terms of average force, virtually all the cases end up with an average of about 735 kN for the dual-rotor turbine. This is also seen from the results shown in Fig. 3.14, in which the average forces for different phase differences are presented. More precisely to say, in a 120°-cycle, the average force exerted on the turbine is the greatest when the phase difference is 60°, and the smallest when the phase difference is either 0° or 120°. Please note that the minimum standard deviations occur for the cases of 30° and 90°, implying that these two cases have the smallest force exerted on the turbine. In other words, an optimized design for reducing the dual-rotor effect is to adopt 30° and 90° phase
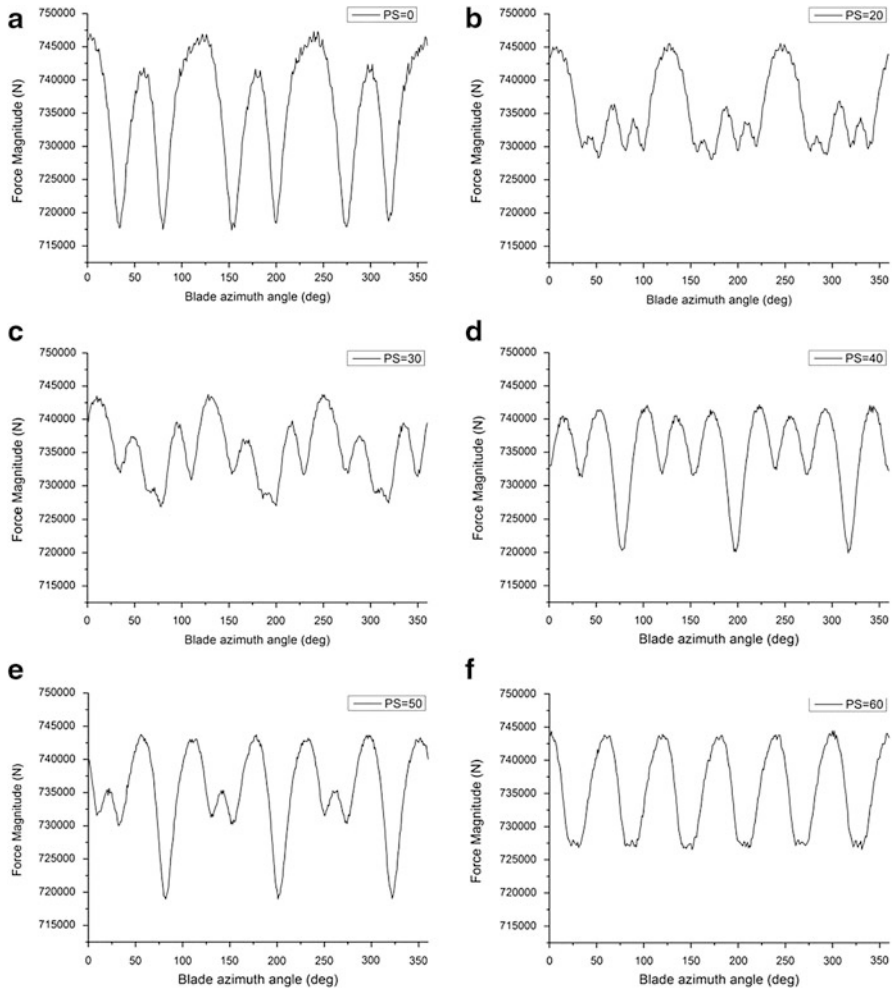
Fig. 3.13 The variation of force exerted on GST under various phase differences (the dual-rotor effect). (**a**) The phase difference is 0°; (**b**) 10°; (**c**) 30°; (**d**) 40°; (**e**) 50°; (**f**) 60°

differences, rather than a zero phase difference (or symmetric) condition. Nevertheless, the largest magnitude of variation is within ±7,800 N which accounts for only 1 % of the total force, implying that the dual-rotor effect due to the phase difference has insignificant influence on the turbine performance.
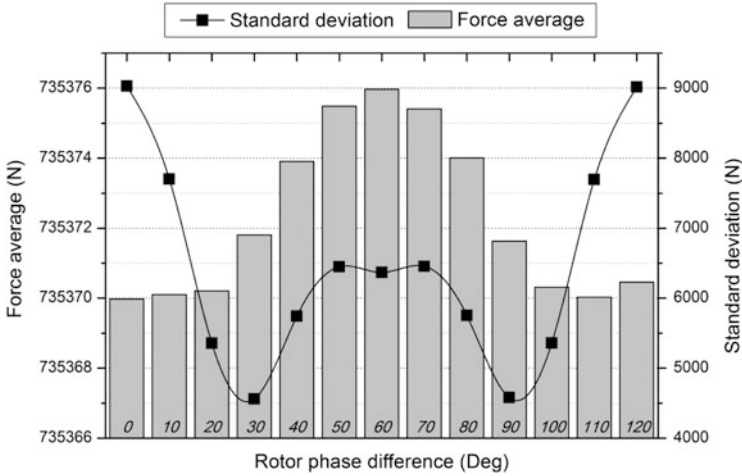
Fig. 3.14 The averaged force and the standard variation of the cyclic change for different phase differences

3.5.4 Cavitation Effect

When the angular speed of the blade exceeds beyond a critical value such that the local pressure on the blade falls below the vapor pressure, a vapor bubble will form on the blade. And then the vapor pressure of the bubble increases continuously due to the vapor accumulation inside the bubble. As the pressure becomes greater than the pressure of surrounding water, it triggers an explosion which often causes serious damage to the blade surface and reduces turbine performance. This effect is referred to as cavitation [19–21].

Figure 3.15 shows that, given $U = 1.2$ m/s, the minimum blade pressure occurring on the tip of the blade changes violently with the blade angle from -216 to -226 kPa. As compared with the threshold pressure of cavitation, as shown in the table below the curve in Fig. 3.15, results suggest that the tip of the blade shall never be at a position less than about 15 m in depth. In other words, as the rotor diameter of GST is 23 m, this result suggests that the turbine axis shall be positioned in the water at 30 m deep or more, so that the tip of the blade will never be in a position less than 20 m deep and the potential occurrence of cavitation can be prevented.

3.6 Comparison of CFD and BEM Results

To verify the reliability of the CFD results shown above, the so-called boundary element method (or BEM) is employed to calculate the blade force and torque of GST. The calculation conditions are the same as those of previous sections:
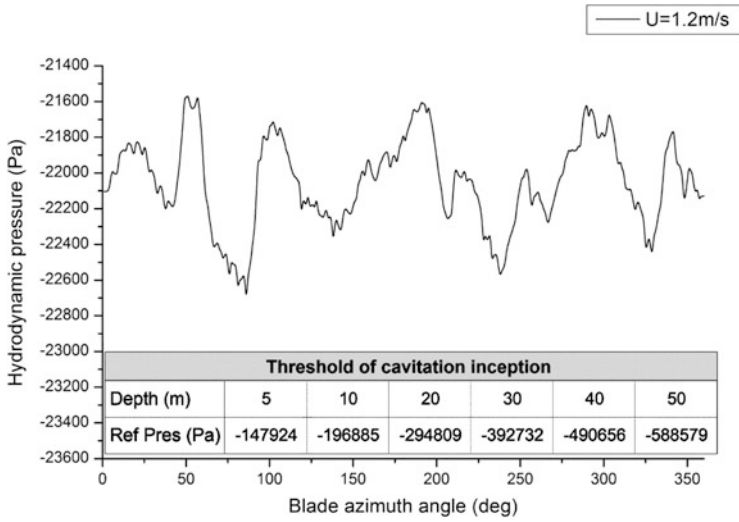
Fig. 3.15 The GST blade surface's minimum dynamic pressure fluctuates with the blade's azimuthal angle. The minimum pressure commonly occurs at the blade tip due to its highest tangential velocity

$U = 1.4$ m/s and $\Omega = 6$ rpm. We divide the blades into 1,000 elements and calculate the force of each element and then the torque with respect to the center of rotation. And the results are used to compare with previous CFD results.

Results showed that, by using CFD, the force on the blades in the X-direction is $-344,135$N while that is $-410,817$N when BEM is employed. The larger BEM results are attributed to the fact that the BEM calculations do not include either the tower shadow effect or the turbulence effect; both have negative contribution on the force exerted on the blade. In addition, CFD takes into account the friction loss of the flow, which is neglected by BEM. Therefore, the fact that the CFD results are about 16 % smaller than the BEM results is reasonable [20].

The above two methods are also used to calculate turbine performance for comparison with the data from Marine Current Turbine, Inc. [16], and the results are shown in Table 3.1. Comparison results show that, given $U = 1.4$ m/s, the CFD and BEM respectively end up with the turbine power output to be 0.237 MW and 0.227 MW, respectively. However, the power output measured by MCT falls between 0.174 and 0.207 MW. This is possibly due to that the MCT data are obtained by actual operational in situ and that the theoretical computations may have neglected some potential factors leading to power loss to some extent. Another possibility may stem from that a different blade is used in this study, which shows a better turbine performance.

In Table 3.1, we also compare the previous data with the so-called Betz limit, the theoretical maximum power output for water turbines. Among the examples given in the table, for the case of $U = 1.4$ m/s, for example, the power outputs of GST from CFD and BEM are respectively 0.237 MW and 0.227 MW, about 25 % and

Table 3.1 Comparison of results from CFD and BEM for the turbines GST and MCT

| | GST ($U = 1.4$ m/s) | | MCT [16] | |
	CFD	BEM	$U = 1.4$ m/s	$U = 2.5$ m/s
C_P	0.442	0.423	0.403–0.481	
Power (MW)	0.237	0.227	0.174–0.207	0.99–1.18
Power (MW) according to Betz limit	0.318		0.256	1.455

40 % respectively less than Betz limit 0.318 MW. The power output of MCT lies within 0.174–0.207 MW, which is about 19–32 % less than Betz limit 0.256 MW. In addition, the C_p values of both GST and MCT can reach as high as 70 % of the limit, showing both designs are of good performance.

3.7 Design of Tail-Wing Stabilizer

To analyze the dynamical effects of the tail-wing stabilizer, we consider a Cartesian Coordinate that the origin is fixed at the center of the base linkage (or point K in Fig. 3.1c), the flow direction is opposite to the X-axis, the vertical direction is the same as that of the Z-axis, and the horizontal direction is parallel to the Y-axis, as shown in Fig. 3.3. Accordingly, the torque with respect to the X-axis is responsible for rolling motion, that to the Y-axis is for pitching motion, and that to the Z-axis is for yawing motion.

Considering that the point K is the cable support point (or the pivot point) of the fuselage, the variation of the torque exerted on the turbine by a single rotor is shown in Fig. 3.16. Results show that the pitching, rolling, and yawing torques are averaged respectively at about −0.3, 0.4, and 4.4 MN-m under the action of the Kuroshio flowing with a velocity of 1.4 m/s, while all fluctuate periodically in every 120°. As two rotors are considered simultaneously, the torques for rolling and yawing are expected to decrease dramatically due to the symmetry of the two rotors. If under some circumstances this symmetry is violated, the design of tail-wing stabilizer will serve to resume the designed altitude (or a horizontal altitude facing against the current) of the turbine in a reasonable time. In the following, the stabilizing mechanism applied by the tail-wing in three axes will be discussed.

3.7.1 Stability on the Rolling Plane

As shown in Fig. 3.17, the torque causing rolling motion (or the rolling torque) can be accounted for by the following relation:

$$Q_x = rF_b \sin\theta, \tag{3.1}$$
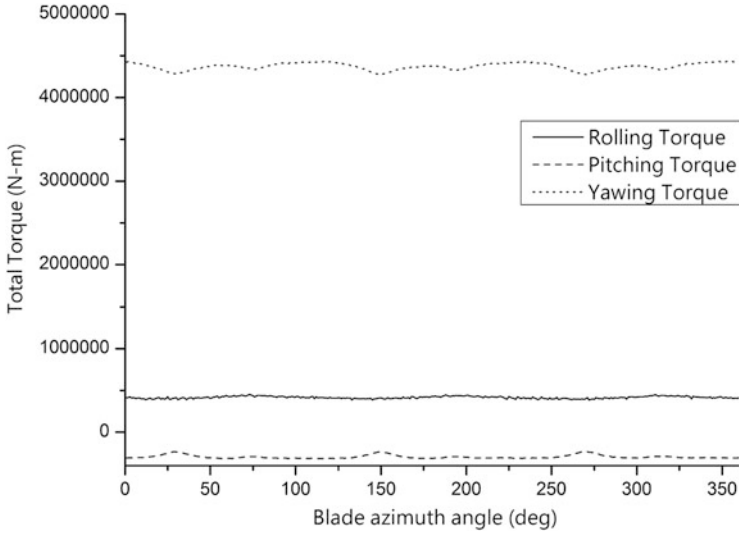
Fig. 3.16 The total torque in rolling, pitching, and yawing planes of a single-rotor turbine. The rolling, pitching, and yawing planes are referred to the coordinate system in Fig. 3.3

| ● center of net buoyancy | ▲ anchor point |
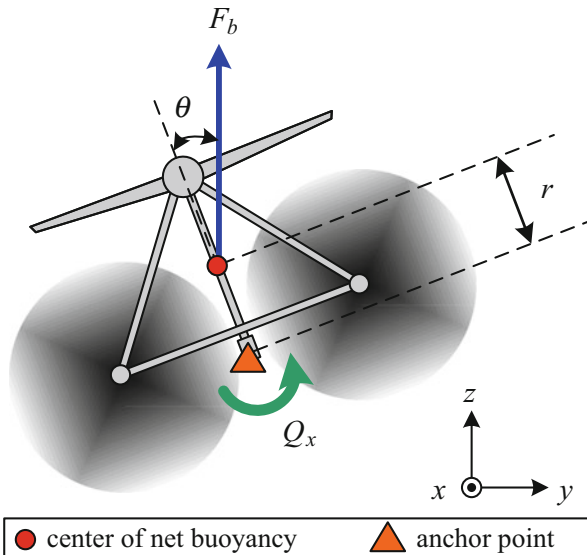
Fig. 3.17 The schematic diagram of the torque and force on the rolling plane

where Q_x is the rolling torque, r is the distance between the anchor point K and the center of the buoyancy, θ is the rolling angle, and F_b is the buoyancy. In a normal situation, the rolling angle is zero and the GST is anchored stably with a vertical altitude. As a perturbation is applied to cause a nonzero rolling angle, which may be

due to the turbulent flow impact on GST from one side or because the torques of the two rotors are not the same, the anti-rolling torque will be generated automatically due to the design shown in Fig. 3.17, i.e., the center of buoyancy locates above the anchor point. In such a design, as the buoyancy force is fixed as a prerequisite, the magnitude of anti-rolling torque is mainly dependent on the vertical distance between the anchor point K and the center of buoyancy, or r of (3.1). A larger distance leads to a larger anti-rolling torque and a more stable GST against the rolling motion.

To illustrate quantitatively the anti-rolling torque required to stabilize the rolling motion, we consider an example by considering the case of buoyancy force $F_b = 1.30$ MN, which is required to maintain the cable anchoring the turbine at an inclined angle $60°$ with respect to the horizontal plane. This buoyancy is also used in Sect. 3.9 to determine the mechanical property of the cable, and also used in Chap. 4 to analyze the structure stiffness of the relay platform. Under the action of this buoyancy, the relation between Q_x, r, and θ is shown in Fig. 3.18. For a constant r, which shall be constant when the turbine design is done, the anti-rolling torque Q_x increases as the rolling angle θ becomes larger. For a constant θ, similarly, the Q_x also increases with r, implying that for a larger turbine having a greater distance between anchor point and center of buoyancy, one needs a larger anti-rolling torque to resume the rolling motion.

The results in Fig. 3.18 can also be interpreted from a different viewpoint. As one had seen from Fig. 3.16, the maximum rolling torque resulting from a single rotor is about 452,000 Nm. We assume that there is a perturbation causing a net rolling torque about 10 % of the maximum value, i.e., 45,200 Nm, which may be due to fact that the flow velocities impinging on the two rotors become different, generating a rolling torque leading to a rolling motion. Under such a situation, we investigate four cases of different buoyancy to calculate the maximum-allowed (or the critical) rolling angle, beyond which the turbine will turn over, for five different $r$. Results shown in Table 3.2 indicate that for a constant r the critical rolling angle decreases as buoyancy increases. It also shows that for a constant buoyancy, the critical rolling angle decreases as r increases. Both results indicate that, for a larger turbine having a larger buoyancy and a longer r, the critical rolling angle is smaller, implying that the stability on the rolling plane is requested in a more restrictive manner.

3.7.2   Stability on the Pitching Plane

The stability on the pitching plane of GST (as shown in Fig. 3.19) is controlled by the vertical distance r between the anchored point and the center of buoyancy and the horizontal distance l between the anchored point to the hydrodynamic center of the horizontal stabilizer (or the tail-wing). As shown in Fig. 3.19, as pitching occurs to the GST, which can be due to the flow disturbance from below, the torque required to resume the designed altitude shall satisfy the following relation or beyond:

Fig. 3.18 The inverse proportion relation between rolling angle and the distance from anchoring point to center of buoyancy under the action of rolling torque. The buoyancy is $F_b = 1.26$ MN
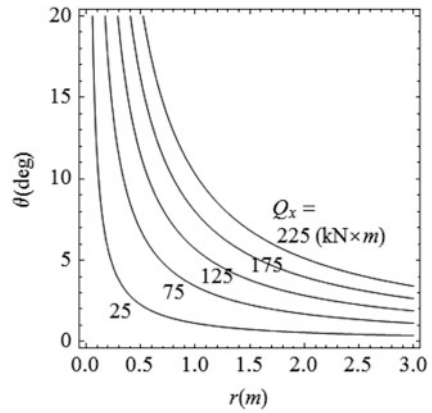
Table 3.2 The critical rolling angles under different buoyancy and different distance from anchor point to center of buoyancy

	$F_b = 500$ kN	$F_b = 800$ kN	$F_b = 1,300$ kN	$F_b = 2,000$ kN
r (m)	θ (°)			
0.2	26.84	16.39	10.00	6.48
0.5	10.40	6.48	3.98	2.59
1.0	5.18	3.24	1.99	1.29
1.5	3.45	2.16	1.33	0.86
2.0	2.59	1.62	1.00	0.65

Fig. 3.19 The schematic diagram of the torque and force on the pitching plane
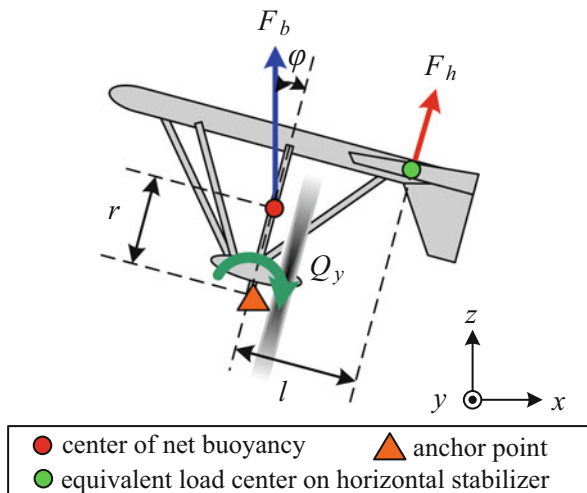
Fig. 3.20 The inverse linear
relation between the pitching
angle and the distance from
anchoring point to
hydrodynamic center of the
horizontal stabilizer
($r = 1$ m and
$F_b = 1{,}300$ kN)
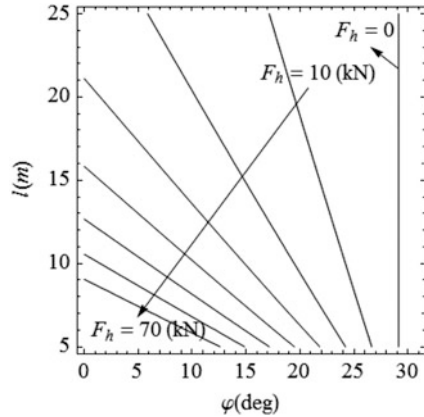
$$Q_y = rF_b \sin \varphi + lF_h, \tag{3.2}$$

where Q_y is the pitching torque, φ is the pitching angle, and F_h is the equivalent load
on the horizontal stabilizer.

To analyze the stability on the pitching plane, we consider that the GST is
designed with $r = 1$ m and $F_b = 1{,}300$ kN and the turbine is disturbed by a
pitching torque of about 633,000 Nm, which is two times the maximum pitching
torque of a single rotor shown in Fig. 3.16. We then calculate F_h for various φ and l
and the results are shown in Fig. 3.20. It is seen that, for a constant l, the F_h required
to resume the turbine's horizontal altitude decreases as the pitching angle φ
increases, implying that the function of the horizontal stabilizer is gradually taken
over by the buoyancy as φ increases. And this function is completely vanished
when φ becomes larger than 29°, as shown in the vertical line of $F_h = 0$ in
Fig. 3.20. On the other hand, for a constant φ, the F_h decreases as l increases,
implying that the stability on the pitching plane is higher for a larger turbine (of a
larger l).

Results of Fig. 3.20 also indicate that, to maintain the altitude of GST horizon-
tally (or $\varphi = 0$), the F_h required increases for a smaller l. That means the horizontal
stabilizer is still needed to provide a lift force to equilibrate the pitching moment
633,000 Nm applied by the flow acting on the turbine. Consequently, the horizontal
stabilizer of GST is better designed with a shape of airfoil which would provide a
lift force (of about 633,000 Nm) when the angle of attack is zero. For the turbine of
$l = 15$ m, for example, the lift force shall be as large as 42 kN, as shown in
Fig. 3.20.

Table 3.3 shows the maximum-allowed (or critical) pitching angle for a turbine
with prerequisite specifications $r = 1$ m and $F_b = 1{,}300$ kN under different designs
of horizontal stabilizer accounted for by the parameters l and F_h. For the case of
$l = 15$ m and $F_h = 35$ kN, for example, the critical pitching angle is 4.77°, which
means the turbine would become unstable on the pitching plane as the pitching
angle increases to 5° or beyond. It turns out that this is a dangerous design due to a

Table 3.3 The critical pitching angles for different equivalent load on the horizontal stabilizer with different distance from anchor point to hydrodynamic center of the horizontal stabilizer ($r = 1$ m and $F_b = 1{,}300$ kN)

l (m)	$F_h = 15$ kN	$F_h = 20$ kN	$F_h = 35$ kN	$F_h = 50$ kN
	φ (°)			
5	25.43	24.21	20.64	17.14
10	21.82	19.46	12.58	5.88
15	18.30	14.85	4.77	–
20	14.85	10.33	–	–
25	11.45	5.88	–	–

small critical pitching angle. Accordingly, one shall redesign the horizontal stabilizer by, for example, shortening the distance l to 10 m to increase the critical pitching angle up to 12.58°, or to 5 m to get a larger critical pitching angle 20.64°. For this case, a larger lift force would reduce the critical pitching angle, making the turbine more unstable. Conclusively, a smaller turbine (of a smaller l) is more stable on the pitching plane because it has a larger critical pitching angle.

To design the horizontal stabilizer for the determination of both l and F_h, one shall calculate the effective area of the horizontal stabilizer. To do this, we start from the force diagram shown in Fig. 3.21, the lift force (F_l) and the drag force (F_d) are obtained as

$$F_l^{(h)} = F_h \cos\varphi = \frac{1}{2}C_l^{(h)}\rho U^2 A_h, \tag{3.3}$$

$$F_d^{(h)} = F_h \sin\varphi = \frac{1}{2}C_d^{(h)}\rho U^2 A_h, \tag{3.4}$$

where the superscript h denotes the horizontal stabilizer, $C_l^{(h)}$ and $C_d^{(h)}$ are respectively the lift and drag coefficients, A_h is the effective area of the horizontal stabilizer, and ρ and U are the seawater density and the flow velocity referring to Sect. 3.4.

Rewriting (3.3) and (3.4), with the aid of (3.2), gives

$$\left|2(Q_y - rF_b \sin\varphi)\cos\varphi\right| = lC_l\rho U^2 A_h, \tag{3.5}$$

$$\left|2(Q_y - rF_b \sin\varphi)\sin\varphi\right| = lC_d\rho U^2 A_h, \tag{3.6}$$

By assuming that $Q_y = 633{,}000$ kN, $r = 1$ m, $F_b = 1{,}300$ kN, $l = 15$ m, $\rho = 1{,}030$ kg/m³, and $U = 1.4$ m/s, the A_h is calculated for various $C_l^{(h)}$ and $C_d^{(h)}$ at different pitching angles, and the results are shown in Fig. 3.22. As one can see from Fig. 3.22a, for a constant $C_l^{(h)}$ (or a constant lift force), the effective area needed is smaller for a larger critical pitching angle. This is reasonable that a turbine of a larger critical pitching angle is more stable by design; it accordingly needs a stabilizer of smaller area. For a constant critical pitching angle, a larger
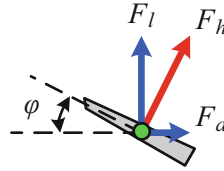
Fig. 3.21 The schematic diagram of the forces acting on the horizontal stabilizer
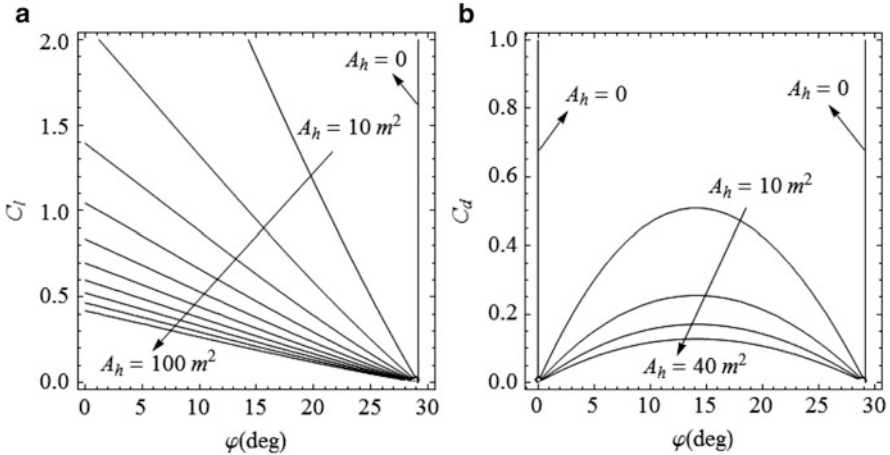
Fig. 3.22 (**a**) The inverse linear relation between the pitching angle and the lift coefficient for different effective areas of the horizontal stabilizer. (**b**) The relation between the pitching angle and the drag coefficient for different effective areas of the horizontal stabilizer ($r = 1$ m, $F_b = 1{,}300$ kN, $l = 15$ m, $\rho = 1{,}030$ kg/m^3, and $U = 1.4$ m/s)

A_h (or a larger horizontal stabilizer) is accompanied with a smaller $C_1^{(h)}$ (or an airfoil with a smaller camber) to generate a pitching moment to counteract with the applied torque Q_y.

On the other hand, the drag force of the stabilizer shall be designed with a smallest value to decrease the loading on the anchoring cable. Results shown in Fig. 3.22b suggest that at a pitching angle of either 0° or 30°, the drag force on the tail-wing vanishes. For the pitching angle being between 0° and 30°, the maximum drag force occurs at the pitching angle equal to 15°, and the drag force decreases with increasing effective area of stabilizer.

According to White [22], theoretically, for a flat-plate horizontal stabilizer, the lift coefficient $C_1^{(h)}$ for a 5° pitching angle is about 0.55. Thus, according to the results shown in Fig. 3.22a [or Eq. (3.6)], the overall effective area of the horizontal stabilizer can be obtained as 62 m^2. Since the stabilizer is composed of two symmetric horizontal plates, the area of each plate is 31 m^2. Meanwhile, the drag coefficient $C_d^{(h)}$ can be obtained as 0.048 from Fig. 3.22b or Eq. (3.6). On the contrary, if an effective area of the horizontal stabilizer is known as a prerequisite,

Table 3.4 The demand flat-plate horizontal stabilizer areas with their lift and drag coefficients for different given pitching angles ($r = 1$ m, $F_b = 1,300$ kN, $l = 15$ m, $\rho = 1,030$ kg/m³, and $U = 1.4$ m/s)

φ (°)	$C_l^{(h)}$ [22]	$C_d^{(h)}$	A_h (m²)
5	0.55	0.05	62.46
10	1.09	0.12	24.29
15	1.63	0.26	11.64
20	2.15	0.55	5.44
25	2.66	1.59	1.89

both the lift and drag coefficients for different pitching angles can be also obtained from Fig. 3.22.

We choose five different pitching angles and calculate the lift coefficient, the drag coefficient, and the effective area of the flat-plate stabilizer, and the relevant data are shown in Table 3.4. In general, after the pitching moment $Q_y = 633,000$ kN is applied on the turbine, both the lift and drag forces required to counteract with this acting torque increase as the pitching angle is larger, while the effective area can be designed with a smaller value. Results of Table 3.4 can also be interpreted from another viewpoint that, as the pitching motion is generated, the drag and lift force shall increase as the pitching angle is enlarged, making the turbine more unstable unconditionally. This may develop into a disaster which shall be avoided in any circumstance. To prevent this disaster, one may consider to use a stabilizer of larger effective area to ensure smaller drag and lift forces.

3.7.3 Stability on the Yawing Plane

The torque leading to an instability on the yawing plane is the moment caused by the forces applied on the GST with respect to Z-axis. This moment may be generated by the imbalance between the forces applied on the two rotors, and which shall be balanced by the torque applied by the hydrodynamic load on the rudder (or the vertical stabilizer) to damp out the yawing motion in a short period.

As shown in Fig. 3.23, in general, the stability on the yawing plane of GST is controlled by the distance between the anchoring point to the hydrodynamic center on the rudder and the force applied on the rudder. To recover the yawing configuration, the torque satisfies

$$Q_z = dF_v, \tag{3.7}$$

where Q_z is the yawing torque, F_v is the equivalent load on the rudder, and d is the horizontal distance between the anchoring point pivot and the hydrodynamic center of the rudder. The thrust and drag forces computed form the equivalent load on the rudder are

Fig. 3.23 The schematic diagram of the force and torque on the yawing plane

| △ anchor point |
| ○ equivalent load center on vertical stabilizer |
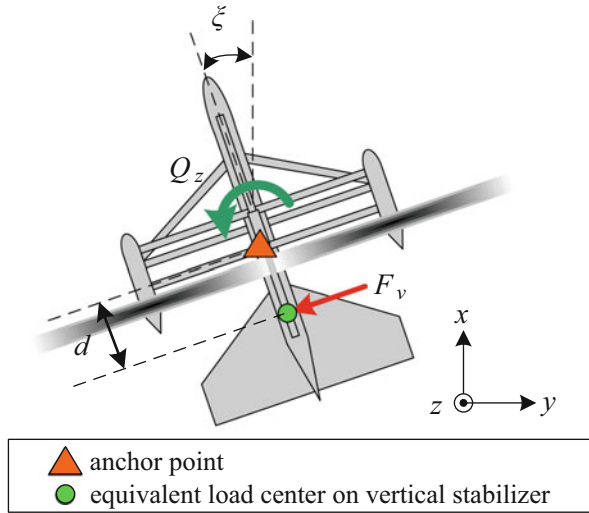
$$F_1^{(v)} = F_v \cos \xi = \frac{1}{2} C_1^{(v)} \rho U^2 A_v, \tag{3.8}$$

$$F_d^{(v)} = F_v \sin \xi = \frac{1}{2} C_d^{(v)} \rho U^2 A_v, \tag{3.9}$$

where the superscript v denotes the horizontal stabilizer, $C_1^{(v)}$ and $C_d^{(v)}$ are the thrust and drag coefficients, ξ is the yawing angle, and A_v is the effective area of the vertical stabilizer.

Results of Fig. 3.16 show that the maximum yawing torque on a single rotor is about 4,436,000 Nm. For the GST having two rotors, we assume that there is a 5 % of the maximum yawing torque applied on GST, namely, $Q_z = 221,800$ Nm, and $d = 15$ m is chosen for the design, the equivalent load needed to apply on the rudder to prevent yawing is $F_v = 14.79$ kN. For the given yawing torque above, the equivalent load on the rudder is inversely proportional to the distance, as shown in Fig. 3.24.

To design the rudder in terms of hydrodynamic characteristics and the geometry, we consider the following equations derived from (3.8) and (3.9), with the aid of (3.7), yielding

$$|2Q_z \cos \xi| = d C_1^{(v)} \rho U^2 A_v, \tag{3.10}$$

$$|2Q_z \sin \xi| = d C_d^{(v)} \rho U^2 A_v. \tag{3.11}$$
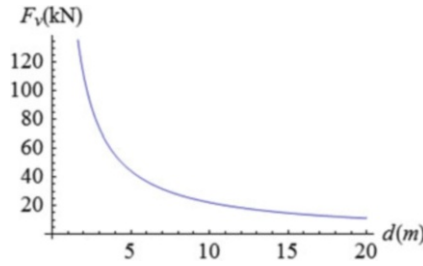
Fig. 3.24 The demand equivalent load on the vertical stabilizer versus the horizontal distance from anchoring point to the hydrodynamic center of the rudder
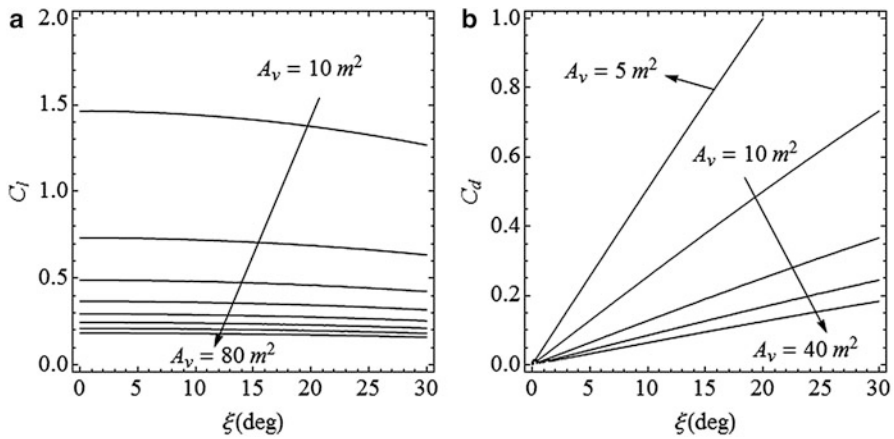
Fig. 3.25 (**a**) The linear relation between the yawing angle and the lift coefficient for different effective areas of the rudder. (**b**) The linear proportion relation between the yawing angle and the drag coefficient for different effective areas of the rudder ($d = 15$ m, $\rho = 1{,}030$ kg/m³, and $U = 1.4$ m/s)

By assuming that $Q_z = 221{,}800$ Nm, $d = 15$ m, $\rho = 1{,}030$ kg/m³, and $U = 1.4$ m/s, the lift and drag coefficients with respect to yawing angle for rudders of various area are shown in Fig. 3.25.

Results shown in Fig. 3.25 indicate that, by giving a critical yawing angle which accounts for the maximum yawing angle the GST will allow in response to various disturbances, both the lift and drag coefficients of the rudder shall decrease for a rudder of larger area. On the other hand, for a given area of the rudder, the lift coefficient virtually remains the same with respect to varying yawing angle, while the drag coefficient increases linearly with the yawing angle monotonically.

If a flat-plate rudder is considered, as discussed in previous sections, the lift coefficient for a 5° yawing angle is about 0.55 [22]. Results shown in Fig. 3.25a give that the effective area of the rudder is 27 m² and those of Fig. 3.25b give that the drag coefficient is obtained to be 0.048. To more clearly illustrate the design parameters for a flat-plate rudder, we summarize in Table 3.5 the results for five yawing

Table 3.5 The demand flat-plate rudder areas with their lift and drag coefficients for different given yawing angles ($Q_z = 221,800$ Nm, $d = 15$ m, $\rho = 1,030$ kg/m^3, and $U = 1.4$ m/s)

φ (°)	$C_1^{(v)}$ [22]	$C_d^{(v)}$	A_v (m^2)
5	0.55	0.05	26.65
10	1.09	0.10	13.38
15	1.63	0.14	8.97
20	2.15	0.19	6.79
25	2.66	0.23	5.50

angles under the conditions $Q_z = 221,800$ Nm, $d = 15$ m, $\rho = 1,030$ kg/m^3, and $U = 1.4$ m/s. Results indicate that, for a GST of a larger critical yawing angle, which means the turbine is more stable on the yawing plane, one shall have a rudder of smaller area while having both larger lift and drag coefficients. On the other hand, as a rudder of larger area is considered, the critical yawing angle is smaller, which means the turbine is less stable on the yawing plane.

3.8   Selection of Turbine Anchor Point

The original design of GST is to anchor the turbine on the point K of Fig. 3.1 [1], which is a single-cable anchoring system, having advantages that the turbine has more degree of freedom to move in three axes and the cost of construction engineering is significantly lower. For different kind of turbine, such as the turbine considered for the Gulf Stream in Florida [23, 24], a different anchoring system shall be considered to secure the stability of the turbine under the action of strong current.

The analyses of turbine dynamics for the case considering anchoring the turbine on the point K have been done in previous sections, and the dynamic characteristics of the GST have been illustrated in detail. There are, however, many other options for anchoring at different points on the turbine, such as those shown in Fig. 3.26. For a different anchoring system, the dynamic characteristics of the turbine shall be different from those anchoring on the point K. As shown in Fig. 3.27 regarding the overall torque applied on the turbine, results illustrate that the dynamic characteristics of the turbine are very different from each other for the cases of different anchoring points considered.

For case B anchoring the GST on the nose of main pontoon, for example, the overall torque is about 50 % higher than that of the case A anchoring on Point K, which is because the torque is dependent with the distance between the anchoring point and the hydrodynamic center on the turbine, and anchoring on the nose of pontoon increases the distance by more than 50 %. For case C anchoring the GST on the noses of the watertight nacelles by two cables, the overall torque is reduced to about one-ninth of that of case A. This is because, due to anchoring by two cables on the two sides of the turbine, both the rolling and yawing motions are restricted to a limited range so that the torques needed to secure the stability on the rolling and yawing planes are reduced to a very low level. For the stability on the pitching plane, the pitching torque is also reduced since the distance between the anchoring
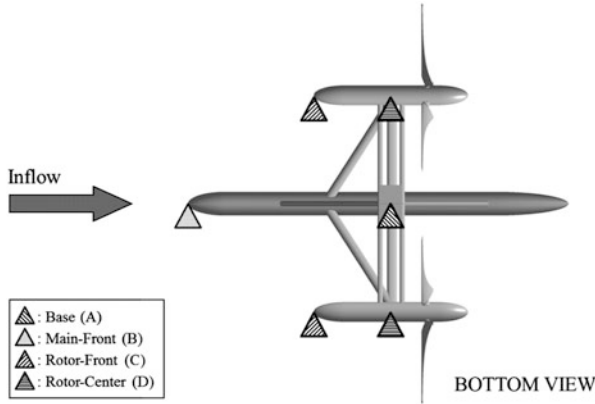
Fig. 3.26 Four types of the anchoring point selection: (**a**) the *center* of the base (point K in Fig. 3.1c); (**b**) the *nose* of the main pontoon; (**c**) the *nose* of the watertight nacelle; (**d**) the *bottom center* beneath the watertight nacelle
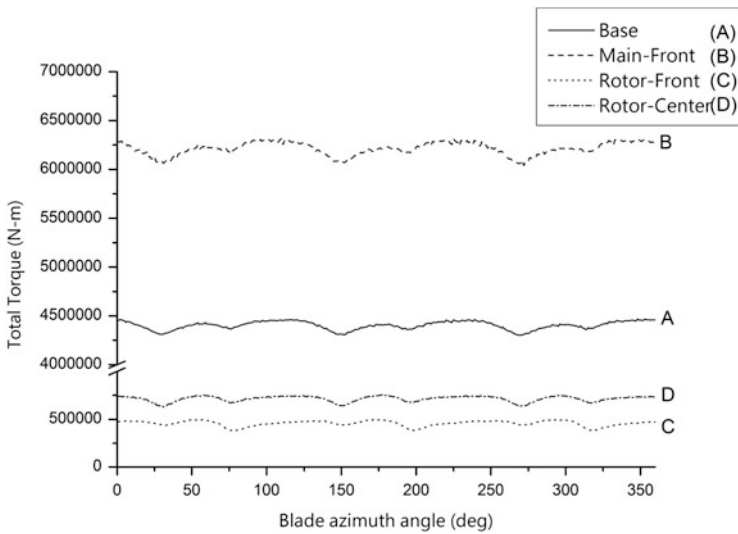
Fig. 3.27 The total torque with different blade azimuthal angles for the four types of the anchoring point selection

point and the hydrodynamic center on the horizontal stabilizer is increased compared to that of case A.

The last case considered is to anchor the turbine by two cables on the center of the bottom of the two nacelles, i.e., the case D. From the fact that the two anchoring points of this case are close to those of case C and that this case also features with two cables anchoring on the two sides of the turbine, one may imply that the hydrodynamic characteristics and the overall torque of the turbine of case D are similar to those of case C, and this is confirmed by the results shown in Fig. 3.27.

Table 3.6 Physical and material properties of various types of cable for anchoring the GST onto the relay platform

	Density (kg/m^3)	Elasticity coeff. (GPa)	Tensile strength (GPa)	Ductility (%)	Source
Nylon	1,120–1,160	2.00–4.00	0.06–0.08	90.0	a
	1,140	5.50	0.85	18.0	b
	1,060–1,140	2.07–2.41	0.05–0.07	20.0–60.0	c
	1,140	–	–	18.0–25.0	d
	1,040–1,140	–	0.04–0.06	150.0–400.0	e
	1,140	–	–	15.0–28.0	f
	1,140	0.87	0.2	–	g
Steel	7,700–8,030	200–205	0.40–0.59	–	a
	7,860	200	2.16	1.1	b
	7,850	210	1.40	–	g
PET	1,360	2.00–2.70	0.06	–	a
	1,380	9.00	1.05	12.5	b
	1,380	3.24	0.08	45.0	c
	1,380	–	–	12.0–15.0	d
	1,270	–	0.07	110.0	e
	1,380	–	–	12.0–15.0	f
	1,380	1.6–10	0.20–0.50	–	g
PP	900–1,240	1.30–2.00	0.03–0.04	–	a
	910	4.20	0.50	12.0	b
	890–1,270	0.03–0.7	0.02–0.10	1.5–600.0	c
	910	–	–	15.0–25.0	d
	900	–	0.03	200.0	e
	910	–	–	18.0–22.0	f
	910	–	–	–	g

[a]http://www.engineeringtoolbox.com/
[b]http://www.offshoreengineering.org/
[c]http://www.sdplastics.com/
[d]http://www.erinrope.com/
[e]http://breezeplastics.com/
[f]http://www.gpjrope.com/
[g]http://www.tensiontech.com/

3.9 Turbine Cable Selection

As mentioned earlier, GST was selected as the basis for analysis because the turbines feature a self-stabilizing balancing device which allows for a single cable to be connected to the center point of the turbine's base (point K in Fig. 3.1c) which is then anchored to the relay platform. Many types of cables fulfill the requirements of high tension and high elongation including nylon rope, steel rope, polyester rope (PET), and polypropylene rope (PP) (see Table 3.6 for their respective mechanical and physical properties). PET is slightly heavier than seawater, has a high tensile strength (second only to steel rope), and is highly stretchable (second only to nylon rope). These advantages make PET rope a good choice for anchoring the turbine. Yet another advantage is that different weaving methods can

be used to produce a variety of cable diameters to meet the requirements of specific design specification; see please Appendix D for more details.

Analysis results for cable force shown in Fig. 3.5 show that, given $U = 1.4$ m/s and $\Omega = 6$ rpm, the averaged current thrust acting on GST is 735 kN, with a standard deviation of 4.5 kN–9 kN. Therefore, the thrust acting on the turbine in the horizontal direction can be as high as 744 kN or more. In calculating the total force of the cable, in addition to the above-mentioned current thrust, the turbine's floating buoyancy in the vertical direction must also be taken into account. We assume that the buoyancy force is 1,270 kN and thrust force is 735 kN so that the combined force is 1,470 kN with an inclined angle of 60° with respect to the horizontal axis. In the marine engineering design, it is reasonable to consider a safety factor of 5, so the design value of the total cable force should be set to 7,350 kN. We will use this design value to select the size and material for the cable used to anchor the turbine.

Traditionally, the anchoring cables are of steel-based material. But, nonetheless, due to the weight and corrosion factors, steel-based cables are not suitable for anchoring Kuroshio turbines. New cables made of plastic composites or polymer compounds, usually being of lighter weight and of better mechanical properties, become the better choice. These cables are light and strong, and, more importantly, their hairy exteriors can reduce high-frequency vibrations caused by ocean flow, making them the best choice for anchoring turbines [25]. As the cable diameter is chosen to be 20 cm, given that the force applied on the cable is 7,350 kN, the tensile strength of the cable shall be 0.0581 GPa or more. As shown in Table 3.6, there are many cables such as nylon 1140, PET 1380, and PP 910 with tensile strength as high as 0.229 GPa or more, being much larger than the required tensile strength of the cable. If a two-cable anchoring system is considered, as cases C and D shown in Fig. 3.6, the required tensile strength of the cable is thus reduced by half to 0.0291 GPa. Consequently, the selection of the cable lies in a much larger range.

3.10 Overview of the GST Performance

The GST is equipped with two rotors, each with three 10 m-long blades rotating with an angular speed of 6 rpm. As it is under the action of 1.4 m/s Kuroshio flow, the total thrust applied on GST is about 735,000 kN and the power generated is about 0.5 MW. It can be anchored on the relay platform (will be discussed in Chap. 4) by a single cable, and is autonomously balancing in the rolling, yawing, and pitching planes by the design of the tail-wing stabilizer and the distance between hydrodynamic center and the anchoring point of the turbine. Analyses of present chapter have shown that this single-strand-anchored and autonomously balancing design has demonstrated superiority for the Kuroshio power plant, which is considered to be deployed in the ocean of several 100 m deep or more.

While the GST works under the action of Kuroshio, the exerted force shows a cyclic change due to the tower shadow effect, which is mainly the result caused by the disturbance of the wakes generated behind the connection linkage on the two

rotors. If we consider that GST is anchored by a cable having an inclination angle of 45 with respect to the horizontal direction, the total force (the net buoyancy combined with the thrust) can be as high as 1,500 kN, and the force amplitude varies within 6 % of the cyclic change. A single cable made of the nylon, PET, or PP with 20 cm in diameter can is strong enough to support GST securely on the relay platform of which the safety factor reaches five. If a dual cable anchored to both the noses of the watertight nacelles, the stability of GST on the rolling and yawing planes is greatly enhanced, and the specifications of the cable can be downgraded, and thus the cost can be saved for diminishing that resulted from the additional works.

The tower shadow effect is the major factor that causes the cyclic change of the turbine reaction force. The variation of this cyclic change may result in the fatigue failure in turbine components. However, the effect cannot be prevented if the connecting linkages are equipped at the upstream side of the rotor. A possibility to diminish the tower shadow effect is to move the rotor to the upstream of the linkages, such as at the nose of watertight nacelle. This change would require a new design of the autonomously balancing mechanism, which is controlled by the tail-wing stabilizer and the anchoring system.

References

1. Robson JH (2007) Submersible electrical power generating plant. US Patent 7291936B1, 6 Nov 2007
2. Batten WMJ, Bahaj AS, Molland AF, Chaplin JR (2008) The prediction of the hydrodynamic performance of marine current turbines. Renew Energy 33(5):1085–1096. doi:10.1016/j.renene.2007.05.043
3. ANSYS FLUENT 12.1 User Manual
4. Duque EPN, Burklund MD, Johnson W (2003) Navier–stokes and comprehensive analysis performance predictions of the NREL phase VI experiment. J Sol Energy Eng 125:457–467. doi:10.1115/1.1624088
5. Sørensen NN, Michelsen JA, Schreck S (2002) Navier–stokes predictions of the NREL phase VI rotor in the NASA Ames 80 ft × 120 f. wind tunnel. Wind Energy 5:151–169. doi:10.1002/we.64
6. Menter FR (1994) Two-equation eddy-viscosity turbulence models for engineering applications. AIAA J 32:1598–1605. doi:10.2514/3.12149
7. Wilcox DC (1993) Comparison of two-equation turbulence models for boundary layers with pressure gradient. AIAA J 31:1414–1421. doi:10.2514/3.11790
8. Patankar SV, Spalding DB (1972) A calculation procedure for heat, mass and momentum transfer in 3-dimensional parabolic flow. Int J Heat Mass Transf 15(10):1787–1806. doi:10.1016/0017-9310(72)90054-3
9. Turnock SR, Phillips AB, Banks J, Nicholls-Lee R (2011) Modelling tidal current turbine wakes using a coupled RANS-BEMT approach as a tool for analysing power capture of arrays of turbines. Ocean Eng 38(11–12):1300–1307. doi:10.1016/j.oceaneng.2011.05.018
10. Lee SH, Jang K, Lee J, Hurt N (2010) A numerical study for the optimal arrangement of ocean current turbine generators in the ocean current power parks. Curr Appl Phys 10:S137–S141. doi:10.1016/j.cap.2009.11.018

11. Myers LE, Bahaj AS (2010) Experimental analysis of the flow field around horizontal axis tidal turbines by use of scale mesh disk rotor simulators. Ocean Eng 37(2–3):218–227. doi:10.1016/j.oceaneng.2009.11.004
12. Harrison ME, Batton WMJ, Myers LE, Bahaj AS (2010) Comparison between CFD simulations and experiments for predicting the far wake of horizontal axis tidal turbines. Renew Power Gen 4(6):613–627. doi:10.1049/iet-rpg.2009.0193
13. Bahaj AS, Myers LE, Thompson G. Characterising the wake of horizontal axis marine current turbines. In: Proceedings of the 7th European wave and tidal energy conference, Porto, Portugal, 11–14 Sept 2007
14. Myers L, Bahaj AS (2007) Wake studies of a 1/30th scale horizontal axis marine current turbine. Ocean Eng 34:758–762. doi:10.1016/j.oceaneng.2006.04.013
15. Myers LE, Bahaj AS (2012) An experimental investigation simulating flow effects in first generation marine current energy converter arrays. Renew Energy 37(1):28–36. doi:10.1016/j.renene.2011.03.043
16. Bahaj AS, Batten WMJ, McCann G (2007) Experimental verifications of numerical predictions for the hydrodynamic performance of horizontal axis marine current turbines. Renew Energy 32(15):2479–2490. doi:10.1016/j.renene.2007.10.001
17. Bahaj AS, Molland AF, Chaplin JR (2007) Power and thrust measurements of marine current turbines under various hydrodynamic flow conditions in a cavitation tunnel and a towing tank. Renew Energy 32:407–426. doi:10.1016/j.renene.2006.01.012
18. Batten WMJ, Bahaj AS, Molland AF, Chaplin JR (2007) Experimentally validated numerical method for the hydrodynamic design of horizontal axis tidal turbines. Ocean Eng 34 (7):1013–1020. doi:10.1016/j.oceaneng.2006.04.008
19. Batten WMJ, Bahaj AS, Molland AF, Chaplin JR (2006) Hydrodynamics of marine current turbines. Renew Energy 31(2):249–256. doi:10.1016/j.renene.2005.08.020
20. Zanette J, Imbault D, Tourabi A (2010) A design methodology for cross flow water turbines. Renew Energy 35:997–1009. doi:10.1016/j.renene.2009.09.014
21. Goundar JN, Ahmed MR, Lee Y-H (2011) Numerical and experimental studies on hydrofoils for marine current turbines. Renew Energy 42:173–179. doi:10.1016/j.renene.2011.07.048
22. White FM (1999) Fluid mechanics, 4th edn. McGraw-Hall, New York
23. VanZwieten J, Driscoll FR, Leonessa A, Deane G (2006) Design of a prototype ocean current turbine—part I: mathematical modeling and dynamics simulation. Ocean Eng 33:1485–1521. doi:10.1016/j.oceaneng.2005.10.005
24. VanZwieten J, Driscoll FR, Leonessa A, Deane G (2006) Design of a prototype ocean current turbine—part II: flight control system. Ocean Eng 33:1522–1551. doi:10.1016/j.oceaneng.2005.10.006
25. Brown DT, Mavrakos S (1999) Comparative study on mooring line dynamic loading. Mar Struct 12(3):131–151. doi:10.1016/S0951-8339(99)00011-8

Chapter 4
Dynamic Design of the Relay Platform and Anchor System

The relay platform is designed specifically for the Kuroshio power plant as the artificial seabed on which tens of turbines are anchored. The platform is a flexible structure floating in the deep sea and is anchored to the physical seabed by hundreds of cables [1]. The platform is simultaneously under the actions of the pulling forces from the turbines at above and from the anchoring cable at below, and the thrust force from the current at surrounding. Due to the unsteady nature of the current, all the forces applied on the platform are also unsteady, leading to a complicate dynamic characteristics of the relay platform.

Under the action of the Kuroshio, the dynamics of the relay platform can be considered to be a force equilibrium system balanced among the thrust of current, the buoyancy of platform, turbine-exerted force, and cable tension. Due to the fact that both the anchoring cables and the relay platform are flexible subject to limited random deformation, the dynamics of the relay platform is highly nonlinear. To tackle this complicate structure dynamics, we conduct a transient dynamic analysis in which the slow dynamic technique [2] is applied to obtain the steady-state results. The objects considered in the analysis include the anchoring cable to the seabed and the components of the relay platform such as the linkages and the universal joint.

Regarding the cable dynamics, it is known that cables are commonly used in undersea structures due to their light weight, small volume, and high tensile strength. In most cases, the forced cable stays within its elastic limit but undergoes significant displacement through geometrically nonlinear behavior because the flexibility of the cable tends to yield a large deflection [3]. In the static analysis for the cable, gravity is the major force applied and the fixed positions of the cable's two ends are prerequisite, and solving the static equilibrium of each subdivided cable section gives the cable tension and the reaction forces at the two fixed ends. The equilibrium configuration of the cable is usually of a curve shape.

In this chapter, in addition to the prerequisites required for the static analysis, both the cable's weight and its drag force due to current flow are taken into account. For cases where the cable's two ends are given (e.g., one end is on the seabed while the other is at the water surface), the problems are categorized as statics of cable towing (or mooring). Problems of this type often focus on the equilibrium

configuration, displacements, and tensions of the cable [4–7]. In cases where one end is fixed while the other end is free (e.g., a floating structure anchored to the seabed), the problem is categorized as dynamics of cable buoying (or anchoring). The displacements and tensions of the cable of this type of problem are time dependent, while can be reduced to constants or fluctuate periodically as they reach the steady state [8–11]. For the present case of the cable anchoring the relay platform, the cable towing problem is to be analyzed.

To analyze the cable towing problem, one may consider the subdivided arc length of the cable as a variable, and then use the finite difference method (FDM) to calculate the displacement and tension of the cable at each time step [12–14]. Alternatively, the finite element method (FEM) discretizes the cable into finite sections. After combined with its geometrical configuration and material properties of each section, the overall equilibrium equations can be solved simultaneously [11, 15–18]. But, nonetheless, FEM is valid only for small rotation conditions when the large rigid body rotation effect is included in the incremental results. This so-called truncation error may accumulate at each time step, resulting in an unreliable solution. But, nonetheless, the truncation-error problem has been resolved by using existing numerical techniques, so that the robustness and rigor of the FEM are still seen to be the most reliable approach for practical engineering problems [3, 11]. We accordingly will employ FEM to numerically solve the nonlinear equations of the cable dynamics.

In addition to solving the cable towing problem for the cable's time-dependent displacement and tension, the displacement and rotation of the components of the relay platform under the action of the Kuroshio are also to be solved simultaneously. Similar problem had been tackled by, for example, Tsukrov et al. [17] who used the piecewise linear elastic constant to analyze the nonlinear elastic mooring cables of the submerged fish cage. They found that the linear approximation may underestimate the maximum tension in high-stretch cables (i.e., the feed hose in their study). But, on the other hand, the linear secant approximation provides a good explanation for low-deformation cables (i.e., the mooring line in their study). Tahar and Kim [18] adapted the nonlinear time-dependent empirical elastic constant to analyze a spar platform with polyester mooring lines. They concluded that the nonlinear model is useful for the verification of the simplified linear model when the material property of the cable varies significantly.

For the relay platform of the Kuroshio power plant, it is designed as a flexible frame structure to support tens of turbines and is anchored to the seabed by hundreds of cables. The cables and the platform are under the actions of various forces simultaneously, such as the platform's net buoyancy, the exerted forces from turbines and anchor cables, and the thrust of the Kuroshio. To solve such a highly nonlinear dynamical problem, we start with the initial conditions of zero deformations of both platform and cables and zero force applied, and adopt a transient analysis to solve the tensions and the displacements of both the platform and the cables under the actions of the aforementioned external forces. The computations evolve over time until the displacements of both platform and cables reach to a steady state. In present analyses, various torsional stiffness constants of

the universal joints (accounted for by the constraint forces in three directions and constraint moment in the axial direction of linkage), different types of cable anchorage, and different formations of turbine deployment are considered. Consequently, the displacement and the tension of the cables and the deformation and the displacement of the platform at the steady state are obtained.

4.1   Force Equilibrium Models for Platform Dynamics

The theoretical model in terms of the force equilibrium equations for the platform is derived in this section. The force equilibrium equations are categorized into three different groups for, respectively, the three major components of the platform, i.e., the cable, the linkages, and the universal joint, as shown in the following subsections. Consequently, a linear combination of these equations forms a complete theoretical model that will be solved for the tension and the displacement of the platform components.

4.1.1   Cable

Force per unit length due to hydrodynamic effects for a submerged body may be expressed as:

$$\mathbf{F} = \mathbf{F}_{hs} + \mathbf{F}_{hd} + \mathbf{F}_{ap}, \tag{4.1}$$

where $\mathbf{F}_{hs}$ is the net buoyancy, $\mathbf{F}_{hd}$ is the current thrust, and $\mathbf{F}_{ap}$ is the external force. Given a current thrust, a generalized Morison's equation [19] is considered :

$$\mathbf{F}_{hd} = 0.5\rho_w D_o (C_D |\dot{\mathbf{u}}_N| \dot{\mathbf{u}}_N + C_T |\dot{\mathbf{u}}_T| \dot{\mathbf{u}}_T + 0.5\pi C_M D_o \ddot{\mathbf{u}}_N), \tag{4.2}$$

where C_D and C_T are the normal and tangential drag coefficients, C_M is the inertia coefficient, $\dot{\mathbf{u}}_N$ and $\dot{\mathbf{u}}_T$ are normal and tangential relative particle velocities, $\ddot{\mathbf{u}}_N$ is the normal relative particle acceleration, and D_o is the outer diameter of the tube structure.

For a static structure analysis, the equilibrium equation may be expressed as

$$\mathbf{Ku} = \mathbf{P}, \tag{4.3}$$

where $\mathbf{P}$ is the external load matrix, $\mathbf{u}$ and $\mathbf{K}$ are the displacement and the stiffness matrices. Calculating the deflections of the cable (a tension structure) from (4.3) using just the initial stiffness matrix $\mathbf{K}$ as

$$\mathbf{u} = \mathbf{K}^{-1}\mathbf{P}, \tag{4.4}$$

would violate the condition of static equilibrium because the displacement $\mathbf{u}$, being large, would alter the initial configuration of the cable, i.e., the configuration for which the stiffness matrix $\mathbf{K}$ is originally calculated. Therefore, a new stiffness matrix has to be found according to the new geometry. The displacement and the new geometry for the next time step can be obtained from

$$\mathbf{u}_{n+1} = \mathbf{K}_n^{-1}\mathbf{P}, \tag{4.5}$$

and

$$\mathbf{X}_{n+1} = \mathbf{X}_n + \mathbf{u}_{n+1}, \tag{4.6}$$

where the subscript n denotes a time step, and the calculation of stiffness matrix $\mathbf{K}_n$ is based on the updated geometry $\mathbf{X}_n$.

If the displacement is large, the new stiffness matrix $\mathbf{K}_{n+1}$ multiplied by the displacement found from Eq. (4.5) would generate an internal load $\tilde{\mathbf{P}}$ by

$$\tilde{\mathbf{P}}_{n+1} = \mathbf{K}_{n+1}\mathbf{u}_{n+1}, \tag{4.7}$$

in which the internal load is out of balance with the external load, and their difference is represented by the out-of-balance force $\mathbf{R}$

$$\mathbf{R}_{n+1} = \mathbf{P} - \tilde{\mathbf{P}}_{n+1}. \tag{4.8}$$

The out-of-balance force yields an increment for the displacement, $\Delta\mathbf{u}$, as

$$\Delta\mathbf{u}_{n+1} = \mathbf{u} - \mathbf{u}_{n+1}, \tag{4.9}$$

or as

$$\Delta\mathbf{u}_{n+1} = \mathbf{K}_{n+1}^{-1}\mathbf{R}_{n+1}. \tag{4.10}$$

The increment in the displacement matrix is subsequently used to update the geometry of the structure, as

$$\mathbf{u}_{n+2} = \mathbf{u}_{n+1} + \Delta\mathbf{u}_{n+1}, \tag{4.11}$$

and

$$\mathbf{X}_{n+2} = \mathbf{X}_{n+1} + \mathbf{u}_{n+2}. \tag{4.12}$$

Subsequently, a new stiffness matrix is calculated which, together with new out-of-balance force, generates a new increment of displacements. The computational procedure above sets up an iterative process of calculations through Eqs. (4.5)–(4.12), which continues until the out-of-balance forces (or displacement increments) are reduced to an allowed tolerance, i.e., the static equilibrium is reached. The iteration procedure above is the well-known Newton–Raphson method [3].

For a dynamic structure analysis, on the other hand, the equilibrium equation may be replaced by

$$\mathbf{M}^{t+\Delta t}\ddot{\mathbf{u}}_{n+1} + \mathbf{C}^{t+\Delta t}\dot{\mathbf{u}}_{n+1} + {}^{t+\Delta t}\mathbf{K}_n\Delta\mathbf{u}_n = {}^{t+\Delta t}\mathbf{F}_{n+1} - {}^{t+\Delta t}\tilde{\mathbf{F}}_n, \qquad (4.13)$$

$$\Delta\mathbf{u}_n = {}^{t+\Delta t}\mathbf{u}_{n+1} - {}^{t+\Delta t}\mathbf{u}_n, \qquad (4.14)$$

where t and Δt are the time and the time increment, $\mathbf{M}$ and $\mathbf{F}$ are the mass and external load matrices, and $\mathbf{C}$ is the damping matrix, which may be specified by the Rayleigh damping matrix as

$$\mathbf{C} = \alpha\mathbf{M} + \beta\mathbf{K}, \qquad (4.15)$$

where α and β are the mass matrix and stiffness matrix multipliers. Based on the Newmark method [20], the acceleration and velocity terms at time $t+\Delta t$ (i.e. the first two terms on the left-hand side of Eq. (4.13)) can be expressed by the displacement at $t+\Delta t$ and the acceleration and velocity at t as follows:

$$^{t+\Delta t}\ddot{\mathbf{u}}_{n+1} = \alpha_1\left({}^{t+\Delta t}\mathbf{u}_{n+1} - {}^{t+\Delta t}\mathbf{u}_n\right) + \alpha_2({}^{t}\dot{\mathbf{u}}) + \alpha_3({}^{t}\ddot{\mathbf{u}}), \qquad (4.16)$$

and

$$^{t+\Delta t}\dot{\mathbf{u}}_{n+1} = \beta_1\left({}^{t+\Delta t}\mathbf{u}_{n+1} - {}^{t+\Delta t}\mathbf{u}_n\right) + \beta_2({}^{t}\dot{\mathbf{u}}) + \beta_3({}^{t}\ddot{\mathbf{u}}), \qquad (4.17)$$

where $\alpha_1 = 1/\zeta\Delta t^2$, $\alpha_2 = -1/\zeta\Delta t$, $\alpha_3 = 1 - 1/2\zeta$, $\beta_1 = \eta/\zeta\Delta t$, $\beta_2 = 1 - \eta/\zeta$, $\beta_3 = \Delta t(1 - \eta/2\zeta)$, and ζ and η are Newmark constants. Note that the solution for $\eta \geq 0.5$ and $\zeta \geq 0.25(0.5 + \eta)^2$ is unconditionally stable [21]. Substituting Eqs. (4.16) and (4.17) into Eq. (4.13) results in

$$^{t+\Delta t}\bar{\mathbf{K}}_n\Delta\mathbf{u}_n = {}^{t+\Delta t}\bar{\mathbf{F}}_{n+1} - {}^{t+\Delta t}\tilde{\mathbf{F}}_n, \qquad (4.18)$$

where $\bar{\mathbf{K}}$ and $\bar{\mathbf{F}}$ are the revised stiffness and revised external load matrices, and

$$^{t+\Delta t}\bar{\mathbf{K}}_n = \alpha_1\mathbf{M} + \beta_1\mathbf{C} + {}^{t+\Delta t}\mathbf{K}_n, \qquad (4.19)$$

Fig. 4.1 The degree of freedom of the platform component: (**a**) *line element* for cables; (**b**) *pipe element* for linkages; (**c**) *joint element* for cross joints
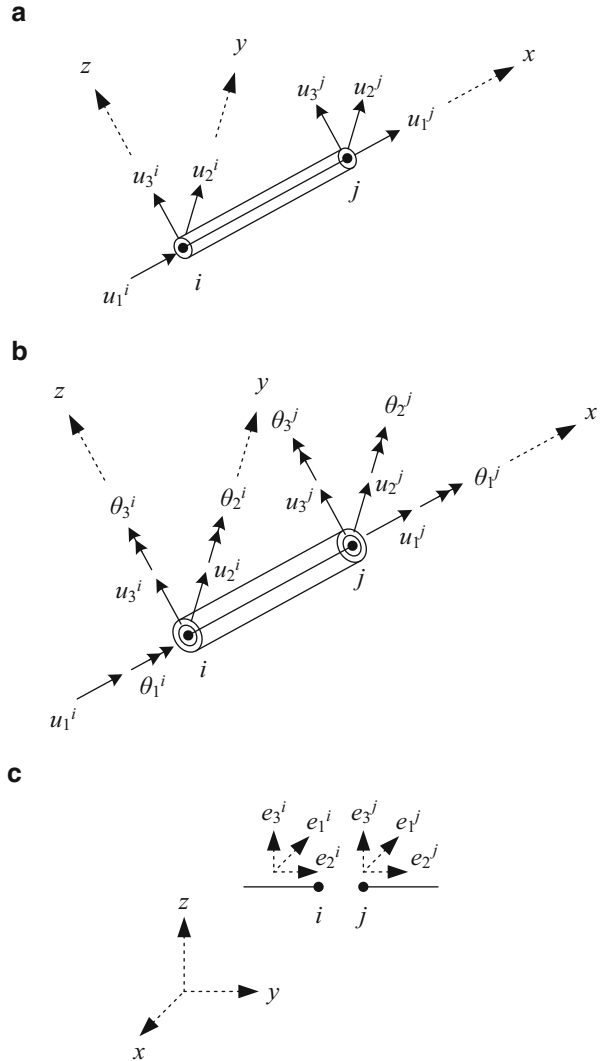
and

$$
{}^{t+\Delta t}\bar{\mathbf{F}}_{n+1} = {}^{t+\Delta t}\mathbf{F}_{n+1} - \mathbf{M}\left[\alpha_1\left({}^{t+\Delta t}\mathbf{u}_n - {}^{t}\mathbf{u}\right) + \alpha_2\left({}^{t}\dot{\mathbf{u}}\right) + \alpha_3\left({}^{t}\ddot{\mathbf{u}}\right)\right]
$$
$$
- \mathbf{C}\left[\beta_1\left({}^{t+\Delta t}\mathbf{u}_n - {}^{t}\mathbf{u}\right) + \beta_2\left({}^{t}\dot{\mathbf{u}}\right) + \beta_3\left({}^{t}\ddot{\mathbf{u}}\right)\right].
$$

$$(4.20)$$

Notice that the revised stiffness and external load matrices are related to the mass and damping matrices.

Based on the FEM discretization process, the cable is divided into hundreds of 3D line (cable) elements (Fig. 4.1a), where each node of an element has three degrees of freedom. The displacement matrix can be expressed as:

$$_{\text{cable}}\mathbf{u}^e = {}_{\text{cable}}\mathbf{N}\,_{\text{cable}}\delta^e, \tag{4.21}$$

where $_{\text{cable}}\delta^e = \begin{bmatrix} u_1^i & u_2^i & u_3^i & u_1^j & u_2^j & u_3^j \end{bmatrix}^{\text{T}}$, u_1, u_2, and u_3 are the displacements in three axial directions, the superscripts i and j denote the two respective nodes, and $_{\text{cable}}\mathbf{N}$ is the 3D line element shape function matrix (see Eq. (C.1) of Appendix C). Accordingly, the strain and stress matrices of the element are:

$$_{\text{cable}}\varepsilon^e = {}_{\text{cable}}\mathbf{B}\,_{\text{cable}}\delta^e, \tag{4.22}$$

and

$$_{\text{cable}}\sigma^e = {}_{\text{cable}}\mathbf{D}\,_{\text{cable}}\mathbf{B}\,_{\text{cable}}\delta^e, \tag{4.23}$$

where $_{\text{cable}}\mathbf{B}$ and $_{\text{cable}}\mathbf{D}$ are the stress–strain and the strain–displacement relationship matrices of the line element. Therefore, the stiffness matrix is

$$_{\text{cable}}\mathbf{K}^e = \int_{V_c} {}_{\text{cable}}\mathbf{B}^{\text{T}}\,_{\text{cable}}\mathbf{D}\,_{\text{cable}}\mathbf{B}\,dV, \tag{4.24}$$

where V_c is the volume of the line element and the stiffness matrix is shown as Eq. (C.3) of Appendix C. Using (4.21), the inertia and damping forces will be

$$_{\text{cable}}\mathbf{F}^e_{(\rho)} = -\int_{V_c} {}_{\text{cable}}\mathbf{N}^{\text{T}} \rho_c\,_{\text{cable}}\ddot{\mathbf{u}}^e\,dV = -{}_{\text{cable}}\mathbf{M}^e\,_{\text{cable}}\ddot{\delta}^e, \tag{4.25}$$

and

$$_{\text{cable}}\mathbf{F}^e_{(d)} = -\int_{V_c} {}_{\text{cable}}\mathbf{N}^{\text{T}} d_c\,_{\text{cable}}\ddot{\mathbf{u}}^e\,dV = -{}_{\text{cable}}\mathbf{C}^e\,_{\text{cable}}\ddot{\delta}^e, \tag{4.26}$$

where ρ_c and d_c are the density and damping coefficient of the cable, and $_{\text{cable}}\mathbf{M}^e$ and $_{\text{cable}}\mathbf{C}^e$ are the mass and damping matrices of the line element as

$$_{\text{cable}}\mathbf{M}^e = \int_{V_c} {}_{\text{cable}}\mathbf{N}^{\text{T}} \rho_c\,_{\text{cable}}\mathbf{N}\,dV, \tag{4.27}$$

$$_{\text{cable}}\mathbf{C}^e = \int_{V_c} {}_{\text{cable}}\mathbf{N}^{\text{T}} d_c\,_{\text{cable}}\mathbf{N}\,dV = \alpha\,_{\text{cable}}\mathbf{M}^e. \tag{4.28}$$

The details of $_{\text{cable}}\mathbf{M}^e$ is shown in Eq. (C.5) of Appendix C.

4.1.2   Linkage

The relay platform is a multi-linkage structure being composed of various kinds of pipe (or tube) connected with universal joints. The 3D pipe element (Fig. 4.1b) has six degrees of freedom on each node, which can be expressed by the displacement matrix

$$_{\text{pipe}}\mathbf{u}^e = {}_{\text{pipe}}\mathbf{N}_{\text{pipe}}\delta^e, \tag{4.29}$$

where $_{\text{pipe}}\delta^e = \begin{bmatrix} u_1^i & u_2^i & u_3^i & \theta_1^i & \theta_2^i & \theta_3^i & u_1^j & u_2^j & u_3^j & \theta_1^j & \theta_2^j & \theta_3^j \end{bmatrix}^{\text{T}}$, θ_1, θ_2, and θ_3 are the rotations in three axial directions, and $_{\text{pipe}}\mathbf{N}$ is the 3D pipe element shape function matrix (see Eq. (C.2) of Appendix C). Similar to Eqs. (4.24), (4.27), and (4.28), the stiffness, mass, and damping matrices of the pipe element are, respectively,

$$_{\text{pipe}}\mathbf{K}^e = \int_{V_{\text{p}}} {}_{\text{pipe}}\mathbf{B}^{\text{T}}{}_{\text{pipe}}\mathbf{D}_{\text{pipe}}\mathbf{B}dV, \tag{4.30}$$

$$_{\text{pipe}}\mathbf{M}^e = \int_{V_{\text{p}}} {}_{\text{pipe}}\mathbf{N}^{\text{T}}\rho_{\text{p}}{}_{\text{pipe}}\mathbf{N}dV, \tag{4.31}$$

and

$$_{\text{pipe}}\mathbf{C}^e = \int_{V_{\text{p}}} {}_{\text{pipe}}\mathbf{N}^{\text{T}}d_{\text{p}}{}_{\text{pipe}}\mathbf{N}dV, \tag{4.32}$$

where V_p is the volume of the pipe element, $_{\text{pipe}}\mathbf{B}$ and $_{\text{pipe}}\mathbf{D}$ are the stress–strain and the strain–displacement relationship matrices of the pipe element (see Eqs. (C.4) and (C.6) of Appendix C), and ρ_{p} and d_{p} are the density and damping coefficient of the pipe.

4.1.3   Universal Joint

Kinematic constraints are specified for the simulation of the behavior of the universal joint. The universal joint element is a two-node element (Fig. 4.1c) that has one translational and two relative rotational degrees of freedom. Each node of the universal joint element belongs to one end of the linkage, and the two nodes of different linkages connected with the same universal joint have identical spatial

coordinates. As a result, at any given instant, the displacement constraints imposed in a universal joint are $u_1^i = u_1^j$, $u_2^i = u_2^j$, and $u_3^i = u_3^j$, and the rotational constraint imposed in a universal joint is $\theta_2^i = \theta_2^j$ or $e_1^i \cdot e_3^j = 0$.

Using the matrix notation, the set of the constraints can be concisely denoted by

$$_\lambda \mathbf{K}_\lambda \delta = 0, \tag{4.33}$$

where $_\lambda \mathbf{K}$ is the constraint matrix, and $_\lambda \delta$ is the nodal displacement. Applying the Lagrange multiplier method, the set of the constraint forces λ can be introduced into the following equation as

$$\mathbf{K}\delta = \mathbf{F} + \mathbf{F}_{(\rho)} + \mathbf{F}_{(d)} - \lambda. \tag{4.34}$$

After moving λ to the left-hand side of Eq. (4.34) and appending it to the nodal displacement matrix, it yields

$$\begin{bmatrix} \mathbf{K} & _\lambda\mathbf{K}^\mathrm{T} \\ _\lambda\mathbf{K} & 0 \end{bmatrix} \begin{Bmatrix} \delta \\ \lambda \end{Bmatrix} = \begin{Bmatrix} \mathbf{F} + \mathbf{F}_{(\rho)} + \mathbf{F}_{(d)} \\ 0 \end{Bmatrix}. \tag{4.35}$$

As a result, the nodal displacement and the nodal constraint force can be obtained from Eq. (4.35). Consequently, the constraint force can be more precisely expressed as—$_\lambda\mathbf{K}^\mathrm{T}\lambda$.

4.1.4   Unit Platform

Figure 4.2 shows the free body diagram of the forces and moments applied on a unit platform, which is a square structure with each side composed of a primary linkage, two auxiliary linkages, and two cross joints. All these components are connected with universal joints. The force equilibrium equations with the inertia and damping effects for the unit platform can be written as

$$\mathbf{K}\delta = \mathbf{F} + \mathbf{F}_{(\rho)} + \mathbf{F}_{(d)}. \tag{4.36}$$

Considering all components of the unit platform, the dynamic force equilibrium equations in terms of the nodal displacement would be:

$$\mathbf{M}\ddot{\delta} + \mathbf{C}\dot{\delta} + \mathbf{K}\delta = \mathbf{F}, \tag{4.37}$$

where $\mathbf{M} = \sum_{e=1}^{n_e} \mathbf{M}^e$, $\mathbf{C} = \sum_{e=1}^{n_e} \mathbf{C}^e$, $\mathbf{K} = \sum_{e=1}^{n_e} \mathbf{K}^e$, and n_e is the element number.
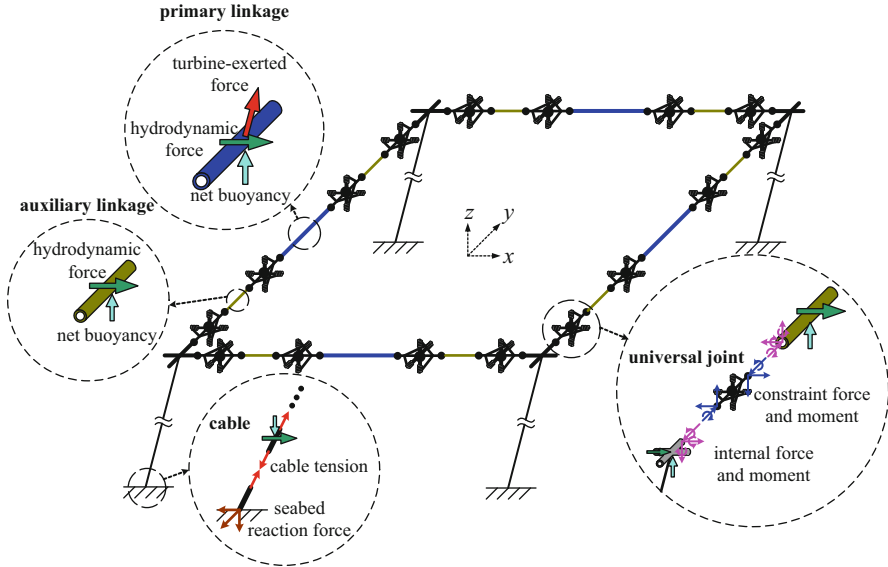
Fig. 4.2 The free body diagram of forces and moments applied on a unit platform. Aside from the additional turbine-exerted force applied to the primary linkage, all components are subject to hydrodynamic force and their own net buoyancy. In addition, each universal joint yields three constraint forces and a constraint moment

To analyze the dynamics of the unit platform with constraints applied by the universal joints, Eq. (4.35) shall be solved simultaneously with Eq. (4.37). The unknown degrees of freedom at each joint location (i.e., the end of the linkage) would be three translational displacements and five rotational displacements, with three unknown constraint forces and a constraint moment. To reduce the relative rotational displacements (i.e., the deflection between two linkages), an additional rotational stiffness k_r is used for the stiffness matrix. More precisely, a_3 in Eq. (C.4) in Appendix C is replaced by $a_3 + k_r$.

4.2 Design of the Unit and Test Platforms

The relay platform is a complicate structure applied with forces exerted by dozens of turbines from above and hundreds of cables from below, and with the thrust of the Kuroshio acting on the platform as well. Not only do these forces produce strain on the platform components, but they also produce deformation and displacement of the overall platform, which can potentially unbalance the platform leading to the loss of its primary functions and more seriously cause fatal damages of the power plant.

Fig. 4.3 Displacement of the unit platform subject to various force and moment constraints of the universal joint. The Kuroshio moves from the left to the right; the turbine is anchored on the linkage at upstream. Results show that the change of the force and moment constraint of the universal joint does not affect the displacement of the platform, while the present vertical anchoring cable arrangement produces significant horizontal and vertical platform displacements
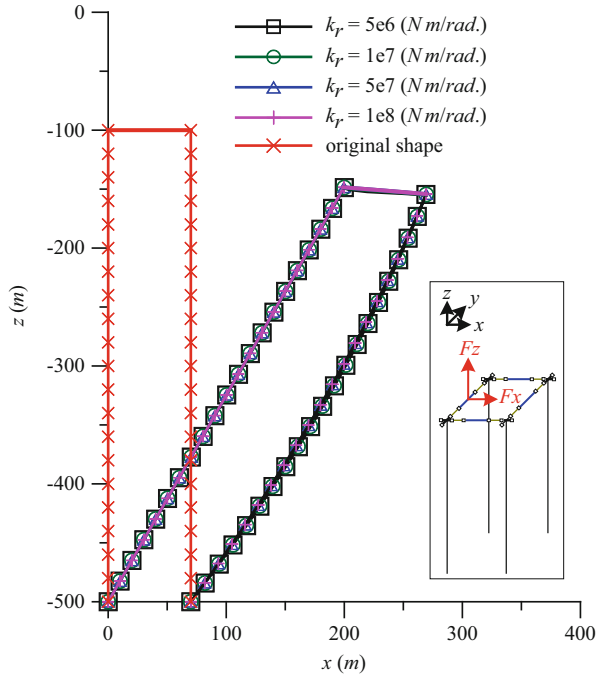
To tackle this complicate problem with a careful manner, we adopt a progressive analysis logic as follows. We begin the analysis for a 1×1 platform (or the unit platform) with a single turbine anchored to its primary linkage to analyze the constraint forces and moment of the universal joint required to maintain the integrity of the platform. The analysis is then extended to a 2×3 platform (or the test platform) anchored with various kinds of turbine cluster formation and different types of anchoring cable arrangements. The results will determine the optimized cable arrangement for the test platform. Finally, a 6×11 platform (or the relay platform) is analyzed with the required universal joint constraints, the optimal turbine cluster formation and the most reliable cable arrangements obtained from the analyses of the unit and the test platforms; results include the overall platform deformation, displacement, and tension of each platform cable, along with the related design parameters.

For the unit platform, the turbine is anchored on the primary linkage of the side facing the current, and the platform is anchored to the seabed by four vertical cables, as shown in Fig. 4.3. Because the platform is mainly composed of hollow floats (the linkages), the net buoyancy of the platform is positive and strong enough to secure that the platform be stably deployed in the current. The combination of the current thrust and the turbine's buoyancy results in an inclined force applied through the cable on the platform, and the inclined angle of the cable, i.e., the angle between the platform and the cable, is designed to be 60°. As mentioned in Chap. 3, the turbine-exerted force varies periodically with blade rotation.

Table 4.1 Size parameters of platform linkages, cross joint, and cable (units: m)

Type	Size	Primary linkage	Auxiliary linkage	Cross joint	Cable
1 × 1 (Unit platform)	Length	30	15	10	400
	Inner diameter	1.5	1	1.5	0.1
	Outer diameter	1.4	0.94	1.4	0
2 × 3 (Type I and II cable arrangements)	Length	30	15	10	400, 565.69, 692.82
	Inner diameter	1.5	1	1.5	0.1
	Outer diameter	1.4	0.94	1.4	0
2 × 3 (Type III cable arrangement)	Length	30	15	10	400, 406.08, 565.69
	Inner diameter	1.5	1.5	1.5	0.1
	Outer diameter	1.4	1.44	1.4	0
6 × 11 (relay platform)	Length	30	15	10	400, 406.08, 565.69
	Inner diameter	1.8	1.8	1.8	0.1
	Outer diameter	1.7	1.74	1.7	0

Accordingly, for a single turbine exerting a total force of 1,455,000 N on the platform, the cable's vertical and horizontal pull exerted on the linkages are, respectively:

$$F_z = 1,260,067 \, (\text{N}), \tag{4.38}$$

and

$$F_x = 727,500 - 12,500 \times \sin(\omega t) \, (\text{N}), \tag{4.39}$$

where $\omega = 0.6276 \, (\text{rad/s})$ is the frequency of the force oscillation generated due to tower shadow effect of the rotors.

Table 4.1 gives the size parameters of the three platform types considered in this study. In general, to provide sufficient buoyancy, the diameter of the hollow float needs to be larger for cases with more cables (e.g., Type III cable arrangement as shown in Fig. 4.5c) and for cases with greater platform size (e.g., the 6 × 11 relay platform). The material properties of the platform and the flow parameters applied on the linkages, both required for the computation of platform dynamics, are listed, respectively, in Tables 4.2 and 4.3. A finite element program ANSYS [21] is

Table 4.2 Material properties of the platform components. Note that primary linkage, auxiliary linkage and cross joint are of the same properties

Component	Material	Elastic parameter (GPa)	Specific gravity	Additional rotational stiffness (k_r) (Nm/rad)	Mass matrix multiplier (α)	Stiffness matrix multiplier (β)
Primary linkage						
Auxiliary linkage	Steel	200	7,860	1×10^8	10	0
Cross joint						
Cable	Polyester	9	1,380	–		

Table 4.3 Flow parameters applied on the platform

| Item	Value
Seawater density (ρ_w) (kg/m^3)	1,030
Normal drag coefficient (C_D)	0.7
Tangential drag coefficient (C_T)	0.05
Added mass coefficient (C_I)	1
Inertia coefficient (C_M)	2
Current speed applied to the relay platform[a] (V) (m/s)	1 for -100 m $\leq z \leq 0$
	$(z + 500)/400$ for -500 m $\leq z \leq -100$ m

[a]$z = 0$ at sea surface

employed to solve the equations, where the Newmark constants are $\zeta = 0.253$ and $\eta = 0.505$, and the displacement increment threshold is set to 1 cm.

4.2.1 Design of the Unit Platform

In the analysis for the unit platform, the required stiffness of the universal joint in terms of constraint forces and moment to secure the integrity of the platform is investigated. Under the conditions shown in Tables 4.2 and 4.3, we consider four different rotational stiffness 5×10^6, 1×10^7, 5×10^7, and 1×10^8 Nm/rad. The calculated final displacement and deformation of the unit platform are illustrated in Figs. 4.3 and 4.4, respectively.

Results of Fig. 4.3 show that the rotational stiffness has virtually no influence on the displacement since the final position of the platform and the cable shape of the four cases are virtually the same. But, on the other hand, as shown in Fig. 4.4, the deformation of the platform is greatly influenced by the rotational stiffness; the platform of a smaller stiffness such as 5×10^6 and 1×10^7 Nm/rad has resulted in a large deformation which may eventually lead to a disintegration of the structure. The platform of a larger stiffness, say 5×10^7 and 1×10^8 Nm/rad, deforms much less than previous cases; both are acceptable to the design of a secured platform. Consequently, to secure the stability and integrity of the platform, we shall consider

Fig. 4.4 The deformed shape of the unit platform subject to various force and moment constraints of the universal joint. Results show that the force and moment constraints have a significant effect on the deformation of the platform. A decrease in the constraints results in an increase in the deformation of the platform
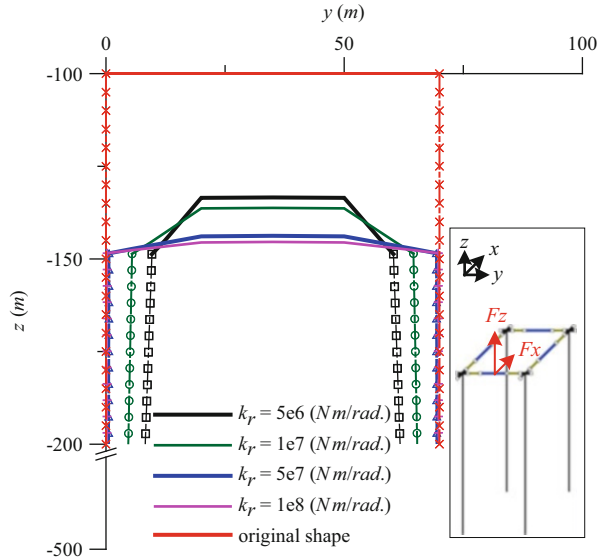
the rotational stiffness $K_r = 1 \times 10^8$ Nm/rad as the design criteria of the relay platform.

4.2.2 Design of the Test Platform

In the analysis for the test platform, we shall focus on the effects of the turbine cluster formation and the anchoring cable arrangement on the deformation and displacement of the platform. To do this, attention is firstly paid to the results shown in Fig. 4.3, which shows that the vertical cable arrangement would lead to a significant displacement of the entire platform, being about 200 m behind and 50 m below the original position, a too-large displacement to be accepted. To reduce the potential displacement, three types of anchoring cable arrangements are considered as follows (please refer to Fig. 4.5):

- (Type I) All cables are vertical: all cables connected to the platform fall vertically to the seabed, as considered for the unit platform of Fig. 4.3.
- (Type II) Vertical cables and 45°-inclined cables: the cables connected to the cross joints at the middle platform fall vertically to the seabed, while those to the circumference of the platform are anchored to the seabed with a 45° inclination.
- (Type III) Double anchoring cables: Each cross joint is anchored by a vertical and an inclined cable. There are two kinds of inclined cables. The inclined cable at the upstream edge of platform is of 45° inclination, while the other inclined cables connect the anchor at seabed and the cross joint of the platform.
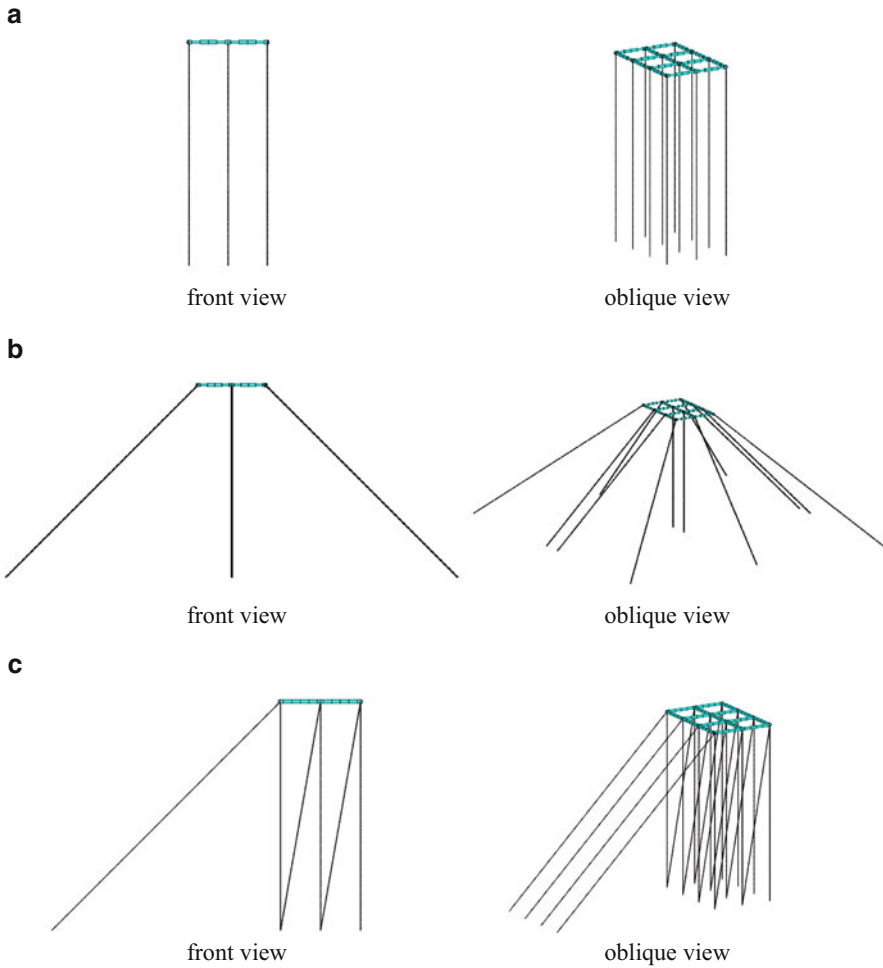
Fig. 4.5 Three types of anchoring cable arrangements: (**a**) Type I: all vertical cables; (**b**) Type II: vertical cables at middle of platform and 45°-inclined cables at periphery of platform; (**c**) Type III: a combination of vertical and inclined cables

For each type of anchoring cable arrangement, we consider six different kinds of turbine cluster formation, as shown in Fig. 4.6. Each kind of formation features with different position and various number of turbine. The number of turbine ranges from 1 to 5, being anchored on the primary linkage of the unit platform. For the case of multiple turbine, the streamwise distance between turbines shall follow the principle that the wake generated by the turbine at upstream shall not cast a significant disturbance on the turbine at downstream. In general, the distance is about 5–10 times the diameter of the rotor. For the GST considered in the present study, the rotor diameter is 23 m; the distance could range from 120 m to 230 m. The formations shown in Fig. 4.6 meet this requirement since the streamwise
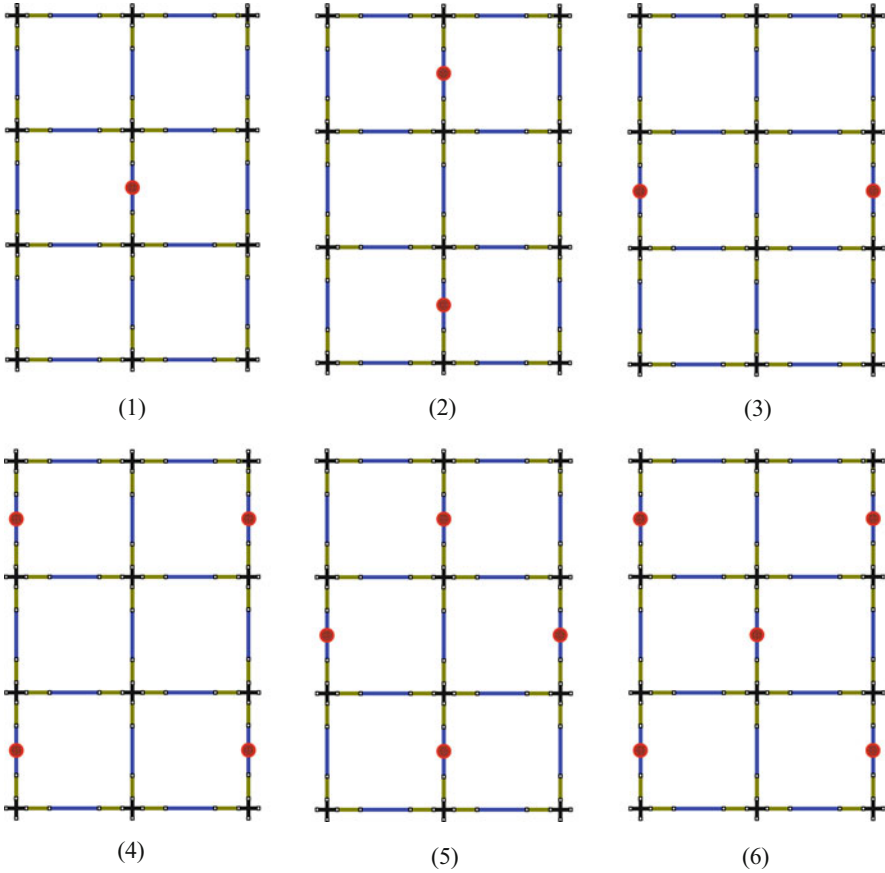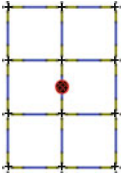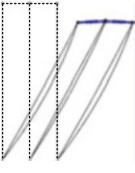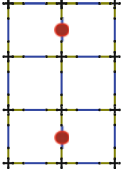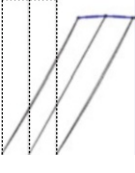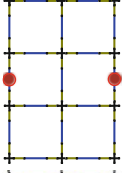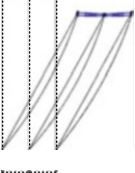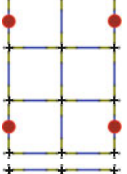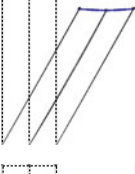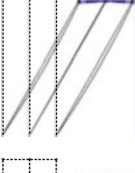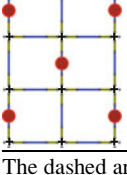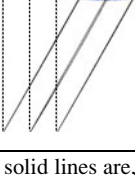
Fig. 4.6 Six kinds of turbine cluster formation. The *red point* accounts for the anchoring position of the turbine. A sleeve, which can freely rotate but cannot move along the primary linkage, is used to anchor the turbine on the primary linkage of the platform. (1) 1st kind of turbine formation, (2) 2nd kind, (3) 3rd kind, (4) 4th kind, (5) 5th kind, (6) 6th kind

distance between two turbines is 140 m (two times the width of the unit platform), which is about seven times the rotor diameter.

For each type of cable arrangement, we consider six different kinds of turbine cluster formation. For Type I cable arrangement, results shown in Table 4.4 indicate that both the displacement and deformation of the platform are not significantly influenced by the turbine cluster formation. Namely, for the six different formations considered, the platform swifts 190–200 m horizontally and −48 to −50 m vertically and deforms by 6–10 m between the highest and lowest points of the platform (or an inclined angle of linkage ranging from 2° to 5° with respect to the horizontal plane).

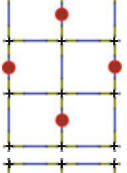The deformation of the platform is closely related to the anchoring position of the turbine, although the difference is insignificant. But, on the other hand, the tension of the cable is greatly influenced by the anchoring position of the turbine, which can be seen from, for example, the 1st and 3rd kinds of formation of
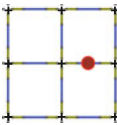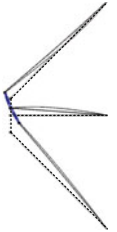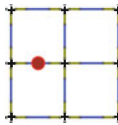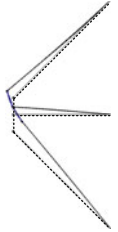
Table 4.4 Displacement and deformation of the Type I anchoring cable arrangement

Turbine cluster formation	Deformed shape	Horizontal displacement (m)	Vertical displacement (m)	Platform deformation (m)	Platform inclination (deg.)
		191.56	−48.64	8.57	3.87
		195.68	−49.42	6.86	4.97
		195.58	−50.77	10.72	4.89
		198.62	−49.39	7.05	5.11
		198.98	−49.71	7.69	2.51
		199.57	−49.13	7.00	5.07

The dashed and solid lines are, respectively, the original and deformed shapes; the displacements are the average distances between the original and deformed shape; the vertical deformation stands for the distance between the highest and lowest points of the deformed platform

Table 4.4. For the 1st kind formation, the tension of the cable at the middle of the platform is larger than those at the edge of the platform, which can be seen from the shape of the cable: the cable of a curved shape is of a smaller tension, and the cable of a straight shape is of a higher tension. For the 3rd kind formation, the tension of

Table 4.5 Displacement and deformation of the Type II anchoring cable arrangement

Turbine cluster formation	Deformed shape	Horizontal displacement (m)	Vertical displacement (m)	Platform deformation (m)	Platform inclination (deg.)
		31.08	−6.14	64.63	21.54
		32.93	−2.82	62.57	23.57
		32.21	−4.25	69.09	22.63
		36.65	2.63	62.89	23.18

The dashed and solid lines are, respectively, the original and deformed shapes. The displacements are the average distances between the original and deformed shape. The vertical deformation stands for the distance between the highest and lowest points of the deformed platform
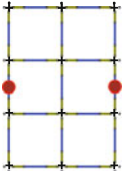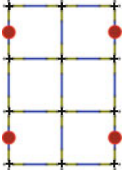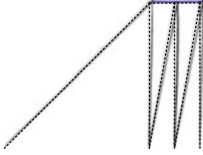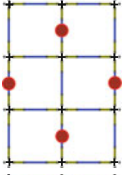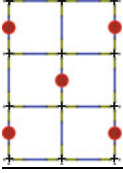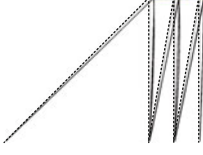
the cables on the two sides of the platform is smaller than those at the middle. For the 6th kind formation, see the bottom case of Table 4.4, the deformations of both platform and cables seem to be the smallest of the six cases considered, implying that the force distribution on the platform is more uniform so that the integrity of both the platform and the cable is the best, so that this kind of the turbine formation will be chosen for the design of relay platform.

Table 4.5 shows the displacement and deformation of the Type II cable arrangement. The platform moves 30–40 m horizontally and -7–3 m vertically, while the platform deforms in a serious manner; the difference between the highest and lowest points of the platform is 62–69 m, and the inclination angle of the platform is $21°$ to $24°$. This slanted shape of platform would cause the interference between turbine and platform, leading to a serious damage of the power plant. For this reason this type of anchoring cable arrangement will not be considered in the analysis for relay platform.

Above analyses of cable arrangement show that the vertical cable leads to a significant displacement but results in a securely horizontal platform altitude. The inclined cable leads to a smaller displacement but results in a seriously slanted platform. Accordingly, the Type III cable arrangement is designed to combine the advantages of the first two types, which is, in addition to the vertical anchor cables, a $45°$ anchor cable is applied to the upstream side of the platform to limit horizontal displacement, while both the vertical and inclined cables are applied to every anchoring point of the platform to limit simultaneously vertical displacements and platform inclination. The results are shown in Table 4.6, from which one can see that, for all the cases considered, the platform moves 2–13 m horizontally and -1–2 m vertically; a line connecting the highest and lowest points of the platform presents an inclined angle of $2°$ to $6°$. Regarding the tension of the cable, for example, the 2nd and 5th kinds of turbine formation lead to a nonuniform force distribution on the platform, which can be seen from that the shapes of cable are of greater difference from original ones. But, again, the 6th kind of formation leads to a more uniform force distribution and an installation of more turbines, being the best case to be considered for the design of relay platform.

We summarize the platform displacements for the three types of cable arrangement in Fig. 4.7. It shows that, as discussed previously, significant horizontal and vertical displacements occur in the Type I arrangement. In the Type II arrangement, although both the horizontal and vertical displacements are limited within a reasonable range, the scattered vertical displacement indicates that this arrangement is not robust since it is highly dependent with the turbine formation. In Type III arrangement, both the horizontal and vertical displacements for different kinds of turbine cluster formation are more concentrated and minimized, showing this type of cable arrangement can provide the best platform stabilization.
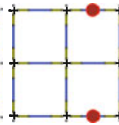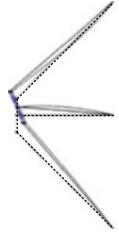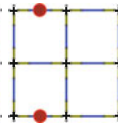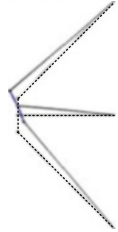
Table 4.6 Displacement and deformation of the Type III anchoring cable arrangement
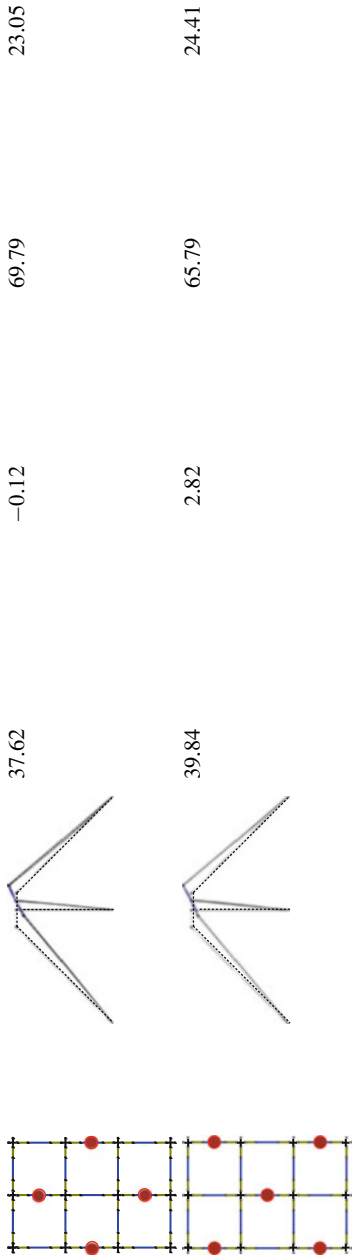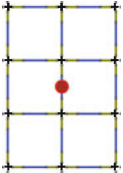
Turbine cluster formation	Deformed shape	Horizontal displacement (m)	Vertical displacement (m)	Platform deformation (m)	Platform inclination (deg.)
		2.49	0.82	4.48	2.01
		7.49	−0.34	8.05	5.85
		4.61	0.87	4.99	2.72
		8.91	1.04	4.07	2.94
		12.18	−0.50	9.89	3.21
		11.54	0.89	3.89	2.79

The dashed and solid lines are, respectively, the original and deformed shapes. The displacements are the average distances between the original and deformed shape. The vertical deformation stands for the distance between the highest and lowest points of the deformed platform
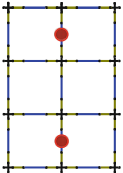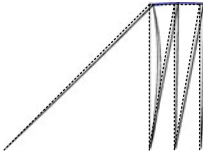
Fig. 4.7 The displacements
for the three different types
of anchoring cable
arrangement
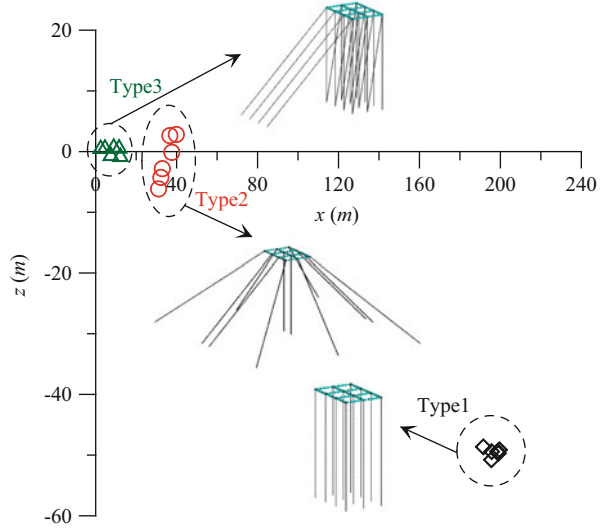
4.3 Design of the Relay Platform

As concluded by previous analyses, the best design of the relay platform structure
shall adopt the Type III anchoring cable arrangement together with the 6th kind of
turbine cluster formation. We shall accordingly follow this conclusion to analyze
the relay platform so that the 6×11 relay platform shown in Fig. 2.3c is consid-
ered. The displacement and deformation of the platform, the stress of the cable, and
the constraint forces and moment of the universal joint are calculated based on the
design parameters of the platform components. Results can be used to determine the
mechanical properties, sizes, and materials of the platform components and cables.

4.3.1 Cable Stress

We first examine the forces exerted on the platform cables. As previously men-
tioned, to ensure that the action of the Kuroshio on the platform does not result in
significant platform drift, the anchor point on each cross joint shall be hold by two
cables to restrict its vertical and horizontal displacements to a reasonable limit.
Figure 4.8 shows the change in the maximum tensile stress of the vertical and
horizontal cables over time as the platform proceeds from the beginning of the
turbine's engagement with the Kuroshio to the steady state.

Results of Fig. 4.8 show that the tensile stress of the inclined cable quickly
increases over time to a maximum of about 226 MPa and then stabilizes, being
similar to a critical damping system. On the other hand, the tensile stress on the
vertical cable quickly increases to a maximum of about 113 MPa, and then
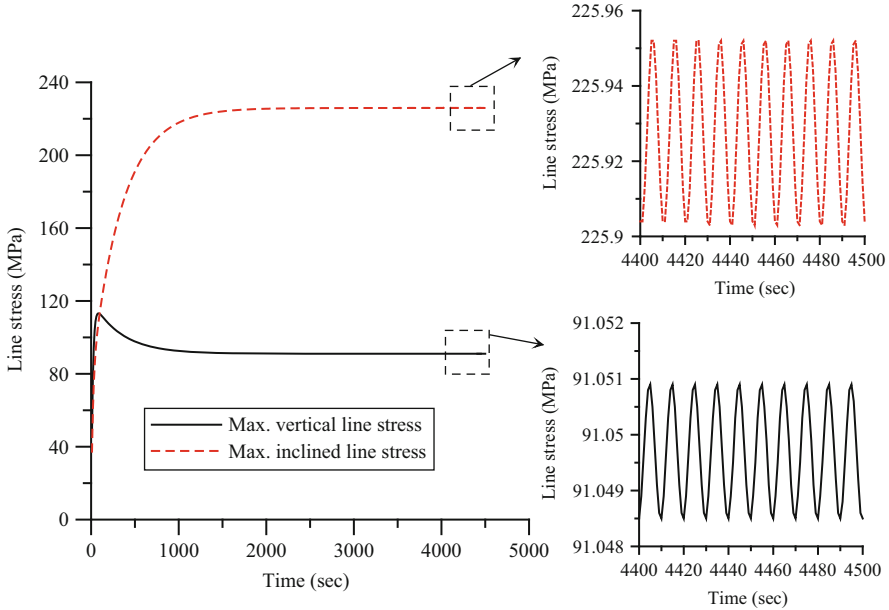
Fig. 4.8 Changes in the tensile stress of the vertical and inclined cables over time. The tensile stress on the inclined cables (*red dashed line*) gradually increases and then stabilizes, while the tensile stress on the vertical cable (*black solid line*) immediately increases to its maximum value and then gradually decreases to a stable value. The stable stress values for the two sets of cables is a cyclical change over time due to cyclical force applied by the turbine

gradually decreases to a stable value of about 91 MPa, being similar to an under-damping system. In Fig. 4.8, the so-called stable value appears actually to be a cyclical change, but with a relatively small amplitude, which resulted from the periodic force generated by the tower shadow effect on the GST. Please note that, for simplicity in analyses, we assume the rotors of the platform's 39 GSTs share the same rotation phase and that the flexible platform can absorb small perturbation in vibration. Thus, the internal stress of each cable presents a regular cyclical change, in contrast to those shown in Fig. 3.5, where the irregular cyclic change is caused mostly by the turbulent flow.

The cable stress shown in Fig. 4.8 is for a single cable under the greatest strain. In reality, however, given that each cable is anchored to a different position of the platform, they shall all come under different degrees of stress. In addition, in the following computation we shall include the weight of the cable into the overall force applied on the cable, so that the maximum stress of the cable occurs at the junction of the cable and the platform. Figure 4.9 presents the distribution of the maximum cable stress on the relay platform. Results show that the stress of the vertical cable (Fig. 4.9a) is generally much lower than that of the inclined cables (Fig. 4.9b), indicating that the inclined cables bear a great majority of the force

a

○13	○29	○55	○29	○55	○31	○38
○51	○89	○91	○89	○91	○91	○70
○37	○81	○82	○81	○82	○83	○61
○33	○79	○81	○80	○80	○82	○60
○32	○79	○80	○80	○80	○82	○59
○31	○79	○80	○80	○80	○82	○59
○31	○79	○80	○80	○80	○82	○59
○32	○79	○80	○80	○80	○82	○59
○33	○79	○81	○80	○80	○82	○60
○36	○81	○82	○81	○82	○83	○61
○51	○89	○91	○89	○91	○91	○70
○13	○29	○55	○29	○55	○30	○39

b

171	84	109	84	109	85	92
212	149	151	150	151	151	131
219	146	147	146	147	148	127
223	147	148	147	148	149	128
225	147	149	148	148	150	128
226	148	149	148	148	150	128
226	148	149	148	148	150	128
225	147	149	148	148	150	128
223	147	148	147	148	149	128
219	146	147	146	147	148	127
212	150	151	150	151	151	131
171	84	109	84	109	85	93

Fig. 4.9 Distribution of tensile stress of the cables: (**a**) vertical cables; (**b**) inclined cables (units: MPa)

applied on the platform, while the vertical cables only bear the buoyancy force from turbine and platform to restrict the platform's vertical displacement.

Results of Fig. 4.9 also show that the inclined cables at the far upstream bear the maximum stress, and those at the far downstream bear the minimum stress; the stress borne by the rest of the inclined cables is fairly uniform. Similar situation occurs to the vertical cables, except that the upstream cables bear the minimum stress. Moreover, regardless of whether the cables are vertical or inclined, the resultant stress of the cable at the two sides of the platform is always smaller than those in other locations. This indicates that the unidirectional current flow produces only a negligible lateral force on the platform and turbines. We accordingly do not need to consider either the displacement or the deformation of the platform in the lateral direction, and thus do not add additional lateral inclined cables to restrict any lateral displacement of the platform.

In conclusion, the inclined cables bear larger force than the vertical cables, especially at the far upstream of the platform. This is because the inclined cables not only have to withstand the platform's buoyancy but are also subject to the thrust from the current and the pull from the turbine, so the left-most inclined cables are

subject to the maximum force in streamwise direction. The stress of the cable in the middle part of the platform is uniformly distributed, indicating that the combination of the Type III cable arrangement and the 6th kind of turbine formation ensure the uniformity of the cable stress of the relay platform. This result is of great advantage for the design of relay platform since the uniformity of cable stress means a simplicity of the platform design, a lower cost of platform construction, and a more reliable platform integrity.

4.3.2   Anchoring Stress at Seabed

At the seabed, the force applied on the anchor determines the specification of anchor mechanism and fixation method. Figure 4.10 shows the distribution of reaction stress over all anchoring points on the seabed. Please note that, except the upstream-most and downstream-most anchor points, for all other anchor points the reaction stress is the summation of the two cable stresses exerted on the anchor point. Because aside from the upstream-most row of anchor points which only support inclined cables and the downstream-most row which only supports vertical cables, all other anchor points support both vertical and inclined cables. Results show that the reaction stress on the anchor points has the following characteristics:

1. The reaction stress on the upstream-most anchor points (on the far left of Fig. 4.10) is similar to that on the upstream-most inclined cables (on the far left of Fig. 4.9b), indicating that the weight of the cable is roughly offset by the current thrust and platform buoyancy.
2. The reaction stress on the first row anchor points at upstream directly beneath the platform is generally lower than that of the other anchor points, which is due to that a considerable amount of the force is absorbed by the upstream-most inclined cables.
3. The reaction stress on the anchor points directly beneath the interior of the platform is a combination of the stresses of vertical and inclined cables, which are nearly identical to each other and to the upstream-most anchor points. This indicates that the force exerted on the platform is uniformly high; thus, the selection of materials and sizes for the platform components and cables can be relatively simple.
4. Compared with other anchor points, the reaction stress on the downstream-most anchor points is almost negligible, indicating that the combination of the vertical and inclined cables can prevent changes in the platform's altitude and to maintain the platform's horizontal attitude.
5. The reaction stress on the lateral anchor point of the platform is much lower than that on the interior point of the platform, as shown in Fig. 4.9. This is because the lateral force is virtually negligible due to the nature of the unidirectional flow.

Figure 4.10 shows the distribution of the reaction stress of the anchor on the seabed, which shall match with the mechanical properties of the local seabed
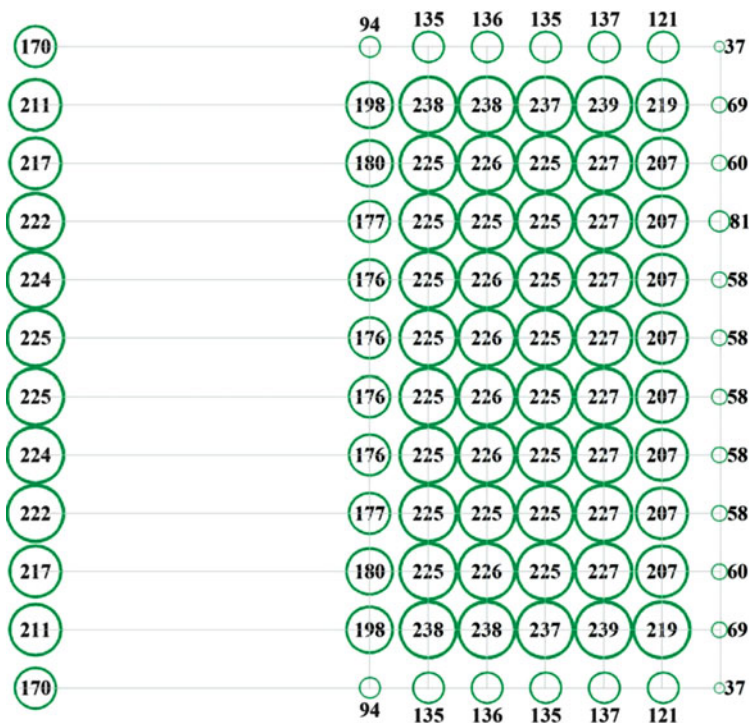
Fig. 4.10 Distribution of reaction stress of the anchors on the seabed (units: MPa). Notice that the anchor reaction stress is the combined stress exerted by the cables on the anchor point

geology and is used to determine suitable anchor mechanism and fixation depth. The examples in the figure show that the seabed rock beneath the platform must carry about 180–239 MPa anchoring stress. If an anchor of 0.25 m^2 forcing area (or equivalently an anchor of a diameter about 30 cm) is used, the force exerted on the anchor may range from 45 to 60 N. In practice, to ensure the safety and reliability of the anchors, a design of safety factor of 5 shall be considered in the design of anchoring system. This can be done by either using an anchor of 1.25 m^2 forcing area or by using cables of tensile limit higher than 1195 MPa.

4.3.3 Constraint Forces and Moment of the Universal Joint

The function of the universal joint is to constrain overall platform deformation within a reasonable range. Figure 2.3b shows that each side of the unit platforms has four universal joints. For the relay platform having 149 unit platforms, there are
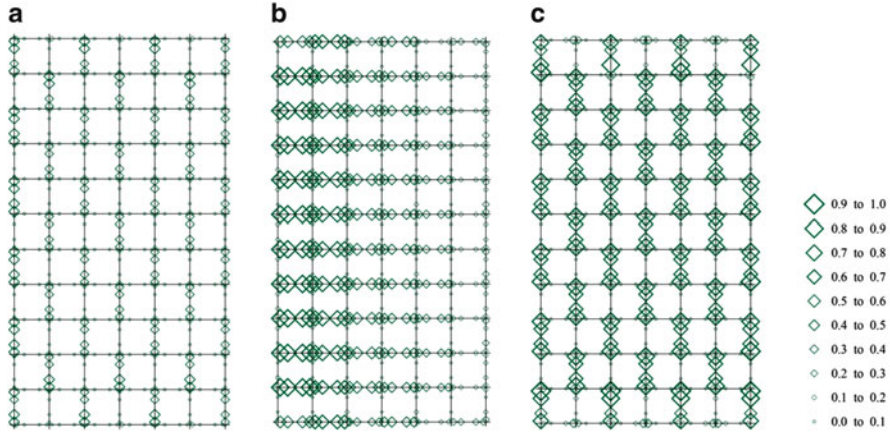
Fig. 4.11 Distributions of universal joint constraint forces in three directions: (**a**) e_1-direction; (**b**) e_2-direction; (**c**) e_3-direction (units: MN)

totally 596 universal joints. Each universal joint exerts constraint forces in three directions, namely, e_1, e_2, and e_3, and for the constraint moment in the axial direction of the linkage, please refer to the coordinate system shown in Fig. 4.2. The former prevents the linkages from deforming away from the axis while latter prevents distortion of the overall platform. We compute the constraint forces and moment of every universal joint of the relay platform, and the results are shown in Figs. 4.11 and 4.12, respectively.

The distribution of the constraint force in three directions of entire relay platform is shown in Fig. 4.11. Results show that the constraint force of the universal joints on the linkages perpendicular to the current flow, i.e., the forces in the e_1 and e_3 directions (see Fig. 4.11a, c), is greater than that on the linkages parallel to the current direction (or e_2 direction). Please note that (Fig. 4.11b) the constraint force in e_2 direction is greater on linkages at upstream and decreases gradually to downstream and virtually vanishes at the end of platform, indicating that the linkages parallel with the flow (i.e., in e_2 direction) at upstream need to be equipped with stronger universal joints to prevent deformation in e_2 direction. On the other hand, the constraint forces on linkages perpendicular to the current in both e_1 and e_3 directions (Fig. 4.11a, c) are generally uniform on the entire platform, while the force in e_1 direction is much smaller than those in e_3 direction, implying that the universal joints on these linkages shall be of anisotropic property. Overall, the universal joints in the upstream area of the platform need to sustain a larger external force, thus requiring higher mechanical specifications. For the universal joints on both sides and downstream of the platform, the specification can be lower because their constrain forces are smaller.

We also examine the constraint moment of the universal joints in order to restrict the torsion of the platform within a limit. Results shown in Fig. 4.12 indicate that the constraint moment of the linkages parallel with the current flow is generally

Fig. 4.12 Distribution of the universal joint constraint moment at the axial direction of linkage (units: MN × m)
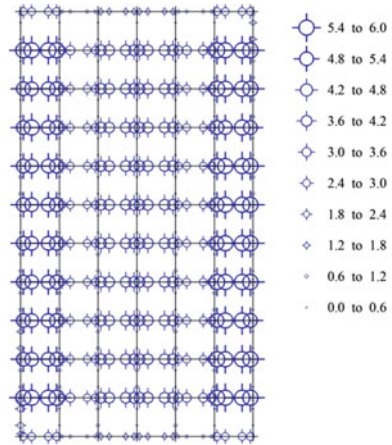
much larger than that of the linkages perpendicular to the current flow. Moreover, universal joints near the upstream and downstream of the platform bear higher constraint moment and thus require higher mechanical specifications. In the central part of the platform, on the other hand, the universal joints bear less constraint moment and thus require lower mechanical specifications.

In summary, universal joints on the linkages on which the turbine is anchored required a higher mechanical specification to withstand a large constraint force in the e_3 direction (see Fig. 4.11c). Universal joints on the linkages running parallel to the current flow need to be able to withstand a greater constraint force and moment and thus a higher mechanical specification is required for these joints (see Figs. 4.11b and 4.12), while those running perpendicular to the current flow but not being anchored with a turbine bear the least force or moment and thus require a lower mechanical specification.

The above analyses offer a detailed map regarding the required mechanical specification of the universal joints of the platform. However, a careful examination of the data may reveal that virtually each joint requires high specification in at least one direction or more. Accordingly, to simplify the design, one may consider that the entire platform uses a single type of high-specification universal joint. Although this will increase the material cost of the platform, it will simplify the design, operations, and maintenance and eventually lower down the overall cost of the power plant construction and operation.

4.3.4 Overall Platform Deformation

We consolidate the displacement of each linkage altogether to illustrate the overall deformation of the relay platform in Fig. 4.13. As shown in the enlarged view of Fig. 4.13a, the displacement of the primary linkage connected to a turbine is much
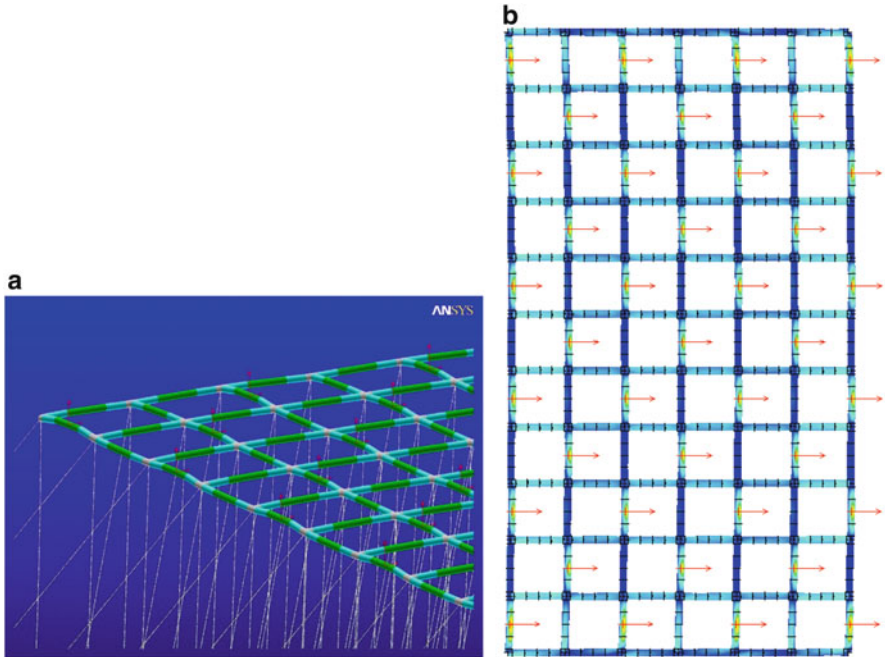
Fig. 4.13 Deformation of the relay platform. (**a**) *Enlarged view* of a corner of the deformed relay platform; (**b**) *top view* of the overall deformation

greater than that of the other linkages, indicating that the turbine-exerted force is the major force causing the platform deformation. Consequently, the deformation of the unit platform anchored with a turbine is greater than that of its adjoining unit platform. It should be noted that the greatest deformation has been restricted within a reasonable range by the constraint moment provided by the universal joint, showing again that the mechanical properties of the universal joint are important to the platform integrity. Aside from the local deformation presented, the top view of the overall platform deformation is illustrated in Fig. 4.13b. It is seen that the middle part of the overall platform is prone to move downstream, which is mainly due to the application by the turbine-exerted forces in this region.

4.3.5 Overall Platform Displacement

The displacement of the platform is the combination of the deformation of platform components and cables. Results shown in Fig. 4.14 illustrate a comparison between the platform without and with displacement, in which the dashed line represents the cables and platform before the Kuroshio action is engaged while the solid line represents the stable position of the cables and platform after the Kuroshio action is
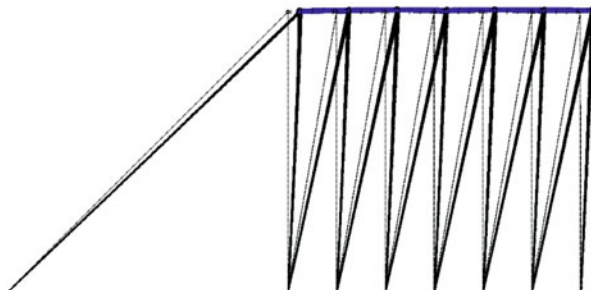
Fig. 4.14 Displacement of the relay platform under the action of Kuroshio. The *dotted line* represents the platform and cable position prior to deformation. For the platform, the horizontal displacement is 17.53 m to the downstream, and the vertical displacement is 2.50 m below the original position

considered. More precisely, the action of the Kuroshio moves the overall platform 17.53 m horizontally to the downstream and 2.50 m vertically below the original position. For an unit platform, the maximum vertical displacement accounted for by the difference between the highest and lowest points of the platform is 4.81 m, and the maximum inclined angle of the platform is 1.87°. Compared with the size of the overall platform, these deformations and displacements are quite small and can be ignored for the purposes of determining the cable and turbine layout.

In summary, results shown in Fig. 4.14 suggest that, first, the constraint force and moment of the universal joint obtained in Sect. 4.3.3 are sufficiently good to restrict the deformation of the platform within a reasonably small range, and second, the cable arrangement in terms of a combination of inclined cables and vertical cables is an effective scheme to keep the platform stay close to the original position under the action of the Kuroshio.

For comparison with the present result, we also study the platform anchored by Type I and II cable arrangements. Results of Type I arrangement show that, although the platform continues to maintain a horizontal attitude under the action of Kuroshio, its position drops vertically by several tens of meters and the vertical cables eventually becoming inclined bearing very small tension, making the function of vertical cables vanished. The results of Type II platform show that the platform becomes slanted with an inclined angle of 20°, a serious result leading to a complete loss of the platform's original design goals and functions. All of these confirm again that the combination of vertical and inclined cables is the best choice for the cable arrangement of the relay platform.

Table 4.7 Maximum and minimum forces (and stresses) applied on the vertical and inclined cables and the anchor at the seabed

| | Steady mean value MN (MPa) | | Transient variation MN (MPa) | |
	Max.	Min.	Max.	Min.
Vertical cable	0.71 (22.8)	0.10 (3.25)	0.89 (28.3)	0.62 (19.8)
Inclined cable	1.78 (56.5)	0.66 (21.0)	1.78 (56.5)	0.66 (21.0)
Seabed force	1.88 (59.8)	0.29 (9.25)	1.89 (60.3)	0.47 (15.0)

4.4 Cable Selection for the Relay Platform

Though steel cables are traditionally and widely used as anchor chains for various type of marine engineering, they are not suited for the Kuroshio power plant due to its weight and propensity for corrosion. On the other hand, new types of cable made of composite and polymer materials that are light in weight and strong in mechanics shall be a good choice for anchoring the relay platform on the seabed often 500 m or more below the surface. Note that for such a depth of seabed, the length of the inclined cable shall be at least 1,000 m or longer.

Table 4.7 presents the aforementioned results regarding the force and stress borne by the vertical cables, the inclined cables, and the anchors at seabed. These results are rearranged from the results such as the one shown in Fig. 4.8, from which one can see that both the variations of the loaded stress of two chosen vertical and inclined cables experience a transient state immediately after the turbines are engaged with the action of Kuroshio, and then reaches to a quasi-steady state, i.e., a periodic change with a steady mean, about 1 h later. After examined the variations of the loaded stress of all the cables of the relay platform, we summarize in Table 4.7 the maximum and minimum of the steady mean stress of all the vertical cables, the horizontal cables, and the anchor at the seabed. Results show that, as also shown in Fig. 4.9, among all the cables of the relay platform, in general, the maximum stress of the inclined cables is more than twice of that of vertical cables, while a bit less than the reaction stress of the anchors at the seabed. The minimum stress of the inclined cables, on the other hand, is more than six times that of vertical cables. As suggested in Sect. 4.3.3, to simplify the design procedure, we suggest to use a single type of cable for the vertical cables and another type for the inclined cables of the entire relay platform, and the maximum stress shown in Table 4.7 be considered as the design specification. Consequently, in general, the strength and the diameter of inclined cables shall be chosen to be larger than those of vertical cables. Note that in calculation of the stress of Table 4.7, the diameter of the cables is chosen to be 10 cm.

However, in reality many other factors in situ might not have been considered in the present analyses; the design of cables shall consider the aforementioned greatest stress and multiply it with a safety factor to ensure the safety and reliability of the cables, thus lowering down the risk possibly occurring during the power plant operation. As discussed in Chap. 3 for the design of the cable anchoring turbine, we choose a safety factor of five which is widely used in the marine engineering.

Accordingly, according to the data of Table 4.7, the maximum stress of the vertical cables is considered to be 0.141 GPa and that of the inclined cables is 0.283 GPa. With these maximum stresses, we may select proper type of cable listed in Table 3.4. Among them, there are three types of cable can be considered. They are nylon 1140 having a tensile strength of 0.85 GPa, PET 1380 having a tensile strength of 1.05 GPa, and PP 910 having a tensile strength of 0.50 GPa. All of them are of a tensile strength much larger than that required to secure the safety and stability of the cables anchoring the relay platform.

4.5 Overview of the Relay Platform Performance

As many experts in ocean engineering mentioned to the author, the most challenging part of the Kuroshio power plant project is the mooring system which serves to anchor tens of turbines securely and stably in the water of hundreds of meter deep, and more seriously the entire power plant is under the action applied by the Kuroshio, a strong ocean current in a huge scale. To tackle this challenging task, we propose to use the relay platform on which the turbine cluster is anchored, and below which hundreds of cables are used to anchor the platform on the seabed hundreds of meters below the surface. The relay platform serves as an artificial seabed floating about 100 m below the surface and is composed of 66 unit platforms. Each unit platform is composed of primary linkages, auxiliary linkages, and cross linkages, and all the linkages are connected with a universal joint. As a result, the relay platform is a flexible marine structure on which tens of turbines are anchored by a single cable of 20 cm in diameter and is made of nylon, PET of PP, as shown in Table 3.4.

Dynamically, the relay platform is under the action of the cyclic force exerted by the turbine above, the pulling force applied by the anchoring cable from below, the buoyancy force generated by the platform, and the thrust applied by the Kuroshio. Within the platform, there are constraint forces and moment built in the universal joint to prevent excessive deformation of platform. As a result, the dynamical behavior of the relay platform is fully nonlinear subject to complicate boundary conditions exerted from the forces above. To tackle this complicate structure dynamics problem, we first analyze the unit platform to determine the constraint forces and moment of the universal joint so that the platform deformation is limited within a reasonable range. Then the test platform composed of six unit platforms is analyzed with six different kinds of turbine cluster formations. The goal of this part of analysis is to determine the type of anchoring cable arrangement. Consequently, a combination of vertical and inclined cables is chosen to be the cable arrangement with which both the deformation and displacement of the test platform are limited to a minimum value, and a turbine cluster formation composed of five turbines anchored on the platform with a form of staggered matrix is considered so that the number of turbine can be the largest.

Finally, the relay platform composed of 66 unit platforms is analyzed, on which 39 turbines are anchored with a form of staggered matrix (as shown in Fig. 2.3) and below which 84 inclined cables and 72 vertical cables are used to moor the platform on the seabed hundreds of meters below the surface. Under the condition that each turbine exerts 1.46 MN force on the relay platform and the velocity of the Kuroshio is 1.4 m/s, the maximum constraint force of the universal joint is 1 MN, the maximum axial constraint moment is 5.81 MN × m, and the overall horizontal and vertical platform displacements are 17.53 m and 2.5 m, respectively. Regarding the forces applied on the platform cables, the maximum and the minimum forces applied on the vertical cables are, respectively, 0.71 MN and 0.10 MN, those on the inclined cables are 1.78 MN and 0.66 MN, and those on the anchors at seabed are 1.88 MN and 0.29 MN, as shown in Table 4.7. To withstand these forces, we choose a cable of 10 cm in diameter and made of either nylon 1140, PET 1380, or PP 910 (check please Table 3.4 for their material properties); all of them are sufficiently strong to serve as the vertical cable or the inclined cables such that the relay platform can be anchored on the seabed securely and stably.

It is confirmed from the present dynamical analyses of the relay platform that the specifications of the platform stated above can sufficiently secure the integrity of the relay platform and the operation of the power plant as well. If, nevertheless, one needs to enhance the stiffness of the platform, for example, one may choose the universal joint of higher constraint force and moment at the cost of the flexibility of the structure. One may also choose a cable of larger diameter so that the security of the mooring system of the relay platform can be ensured furthermore, while the cost of construction shall accordingly increase significantly. We trust that the specifications shown in the present chapter can sufficiently ensure the integrity of the platform and its mooring system, which is the most important part of the design of the Kuroshio power plant.

References

1. Chen F (2010) Kuroshio power plant development plan. Renew Sustain Energy Rev 14:2655–2668. doi:10.1016/j.rser.2010.07.070
2. Kutt LM, Pifko AB, Nardiello JA, Papazian JM (1998) Slow-dynamic finite element simulation of manufacturing processes. Comput Struct 66(1):1–17. doi:10.1016/S0045-7949(97)00069-2
3. Lewis WJ (2003) Tension structures: form and behaviour. Thomas Telford, London
4. De Zoysa APK (1978) Steady-state analysis of undersea cables. Ocean Eng 5(3):209–223. doi:10.1016/0029-8018(78)90038-0
5. Wang CM, Cheong HF, Chucheepsakul S (1993) Static analysis of marine cables via shooting-optimization technique. J Waterw Port Coast Ocean Eng 119:450–457, ASCE
6. Friswell MI (1995) Steady-state analysis of underwater cables. J Waterw Port Coast Ocean Eng 121:98–104
7. Matulea IC, Nastase A, Talmaciu N, Slamnoiu G, Goncalves-Coelho AM (2008) On the equilibrium configuration of mooring and towing cables. Appl Ocean Res 30:81–91. doi:10.1016/j.apor.2008.06.002

8. Kamman JW, Huston RL (1985) Modelling of submerged cable dynamics. Comput Struct 20:623–629. doi:10.1016/0045-7949(85)90110-5
9. Haritos N, He DT (1992) Modelling the response of cable elements in an ocean environment. Finite Elem Anal Des 19:19–32. doi:10.1016/0168-874X(92)90026-9
10. Leonard JW (1988) Tension structure: behavior & analysis. McGraw-Hill, New York
11. Sun FJ, Zhu ZH, LaRosa M (2011) Dynamic modeling of cable towed body using nodal position finite element method. Ocean Eng 38:529–540. doi:10.1016/j.oceaneng.2010.11.016
12. Ablow CM, Schechter S (1983) Numerical simulation of undersea cable dynamics. Ocean Eng 10:443–457. doi:10.1016/0029-8018(83)90046-X
13. Milinazzo F, Wilkie M, Latchman SA (1987) An efficient algorithm for simulating the dynamics of towed cable systems. Ocean Eng 14:513–526. doi:10.1016/0029-8018(87)90004-7
14. Fang MC, Hou CS, Luo JH (2007) On the motions of the underwater remotely operated vehicle with the umbilical cable effect. Ocean Eng 34:1275–1289. doi:10.1016/0029-8018(87)90004-7
15. Wang PH, Fung RF, Lee MJ (1998) Finite element analysis of a three-dimensional underwater cable with time-dependent length. J Sound Vib 209:223–249. doi:10.1006/jsvi.1997.1227
16. Aamo OM, Fossen TI (2000) Finite element modelling of mooring lines. Math Comput Simul 53:415–422. doi:10.1016/S0378-4754(00)00235-4
17. Tsukrov I, Eroshkin O, Paul W, Celikkol B (2005) Numerical modeling of nonlinear elastic components of mooring systems. IEEE J Oceanic Eng 30:37–46. doi:10.1109/JOE.2004.841396
18. Tahar A, Kim MH (2008) Coupled-dynamic analysis of floating structures with polyester mooring lines. Ocean Eng 35:1676–1685. doi:10.1016/j.oceaneng.2008.09.004
19. Morison JR, O'brien MP, Johnson JW, Schaaf SA (1950) The force exerted by surface waves on piles. Pet Trans 189:149–154. doi:10.2118/950149-G, AIME
20. Bath KJ (1996) Finite element procedures. Prentice Hall, New Jersey
21. ANSYS@Theory reference for the mechanical APDL and mechanical applications, release 12.1, Help System. ANSYS Inc.

Chapter 5
Assessment of Environmental and Ecological Impacts

The installation of Kuroshio power plant entails the sudden appearance of hundreds of 50 m-wide power generating turbines anchored to relay platforms covering an area measured in square kilometers which, in turn, are anchored to the seabed by hundreds of cables, each several hundred meters in length. These installations are sure to have considerable anticipated and unanticipated impacts on local hydrological, ecological, and environmental conditions. On the other hand, natural disasters and climate changes may cause operational difficulties or damage the ability of the power plant to provide a steady source of power. These two types of impact, the impacts from and on the power plant, can be broken down into four categories (1) the impact of power plant operation on the Kuroshio motion, (2) the environmental impact due to power plant construction and operation, (3) the ecological impact due to power plant construction and operation, and (4) the impact of natural disasters and climate changes on power plant operation. All these issues must be carefully evaluated before construction is commenced, and will be discussed in details in this chapter.

5.1 Impacts of Power Plant Operation on the Kuroshio Motion

The turbines are deployed in the Kuroshio to convert current's linear momentum into angular momentum to drive the generators. This power conversion could slow down the current's motion; it then could have an impact on the circulation of the North Pacific Gyre, thereby affecting the ocean's ability to regulate the Earth's climate and potentially causing irreparable environmental and ecological damages. This issue needs to be carefully and thoroughly investigated to ensure that no such damage could have ever occurred. We begin this exploration with using control volume analysis to investigate the basic conditions required to maintain the Kuroshio's linear momentum. The simulation results derived from Chao's
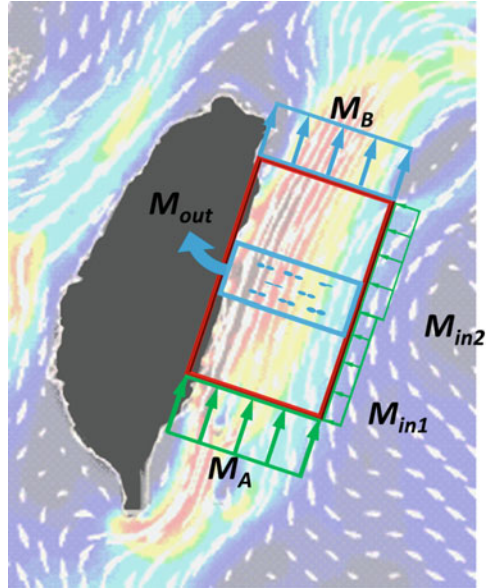
(Exploring Kuroshio's energetic cores with an ocean nowcast/forecast system. Private communication, University of Maryland, 2008) global ocean computations are used to explain the turbines' impact on the Kuroshio's flow so that principles for turbine distribution in the Kuroshio can be proposed.

5.1.1   Conditions for Maintaining Kuroshio's Momentum

Figure 5.1 illustrates a control volume for the Kuroshio momentum. The control volume is set in the sea off Taiwan's east coast, with Taiwan on the left and no flow crossing this border. Assuming that a momentum M_A is for the northward flow entering the control volume from below, a momentum M_B is for the northward flow leaving the control volume at above and the momentum loss due to the turbines is M_{out}. The momentum loss should be amended by the flow coming from the Pacific Ocean on the right. Given this inflow momentum from Pacific at upstream of the turbine to be M_{in1} and at downstream to be M_{in2}, the balanced relationship of these five momentums can be expressed as:

$$M_A + M_{in1} + M_{in2} = M_B + M_{out} \tag{5.1}$$

To ensure that the linear momentum of the Kuroshio is preserved after passing through the control volume, one shall have $M_A = M_B$, and this can be done only with the condition $M_{out} = M_{in1} + M_{in2}$ holds. The two Pacific inflows to the control volume are generated due to the geostrophic balance relation of the Kuroshio.

As explained in Chap. 1, the Kuroshio is primarily driven by the shear stress from atmospheric circulation. As passing along the east coast of Taiwan, the Kuroshio is pushed to the right due to Coriolis force generated by Earth spinning. As a result, taking the mainland Taiwan as a wall to restrict the Kuroshio to move to the left, the sea level on the right hand side of the Kuroshio increases, which in turn generates a hydrostatic pressure pushing the Pacific water to enter the Kuroshio. This balance among the Kuroshio's linear momentum, the Coriolis force, and the hydrostatic pressure ensures the steady motion of the Kuroshio at east Taiwan. On the other hand, nevertheless, disturbing one of these three balanced forces would cause changes in the other two. For example, the appearance of the turbine cluster in the Kuroshio consumes the linear momentum of the Kuroshio, which in turn drives the inflows from Pacific into Kuroshio by hydrostatic pressure to form the momentum of the two inflow momentums M_{in1} and M_{in2} such that the balance of $M_{out} = M_{in1} + M_{in2}$ may hold still. Please note that, without the presence of mainland Taiwan on the left of the Kuroshio, the inflow moments will not sustain and the Kuroshio momentum may dissipate through turbine's interaction.

To check the momentum balance of Fig. 5.1, Chao (Exploring Kuroshio's energetic cores with an ocean nowcast/forecast system. Private communication, University of Maryland, 2008) uses the surface data of sea level, temperature, and salinity of the water surrounding the Kuroshio of November 4, 2008 and employ the global ocean simulation code to compute the ocean motion at east Taiwan. Results shown in Fig. 5.2 indicated that the surface level gradually increases towards the east to its highest point at 125°E, 22.5°N, as shown in Fig. 5.2a, and the velocity vector diagram (Fig. 5.2b) shows that the highest elevation locates exactly at the center of the large eddy in the Pacific. The rotation of this eddy is obviously driven by the Kuroshio, and the Coriolis effect generated by the Kuroshio's flow elevates the sea level around the eddy, and this difference in sea level between the eddy and the Kuroshio generates the hydrostatic pressure to balance the Coriolis force generated by Earth spinning (Fig. 5.2c).

From the above discussion, we can derive the following conclusions: To ensure the appearance of turbines does not impact the Kuroshio's flow conditions, the location and the number density of the turbine installation must be carefully designed to ensure that there are sufficient seawater inflow into the Kuroshio from the Pacific Ocean to compensate for the current momentum lost to the turbines. Once this principle of maintaining the Kuroshio's momentum is securely established, we can consider using a staggered matrix formation to install turbine cluster so that the number of turbine can be maximized and the performance of downstream turbines is not compromised by wakes generated by upstream turbines [1, 2].

Although the conditions for maintaining the Kuroshio flow are simply straight forward, in practice such ideal conditions must be carefully benchmarked on the basis of field test data. But, however, the in situ test is expensive and dangerous, we therefore suggest that, prior to the actual installation of turbines at sea, Chao's global ocean computation code (Exploring Kuroshio's energetic cores with an ocean nowcast/forecast system. Private communication, University of Maryland,
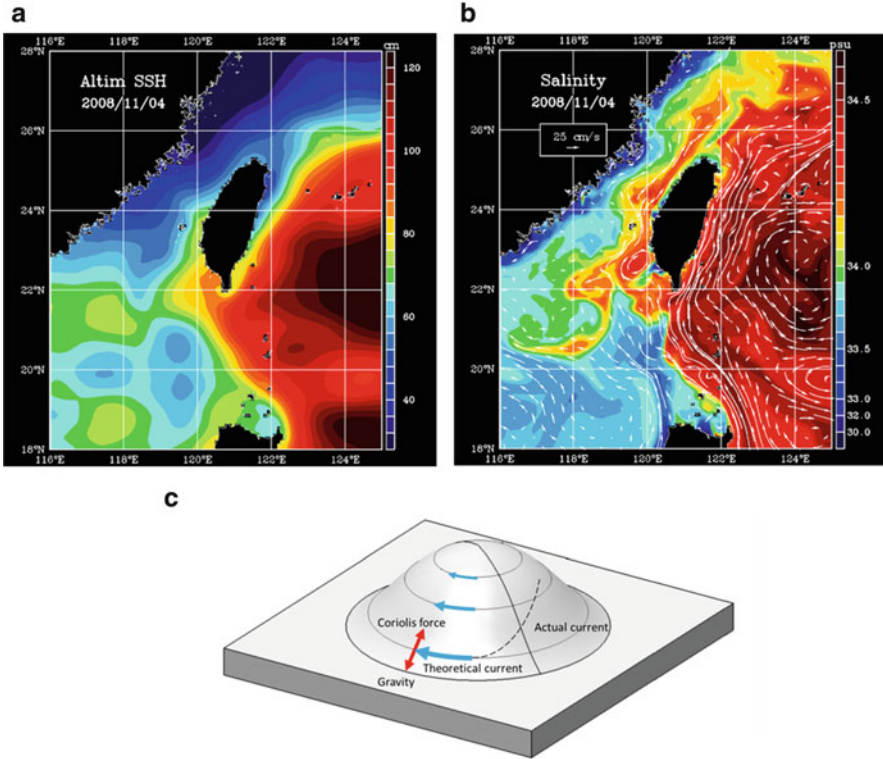
Fig. 5.2 Examples to explain the geostropic nature of the Kuroshio at east Taiwan. (**a**) Sea level distribution of the Kuroshio waters at east Taiwan. (**b**) Velocity vectors of the ocean flow and salinity distribution of the Kuroshio waters at east Taiwan (Courtesy of Professor Shenn-Yu Chao [Exploring Kuroshio's energetic cores with an ocean nowcast/forecast system. Private communication, University of Maryland, 2008]). (**c**) Schematics of the balance sustained among the flow momentum, the Coriolis force, and the hydrostatic pressure due to sea level difference

2008) shall be used to implement computational experiments, such as the cases shown in Sects. 5.1–5.3 and the two representative experiments to be illustrated in the following two sections.

5.1.2 Case 1: The Impact of a Spanwise-Deployed Turbine Cluster

Chao (Exploring Kuroshio's energetic cores with an ocean nowcast/forecast system. Private communication, University of Maryland, 2008) placed a 60 MW turbine cluster between Lu-Dao and Tai-Dong, which is simulated by a series of
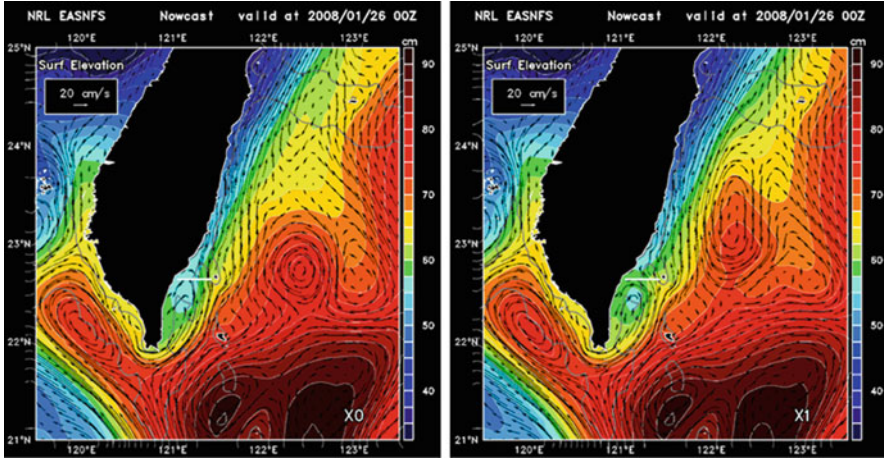
Fig. 5.3 Influence of the 60 MW turbine cluster deployed in the spanwise direction of the Kuroshio between Taiwan and Lu-Dao. The image on the *left* figure shows the flow velocity and sea level distribution without turbine, while the *right* figure shows those with turbines deployed along the white line. The *color* gradation indicates sea elevations, while the *arrows* indicate the flow velocity and direction (Courtesy of Professor Shenn-Yu Chao [Exploring Kuroshio's energetic cores with an ocean nowcast/forecast system. Private communication, University of Maryland, 2008])

momentum sink uniformly distributed in the spanwise direction of the Kuroshio, as shown by the white line of Fig. 5.3. Note that, in Fig. 5.3, the results of the left figure are for the case without turbine cluster while those of the right figure are for the case incorporating the 60 MW turbine cluster. Computations were conducted over a 5-month period from January 1, 2008, with initial conditions taken from real-time forecasting data for the same period in the Western Pacific. Figure 5.3 shows the results averaged over 5 months, with colors representing sea elevation (cm) and the length of the black arrows indicating the speed of the current.

When performing the computations, Chao distributed the turbines along the white line at a depth of 50 m to feed off the Kuroshio's energy, evenly dispersing a loss of 60 MW of energy along the white line. The 60 MW power is accounted for by 300 turbines each generating 0.2 MW of electricity. The turbines have a cut-in speed of 0.5 m/s and a nominal flow speed of 1.2 m/s (i.e., the flow speed required to produce 0.2 MW of electricity per turbine). Note that, due to unsteadiness of the Kuroshio, power output cannot always be maintained at 60 MW.

The computational results show that, without the turbine cluster (left figure), a clockwise vortex forms at the eastern edge of the Kuroshio at 122.2°E, 22.8°N. Adding the 60 MW turbine cluster (right figure) causes this vortex to move northwest, compressing the current and increasing the Kuroshio's flow rate north of the white line. These results indicate that the Kuroshio and its adjacent waters are

affected by the presence of turbines. However, carefully comparing these two flow velocity vectors reveals that the presence of turbines of this case does not reduce the Kuroshio momentum. Rather, the closing of the distance between the vortex on the right and Taiwan causes a compression of the Kuroshio, which in turn slightly accelerates the Kuroshio's flow speed. This result confirms the control volume scenario of the previous section that the waters of the Kuroshio are fed by two sources, one from the south and one from the east, and the added momentum from the Pacific will compensate for momentum lost to the turbines.

5.1.3 Case 2: The Impact of a Streamwise-Deployed Turbine Cluster

In this case, Chao (Exploring Kuroshio's energetic cores with an ocean nowcast/ forecast system. Private communication, University of Maryland, 2008) installed five turbine clusters along the Kuroshio Front, the band of greatest flow velocity. These installations each produced 100 MW, for a total installed capacity of 500 MW, and the location of each cluster is represented by an X in Fig. 5.4. Computations were run over 12 months beginning in January 2012, using data taken from the above-mentioned satellite of weather forecasting system. The figure on the left shows the results without the turbines, and shows a large eddy on the right with surface elevations more than 40 cm higher than that of the Kuroshio. The figure on the right shows the flow with five turbine clusters being placed, implying that the presence of 500 MW turbines has no apparent impact on either the eddy or the flow rate of the Kuroshio, thus fulfilling the key requirement of turbine installation mentioned above. In addition to the minimal impact on the Kuroshio flow, the placement of these turbine clusters relatively close to land means they can be anchored with shorter cables, thus simplifying construction and maintenance and lowering down the cost in general.

Figure 5.5 shows the changes over time for the energy absorbed by the five turbine clusters in Chao's example (Exploring Kuroshio's energetic cores with an ocean nowcast/forecast system. Private communication, University of Maryland, 2008), with results showing that the average extracted energy is 414 MW, with an variation amplitude of 90.2 MW. Assuming turbine efficiency to be 33 %, the total average power generation reaches about 138 ± 30 MW. Figure 5.5 illustrates an interesting phenomenon: at the outset of winter (November), turbine energy absorption can reach about 500 MW, with absorption levels remaining above average between January and June. However, in summer and autumn, this energy changes several times, dropping to about 100 MW on several occasions. This phenomenon does not correspond to that illustrated in Chap. 1, where the Kuroshio's energy peaks in spring and summer before weakening in winter. Chao's proposed explanation hold that this change in power output is caused by the Kuroshio's Front sweeping past the turbine clusters, and not by the seasonal change of the Kuroshio
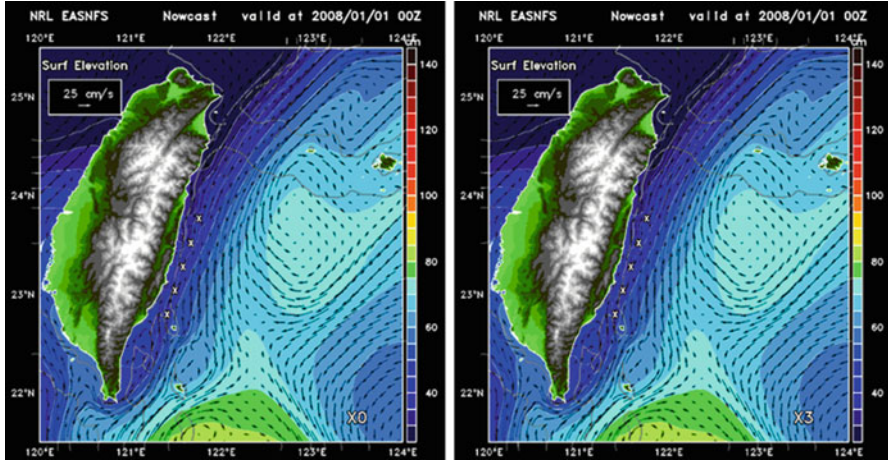
Fig. 5.4 Influence of the 500 MW turbine clusters deployed along the streamwise direction of the Kuroshio at east Taiwan. The *left* and *right* figures, respectively, show the flow field without and with turbine clusters. The turbines are separated into five clusters, each is of 100 MW and denoted by a *white X*. The *color* gradation indicates sea level, showing that the sea level of Pacific at east is in average 40 cm higher than that of the Kuroshio at west (Courtesy of Professor Shenn-Yu Chao [Exploring Kuroshio's energetic cores with an ocean nowcast/forecast system. Private communication, University of Maryland, 2008])
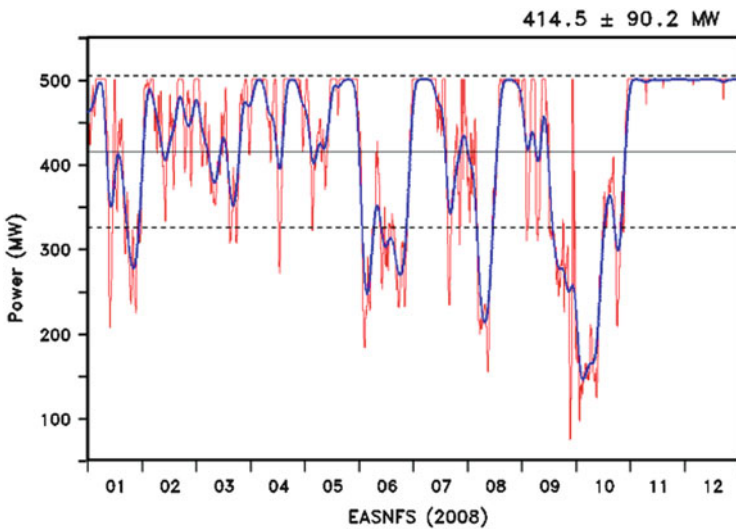
Fig. 5.5 The variation of the power output of the above-mentioned 500 MW turbine clusters in 2008. The *red line* shows instantaneous change, while the *blue line* shows a 5-day moving average (Courtesy of Professor Shenn-Yu Chao [Exploring Kuroshio's energetic cores with an ocean nowcast/forecast system. Private communication, University of Maryland, 2008])

itself. In other words, this distribution and placement of turbines are closely related to the stability of the Kuroshio's frontal moving lines. Therefore, to properly place the Kuroshio power plants, one must not only consider the quality of the Kuroshio's velocity but also its stability.

However, how much energy can be developed in the Kuroshio basin without impacting the normal circulation of the North Pacific or the local marine environment and ecology? Answering this question requires detailed computer simulations with long-term monitoring of the selected site to form an overall assessment. Generally speaking, the degree of impact generated by extracting energy from the Kuroshio is related to the following natural or human factors (1) the type of turbine used, (2) the density of turbine distribution, (3) characteristics of surrounding flow, seabed terrain, and geology, and (4) other factors such as measures for environmental protection, fishery rights, national defense, and international intervention. On the understanding that the Kuroshio's driving force will promptly compensate for the extracted force, the initial assessment should consider the development of 10 GW of installed capacity off Taiwan's east coast. Nevertheless, accurate investigation and simulation of the Kuroshio along with a careful selection of the development site should allow for the potential development of 30 GW of installed capacity [3]. Note that Taiwan's current total installed electrical generation capacity is 43 GW, implying that the development of the Kuroshio power plants can be of significant impact on Taiwan's energy policy.

Although the flow characteristics of the Kuroshio near Taiwan are known through many initial computations and test results, during the development of site selection and plant operations, on-site computations, measurements, and analysis shall be conducted on a continuous basis. This can be accomplished using global nautical analysis software with timely satellite data, thus providing a complete and timely analysis of overall flow changes in the Kuroshio. To meet the actual operating needs of the power plants, forecasting capabilities should be established to offer predictions at least 3 days in advance. Overall computations and regular measurements are a necessary part of selecting the development site, and are core technologies which must not be neglected after operations begin.

5.2 Environmental Impacts of Power Plant Construction

It was described in Sect. 2.3 the extensive range of large-scale equipment and rigs required for the construction of the Kuroshio power plant, along with the hundreds of anchors and cables required to fix the installations in place. In particular, the construction of the turbines and relay platforms is a long-term, large-scale, highly complex construction project. Once construction is complete, the operation of the power plants is subject to an even greater array of known and unknown influential factors. All of these may have a significant impact on environmental and ecological conditions in the Kuroshio waters.

The ecological investigation presented in Chap. 1 indicates that the Kuroshio water ecosystem includes a wide range of native and migratory species which breed in the area. The environmental impact of the installation of Kuroshio power plants can be classified as short-term, medium-term, and long-term effects, each with different impact levels and causes. This chapter discusses the impact of power plant construction and operation in terms of these three time frames, noting that there are three types of potential environmental impacts: (1) the construction of new harbor facilities may impact the coastal environment, (2) the power plant anchorages may impact the seabed environment, and (3) the floating power plants may impact the seaborne environment through various kind of pollution. In the following, detailed discussions on above factors are made, and results may serve as a point of reference for the enactment of relevant legislation and regulations for the power plant construction.

5.2.1   Impact on the Coastal

Constructing the Kuroshio power plant will require temporary and permanent harbor facilities for the assembly, storage, and loading of the turbine and relay platform components. Among eastern Taiwan's current harbors, only Hua-Lien Harbor and Su-Au Harbor are of a relatively large scale, but still offer insufficient space and inadequate facilities for the construction of the Kuroshio power plants. As will be noted in Chap. 6, the optimal installation site is in the seas between Tai-Dong and Lu-Dao, an area not served by any large-scale port, thus it's clear that new harbor facilities and piers may need to be built and land reclaimed.

Port facilities commonly use breakwaters or gravel embankments, which will change local geological and geomorphological conditions and cause siltation which, if not carefully planned, can render the facilities unusable for the long term. At the same time, the construction of large breakwaters on sandy shores can result in large-scale erosion, which will significantly increase the turbidity of local water and interfere with local sediment conditions, thus indirectly causing significant changes to the local topography. These changes can have a significant impact on nearby benthic organisms, coastal fish, and crustaceans, such as crabs living in sandy areas which will migrate or disappear given loss of their habitat. Breakwaters can also kill coral reef formations: dumping large blocks stirs up sediments, covering local habitats and increasing local turbidity, while considerable quantities of dust will be washed downstream from the construction area, thus increasing local turbidity conditions out at sea.

Both new harbor construction and pier expansion will require coastal engineering including various kinds of harbors, coastal highways, breakwaters, tidal barriers, and land reclamation which will have varying degrees of impact on coastal and marine ecosystems. Therefore, an in-depth investigation of coastal environment conditions is needed prior to any development. During construction, constant attention must be paid to minimize changes in local ecological conditions, and the

area must be restored after construction is completed. An overall assessment must be made of all possible construction-related damage, and a plan must be prepared for post-construction restoration before construction commences.

In addition, the above-mentioned coastal construction may also cause coastal habitat loss or degradation, resulting in population depletion or even the destruction of certain species. For example, seawalls and breakwaters in Kin-Men, an island belonging to Taiwan located at south-eastern China, were built along the high tide line destroying the breeding grounds of local horseshoe crabs. In another example, the Peng-Hu branch of the National Ocean Species Repository was constructed on a natural intertidal reef, causing the destruction of fry, octopus, snail, shellfish populations along with local seaweeds.

There are two main causes of habitat destruction. The first is land reclamation or breakwater construction, covering natural coastlines in cement and damaging biological growth of coastal habitats (reefs, sandy shorelines, and wetland). Second, the construction of jetties interrupts the movement of sediment, causing silting upstream of the jetty and erosion downstream. This unbalanced sediment load changes the feeding conditions for benthic species, while also changing the composition of their habitats.

The above-mentioned disruptions of habitat quality or survival conditions are primarily caused by the construction of seawalls and tidal barriers, which block the hydrological cycle of coastal wetlands and reduce tidal water level fluctuations, while changing seawater in- and outflows and salinity levels, thus gradually compromising the functions of wetlands ecosystems. Construction can also result in the concentration of suspended solids, noise, and vibration, which can interfere with the respiration, feeding, and breeding behavior of marine organisms, especially fixed or poorly mobile organisms. This phenomenon is already visible in the waterfowl conservation area in I-Lan's Wu-Wei Harbor, in the reservoirs of Hsin-Chu's South Harbor, in Taipei's Guan-Du Nature Park, and in coastal wetlands all around Taiwan.

On the other hand, the Kuroshio power plants will produce electricity which is transmitted to the coast via transmission cables. Studies have shown that the magnetic field formed by the transmission cable may slightly alter the geomagnetic characteristics of the surrounding rock, which can impact the direction or delay the timing of the migration of fish. However, currently, there is no clear evidence to indicate that the submarine cable's magnetic field will have a significant impact on benthic or migratory fish [4, 5], but this may simply indicate insufficient research. Thus, it is important to continuously monitor relevant data upon project completion to provide a reference for future construction.

Finally, we must mention the potential impact on the many government-recognized culturally sensitive sites on Taiwan's east coast. Prehistoric cultures—including Nagahama Culture, Jomon Pottery Culture, Kirin Culture and Jingpu Culture—have been identified in five sites, with another 21 sites to be developed. At the same time, there are ten protected fisheries where all extraction of aquatic plants and animals is prohibited in a 500 m band extending out from the mean high tide line. These restrictions have not only contributed to the restoration of coral reefs but

have also lured back large groups of migratory reef fish, and protected loggerhead turtles have been seen coming ashore. If the Kuroshio power plants are installed in this area, a strict environmental impact assessment would have be required to guarantee the design and construction are in line with the relevant laws and regulations to ensure the sustainable development and operation of the power plants.

Based on the above discussion, we propose the following conclusions: Poorly designed marine engineering will result in an increased adverse environmental impact while also increasing future maintenance and management costs, such as the dredging of silted harbors, and the storage and disposal of silt. At the same time, additional investments must be made to prevent the collapse of the foundations of coastal highways through the increased installation of breakwaters. New harbors and embankments will severely disrupt sediment flows, resulting in coastal erosion and soil loss. This significant ecological impact will significantly interfere with coastal flow conditions and sediment transport while decreasing sediment stability and water quality, reducing biodiversity and causing potentially irreversible soil loss in coastal areas [6].

5.2.2   Impact on the Seabed

The seabed refers to the areas of extremely steep slopes at the sea floor, most produced by multiple geological processes and reactions of the oceanic plates, including sedimentation and plate tectonics, and occasionally underwater volcanoes. On the east coast of Taiwan, the most famous such feature is a series of small undersea volcanic hills off of Gui-Shan Island, which are characterized by a unique ecology. In addition, some undersea areas feature seabed hot springs which form their own special ecosystems with sulfur as the main metabolic element. Bacteria thrive in these environments, along with tubeworms and crabs which feed on the bacteria. Benthic organisms (e.g., crustaceans, mollusks, benthic fish, and some sessile organisms such as ascidians and sponges) are found in tide pools, close to shore, and on the continental shelf and slope. Most fishery resources, including more valuable lobsters and groupers, are also concentrated along the coastal continental shelf. The continental shelf harbors a biological habitat vulnerable to the impact of fishing, including bottom trawling, which can permanently damage benthic habitats. Marine debris isn't necessarily destructive and may, in cases, provide an improved shelter in the form of artificial reefs.

Figure 2.4 shows the Kuroshio power plant's relay platform anchored to the seabed by hundreds of cables. Each anchor needs to be drilled, piled, and grouted, processes that may destroy seabed sediment and rock. However, Chap. 4 notes that the seabed anchor points are separated by a distance of approximately 70 m, resulting in a relatively low density of anchorage, thus ensuring the damage can be rapidly restored. Upon completion, hundreds of seabed anchors will be installed on the seabed, connected to a double-number of cables, and this large-scale

introduction of foreign objects may produce a significant impact on local seabed ecology. In addition, the construction and operation of Kuroshio power plants may result in the loss of large-scale equipment and rigs on the seabed. Such objects are usually made mostly of steel and, if it cannot be recovered, would form an artificial reef with an impact on benthic habitats. In general, artificial reefs are made to simulate natural reefs, changing the surrounding seabed and currents, boosting marine biodiversity and biomass to restore or extend existing fishing grounds or seed new fishing grounds.

The waters off of western Taiwan feature many artificial reef installations including several decommissioned warships. Warship reef projects are governed according to certain criteria including full appearance, barrier-free, and zero pollution. Certain components are completely removed prior to sinking the ship, including on-deck towing winches, anchors, booms, lifeboats and their fixtures, and gun mounts. The interior is cleaned of rubbish, instrument panels, machine oil and grease, asbestos bulkheads, and other potential pollutants, and the hull is thoroughly cleaned to prevent contamination of the marine ecological environment. A year-long survey of the entire warship reef zone found over 7 phyla, 11 families, and 14 genus of organisms, including mollusca, arthropoda, echinodermata, annelid, protochordata, ectopora, and proifera. In addition, over 18 families and 28 genus of fish of different sizes were found, suggesting good potential for the development of sport fishing and diving.

The Kuroshio basin has depths reaching into thousands of meters and, unlike the above-mentioned warships, objects sinking from the Kuroshio power plants would not be dropped specifically for the purposes of creating artificial reefs. Thus, careful ongoing observation would be required to determine whether these objects do, in fact, create artificial reefs. However, the large-scale structures of the power plants, suspended at a depth of several tens of meters, may attract concentrations of plankton, thus creating a form of aquatic habitat, providing aquatic life with a place for breeding, feeding, migration, and predator evasion. In addition, given the distribution of thousands of anchors and cables across the seabed may result in the development of alternative habitats for deep sea dwellers.

5.2.3   Impact on the Water: Material Contamination

Most coastal engineering involves the use of concrete, with seawalls and breakwaters forming a smooth, nonporous structure which changes little over time, leaving snails, crabs, sea urchins, and other animals no place to hide from predators, thus reducing overall biodiversity. At the same time, concrete has a high endothermic coefficient, especially when applied in large-scale seawalls. In summer, this raises the temperature of adjacent waters, resulting in thermal pollution. Marine organisms have a low tolerance for sudden temperature increases, and such high temperatures can result in malformations or death.

However, on the other hand, the porous surface of concrete provides cover for crustaceans and polychaetes, making it suitable for artificial and algal reefs. The interior of lightweight, porous concrete features continuous pores and is highly permeable, making it useful for balancing local ecological environments, but its low strength and light weight requires careful engineering design. Interstitial biofouling between the matrices can provide fry or other marine animals with places to hide and rest, but the number of pores must be limited to inhibit the overproduction of algae-eating animals, such as sea urchins [7].

The construction of Kuroshio power plants is unlikely to use concrete outside of the caissons for the seabed anchoring system. However, power plant construction could still cause significant and complex damage to the seabed environment, and thus should not be included in the selection range. The Kuroshio power plant primarily consists of three elements: the turbines, the relay platform, and the cables. Aside from the metal turbine blades and structural supports, the rest of the structure is built from composite materials which have a very small chance of causing seaborne pollution. Similar to the turbines, the links connecting the relay platform components are made of metal or composite materials. Two possible contamination sources are the lubricant leaking from the bearings or universal joint, but the design should specify the long-term stability of the seals for these two components, which should prevent such leakage from occurring. In addition, given the potential for corrosion and biofouling, all coatings used must be environmental grade to avoid releasing toxins into the water. Finally, the cables will be made of a light, tough polyethylene material that does not pose potential contamination issues.

5.2.4 Impact on the Water: Chemical Contamination

Marine chemical pollution can result from heavy metals, oil, toxins, and environmental hormones from river runoff, boats, or underwater equipment and drilling platforms. Heavy metal pollution is mainly caused by the introduction of copper, silver, mercury, or other toxic elements into otherwise clean water. For example, the chain plating industry creates large volumes of wastewater contaminated with heavy metals, and silver contamination primarily comes from the production of $AgNO_3$ by the photographic negative industry (though modern digital cameras produce virtually no silver contamination). Mercury has many uses, but mercury contamination is less of a problem these days. Oil pollution is an almost daily occurrence in the oceans, with marine oil spills occurring from ship-board mixing plate and crane operations, or from damaged oil tankers.

Most sources of large-scale toxic contamination are related to stranded ships or human-applied pesticides. Taiwan has experienced ship-borne toxic leaks in the past, including leaks of toluene in 2005 and ethyl acetate in 2006. Pesticide contamination is not only toxic to fish but also results from the use of antifouling paint on ship hulls. In addition, environmental hormones refer to the release into the environment of molecules having a hormonal effect. Sources include pesticides,

plasticizers, dioxins, and metals, and can damage the immune, nervous, and endocrine systems. In the past, antifouling paint included tributyltin (TBT), which included environmental hormones which can damage the internal navigation system of cetaceans, causing them to beach.

The most serious source of chemical contamination may be oil from the wrecks of large ships or tankers, leading to the large-scale and long-term destruction of the ocean and coastal environments. For example, in March 1989, the U.S. Exxon Valdez oil tanker ran aground off of Anchorage, Alaska [7], while in September 2002, the Prestige sunk off the coast of Spain [8], both causing extreme damage to the local environment which have yet to completely recover. Instances of large-scale pollution have also occurred in the waters around Taiwan. In February 1977, the Kuwaiti tanker Borag, carrying 32,000 metric tons of crude oil, ran aground off the northern coast of Taiwan, spilling at least 15,000 tons of crude and contaminating the entire north coast. Data from an ecological and environmental investigation provided by north Taiwan's nuclear power plant indicated that the spill cost local fisheries substantial losses of over USD32m [9]. In January 2001, a Greek-registered cargo vessel—the Argos—ran aground in southern Taiwan, spilling about 1,100 metric tons of fuel oil, contaminating an area measuring 20 ha and causing serious damage to the local marine ecology and biological resources [10]. In addition, the back-to-back wrecks of the Sam-Ho Brother and Dewi Bunyu in 2005 and 2006 spilled vast amounts of chemicals and fuel oil into the waters off Taiwan, causing irreparable harm [11].

The Kuroshio power plants may prove to be a source of pollution, most likely due to a leakage of the lubricant used in the universal joints. Lubricants do not easily dissolve in water, and may accumulate on the seabed where they can persist for up to 5 years, causing extensive damage to local ecosystems [12, 13]. To reduce the potential for environmental damage, the lubricants used must be durable but biodegradable, such as Fuch Titan GT1 biodegradable oil [12]. In addition, the rust-proofing or anti-biofouling coatings of the turbine bodies and relay platform floats may cause toxic discharge into the environment, but this can be avoided through redesign following stringent antipollution requirements. If occasional toxic discharges do occur, the amounts involved will be too small to cause damage. Finally, engineering processes must be designed to minimize or entirely avoid chemical pollution caused by dust or paint from the construction process.

In conclusion, the construction process must consider and prevent many types of chemical pollution on land and sea, including heavy metals and oils. Long-term monitoring will be required to guard against contamination from the anticorrosion coatings of vessels and the generators and from lubricant leaks. The following table lists the characteristics and durability of several anti-biofouling paints [14–17]. Regardless of whether these paints are cytotoxic or not, the selected materials must be free of organotins and be in wide use worldwide. The inherent difficulty of maintaining the turbines beneath the surface also puts a premium on the durability of these materials. If the generators can support it without losing too much efficiency, an electrical antifouling system would be ideal but cost considerations may result in a biological cytotoxic solution being more practical. Irgarol 1051 is

Table 5.1 Characteristics of various products for antifouling coatings [14–17]

Product ID/coating type	Effect	Target organism	Features	Durability
Irgarol 1051	Biological poison	Algae	Durable	1–3 years
Diuron	Biological poison	Algae	Durable	5 years
Chugoku Sea Grandprix 500	Biological poison	–	Extensively used in deep-sea vessels	3 years
Jotun Sea Quantum	Biological poison	–	Contains copper hydrolysis paint	5 years
Sigma Alphagen	Biological poison		Contains copper hydrolysis paint	5 years
Electrical Anti-fouling System	Current used to prevent biofouling	None	Used on large cargo vessels, minimal environmental impact	61 months[a]
Silicon fouling-release coating	Reduces biofouling	None	Easy to clean, rarely needs to be reapplied	At least 2 years[b]

[a]Actual vessel data
[b]Data taken from a hull rinsed after 2 years of use

currently one of the most widely used coatings, but its limited durability potentially makes it less suitable for use for the Kuroshio power plants. In addition, while a copper coating is durable, high concentrations of copper are harmful to biological organisms; thus, the use of any coating containing copper must ensure not to increase the background copper concentrations in the Kuroshio (Table 5.1).

5.2.5 Impact on the Ocean: Noise Pollution

"Noise" refers to sounds that are either unfamiliar or unpleasant to marine animals, or which exceed a certain frequency, causing changes in their behavior or physiological state. In the ocean, noise sources can be generated by wave and wind action, seismic activity, or human and animal activity. These noises are referred to as "background noise," and are primarily caused by bubbles resulting from the action of wind on the water. In tropical waters, some background noise is caused by the activity of biological organisms, such as shrimp which use sound to stun their prey and warn off predators, or by the rapid movements of mammals while swimming or feeding. Generally speaking, the frequency of these sounds can exceed 100 kHz. An additional source of background ocean noise is sound waves used by cetaceans for communication, courtship, navigation, and to locate food and obstructions.

Over the past few centuries, increased human activity on the seas has also contributed to background noise. The main sources of anthropogenic noise in

coastal areas include recreational activities, coastal construction, shipping, and industrial activity. Offshore man-made noise comes mostly from ship propulsion systems and turbines, along with sound generated from waves slapping against the hulls of fishing boats, cargo vessels, military ships, submarines, and research vessels. Regardless of source, anthropogenic noise has an impact on other organisms. For example, the activity of fishing boats and whale watch boats can drive dolphins and other cetaceans away from their habitats near ports or otherwise change their behavior to avoid the sound. In addition, some migratory fish have been found to change their movement and group behavior to avoid sources of industrial noise, including forming denser schools and reducing their foraging. Noise pollution poses a threat to various biological organisms, not only changing the ways in which they interact but also disrupting their ability to procreate. Because sound can travel ten times faster in water than in air, the effects of noise pollution at sea are vastly magnified.

Many studies of ocean noise have pointed out that commercial shipping, seismic activity, sonar applications, marine engineering, dredging, and offshore drilling generate significant noise pollution which poses a threat to marine life [18–22]. These studies show a link between noise pollution and behavioral change in many marine animals, with many examples of animals abandoning their preferred habitats, and changing their feeding and diving habits. Other effects include changes to the form, volume, and rhythm of their own sounds, causing miscommunication and confusion which can result in mass beachings and collisions with ships. Many fish and marine mammals rely on sound for navigation, foraging, breeding, and communication. This reliance on sound is particularly acute among whales and dolphins: without external interference sound waves generated by whales can travel over 280 km, but external noise can reduce this range to below 90 km. Given background noise at 120 dB, the range is further reduced to less than 20 km, seriously affecting animal judgment and behavior [6]. Noise pollution at sea can also impact the fertility of marine animals and cause structural damage to fish to the point of rupturing fish maws. In marine mammals, it can cause deafness, loss of fertility, or even death.

In addition to marine animals, cephalopods and other marine animals are also vulnerable to the effects of noise pollution. Studies have found that sound can harm cephalopods in two ways: through the direct impact of sound waves and through partial damage to their internal balancing mechanisms. This can damage the animal's sense of direction which, in the case of giant squid, could lead it to be unable to distinguish up from down, leaving it vulnerable to extreme temperature change at varying depths which could prove fatal [19]. In recent years, noise pollution at sea has also resulted in numerous instances of dolphin strandings at different scales, including eastern Florida in 1998, and the Canary Islands in the late 1980s and again in September 2002 [18]. Noise problems are quite serious and should be carefully considered in the development of any marine facilities.

Construction of the Kuroshio power plant presents two key potential sources of noise: mechanical noise from the activities of ships and the construction platform and from seabed piling and anchor engineering. Both sources produce

low-frequency, high-decibel noise which could have a considerable impact on local marine life habitats and must therefore be carefully evaluated. Power plant operation may also generate high-frequency, low-decibel noise from the interaction of the turbine rotor blades and the ocean current. However, as shown in Chap. 3, the turbines are designed to rotate slowly, at about 6 rpm. The potential separation of the flow field due to pressure change would limit the production of low-energy, high-frequency, low-decibel noise to the tips of the blades, and the acoustic distance this noise travels would be restricted to within 100 m of the turbine, and thus not affect the ocean environment.

5.3   Ecological Impacts of Power Plant Construction

Taiwan's Kuroshio features a rich ecosystem, and the impact that the introduction of a huge underwater installation such as the Kuroshio power plant will have on the fish and cetacean populations must be carefully evaluated. Especially, how cetaceans would respond to the installation of power plants in the Kuroshio shall be investigated carefully. Questions such as "Will they seek out new habitats, or will they gradually become accustomed to living among the installations? Could they possibly be killed by these artificial structures?" shall be answered before construction commences. Aside from cetaceans, other fish species may face similar problems. These are important conservation issues, and a comprehensive ecological impact assessment must be implemented by referring to all relevant domestic and international researches into marine conservation [23].

Animals potentially affected by the ecological impact of power plant construction in the Kuroshio water can be classified as phytoplankton, zooplankton, fish larvae and fish, and migratory fish and mammals. In addition to habitat destruction, the present assessment focuses on the potential effects on factors which can affect the growth of these populations. The impacts are categorized as occurring during construction and after construction, and are further classified as short term and long term. Details are shown in the following.

5.3.1   Impact on Phytoplankton

The key factor limiting the phytoplankton population of the Kuroshio is the supply of nutrient salts (to be discussed in conjunction with trace elements). The construction process may provide additional sources of nutrients. For example, the cement pumping and the large number of ships coming and going will agitate the water, thus resuspending inorganic particles, and localized human activity will introduce human waste and garbage. Iron and other elements from the ships and the generators may dissolve in the water, potentially spurring rapid phytoplankton growth [24]. On the other hand, low-level vibrations from construction will also

increase water turbidity, increasing and agitating suspended particles, and thus decreasing light penetration to drive photosynthesis, which could reduce the total biological productivity of the entire upper water layer.

It's worth noting that phytoplankton biomass reaches its maximum density at depths between 30 and 100 m due to the abundant available light and relative scarcity of predators. Unfortunately, however, this depth range overlaps with the operational depth of the generators which will have an impact on multiple water layers. As such, the turbine clusters and relay platforms may have a "blackout" effect which may result in changes to the depth range for maximum chlorophyll concentrations. In addition, the rotation of the turbine blades may damage phytoplankton, and this rotation will cause vortices which may disrupt the normal exchange of water between upper and lower layers. Generator operation may also cause the temperature of the surrounding water to rise, which may alter local ecological structures. Metal used in power plant equipments may dissolve in water, thus increasing the nutrient concentrations of the surrounding water leading to an increase in algae growth and a corresponding increase in the growth of algae-eating animals. However, at the same time, this increased animal population will consume greater amounts of nutrients, thus reducing the overall nutrient supply and causing the algae to die off, reducing the supply of dissolved oxygen and thus impacting the growth of other organisms through a chain reaction. Finally, the phytoplankton in the area is already adapted to a low-nutrient environment. Introducing additional nutrients may spur phytoplankton growth, increase dissolved oxygen concentrations, and accelerate the settlement of carbon, but nocturnal phytoplankton respiration will release copious amounts of carbon dioxide which will likely contribute to global climate change.

As indicated by the above discussion, power plant construction is likely to increase the concentrations of seawater nutrients and suspended particles, which present both advantages and disadvantages for phytoplankton growth. Long-term operation of the generators and relay platform will interfere with water flow patterns that will have the greatest impact on chlorophyll in the water, and the dissolving of metals in the water will have a negative chain reaction impact on phytoplankton productivity. In addition, power plant construction and operation will have an impact on the type and volume of phytoplankton in the area, which will have a knock-on effect on local zooplankton. This is to be discussed in the following section.

In addition to the above-mentioned ecological impacts, the rapid growth of phytoplankton has the potential to impact the operating lifespan of the power plants. Equipments and mechanisms must be put in place for long-term observation of changing conditions, allowing for the implementation of controls and adaptations to avoid irreparable damage to the power plant facilities.

5.3.2   Impact on Zooplankton

The primary factor affecting zooplankton populations in the Kuroshio is the availability of food; thus, zooplankton populations are closely related to the distribution and productivity of phytoplankton. During the day, most zooplankton moves to deeper waters to avoid predators where they respond to lower temperatures by curtailing physical exertion. To ensure their safety and growth, they then move to the surface at night to feed and breed. Some zooplankton travel considerable distances during this vertical migration, following the greatest chlorophyll concentrations. With development and sexual maturity, they cease vertical migration and move to deeper water layers [25, 26]. While some carnivorous zooplankton exhibit no vertical migration (possibly related to their survival strategies) [27], overall the vertical migration ranges between 50 and 400 m below the surface.

The construction and operation of Kuroshio power plants may have a significant impact on the vertical migration of zooplankton. Construction will entail the frequent movement of many ships and operation of construction equipment which will cause vibrations, and power plant equipment will have an impact on the composition of adjacent water, both of which will affect the scope and timing of vertical migrations. In addition, the target depth of the power plant installation overlaps with the vertical migration range, and the rotation of the turbine blades may directly injure or kill zooplankton. In addition, the turbines may affect the lateral flow surrounding the zooplankton, thus causing them to be transported to another area which could affect the overall zooplankton ecology, or increase the competition for food thus changing the ecological structure. Once the power plants begin operations, this will become a daily occurrence, and will have a significant impact on zooplankton ecosystems near the power plants.

There are several ways to possibly remedy this situation. For example, power plant construction could be halted at night, thus reducing the amount of time zooplankton is exposed to disruption. An artificial chlorophyll water layer could also be implemented away from the Kuroshio water to create an environment for zooplankton vertical migration, thus maintaining the zooplankton ecological structure for the entire area. Additional research is required to establish the feasibility of other ecological preservation methods.

5.3.3   Impact on Fish Larvae and Fish

The migration and structure of larval fish is dependent on the ecology of the zooplankton on which they feed and any disruption of zooplankton populations by the power plants will be felt in the ecology and population structure of larval fish. Reef fish populations are dependent on the health of their habitats. Sediment disturbances caused by construction can cause massive damage to coral reefs, or anchors may be sunk in reef areas, making it difficult for fish to continue to inhabit

the area, let alone continue to spawn normally, thus resulting in large-scale migration or destruction of fish populations. Once construction is complete, the power plant equipment will also create shade, thus reducing the light available to algae for photosynthesis, causing them to detach from coral reefs, killing the reefs, and disrupting fish habitats.

Habitat destruction and reduced food availability will also reduce the numbers and diversity of some large fish species. Although power plant equipment can form artificial reefs which can attract some types of fish to remain in the area, some species will be unable to transition from their natural habitats to artificial reefs. The eggs of some species, such as zooplankton, will be dispersed and may be damaged or destroyed by the action of the rotating turbine blades. Furthermore, the anticorrosion coating on power plant equipment may introduce a degree of biological toxins into the water, killing or driving off fish. Also, frequent ship traffic will frighten the fish, causing them to temporarily abandon their habitats.

On the other hand, the power plant's relay platform and many anchor cables may form a base for coral or ascidians to form another kind of "artificial reef." Given the large area of the power plant structure, this could provide a degree of shelter, allowing smaller animals to avoid predators and improving their chance of survival. However, there are different opinions on the ability of artificial reefs to attract fish, with some reports suggesting that artificial reefs are not actually related to the diversity or numbers of fish, nor do they clearly attract more types of fish or fish schools [28].

Once the power plants begin operation, the component with the greatest potential effect on fish species are the rotating blades of the turbines. As noted in Chap. 3, the design of the Kuroshio power plants intentionally calls for the blades to rotate at a rate of 6 rpm or less, in the hope of reducing the likelihood of the blades injuring smaller fish species and so that medium and large fish would instinctively avoid the blades or even become familiar with and synchronize their movements to the blade rotation, allowing them to coexist.

5.3.4 Impact on Migratory Fish and Mammals

Migratory fish and marine mammals largely travel in search of food, thus their numbers are restricted by food availability. As noted in the previous two sections, zooplankton and fish populations will both be impacted by power plant construction and operation; thus, we can expect that the numbers and distribution of migratory fish will also be affected. Previous surveys have shown that dolphins mostly live along the continental shelf at depths of 200 m and their distribution is closely related to the distribution of their preferred foods such as squid. Squid surface at night to forage, and dolphins follow them [29, 30]. Migratory fish such as swordfish and tuna forage in coastal areas on smaller migratory fish and reef fish. Prior research has shown that cargo ships and leisure boats have an impact on cetacean behavior. For example, female whales and dolphins try to avoid boats [31, 32].

In addition, cetaceans are usually driven off by offshore oil field construction and operations with their attendant ship traffic, drilling, and oil spills [33]. In addition, cetaceans are frequently injured by ship propellers.

Kuroshio power plant construction will assuredly entail noise and frequent ship traffic. If construction coincides with peak migration season (from early spring to the end of summer), migratory animals may avoid the area or detour around it. However, if construction occurs close to shore or in an important forage area, there is a high probability of injuries from turbine blades or accidental collisions with the platform, especially at night. Although some cetaceans rely on sonar rather than sight to forage, a lack of research into the impact of underwater equipment on cetaceans leaves us unable to conclude that cetaceans know to evade the turbines or whether the animals will suffer from being deprived of sustenance if the power plants are located near their important forage grounds.

The above-mentioned factors and degrees of severity are compiled in Table 5.2 below to provide a reference in assessing the impact and severity of Kuroshio power plant construction and operation on local ecosystems. Considering the cost of construction and environmental protection, we recommend selecting sites which avoid highly productive reefs or continental shelf areas to ensure local ecological conservation. Of course, no site selection will be completely harm-free but if, once built, the site attracts fish schools along with migratory fish and cetaceans, it could be beneficial to local ecologies and tourism. However, commercial fishing must be carefully managed and closing the power plant area to fishing would help ensure protect the generators and the local ecology.

In summary, the shipping activity and noise that Kuroshio construction would entail will cause migratory animals to avoid the area. Plant operation may generate noise levels which, combined with local ecological changes, may result in species leaving the area due to lack of food. Given that the width of the Kuroshio is at least 100 times greater than that of the power plant installation, the impact on fish migration will be limited but cannot be completely avoided. After all, the impact of the Kuroshio power plants on the Kuroshio ecosystem will be limited and localized. However, the ocean is constantly in motion, and chemical and noise contamination from the power plants will eventually have an effect on the local ecological balance.

5.4 Impacts of Natural Change on Power Plant Operation

Change due to natural cause will have far-reaching effects on the operation of Kuroshio power plants. The area off Taiwan's east coast is prone to typhoons and earthquakes, not only posing a significant threat to the security of the turbines and relay platform but also affecting power plant performance. In addition, climate change may exert long-term effects on the Kuroshio flow. This section explores these issues in depth.

Table 5.2 The level of impact of Kuroshio power plant on local ecosystems

	Habitat disturbance due to construction	Construction noise	Operational disturbance to habitat	Operational noise	Operational chemical contamination	Overall assessment
Phytoplankton	▲	▲▲	▲▲	▲▲	▲▲	▲▲
Zooplankton	▲	▲	▲▲	▲▲	▲	▲
Fish Larvae	▲	▲	▲▲	▲▲	▲▲	▲▲
Reef fish	▲▲▲	▲▲▲	▲▲	▲▲	▲▲	▲▲
Migratory fish	▲	▲▲	▲▲	▲▲▲	▲▲▲	▲▲
Cetaceans	▲	▲▲	▲	▲▲▲	▲▲▲	▲▲▲

Note: ▲, Light impact; ▲▲, Medium impact; ▲▲▲, Severe impact

Table 5.3 Typhoons attacked Taiwan over the past 30 years (1982–2012), including maximum wind speed and wave height [34]

Typhoon grade	Number of instances (1982–2012)	Maximum wind speed (m/s)	Wave height (m)	
			Generally	Maximum
Light	60	18.0–33.0	6–11.5	7.5–16
Medium	88	33.0–48.0	11.5–14 or above	Above16
Strong	44	51.0–70.0	Above 14	Above 16

5.4.1   Impact of Typhoon

Typhoons, also known as tropical low-pressure cyclones, occur in tropical and subtropical seas, and are a frequent cause of serious disasters in coastal countries and regions. Taiwan is situated in the Northwest Pacific and, on average, is hit by four to five typhoons per year, typically in a period lasting from late April to December, but with most storms concentrated in July through September. Over the past 30 years, Taiwan has experienced 192 typhoons. An average year will see about 80 tropical cyclones globally, of which more than one quarter occur in the Northwest Pacific region, making it the world's most active area for tropical cyclones (see Table 5.3).

Typhoons have a significant impact on the physical and chemical characteristics of the waters of the Kuroshio. The storms disturb the Kuroshio's path and reduce its flow rate, while strengthening upwelling and lowering the surface temperature. The impact of typhoons on the upper water layers are quite dramatic in the Kuroshio. Tsai and Chern [35, 36] found that when the movements of typhoon and the Kuroshio interact to produce a resonance, the energy of the wind can drive the seawater into a vertical mixing which reduces overall water temperatures. Without resonance, wind shear can result in lower water layers to rise through Ekman Pumping, thus cooling the upper layers. To provide a specific illustration of the types of disturbances and cooling phenomena typhoons cause in the Kuroshio, we present research findings for Typhoon Morakot.

On August 2, 2009, the 11th tropical cyclone of the year (later named Morakot) formed about 1,000 km off the east coast of the Philippines. At 23:50 of August 7, the eye of the typhoon landed near Taiwan's Hua-Lien County, crossed northern Taiwan, and moved into the sea at west Taiwan from Taoyuan County at 14:00 of August 8. At the time of landing, the storm's central pressure measured 970 hPa, with winds near the center gusting to 33 m/s, making it a grade 12 storm. By 05:30 of August 10, Taiwan canceled the typhoon alert but maintained a storm warning. Over the course of less than a day, it brought heavy wind and rains that caused Taiwan's greatest natural disaster in 50 years and killed over 600 people. Figure 5.6 shows the path and the cloud image of Typhoon Morakot.
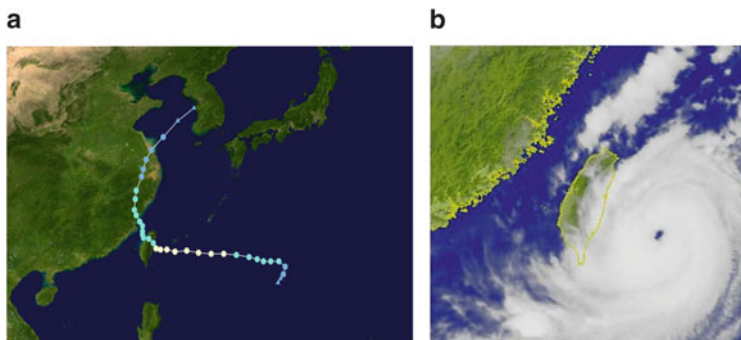
Fig. 5.6 The path and image of Typhoon Morako. (**a**) Typhoon's path. http://www.upload.wikimedia.org/wikipedia/commons/f/fd/Morakat_2009_track.png. (**b**) Typhoon satellite image. http://www.rdc28.cwb.gov.tw/data.php?num = 2009080804&year = 2009&c_name= =MORAKOT

As Morakot swept over Taiwan, sensors positioned by Tang et al. [37] between Taiwan and Lu-Dao found that a downwelling caused by the storm coincided with the ceasing of the current's northward flow of the current at depths between 50 and 150 m. However, at depths between 150 and 350 m, the northward current was found to be normal, while the east–west flow field turned west. This chaos persisted for over a day and a half. On August 9, after the typhoon had passed, the Kuroshio resumed its northeast flow at depths between 50 and 150 m. The cause of this disruption is still uncertain. In addition to the storm-caused downwelling, at the time the Kuroshio may also have been shifted west by the typhoon's landfall, causing the current's axis to bump up against Taiwan's landmass and sinking. In addition, it's possible that, at the coast, the typhoon triggered an edge wave to spread outward which impacted the Kuroshio. In addition to causing changes to the flow field, the typhoon also had an impact on the temperature field. As the typhoon made landfall, the waters at a depth of 270 m off the coast of Hua-Lien increased by 1 °C, likely as a result of the downwelling caused by the typhoon. However, this rise in temperature was followed by a gradual fall of 2.98 °C by August 9. This temperature drop may be related to a cold wake generated by the storm.

This cooling phenomenon was studied in depth by Dr. Ke Tungshan (2012) at Naval Research Lab of Miami. Using the East Asian Seas Nowcast/Forecast System developed by the U.S. Naval Research Laboratory, Dr. Ke simulated the flow conditions of the surrounding waters before and after Morakot hit Taiwan. Results indicate that, before the typhoon (Fig. 5.7a), a cold current flowed north between Taiwan's east coast and the Kuroshio's main axis, connecting to a cold eddy in the waters to the northeast. The approaching typhoon (Fig. 5.7b) brought large amounts of warm water from the western Pacific, temporarily blocking the northward flow of cold water and creating an anticlockwise cold eddy near Lu-Dao, which may be related to the above-mentioned westward flow. After the typhoon passed (Fig. 5.7c), the cold eddy began to drift north along the previously
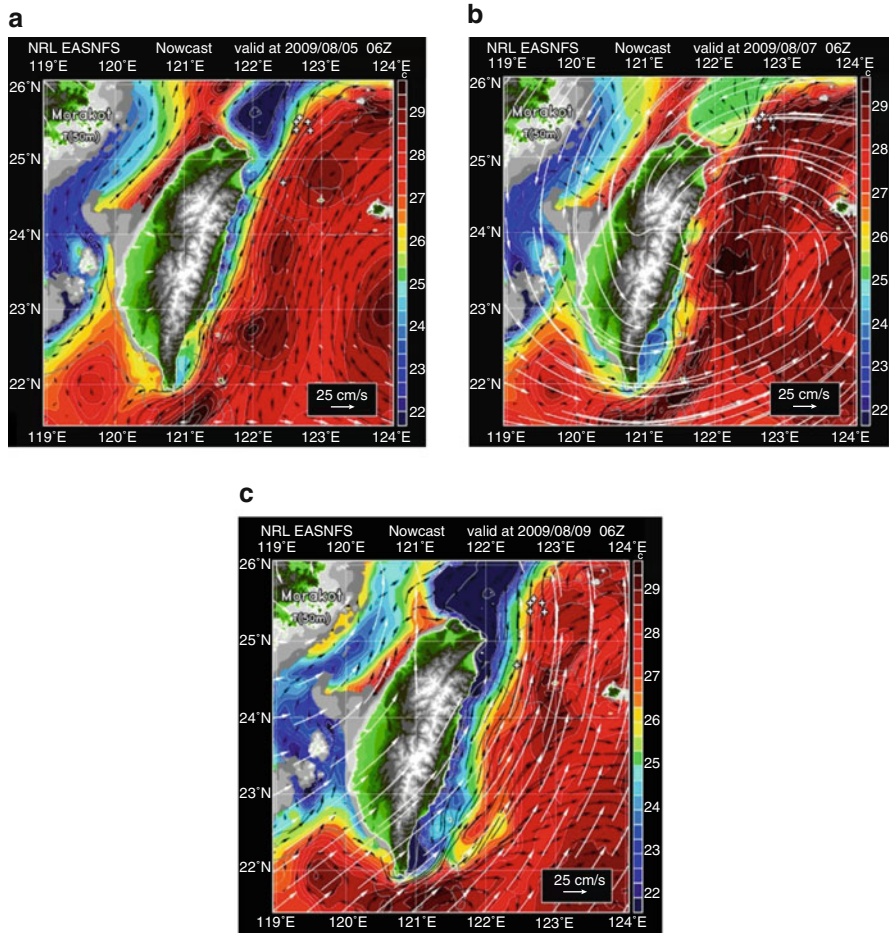
Fig. 5.7 Simulation results of the oceanic flow around Taiwan due to Typhoon Morakot's impact. The velocity of ocean flow is denoted by the black vectors, the velocity of typhoon is denoted by *white* vectors, and the *color* degradation denotes the sea level distribution. These computational results are obtained by running the global ocean model based on the East Asian Seas Nowcast/ Forecast System developed by the U.S. Naval Research Laboratory. (**a**) Before the attack of typhoon; (**b**) as the typhoon attacks Taiwan from the east; (**c**) after the attack of typhoon (*Source*: Tang et al. [37], courtesy of Dr. Ko Dong-Shan, NRL 2012)

established path, and was then incorporated into the cold eddy to the northeast. Finally, the cold current between Taiwan's east coast and the Kuroshio was restored. These simulation results are consistent with the analysis provided by Tsai and Chern [35, 36] in which typhoons coincide with a rise of cold water from the lower layers of the Kuroshio, followed by turbulent vertical mixing. Tsai and Chern noted that the degree of cooling is influenced by both the shape of the

coastline and the topography of the local seabed, which also drive changes in the water temperature distribution.

Aside from reducing the performance of the Kuroshio power plants, the typhoon could also generate gigantic waves which could threaten the safety of the power plants. In ocean, most waves are wind-driven, beginning with tiny wind-blown ripples which gradually accumulate energy to become irregular oscillations. As they leave the wind zone, these oscillations gradually become more regular, forming wave with longer wavelengths before transforming into broken waves in the coastal shallows. Physical property analysis shows waves to generally have the following characteristics (Chiu, Feng-Chen. Private communication, National Taiwan University, 2012):

1. The movement of fluid particles as a function of depth beneath surface waves is an exponential function of wavelength attenuation. When depth is half the wavelength, the fluid particles are essentially free of wave interference.
2. The impact of waves on a given depth depend on wavelength rather than wave height. Usually depths of one-half wavelength are not affected. Insufficient depth will result in interference, with interference increasing with wave height.
3. Wavelength and wave period that meet the dispersion law criteria have a set relationship, where wavelength (m) $= 1.56 \times T$ (s) $\times T$ (s). For a wave of a period $T = 10$ s, the wavelength is about 156 m; for a wave of a period of 8 s wave, the wavelength is about 100 m. This varies across waters of different depth, but most of waves occur with a period of 4–6 s.
4. A wave height/length ratio greater than 1/7 makes it difficult to sustain the wave shape, resulting in broken waves. Normally, a wave height/length ratio of 1/20 results in a fairly steep wave with a significant nonlinear phenomenon.

Typhoon-driven waves can reach an average height of 10 m, and the impact of these waves on subsurface waters decreases with depth exponentially. Given a wave height/length ratio of 1/10, being a steep wave, a wavelength of 100 m would have a small impact on turbines placed at a depth of 50 m. However, before a typhoon coming from the Pacific hits Taiwan's east coast, it will exhibit a particularly large fetch which may result in long waves of a period greater than 10 s, potentially making the 50 m depth insufficient to ensure turbine safety. Thus, power plant operations will require the real-time collection and analysis of measured wave spectra during typhoons.

5.4.2   Impact of Earthquake

Earthquakes are caused by collisions between tectonic plates, volcanic eruptions, and meteor impacts. Plate collisions primarily occur in the middle of the ocean, with lava outflows that form the rugged seabed crust. This continuous outpouring of lava pushes the two sides to form a mid-oceanic ridge. When the force of the
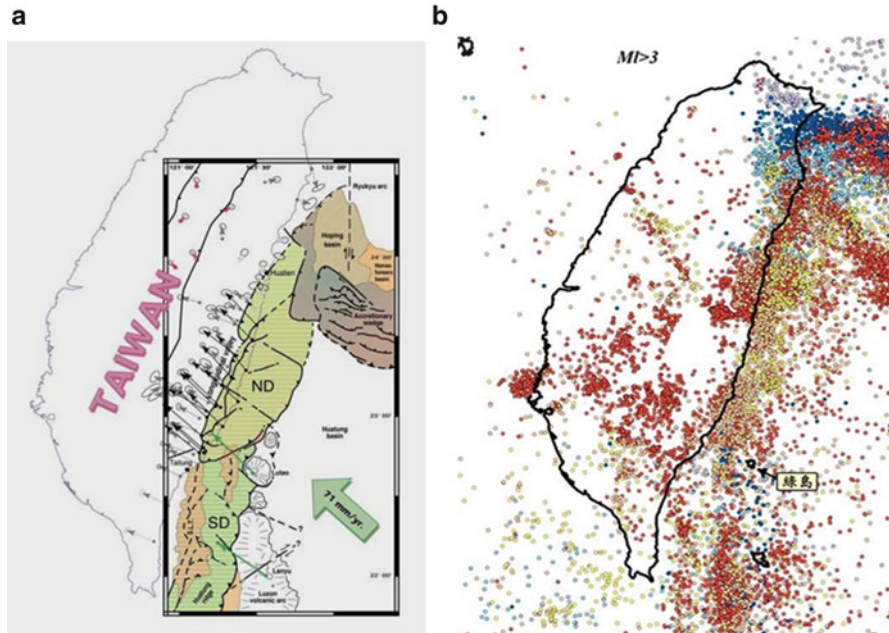
Fig. 5.8 Earthquake epicenters in eastern Taiwan. (**a**) Taiwan's eastern arc—land collision zone structure with GPS displacement volume distribution by year. The Philippine Sea Plate moves northwest towards the Eurasian Plate at an average rate of 71 mm/year. The western edge of the Luzon Arc collides with the eastern edge of the Asian mainland, resulting in crust deformation and orogenesis. The *arrows* in the figure represent annual changes in GPS displacement relative to the Baisha station on Peng-Hu islands. Lu-Dao and Lan-Yu are seen to move northwest at a rate of about 82 mm/year. The *dashed black line* represents the position of the thrust fault. "ND" and "SD," respectively, represent the North Domain and South Domain of the Luzon Arc deformation band [38]. (**b**) Earthquake distribution map of Taiwan based on earthquake data from the Central Weather Bureau. Events are color coded by depth (Courtesy of Prof. Char-Shine Liu 2012)

collision overwhelms the stress tolerance of the rock, the crust can fracture or dislocate, resulting in an earthquake. Taiwan is located at the junction of the Eurasian Plate and the Philippine Sea Plate, formed by the Philippine Sea Plate pushing against the Eurasian plate at a rate of about 72–82 mm per year (see Fig. 5.8a). Taiwan's east coast pushes towards the Central Mountain Range at a similar rate, with the islands Lu-Dao and Lan-Yu moving towards Taiwan also at a similar rate [39, 40]. Taiwan was formed by the collision and lifting of these plates, resulting in the formation of several mountain ranges [41, 42]. On the sea, looking towards the area around Hua-Lien and Tai-Dong, these formations include the Ryukyu Arc, the Luzon Arc, the Hua-Dong Basin, Tai-Dong Canyon, and the Gagua Ridge [43].

Due to the movement of these tectonic plates, Taiwan experiences frequent earthquakes, most frequently in the area between Hua-Lien and Tai-Dong [44]. These earthquakes are all quite shallow (<30 km) [43] and are thus quite destructive. The number of earthquakes in the Tai-Dong area is relatively lower but tend to occur at a shallower depth [40, 43]. Shallower earthquakes have a greater impact on the seabed and land and tend to occur with a higher frequency, thus it is appropriate to discuss the possible impact of very shallow earthquakes on the power plants.

Earthquake data for Taiwan from 2000 to 2012 [45] show a total of 3,548 earthquakes (see Fig. 5.8b), of which 1,046 (30 %) were rated 4 or above. Of these, 732 were very shallow earthquakes, accounting for 70 % of the quakes above a rating of 4, indicating that most of the 4 and above quakes between Hua-Lien and Tai-Dong occurred at very shallow depths. The historical earthquake distribution shown in Fig. 5.8b indicates that, between 2000 and 2012, the majority of 4-and-above very shallow earthquakes occurred near Hsiu-Lin Township in Hua-Lien County and near Hua-Lien City, with the majority of those near Tai-Dong occurring near Cheng-Kung and Dong-He Townships. Most undersea earthquakes also occurred off the coast of these locations as well. In addition, earthquakes also occur frequently in the ocean east of Hua-Lien in an area belonging to the Ryukyu Arc. Vibrations caused by 4-and-above quakes in this area push at seismic faults, resulting in a fractured seabed, and result in a relatively unstable geological structure.

The plate movement results in a dense network of faults under the sea off the east coast of Taiwan, the rugged appearance of the seabed, and the rapid erosion of the mountains extending from Taiwan to Lu-Dao and Lan-Yu, and the ensuing accumulation of sediment. The frequent seismic activity also contributes to ubiquitous seabed landslides. Continuous pressure along the east side of the Luzon Arc results in continuous erosion in the Tai-Dong Canyon to the west. Several normal faults have developed along the central axis of the Tai-Dong Canyon, opening up to the seabed, and the continued activity of these faults indicates that the geological structure is highly unstable.

Both the east side of the Tai-Dong Canyon and the west side of the Luzon Arc feature a major undersea landslide, the sliding surface of which is primarily located along the western edge of the Luzon Arc. The slide has resulted in the accumulation of a large amount of sediment accumulated in many layers from the north or west sides of the canyon [37]. This seabed deformation is caused by earthquake-triggered landslides, and this debris flow is very likely to negatively impact power plant equipment and foundation engineering in the area. Taiwan's eastern submarine telecommunications cable has frequently been damaged by this type of collapse, and the seabed anchoring system for the Kuroshio power plant will unavoidably be vulnerable to similar effects.

5.4.3   Impact of Climate Change

The flow of the Kuroshio can be divided into two types: the first is wind-driven circulation, while the other is caused by uneven distribution of water densities, referred to as thermohaline circulation. Most wind-driven currents take place in the upper layers, where the flow direction and rate are affected by the wind, the Coriolis force, and the Ekman transmission factor. Lower or deeper currents are primarily affected by gravity, only a few of these currents globally can be observed, and most of these currents are identified by speculations of measured temperature and salinity.

The direction and speed of wind-driven currents are mainly determined by the strength and persistent direction of the wind. Therefore, any discussion of such currents requires an understanding of wind-related changes, including changes to temperature and climate. To determine past Kuroshio flow scenarios and explore the effect of change factors, one must first determine whether and how past climate and geological changes have affected the flow direction and rate of the Kuroshio. At the same time, recent research investigations comparing past and present temperature and salinity data provide a more complete perspective on the generation and change of the Kuroshio. Therefore, investigating the change and origins of the Kuroshio entails a highly complex investigation which incorporates climate change from the ice age to the present, recent *El Nino* phenomena and global warming, along with monsoon and typhoon factors [38, 46].

Today, research on the Kuroshio's ancient flow patterns and changes are based on core samples from the Kuroshio basin, using isotope analysis of foraminifera and algae to determine sea surface temperatures, sediment deposition rates, and types to determine sediment sources. These determinations can help researchers infer the Kuroshio's flow rate at the ancient time, and cross-analysis can be used to determine flow's possible direction and speed, allowing for the possible reconstruction of past climate conditions, along with monsoon change and influence on ocean currents.

Global core samples were used to recreate conditions from 18,000 years ago, indicating that global ocean temperatures today are 2 °C higher but 6 °C higher in the polar areas [47]. Intense solar radiation at the equator from 6,000 to 12,000 years ago generated a strong summer monsoon and also enhanced the flow rate of the North Equatorial Current [48] (see Fig. 1.1) which spread heat to high latitudes. During the last ice age, sea levels dropped by an average of at least 100 m, leaving Taiwan and China high and dry, while Japan's Okinawa Trough and the Ryukyu Islands near Taiwan theoretically should have been located further east due to the Kuroshio. Core data from near Japan also shows that about 7,300 years ago the Kuroshio returned to the Okinawa Trough. Based on changes to oxygen-18 isotope concentrations in foraminifera, our understanding of temperatures and sediment deposit rates for 2,700–4,600 years ago leads to speculation that the Kuroshio at the time had a very weak effect, while the northeast monsoon had a very strong impact [49]. Core research from the Ryukyu Islands indicate that, during the ice age, the

Kuroshio would have been unable to extend to the western edge of the Ryukyu Islands, and must have flowed north along the islands [50].

On the other hand, research along Japan's Nishishichitou Ridge indicates that the Oyashio Current once extended as far as 35N^o, meaning that the Kuroshio was located further to the south. Meanwhile, at 7,000–8,000 years ago, strong warming resulted in temperature change, strengthening the North Equatorial Current, thus allowing the warmth from the Kuroshio to reach the Nishishichitou Ridge [51]. The research also indicates that between 18,500 and 17,500 years ago, sea levels off Taiwan's southeast coast reached their lowest point, 150 m lower than current levels. But that sea levels suddenly rose years later, accelerating the Kuroshio's flow. If the sea level rose slowly and the Kuroshio's flow rate fell, the Kuroshio would assume a clear eastward shift [52].

Studies of small-scale annual changes indicate that the Kuroshio followed a significantly different route. From 1959 to 1962, the Kuroshio clearly shifted south from Shikoku in Japan, and then shifted northeast. From 1956 to 1959, and then again in 1963, it flowed directly northeast [53, 54]. The relationship between the Kuroshio and *El Nino* indicates that *El Nino* and the southern oscillation both influence the speed of the Kuroshio, and in *El Nino* years the Kuroshio flows more straight than it does between *El Nino* years [55]. As a result of global warming, temperature rise would enhance the speed and straighten the course of the Kuroshio, exerting a decisive influence on global heat transfer and sea levels [56]. Monsoons and typhoons have a smaller time-scale effect on the Kuroshio's location and flow rate. Given a strong northeast monsoon, the Kuroshio's average flow rate will be relatively low, but a strong southwest monsoon will increase the Kuroshio's flow rate and cause it to take a clearly straightened course [57]. The wind field generated by typhoon Nari slightly offset the Kuroshio's position [58], reduced the sea surface temperature, stirred the subsurface layers, and changed the flow direction [59, 60].

From the above-mentioned studies, one can infer that the flow and direction of the Kuroshio can be influenced by large-scale ice ages, short-term interglacial changes, inter-*El Nino*-years changes, short-term seasonal changes and typhoons. These impacts depend on atmospheric conditions at the time (e.g., the influence of the equatorial trade winds) which are the key driver of the Kuroshio. On the other hand, in high latitudes, the Kuroshio plays an important role in heat transfer globally. In past brief ice ages, this was because ice melt into the North Pacific would pump fresh water into the ocean, forcing the Kuroshio to change direction while reducing the density of the surface seawater and slowing thermohaline circulation. This reduced the northward flow of warm water, with the result that most of northern Asia and North America were covered with ice. This period is referred to as the Younger Dryas, and its effects are recorded in rock cores in the Asian landmass [36]. These changes to the circulation of the North Pacific indicate that the Kuroshio not only is impacted by climate change but also that the Kuroshio's flow direction can also influence climate change in the higher latitudes. Therefore, any deceleration of the Kuroshio or change in its direction is bound to have an impact on the climate in higher latitude areas [61].

In view of that the operating time scale of the Kuroshio power plant is often within a 100 years or less, the Kuroshio flow should not experience any significant difference due to the climate change. On the other hand, while the overall energy of the Kuroshio may be reduced, the scale of the power plants is small enough that the operation of the power plant should not have any significant impact on the Kuroshio's flow momentum.

References

1. Myers LE, Bahaj AS (2007) Wake studies of a 1/30 scale horizontal axis marine current turbine. Ocean Eng 34:758–762. doi:10.1016/j.oceaneng.2006.04.013
2. Myers LE, Bahaj AS (2012) An experimental investigation simulating flow effects in first generation marine current energy converter arrays. Renew Energy 37(1):28–36. doi:10.1016/j.renene.2011.03.043
3. Chen F (2010) The Kuroshio power plant development plan. Renew Sustain Energy Rev 14:2655–2668. doi:10.1016/j.rser.2010.07.070
4. Gill AB, Bartlett M, Thomsen F (2012) Potential interactions between diadromous fishes of U.K. conservation importance and the electromagnetic fields and subsea noise from marine renewable energy development. J Fish Biol 81:664–695. doi:10.1111/j.1095-8649.2012.03374.x
5. Andrulewicz E, Napierska D, Otremba Z (2003) The environmental effects of the installation and functioning of the submarine SwePol Link HVDC transmission line: a case study of the polish Marine Area of Baltic Sea. J Sea Res 49:337–345. doi:10.1016/S1385-1101(03)00020-0
6. Tyack PL (2009) Human-generated sound and marine mammals. Phys Today 11:39–44. doi:10.1063/1.3265235
7. Alvarez-Salgado XA, Herrera JL, Gago J, Otero P, Soriano JA, Pola CG, Garcia-Soto C (2006) Influence of the oceanographic conditions during spring 2003 on the transport of the Prestige tanker fuel oil to the Galician coast. Mar Pollut Bull 53:239–249
8. Amundsen I, Iosjpe M, Reistad O, Lind B, Gussgaard K, Strand P, Borghuis S, Sickel M, Dowdall M (2002) The accidental sinking of the nuclear submarine, the Kursk: monitoring of radioactivity and the preliminary assessment of the potential impact of radioactive releases. Mar Pollut Bull 44:459–468
9. Canada. Department of Fisheries and Oceans; Canadian Coast Guard; Canadian Petroleum Products Institute (1995) Oil spill response field guide. Canadian Coast Guard, Ottawa
10. Wang MH (2002) Enhanced prevention ability against oil pollution in Taiwan's territorial waters: experience based on the oil pollution case by the M/S Amorgos Cargo Ship. J China Coll Mar Technol Commerce 91:1–30
11. Lin CL, Hsieh WC, Wu CH (2008) Treatment and countermeasures of sunk ships at Taiwan's waters. A research report of coast guard administration, Executive Yuan, Taiwan
12. Thompson BAW, Goldsworthy PM, Riddle MJ, Snape I, Stark JS (2007) Contamination effects by a 'conventional' and a 'biodegradable' lubricant oil on infaunal recruitment to Antarctic sediments: a field experiment. J Exp Mar Biol Ecol 340:213–226. doi:10.1016/j.jembe.2006.09.010
13. Powell SM, Snape I, Bowman JP, Thompson BAW, Stark JS, McCammon SA, Riddle MJ (2005) A comparison of the short term effects of diesel fuel and lubricant oil on Antarctic benthic microbial communities. J Exp Mar Biol Ecol 322:53–65. doi:10.1016/j.jembe.2005.02.005
14. Almeida E, Diamantino TC, de Sousa O (2007) Marine paints: the particular case of antifouling paints. Prog Org Coat 59:2–20. doi:10.1016/j.porgcoat.2007.01.017

15. Yebra DM, Kiil S, Dam-Johansen K (2004) Antifouling technology—past, present and future steps towards efficient and environmentally friendly antofouling coatings. Prog Org Coat 50:75–104. doi:10.1016/j.porgcoat.2003.06.001

16. Omae I (2003) General aspects of tin-free antifouling paints. Chem Rev 103:3431–3448

17. Champ MA (2001) The status of the treaty to ban TBT in marine antifouling paint and alternatives. In: Proceedings of the 24th UJNR (US/Japan) marine facilities panel meeting in Hawaii, 7–8 Nov 2001

18. Environment News Service (2011) UN to investigate undersea noise impact on marine mammals. http://www.ens-newswire.com/2011/08/22/un-to-investigate-undersea-noise-impact-on-marine-mammals/. Accessed 20 Mar 2013

19. Than K (2011) Giant squid killed by sound? National Geographic News. http://www.news.nationalgeographic.com/news/2011/05/110503-giant-squid-octopus-sonar-acoustic-tests-science-whales-sound/. Accessed 20 Mar 2013

20. Horowitz C, Jasny M (2007) Precautionary management of noise: lessons from the U.S. marine mammal protection act. J Int Wildl Law Policy 10:225–232. doi:10.1080/13880290701769288

21. Umlauf-Garneau E (2000) Noxious noise environmental groups work to reduce ocean noise. Rotarian, January, pp. 18

22. European Commission, Research & Innovation (2010) Study finds noise pollution affects marine life. http://www.ec.europa.eu/research/infocentre/article_en.cfm?id=/research/headlines/news/article_10_09_20_en.html&item = &artid = 17953. Accessed 20 Mar 2013

23. Polagye B, Cleve BV, Copping A, Kirkendall K (eds) (2010) Environmental effects of tidal energy development. In: Proceedings of a scientific workshop, 22–25 Mar 2010. NOAA Technical Memorandum NMFS F/SPO-116

24. Hutchins DA, Witter AE, Butler A, Luther GW (1999) Competition among marine phytoplankton for different chelated iron species. Nature 400:858–861. doi:10.1038/23680

25. Marshall SM, Orr AP (1960) On the biology of Calanus finmarchicus XI observations on vertical migration especially in female Calanus. J Mar Biol Assoc UK 39:135–147

26. Osgood KE, Frost BW (1994) Ontogenic diel vertical migration behaviors of the marine planktonic copepod Calanus pacificus and Metridia lucens. Mar Ecol Prog Ser 104:13–25

27. Terazaki M (1992) Horizontal and vertical distribution of Chaetognaths in a Kuroshio warm-core ring. Deep Sea Res 39:S231–S245. doi:10.1016/S0198-0149(11)80014-2

28. Chen CP, Jan RK, Kuo RW, Huang CH, Chen YC (2009) Fish spectrum in the coastal area around Lu-Dao island (in Chinese). Natl Park Bull 19(3):23–45

29. Yeh CC (2001) The cetacean species, distribution and habitat at waters of southeast Taiwan (in Chinese). Master thesis, National Taiwan University

30. Wang MC (2002) Study of the feeding habit, food resource segmentation and feeding groups of the Toothed Whales at Taiwan's waters (in Chinese). Master thesis, National Taiwan University

31. Stensland E, Berggren P (2007) Behavioural changes in female Indo-Pacific bottlenose dolphins in response to boat-based tourism. Mar Ecol Prog Ser 332:225–234

32. Constantine R, Brunton DH, Dennis T (2004) Dolphin-watching tour boat change bottlenose dolphin (Tursiops truncates) behavior. Biol Conserv 117:299–307. doi:10.1016/j.biocon.2003.12.009

33. Richardson WJ, Davis RA, Evans CR, Ljungblad DK, Norton P (1987) Summer distribution of Bowhead Whales, Balaena mysticetus, relative to oil industry activities in the Canadian Beaufort Sea, 1980–1984. Arctic 40:93–104

34. Data base of National Weather Bureau of Taiwan. http://www.rdc28.cwb.gov.tw/. Accessed 20 Mar 2013

35. Tsai YL, Chern CS, Wang J (2008) The upper ocean response to a moving typhoon. J Oceanogr 64(1):115–130

36. Tsai YL, Chern CS, Wang J (2008) Typhoon induced upper ocean cooling off northeastern Taiwan. Geophys Res Lett 35(14):L14605. doi:10.1029/2008GL034368

37. Tang TY, He CR, Wang YH, Jan S, Hsu SK, Wen LS, Yang TY, Song SR, Chen HY, Song GS, Chang TY, Chiao LY (2008–2010) Comprehensive research on the natural resources of the east waters of Taiwan: a precisely topographic, geological, hydrological, and ecological surveys of the waters around Green Island. A research report of the project sponsored by National Science Council

38. Qiu B, Lukas R (1996) Seasonal and interannual variability of the North Equatorial Current, Mindanao Current, and the Kuroshio along the Pacific western boundary. J Geophys Res 101:12315–12330

39. Bruce J, Shyu H, Sieh K (2005) Neotechonic architecture of Taiwan and its implication for future large earthquake. J Geophys Res 110:B08402. doi:10.1029/2004JB003251

40. Lin KC, Hu JC, Ching KE, Angelier J, Rau RJ, Yu SB, Tsai CH, Shin TC, Huang MH (2010) GPS crustal deformation. Strain rate, and seismic activity after the 1999 Chi-Chi earthquake in Taiwan. J Geophys Res 115:B07404. doi:10.1029/2009JB006417

41. Wu WN, Hsu SK, Lo CL, Chen HW, Ma KF (2009) Plate convergence at the westernmost Philippine Sea Plate. Tectonophysics 466:162–169. doi:10.1016/j.tecto.2007.11.011

42. Sibuet JC, Hus SK, Normand A (2004) Tectonic significance of the Taitung Canyon, Huatung Basin, east of Taiwan. Mar Geophys Res 25:95–107. doi:10.1007/s11001-006-8182-3

43. Yeh YH, Barrier E, Lin CH, Angelier J (1991) Stress tensor analysis in the Taiwan area from focal mechanisms of earthquake. Tectonophysics 200:267–280. doi:10.1016/0040-1951(91)90019-O

44. http://www.cwb.gov.tw/V7/knowledge/encyclopedia/eq000.htm. Accessed 20 Mar 2013

45. http://www.cwb.gov.tw/V7/earthquake/rtd_eq.htm. Accessed 20 Mar 2013

46. Malavieille J, Lallemand SE, Dominguez S, Deschamps A, Lu C-Y, Liu C-S, Schnürle P, The ACT scientific crew (2002) Arc-continent collision in Taiwan: new marine observations and tectonic evolution. In: Byrne T, Liu CS (eds) Geology and geophysics of an arc-continent collision, Taiwan. Geol Soc Am. Special paper 358, pp 187–211

47. Qu T (2003) Mixed layer heat balance in the western North Pacific. J Geophys Res 108:3242. doi:10.1029/2002JC001536

48. CLIMAP Project Members (1976) The surface of the ice-age earth. Science 191:1131–1137. doi:10.1126/science.191.4232.1131

49. CHOMAP Members (1988) Climatic changes of the last 18,000 years: observations and model simulations. Science 241:1043–1052. doi:10.1126/science.241.4869.1043

50. Wang JL, Yoshiki S, Tadamichi O, Jian ZM, Wang PX (2001) High-resolution records of thermocline in the Okinawa trough since about 10000 aBP. Sci China 44:193–200

51. Ujiie H, Ujiie Y (1999) Late quaternary course changes of the Kuroshio Current in the Ryukyu Arc region, northwestern Pacific Ocean. Mar Micropaleontol 37:23–40. doi:10.1016/S0377-8398(99)00010-9

52. Diekmann B, Hofmann J, Henrich R, Fütterer DK, Röhl U, Wei KY (2008) Detrital sediment supply in the southern Okinawa trough and its relation to sea-level and Kuroshio dynamics during the late quaternary. Mar Geol 255:83–95. doi:10.1016/j.margeo.2008.08.001

53. Chen MP, Huang CK, Lo L, Wang CH (1992) Late Pleistocene palleoceanography of the Kuroshio Current in the area offshore southeast Taiwan. Terr Atmos Oceanic Sci (TAO Science) 3:81–110

54. Sawada K, Honda N (1998) Variablilty of the path of the Kuroshio ocean current over the past 25,000 years. Nature 392:592–595. doi:10.1038/33391

55. Yasuda I, Yoon JH, Suginohara N (1985) Dynamics of the Kuroshio large meander – barotropic model. J Oceanogr Soc Jpn 41:259–273

56. Yamagata T, Shibao Y, Umatani S (1985) Interannual variability of the Kuroshio extension and its relation to the Southern Oscillation/El Nino. J Oceanogr Soc Jpn 41:274–281. doi:10.1007/BF02109276

57. Sakamoto TT, Hasumi H, Ishii M, Emori S, Suzuki T, Nishimura T, Sumi A (2005) Responses of the Kuroshio and the Kuroshio extention to global warming in a high-resolution climate model. Geophys Res Lett 39:L14617. doi:10.1029/2005GL023384

58. Runnick DL, Jan S, Centurioni L, Lee CM, Lien RC, Wang J, Lee DK, Tseng RS, Kim YY, Chern CS (2011) Seasonal and mesoscale variability of the Kuroshio near its origin. Oceanography 24:52–63. doi:10.5670/oceanog.2011.94
59. Wu CR, Chang YL, Oey LY, Chang CW, Hsin YC (2008) Air sea interaction between trophic cyclone Nari and Kuroshio. Geophys Res Lett 35, L12605. doi:10.1029/2008GL033942
60. Liang WD, Tang TY, Yang YJ, Ko MT, Chuang WS (2003) Upper-ocean currents around Taiwan. Deep Sea Res II 50:1085–1105. doi:10.1016/S0967-0645(03)00011-0
61. Porter SC, An ZS (1995) Correlation between climate events in the North Atlantic and China during the last glaciations. Nature 375:305–308. doi:10.1038/375305a0

Chapter 6
The 30 MW Pilot Power Plant

The Kuroshio provides a source of high-quality renewable energy with many competitive advantages, including (1) environment-friendly advantage: zero carbon emissions, no-pollution, zero waste; (2) fuel-free advantage: requiring no fuel; (3) global advantage: global encouragement to explore renewable energy sources; (4) advantages over other forms of renewable energy: continuous power supply with a capacity factor of 0.7, as opposed to 0.4 for offshore wind power or 0.2 for solar power; (5) construction technology advantages: only mature and traditional construction techniques are involved, no need for intensive R&D, no fatal technologic bottleneck; and (6) cost advantage: once the technology is successfully developed, construction and operating costs will be competitive with offshore wind power.

According to a survey on Taiwan's east offshore by Tang et al. [1], the first Kuroshio power plant could be built in the seas between Lu-Dao and Tai-Dong. This is mainly because the seabed terrain in this area causes the Kuroshio to accelerate, resulting in a strong and stable force which can propel the turbines for a higher power output. In this area, the speed of the Kuroshio can be as high as 2 m/s; at least 100 turbines can be installed at each cross section of the Kuroshio. If the GST of Chap. 3 is chosen, namely each turbine has a capacity of 0.5 MW, totaling 50 MW installation power can be obtained for each cross section of the current. In the streamwise direction, the turbine cluster of each cross section can be installed at every 1 km; there are accordingly ten clusters that could be installed over 10 km with a total capacity of 500 MW. Generally speaking, if the capacity factor of the Kuroshio could be as high as 0.7, as estimated in Chap. 1, there would be an annual generating power capacity over 3.07 TWh. The installation power density ($5 \, MW/km^2$) mentioned above is still fairly conservative, and this density could be potentially increased by 30–50 % given upgrades of turbine performance, more precise flow computation of the Kuroshio, and more accurate dynamic analyses of the power plant are available.

Prior to the construction of commercial power plants, we suggest that a pilot plant should be first constructed in the targeted area. The goal of building the pilot plant is to test the design specifications, mechanical properties, and ocean

engineering feasibility of three key components: the turbine generator, the relay platform, and the anchoring system. Specifically, the following specifications need to be tested and verified: the diameter, rotational speed, blade specification, and fin-stabilizing mechanism of turbine rotors; the structural integrity, the overall displacement, and mechanical properties of each component of the relay platform; and the materials, the geometries, and the stress and strain of the anchoring cables, along with the related designs of the anchor at seabed. Careful monitoring of the above aspects of the pilot plant will provide valuable references to the construction of commercialized power plants.

We recommend that the construction of a 30 MW pilot plant to be done. It is composed of 12 test platforms; each has five turbines having a totally 2.5 MW of installation power and Type III cable arrangement as shown in Table 4.5. The 12 test platforms shall be deployed in different sites having various characteristics of flow and geology. The test shall be done for clarifying the design parameters regarding, for example, the mechanical properties and design specifications of the turbine, the relay platform, and the anchoring system, along with the observation and measurement of the impact of the power plant on local environment and ecology.

As the Kuroshio power plant, the pilot plant is comprised of three main components: the turbines, the relay platform, and the anchoring system including cables and anchors. Chapters 3 and 4 have discussed their preliminary design and specifications. Therefore, unless there are contradictions revealed in the detailed engineering designs or the feasibility issues requiring significant redesign, the design of the power plant components will rely on the analyses resulted in these two chapters.

6.1 Site Selection

Beginning in 2009, Tang et al. [1] conducted a 2-year survey about the possible sites of the Kuroshio power plant in the sea between Lu-Dao and Tai-Dong. The selection of this area was based on an understanding derived from a long-term research which indicated that the sea between Lu-Dao and Tai-Dong features with a strong and stable current. The survey contents can be divided into three main areas:

1. Observations of current's strength, stability, and distribution: the anchor-typed and boat-typed ADCPs were used to perform fixed point and long-term current observations, for example, assessing the current strength and stability and studying the physical oceanic phenomena possibly caused by the local current changes.
2. Studies of sediment deposits and base plates, including a detailed survey on seabed terrain and seismic activities: Taiwan's east coast is vulnerable to seismic activities, potentially resulting in seabed movement or collapse that may impact the distribution of local ecological populations or the marine chemical compositions. Hydrothermal volcanic activity is corrosive and could potentially

Fig. 6.1 Depth and seabed topography between Lu-Dao and Taiwan. Lu-Dao is an island at east Taiwan (22°40′N, 121°30′E). Three volcanic peaks form a ridge extending northwest from Lu-Dao to Taiwan mainland (Courtesy of Prof. Tsun-Yong Tang [1])
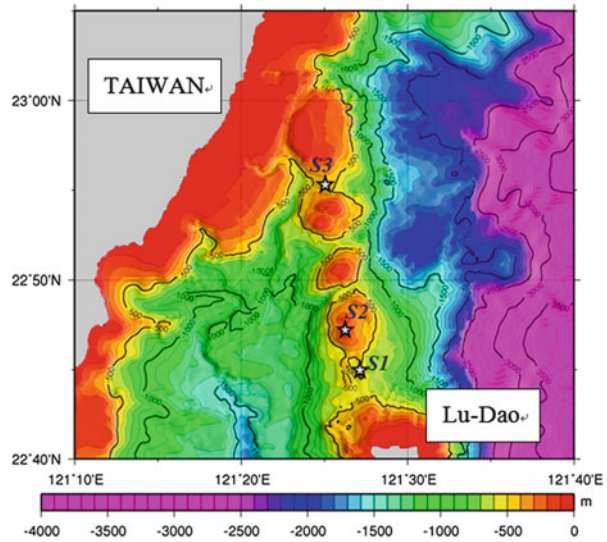
endanger the power plant's equipment or anchoring system, and thus needing a careful examination.

3. Surveys on environmental chemistry, fundamental ecological resources, and mammals: These surveys are to study the biochemical environmental changes in the sea area to determine whether the chemical properties would endanger the power plant equipments. The data obtained can also be used as a reference for the future impact assessment by the power plant on local environment and ecology.

Figure 6.1 shows the seabed depth and topography of the water between Taiwan and Lu-Dao. A line of volcanic oceanic ridges extends northwest from Lu-Dao to Tai-Dong and forms a shallow area with a depth of 1,000 m approximately; meanwhile, in the direction towards the east, the depth of seabed rapidly drops to 3,000 m or more in the area of western Pacific Ocean. Moreover, the ocean ridge features three key volcanic peaks rising to a level of approximately 50 m deep, where the troughs between the peaks lie at the levels between 400 and 600 m deep approximately. This area gives the Kuroshio an unusual shallow area, thus providing an advantageous location for the construction of the pilot plant.

6.1.1   Characteristics of the Current

As shown in Fig. 6.1, Tang et al. [1] conducted a long-term measurement of the speed of the Kuroshio through three ADCP groups along the volcanic ridge. The anchoring points are approximately located at S1, S2, and S3. Except in the range of
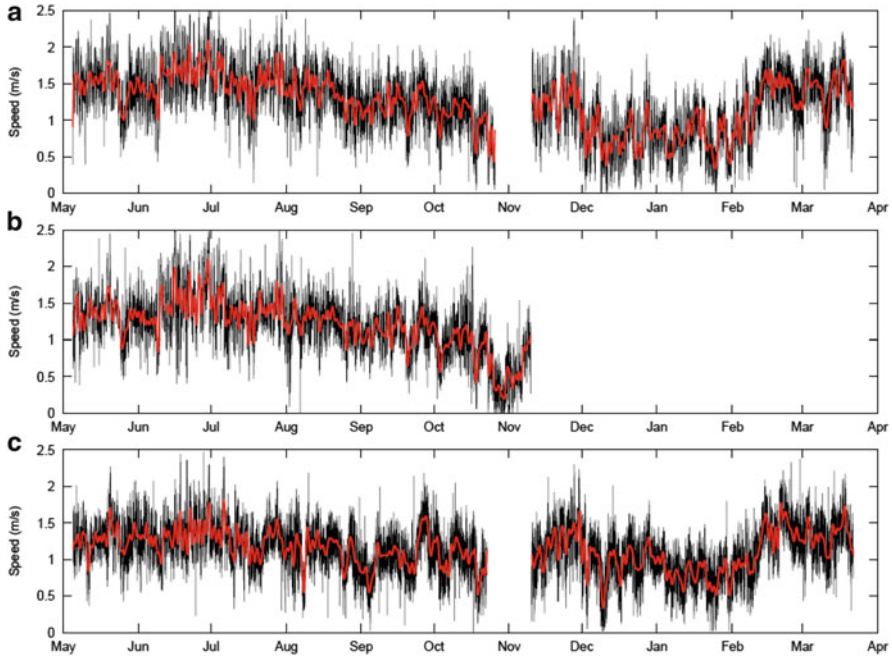
Fig. 6.2 Variation of the speed of Kuroshio from May 2009 to April 2010, measured by the fixed-point ADCP at a depth of 50 m with a data sampling frequency of 1 min. (**a**) Measurements at S3 site; (**b**) at S2 site; (**c**) at S1 site (Courtesy of Prof. Tsun-Yong Tang [1])

30 m from the surface and 20 m from the seabed, where the measurements are unable to make, the data-obtainable area nearly cover the entire level of the Kuroshio. Data sampling frequency was set to 1 min. It took about 11 months to finish the measurements on S1 and S3, retrieving data more than 40,000 samples. On S2, the measurement covered a time span for about 5.5 months, totalizing about 24,000 samples of data.

Results shown in Fig. 6.2 illustrate that, at an average depth of 50 m, the flow speeds are 1.4 m/s, 1.19 m/s, and 1.21 m/s, respectively at S1, S2, and S3, under a fluctuating amplitude of approximately ±0.3 m/s. General speaking, in this area, the Kuroshio can maintain a flowing speed above 1 m/s, which is quite typical to the Kuroshio. In addition, at the depth of 100 m, the average flow speeds at S1, S2, and S3, respectively, slow down to 1.2 m/s, 1.0 m/s, and 0.9 m/s, while the fluctuating amplitude remains ±0.3 m/s. Although the speed is reduced, the average flow speed at deeper water is still remained as high as 1 m/s [2, 3].

It is worth mentioning that, in Fig. 6.2, the momentary speed change in the sea area around Lu-Dao significantly differs from the average change of kinetic energy of the entire Kuroshio, as presented in Fig. 1.3. The latter is significantly strong in
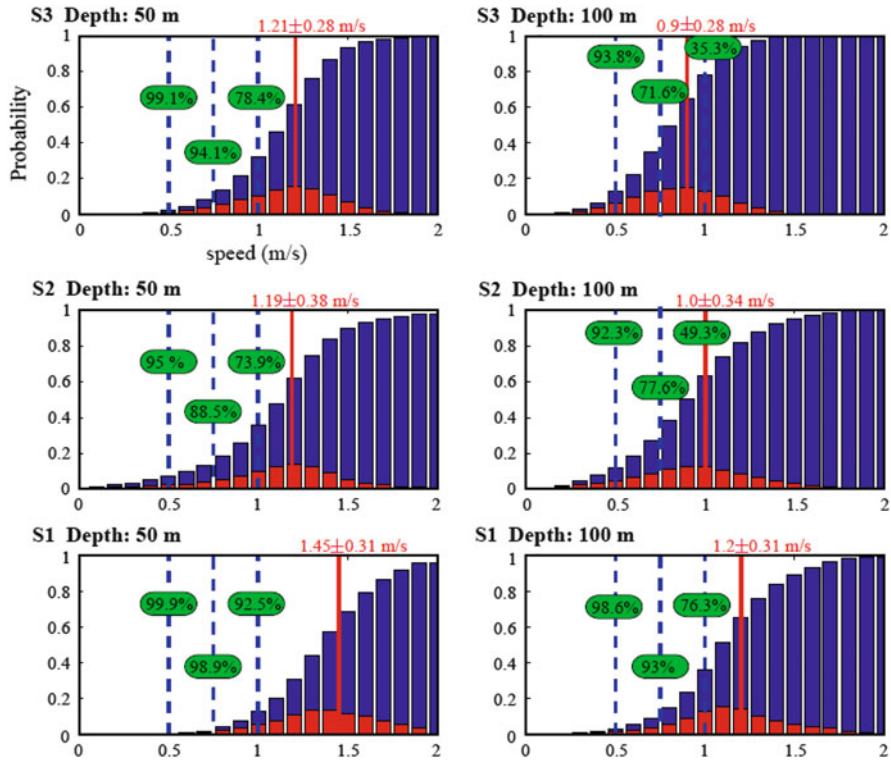
Fig. 6.3 Probability distribution of annually average flow speeds measured at three measurement sites at two different depths. At the depth of 50 m, S1, S2, and S3, respectively, have average speeds of 1.45 m/s, 1.19 m/s, and 1.21 m/s, which are all above 1 m/s (i.e., the Kuroshio's typical flow speed). At the depth of 100 m, the average speeds measured at S1, S2, and S3 are, respectively, 1.2 m/s, 1.0 m/s, and 0.9 m/s, which are still about 1 m/s (Courtesy of Prof. Tsun-Yong Tang [1])

summer but weak in winter, while the former varies little through the year [4]. However, the flow speeds measured at all three sites steadily maintain above 1.0 m/s all year round. This strong and steady current flowing between Lu-Dao and Taiwan provides certain advantages for a long-term test of the pilot plant.

Figure 6.3 shows the probability distribution of the annually average flow speed of the three sites at different depths. Chapter 3 recommends a cut-in speed of 0.6 m/s for the GST. At the depth of 50 m, the probabilities of flow speeds measured at S1, S2, and S3 to meet this criteria are 99 %, 93 %, and 98 %, respectively. At the depth of 100 m, the probabilities exceeding this threshold are all over 90 %. However, for the GST the flow speed to achieve the highest power output is 1.4 m/s, which only occurs at the site S1 close to Lu-Dao.
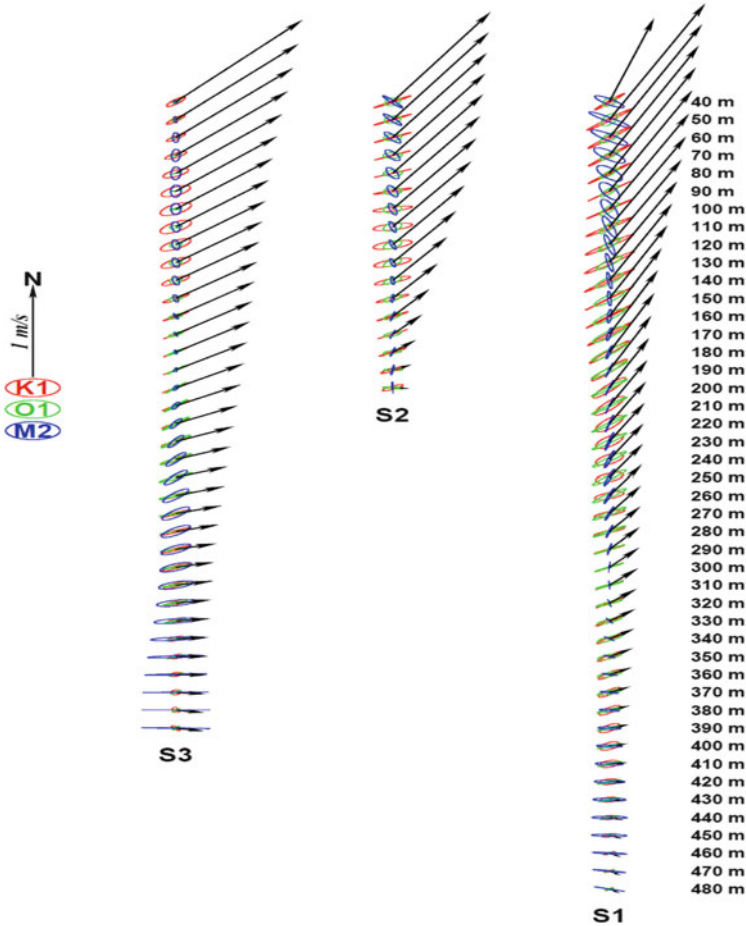
Fig. 6.4 Spatial distribution of the flow speed at S1, S2, and S3 in terms of varying depths (Courtesy of Prof. Tsun-Yong Tang [1])

If adopting larger turbines, the cut-in speed can be reduced (e.g., to 0.5 m/s); thus, the probabilities to exceed this threshold at the three sites would increase. If using smaller turbines, the cut-in speed might rise to 0.75 m/s. Under this threshold, S1 has a fulfillment probability of 90 % at depths between 50 m and 100 m, while S3 has a fulfillment probability of 90 % at a depth of 50 m. In summary, the fulfillment probability is 92 % when the Kuroshio flows at a speed of 1 m/s at the depth of 50 m, but the corresponding fulfillment probability drops to 76 % at the depth of 100 m. These measurements have substantially verified that the water between Taiwan and Lu-Dao is an ideal area to construct the pilot power plants and the commercial power plants as well.

Tang et al. [1] also plotted Fig. 6.4 to illustrate the Kuroshio flow speed versus depth for the three measurement sites. The figure shows that the Kuroshio current

roughly flows in the direction of north easterly, where the north–south flow component is the greatest. However, near the seabed, the current trends slightly south. In addition, in this area, the diurnal period averages between 23.93 and 25.83 h, while that of the semidiurnal period is approximately 12.42 h. If adding up the speeds of Kuroshio and the two tides, we can find that the average tidal variation is below 0.2 m/s. Relative to the Kuroshio's average speed of 1 m/s, the tidal disturbance is virtually insignificant. Moreover, at depths over 200 m, the impact of the tides on the Kuroshio is more significant due to the current's low flow speed at deep water.

In summary, at various depths of the water between Taiwan and Lu-Dao, the Kuroshio moves roughly in parallel to the coastline and has the strongest power intensity within the depths less than 100 m, where the average flow speed is about 1–1.5 m/s. Between the depths of 100–200 m, the average speed is about 0.9–1.2 m/s. At both depths, the variations of the flow speed are within ±0.3 m/s. Meanwhile, the flow directions are virtually fixed and the current speeds are mostly steady, making them as advantageous power generation sites. In terms of engineering design, if the cut-in speed of the turbine was set as 0.5 m/s, the probability of full power generation would be over 95 % in the water of 50 m deep for the three sites considered, while the probability of S1, which is nearest to Lu-Dao, will be 100 %. Even in the water of 100 m deep, the overall probability is still greater than 92 %.

The fluctuations of Kuroshio flow speeds, caused by the diurnal and semidiurnal tides, eddy flows, and high frequency internal waves, can all be ignored from an engineering point of view. Although the flow conditions of the three test sites along the Lu-Dao oceanic ridge are all suitable for power generation, the S1 station, closest to Lu-Dao, provides the optimal conditions in terms of current strength, fluctuation factors, and flow strength across the whole depth distribution fields. Thus, an assessment of the flow quality shows that the area surrounding the S1 test site is the best choice for the construction of a 30 MW pilot power plant.

6.1.2   Characteristics of the Geology

In the course of their research, Tang et al. [1] sailed in a latitudinal direction across the aforementioned ridge, traveling back and forth between Taiwan and Lu-Dao, conducting seismic tests to investigate the geologic structure of the seabed, totally tracking nine east–west survey lines from north to south. Figure 6.5 shows the stratum sections taken at the northernmost and southernmost passes. Results show that the seabed is nearly entirely made up of an andesite plate, with a small amount of crushed andesite rocks scattered around. Most of the area is also featured with coral reefs. The oceanic ridge peaks primarily rest on the igneous base plates, with a steeper slope on the eastern side (or the backside to the current) where the depth of seabed increases rapidly down to over 2,000 m, resulting in sediment accumulation on and along the eastern side of the ridge (see Fig. 6.5a). The western side of the ridge peaks (facing the current) may also be covered with a thick layer of sediment
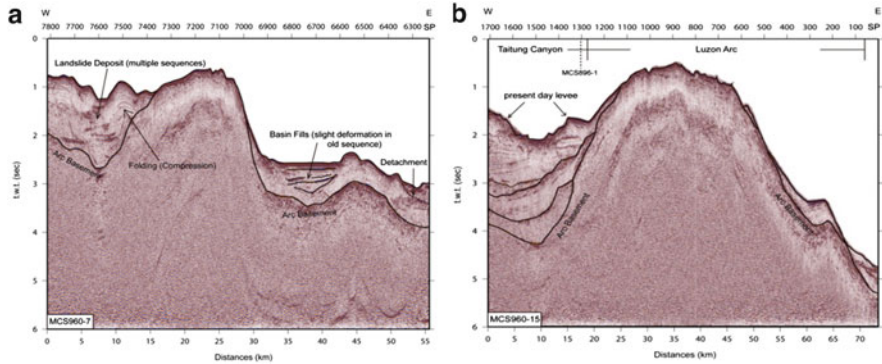
Fig. 6.5 Seismic test results between Tai-Dong and Lu-Dao. (**a**) East–west cross-sectional view at approximately 10 km north of Lu-Dao. A deposition layer caused by landslides is seen at the left of the ridge, while an older deposition layer is seen at the right of the ridge. (**b**) East–west cross-sectional view at approximately 5 km south of Lu-Dao. The central ridge is composed of igneous rock, with sediment layers on the left covering the Tai-Dong submarine canyons (Courtesy of Prof. Tsun-Yong Tang [1])

(see Fig. 6.5b). The loose sedimentary structure is unable to support the pull of the anchor, making it an inappropriate site for cable anchoring.

The Kuroshio current causes significant erosion in this area, leaving it vulnerable to submarine landslides caused by the earthquakes and typhoons, resulting in the formation of a series of submarine canyons such as those at the south of Tai-Dong. The formation time of this collapsed area can be divided into "early" and "recent" stages, resulting in two sedimentary layers (one deep and one shallow). These collapsed fields are distributed on both sides of the ridge but not on the oceanic ridge itself.

Seismic test results show that the Tai-Dong marine canyon has several normal faults across the canyon's central axis and also the findings are the remains of submarine landslides. The seabed near Taiwan is repeatedly accumulated with sediment dumped from onshore rivers. In the other words, the sedimentary layer has experienced many slides and collapses, resulted from the extrusion of the Luzon Arc and the erosions of Tai-Dong Canyon. The three test sites mentioned above are situated west of Lu-Dao in an area belonging to the extension of Luzon Arc. Both sides of Luzon Arc show evidences of sediment accumulation and marine landslides, but the sediment layer at the top of the Arc is thin or nonexistent, leaving the andesite frequently exposed on the seabed (see the ridge peaks in Fig. 6.5).

Sediment is comprehensively distributed in this area. Earthquakes caused the sediment accumulated on slopes to collapse, thus making the area unsuitable for cable anchoring. However, on the top of the ridge peaks, there is little sediment accumulation, making them suitable for anchor installation. In addition, since the flat seabed terrain is featured with a base plate made of hard igneous rocks under several meters of sediment (refer to Table 1.1 for the geological properties of andesite), it is also quite suitable for anchor installation. In addition, the probability

and frequency of collapse are lower on the east side of the ridge, making it a better choice for laying cables.

6.1.3   Characteristics of the Hydrology and Ecology

It takes a long time for marine environment and ecological systems to develop into a state of equilibrium. Constructing large-scale Kuroshio power plants in the ocean may change the composition and flux of both nutrients and heavy metals in the water, thus changing the fragile biological population structures and ecologies and eventually disturbing the natural equilibrium. Tang et al. [1] conducted six investigations to address this issue; the results are presented as follows:

(a) Structure of basic hydrological chemical

   The waters off Taiwan's east coast have different origins, including a deep subsidence of water from the Arctic, a middle layer of water from the northern Pacific, a central water from the north Pacific, and the water from surrounding rivers [5]. The data from the three test sites show that the water level structure between Tai-Dong and Lu-Dao is highly stable, characterized by high clarity, low concentrations of suspended particles, and rich in phytoplankton.

(b) Structure of nutrient concentrations

   Phosphates, nitrate, nitrite, ammonium salts, and silicates are the bases of marine food chains, the amounts of which are easily affected by marine organism activities and currents [6, 7]. In the sea between Tai-Dong and Lu-Dao, concentrations of phosphates, nitrates, and silicate salts, respectively, are 0–2 μM, 0–28 μM, and 1–66 μM. The vertical variations in these concentrations are similar to those in the western Pacific and Philippine Sea.

(c) Structure of heavy metal concentrations

   Heavy metals are also important nutrition elements for marine organisms, but they may also be highly toxic pollutants. Depending on their positions in the food chain, marine organisms have different feeding habits for heavy metals including different patterns of absorption, excretion, and acceptance. Thus, concentrations of heavy metals are closely tied to the overall condition of marine ecosystems [6, 7]. Research results show that the vertical variations of heavy metal concentrations in the sea between Tai-Dong and Lu-Dao are similar to those in the western Pacific and the Philippine Sea.

(d) Structure of phytoplankton populations

   Phytoplankton, being quite sensitive to environmental changes, forms the basis of the entire marine food chain. The phytoplankton population is often a key indicator for understanding the ecological and environmental disruptions, especially that of microbial algae of short life cycle [8–10]. Phytoplankton populations in the sea between Tai-Dong and Lu-Dao are dominated by Prymnesiophyte, followed by Prochlorophyte.

(e) Structure of zooplankton populations

   The waters between Tai-Dong and Lu-Dao feature many different types of zooplankton, including coelenterates, ctenophores, rotifers, crustaceans, and gastropods, while the mid upper depths feature important food supplies for fish and other economic animals. These organisms are also served as an important indicator of water pollution levels [11–13]. The area around Lu-Dao is rich in zooplankton (copepods) including *Paracalanus parvus*, *Farranula gibbula*, *Macrosetella gracilis*, *Clausocalanus furcatus*, *Oncaea media*, and *Euterpina acutifrons*.

(f) Structure of fish larvae communities

   Fish larvae classifications are quite complex. They have very brief life spans, and their distribution is largely in line with fish spawning grounds. The spawning grounds of most benthic fish are not far from other mature fish habitats. Once the larvae grows into mature fish, surface fish will move to deeper waters, while benthic fish moves to shallower waters. The area around Lu-Dao features a dense population of fish larvae, especially those of Genus *Bregmaceros* and *Bregmaceros nectabanus* [14, 15].

It's worth noting that Tang et al. [1], while conducting their measurements in the sea between Tai-Dong and Lu-Dao, encountered a group of dolphins about 300 m from their research vessel. Although this was an unusual scene, we can't just rule out that this area of sea is a part of a rich marine food chain that occasionally attracts large marine mammals. The impact of the construction of Kuroshio power plant on large fish should be assessed, and should be taken as a key research goal through long-term observation.

6.1.4 A Priority Site: Area Surrounding S1 Test Site

The above measurement results provided by Tang et al. [1] for the area around Lu-Dao (see Figs. 6.2 and 6.3) show that the Kuroshio in the area around the S1 test site is stable and strong over long periods of time, the flow speed of which exceeds 1 m/s over 90 % of the time. Given that this is considerably faster than the 0.7 m/s cut-in speed of most turbines (e.g., the GST of Chap. 3), this site is quite suitable for turbine installation. In addition, the flow direction in this area is stably running north by northeast. In comparison, in the waters around Lan-Yu, another small island at the south to Lu-Dao, the flow speed of the current exceeding 1 m/s only occurs 41 % of the time, and the flow direction changes frequently, making the area around Lu-Dao an obviously better site for power plant installation.

   In addition, the seabed in this area features a wide variety of topography, where there are an oceanic ridge and widespread sediment, with depths plunging from 200 to 800 m. As the Kuroshio passes through this area, it produces a variety of changes by the seabed topography, even generating a wake zone or different scales of turbulence vortexes behind the volcanic ridge. This variety fulfills one of the key

goals of the pilot plant: to test the performance and reliability of the power plant's design specifications and mechanical properties under a wide variety of different conditions. This variety of conditions is especially critical for testing the design of the power plant's three main components: turbine, relay platform, and anchoring system.

6.2   Composition of Pilot Plant and Anchoring Location

Tang et al. [1] noted that the experience with ADCP indicated that, at the three test sites, the change of the inclination angle of the cable of ADCP was limited to 3°, the change of the rotation angle was less than 1°, and the change of anchor's vertical displacement was about 20 m or less. All of which indicated the long-term stability of the anchor installations in this area. The data of local geology also show the superiority to secure the test platform in the Kuroshio [16, 17]. However, Tang et al. [1] also pointed out that this area featured with an active fault line is subject to frequent landslides, which was evidenced by the recycled anchor equipment covered with sediment that indicated there are frequent collapses caused by earthquakes. Therefore, Tang et al. [1] suggested that there are three or four underwater hills suitable as anchor locations, because of their relatively flat tops created by the cumulative erosion from the Kuroshio current on which the exposed hard bedrock is the particularly suitable for anchor installation. However, the area's hills and canyons consist of a complex terrain, and the interaction between the strong current and the complex terrain produces turbulence. Consequently, the lack of long-term observational data, which can be an important reference, needs to be addressed urgently.

Based on above results, we summarized the conclusions of Tang et al. [1] into the following suggestion: a 30 MW pilot power plant is proposed to be constructed near the S1 test station northwest of Green Island. The pilot plant would be composed of 12 test platforms; each has an area of 201×140 square meters, supporting five turbines formed with a staggered configuration. Each turbine has an installation capacity of 0.5 MW, giving one test unit a total installation capacity of 2.5 MW. The 12 test platforms are to be installed around the S1 test site where the seabed lies at a depth of 400 m–800 m. The seabed here is covered by a relatively thin layer of sediment and the local geology is stable and hard, making it highly suitable for the engineering work required for the anchoring system. In this proposed site, the strength and direction of the current are stable, while a full power generation load could exceed 7,000 h. The complex seabed topography allows the verification of a wide range of potential design problems, making it an ideal location for the pilot plant.

Figure 6.6 shows the locations of 12 test platforms, each with its own unique test items divided into five categories as follows:
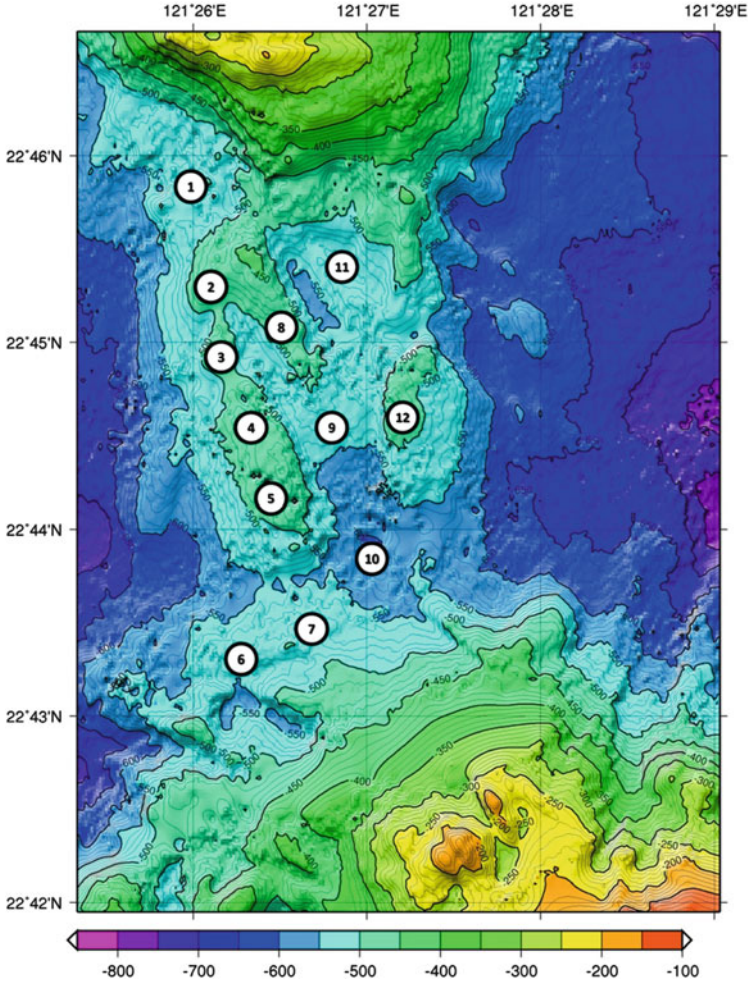
Fig. 6.6 Priority sites to install the 12 test platforms of the 30 MW pilot power plant. Each *circle* represents a test platform carrying five turbines with a 0.25 MW installation power. The background is the seabed topography at the S1 site of Fig. 6.1 (Courtesy of Prof. Tsun-Yong Tang 2012)

1. The stability of platform under the action of strong current: Six groups of test platforms will be placed on the undersea ridge (e.g., the platforms 2, 3, 4, 5, 8, and 12). Squeezed by the rising seabed, the Kuroshio current increases its strength along the ridge to an average flow speed over 1.5 m/s. Besides the current flows in a north by northeast direction for sure, the vertical component of the flow is considerably more complex compared with those of other waters. The six test units are placed in such positions as to determine whether the turbine anchored by a single chain can reliably maintain optimal power generation in the

powerful and complex valley flow, and whether the deformation and displace-
ment of the test platform can be maintained within the design specifications.

2. The stability of anchoring system in the areas without sediment: The same test
   platforms of previous category would also serve well for the present tests. As
   shown by the above geological survey results, the seabed along the ridge has
   been eroded seriously by the Kuroshio for a long time, now, only leaving a thin
   layer of sediment. Thus, the installation process and engineering parameters
   used to anchor test platforms in this area will end up with valuable test data for
   the ocean engineering on the seabed, along with the test of the reliability and
   stability of the anchoring system.

3. The stability of anchoring system in the areas with sediment: The seabed, where
   the platforms 1, 6, 7, 9, 10, and 11 are placed, may feature different depths of
   sediment accumulated on top of the igneous rock. Of these six locations, the
   sediment may be the thickest at positions 9, 10, and 11, due to their locations on
   the lee side of the ridge, where sediment from Lu-Dao is easily accumulated due
   to the weak current. Given the different thicknesses of the sediment layers, the
   procedures for installing the test platforms on these positions will be more
   complex compared with those on the top of range, and the anchors must be
   buried into a greater depth. The installation of these six test platforms will help
   verify relevant engineering concerns.

4. The impact of unstable flow on turbine operation: Positions 9, 10, and 11 are on
   the lee side of the ridge. As such they will be likely exposed to a wake of
   vortexes in different intensities, which will significantly impact the turbine
   performance and the reliability of turbine anchor system. These three test
   platforms will verify the impact of these two factors.

5. The impact of near shore currents and geologic features on the power plants:
   Platforms 6, 7, and 10 are positioned near Lu-Dao to test the impact of current
   instability on the power plant as the Kuroshio flows along the near shore.

In this 30 MW test plan, no platform will be installed in the waters of 800 m deep
or more, partly because installation costs rise sharply with the increase of depth and
also because the nature of the construction is largely similar over the depth of
200 m. Thus, it is unnecessary to carry out the tests in the extremely deep areas.
Unless the planned tests reveal new problems, the 12 selected sites above should
meet the requirements of all test items.

6.3   Construction Parameters

The following presents estimates for the costs of the construction and operation of a
30 MW pilot power plant from a viewpoint of investment. The logic of the
estimation has been discussed with the executives from related industries, and the
actual implementation conditions and contents will be further adjusted according to
the actual situation to improve the plan's overall feasibility.

Below we present a list of capital sources, investor structures, operator structures, work schedules, construction and operational costs, and operational revenue potential. Details are shown in the following:

1. Construction costs: approximately NTD6b (the so-called New Taiwan Dollar, NTD30–USD1; b means billion).
2. Investment shares: Private enterprise NTD4b (67 %, creditable), government and state-owned enterprises NTD2b (33 %).
3. Stock shares:

   - 10 % (R&D share) owned by Kuroshio Power Generation Research Team (primarily responsible for R&D)
   - 20 % (cash) invested by Taiwan Power Co. (who owns the power grid nationwide)
   - 13 % (cash) invested by Ministry of the Interior Development Fund (for the backup by government policy)
   - 50 % (cash) invested by enterprise groups (which will become business entities to run the power plant)
   - 7 % (technology patent shares) owned by the inventors of turbine generator, anchoring system and/or marine engineering technology

4. Construction preparation time: 3 years, with NTD750m (m means million) invested in unit platform tests, construction engineering design, environmental impact and risk assessment, site selection, personnel train, and legislative and regulatory consultation.
5. Construction time: 5 years requiring an investment of NTD5b.
6. Power plant operations: the establishment of "Taiwan Kuroshio Power Company" will cost NTD250m cash
7. Operation revenue:

   - Income from electricity sales: 30,000 kW × 365 (days/year) × 24 (h/day) × 0.7 (capacity factor) × 2.8 (NTD/kWh) = NTD5.145b/year (assuming the capacity factor to be 0.7, and a electricity sale price is 2.8 NTD/kWh)
   - Carbon trade income: annual power generation is 189.75 million kWh, electricity emissions factor is 0.8 kg-CO_{2e}/kWh, annual emissions quota is 147,000 tons, 1 ton of carbon reduction worth USD20, carbon trade income is USD2.94m (~NTD94.08m).
   - Operation expenses (first 5 years): fuel costs is 0, maintenance cost is NTD20m/year, the cost of personnel, insurance, and loan interest is about NTD100m/year, which is subject to change depending on circumstances and requiring a separately detailed assessment.
   - Annual net income is NTD488.58m, including electricity sales and carbon trade income.
   - Recovery period is 11 years.
   - Plant lifetime is set to be 20 years.

The above cost calculations are based on a cost analysis from the plans of the construction of seven tidal power plants in the USA (please refer to Appendix E).

This calculation is also supported by a breakdown of bids from relevant international ocean current power generating firms for this project (given that these bids constitute commercial secrets, detailed information cannot be disclosed). Figure E.2a in Appendix E shows that the average construction cost of a pilot tidal power plant would be USD6,000/kW. Assuming that the construction costs for the Kuroshio power plant are close to those of tidal power plants [18–22] (please refer to the analysis in Sect. E.3 of Appendix E), the construction cost of this 30 MW Kuroshio power plant would be NTD5.4b. We recommend that NTD6b be budgeted as for total funding, including the operation costs of the new company and the marginal allocation for occasional expenses.

In calculating the operation revenue, we took the FIT (Feed-in tariff, a policy mechanism designed to accelerate investment in renewable energy technologies) [23] of offshore wind power generation, i.e., 2.8 NTD/kWh, as a reasonable electricity sale price of the future Kuroshio power plant. Wherein, the carbon trade income accounts for about 20 % of the future operation revenue. However, given the difficulty for predicting the activities in the carbon trade market, this income estimate may be too optimistic to realize. Another project requirement, which may be too difficult to fulfill, is that the all undersea equipments, including the turbines, platforms, cables, and anchors, should be maintenance free for 5 years except for local maintenance. This kind of guarantee may be provided by turbine manufacturers, but since these turbines have not yet been applied in this type of installation, it is still impossible to verify the feasibility or authenticity of such kind of guarantee. However, if the above conditions cannot be met, costs could increase by 30–40 %, with the extension of the recovery period to 15 years. Given that the pilot plant is not going to be operated on a profitable basis and due to the large-scale investment in terms of an new energy industry, this period of recovery time is still regarded as a reasonable range.

6.4   Content and Agenda of the Construction Task

Construction planning for the pilot plant will divided into two phases. The first phase will last 3 years, including the preparatory work for the construction of the power plant, mainly focused on the detailed designs of overall plant engineering, the research results of which will be directly applied to the contract specifications or construction blueprints. The second phase is the actual construction engineering, the result of which will be a 30 MW power plant consisting of 12 test platforms completely distributed in predetermined locations on the seabed.

Construction preparation work consists of the following six items:

1. Location confirmation: Data from the Tang et al.'s [1] survey of the area between Lu-Dao and Tai-Dong need to be reconfirmed and supplemented with detailed engineering design data. The geologic features of the 12 recommended

anchor locations in Fig. 6.6 need to be investigated and analyzed in line with the detailed engineering specifications.

2. Turbine and anchoring system selection: The analysis work outlined in Chaps. 3 and 4 will be executed to select and design turbines and anchoring systems that are appropriate to Taiwan's Kuroshio and to the seabed geological features of the targeted sites. Work will include systematic mechanical analysis, power generation configuration design, maintenance procedure design, and reduced-scale model experiments.

3. Marine engineering procedure design: Domestic and international engineering consultancies, along with corporate research institutes, will collaborate to design marine engineering procedures and to develop the required rigging and construction platforms.

4. Environmental impact and risk assessment: Assessments of the impacts on the surrounding environment, ecosystem, and shipping operations due to the installation and operation of the power plant shall be done before construction commences. In addition, the assessments of the impacts of earthquakes, typhoons, climate, government policy, and economic situation on the operation of the power plant are also crucial to the investors.

5. Formulation of legislation and regulations related to the Kuroshio power plant: Lobbying government agencies to formulate relevant laws and regulations specific on the Kuroshio power harness development, along with the development of related incentives and subsidies.

6. Develop power plant operational mode: Developing the Kuroshio power plant into an energy industry with commercial and economic values. At the same time, engineering and operations personnel are needed to be trained through a comprehensive training program.

In terms of construction engineering and practical considerations, we recommend an establishment of a joint public–private company to manage the construction work and the follow-up operations. There are many factors to be considered during the construction period:

1. Sites selection: the sites selected should be close to shore, in a shallow seabed featured with strong steady currents, as found in the previously mentioned waters between Tai-Dong and Lu-Dao.

2. Turbine selection: the ideal turbine should be featured with simple structure, easy service, high stability under static and dynamic forces, robust ability, long lifespan, high efficiency, and low cost. The results of design parameter analysis presented in Chap. 3 can be used to screen dozens of turbine models listed in Appendix A.

3. Power transformer and transmission: A permanent magnet generator could be considered to reduce the need of frequent repair.

4. Conduction cable: Deep-sea floating power cables could be considered, such as 69 KV XLPE power cable.

5. Power adapter and transmission: the power produced by the 30 MW generators should be connected to the grid of Taiwan through an existing Taipower

substation in Tai-Dong where the power could be transmitted to Tai-Dong City under an ultrahigh voltage through a 345,000 V adapter.

6. Relay platform structure: We recommend the platforms analyzed in Chap. 4 be built in the Kuroshio waters, which are high-pressure resistant, capable of adapting depths, flexible, and shock resistant.

7. Professional deep sea anchor installation: We recommend using deep sea anchor fixtures with a total capacity of 20,000 tons. Finally, the deep sea monitoring management systems, such as VPS, INTER OCEAN, DGPS, ROV or SEA POWER, could be selected as the power plant managing operations.

6.5   Key Technologies to Be Secured

The development of Kuroshio power plant will produce many key technologies in the future that will be needed to be quickly patented to protect the intellectual properties resulted from R&D and project involvement. In the context of current planning, we expect the following core technologies needed to be carefully handled as soon as possible:

1. Predictive ability on the Kuroshio: It is necessary to develop a proprietary "Kuroshio Power Predictive Model," establish a global ocean analysis program, and acquire a reliable channel to continuously access ocean data from satellite, as did by Chao (Exploring Kuroshio's energetic cores with an ocean nowcast/forecast system. Private communication, University of Maryland, 2008). The model is critical to enhancing Kuroshio power plant performance and quality and is a basic requirement for efficient power plant operations. Turbine generator technology: Currently, the globally available turbines can be grouped into four big categories as shown in Appendix A. In the total of 63 types of marine turbines, 16 of which have already been subject to scale model tests at sea, while 12 have been subject to scale model tests in the laboratory. Although most of these models are designed for shallow water operation, the basic principle is ultimately the same. In fact, it is not difficult to modify shallow water turbines for deep sea use (please refer to Chap. 3 for an analysis of GST turbines as the basis for developing new turbine models).

2. Anchoring system technology: The selected turbine model should be statically and dynamically analyzed in terms of its triaxial stress and moment. The results of these analyses will be applied to design the anchoring system. The anchoring system and turbines are required for laboratory-based scale model tests followed by real size test at sea. Finally, the turbines in line with the platform designs will be tested at sea.

3. Maritime engineering technologies: This includes the installation procedure designed for turbines, generators, transformers, and cables, and the processes designed for system maintenance, the installation of all surface rigs, and working platforms.

4. Power plant operation modes: This includes the design of the standard operation procedures such as the maintenance specifications, power plant security, ecological preservation, and other related work.

The first four technologies are already quite mature. Therefore, while developing the first plant, it will require proactive cooperation with foreign technology providers. The site selection, equipment manufacturing, and construction engineering for subsequent power plants can be completed domestically, after the successful operation of the first power plant.

6.6 Potential Problems and Countermeasures

Several problems that may occur during construction and operations are listed below, along with potential solutions. However, the number of issues involved is quite extensive; thus, the issues addressed here are only directional suggestions, and the actual execution will be handled by on-site personnel to enhance the effectiveness.

1. Typhoons: The turbines are distributed under sea in a level of 30–50 m deep, and thus they can avoid the impact of waves driven by typhoon, for example, to 10 m high.
2. Earthquakes: The proposed test platform is designed being composed of multi-point anchors and floating platforms, which will reduce the impact of earthquake-induced landslides on the anchoring system.
3. Corrosion: At a depth of 30 m, where the equipment does not in direct contact with the sea surface, thus greatly reducing the potential oxidation, and making corrosion problems easy to handle through appropriate application of anticorrosive treatments.
4. Biofouling: The power plant is deployed at a depth of 30 m or more, where weak sunlight results in a scarcity of biological activity, except of few large marine mammals and fish, thus reducing the likelihood of biofouling. The use of an appropriate environmentally friendly paint can further prevent equipment from biofouling.
5. Kuroshio stability: The Kuroshio flows north along Taiwan's east coast in a relatively stable path. Aside from the northeast monsoons in winter marginally slowing the flow speed, the current flow is normally strong and steady.
6. Responsible parties: In Taiwan's current system of government, the Ministry of the Interior is responsible for the permission of energy exploration, while electrical power plant operation is under the jurisdiction of the Ministry of Economic Affairs, and the data of near-shore seabed topography and geology are managed by the Ministry of National Defense. Thus, the construction and operation of Kuroshio power plant require government policy coordination at the level of the Executive Yuan.

7. Protection of marine ecosystems: The turbines will be distributed at depths ranging from 30 to 100 m, a water featured with relatively small amounts of plankton and small fish (due to the warm temperature of the Kuroshio), while large fish such as dolphin can be kept off by sonar warning alarm. The impact of plant construction on seabed ecosystems will be quickly restored after the construction is completed.

8. Impacts caused by the variation of Kuroshio's flowing speeds and directions on the turbines: The distribution density of the turbines is significantly influenced by the driving forces of the Kuroshio, and designs must be carefully analyzed in line with the current's features in the targeted construction zone. The optimal formation and distribution density of turbine cluster are described in Sect. 6.1.

9. Site selection: selected site needs to consider the following priorities: (1) proximity to land to reduce the engineering costs, (2) shallow seabed to reduce construction costs, (3) stable current speed and direction to ensure stable power generation and ease of maintenance, and (4) fast current to ensure maximum power generation. All of which have been shown in Sect. 6.1 obtained by detailed survey work.

10. Site development strategy: A comprehensive assessment of the developable sites within the Kuroshio water must be undertaken, including technical feasibility, operational value, environmental and ecological preservation issues, and other related conditions, whereby the development priorities for each site are examined. No development permit shall be released without such kind of overall strategy development.

6.7 Public Relations and Marketing

Whether the construction plan will be successful or failure depends on the assistances from the central and local governments, the recognition of local residents, and nationwide civil support, which are all well closely related to the media relations.

1. Central Government (1): It is needed to apply the "Kuroshio Electricity Development Permit," which belongs to the legal category of "Mining Rights Usage," under the jurisdiction of the Ministry of the Interior.

2. Central Government (2): An operation license for the "Kuroshio Power Company," basically a kind of IPP (independent power plant), will need an application procedure through Ministry of Economic Affairs, under the existing "Private Electricity Act."

3. Central Government (3): An application of "Offshore Mining Permit" should be submitted to the Ministry of National Defense; the acquisition of the data related to offshore current flow and seabed is under the jurisdiction of the Ministry of National Defense.

4. Local Government (1): Apply for permits for the use of onshore bases for the offshore power plant (e.g., acquiring the land needed for power plant operations and power management personnel).
5. Local Government (2): The use permits of harbor facilities and space (e.g., acquiring the port space and facilities for power plant maintenance, e.g., equipment and rigs).
6. Local Government (3): Compensation to the local fishermen due to the loss of livelihoods (compensation amount is based on the fishermen average income for the past 10 years), or the creation of Kuroshio-related industries to benefit local residents.
7. Legislative Yuan: To ensure the smooth operation of the power plants, existing legislation needs to be amended to make the Kuroshio power generation compatible thereto, including the amendments of the Renewable Energy Development Act (e.g., construction grants and guarantees of electricity prices) and the incentives for renewable energy according to the Energy Tax Ordinance.
8. Local councils: The development of Kuroshio power plants will be very helpful to local industries, including the development of undersea tourism and sightseeing, security services, and marine recreation. These industries can attract business investment and promote local prosperity. These types of investments will require legislative guarantees, along with the cooperation of local community leaders.
9. Marketing: Energy utilities are a long-term business for profit-stable enterprises, but it is also susceptible to country's energy policy. For example, California had implemented free electricity market but ended up with Enron scandal, which should be avoided in the Kuroshio case. In Taiwan, the power generation is not a monopoly, but must be sufficiently funded. Because of high technical threshold, it is not easy to fulfill by general enterprises. Therefore, for Kuroshio power plant, there must be a long-term business planning and intention, and the operations must be lasted for 20 years or more. Thus, marketing is definitely a crucial factor.

6.8 Other Related Analyses and Research Works

Other required analyses related to the construction, operations, and costs are listed as follows:

1. Financial and market analyses: This includes construction cost, operation cost, risk cost, fund raising, customer groups, electricity purchase, etc.
2. Risk assessment and management: There are political risks (e.g., changes in renewable energy grants and incentives, carbon energy tax implementation, acquisition of land and sea development permits, and involvements of local politics and interest groups), natural disasters (e.g., typhoons, earthquakes, and climate changes), destruction of marine lives (e.g., biofouling, impact on fish,

and seagrass fetters), environmental risks (e.g., the failure, weakening, or displacement of the Kuroshio), financial risks (e.g., changes of preferential loan policies, changes of public and private investment structures, and the fluctuations impact of electricity price), man-made disasters (e.g., damage from fishing boats, terrorist activities, and submarine collisions), and the risk of war.

3. Development of relevant regulations: Many laws and regulations need to be studied or amended, including regulations related to offshore mining, energy development on the public seas and Kuroshio current, harbor usage and land acquisition, offshore seabed data acquisition, electricity sales (e.g., provisions of ocean-based renewable energy development), and investment incentives and mandatory measures for renewable energy development.

4. Long-term assessment: Long-term observation is required to assess the potential impact of rising political populism on relevant government policies such as those related to renewable energy, energy pricing, carbon tax and carbon trade, environmental and ecological preservation, marine development, economic and financial development, and private power plants. Other policy trends related to the global energy technology development and national energy policy need to be considered as well.

5. Environmental impact assessment of targeted sites: During construction and operation, assessments need to be conducted about the impacts caused by the power plant on: ships (e.g., the commercial ships, fishing boats, military vessels), the Kuroshio itself, the marine and seabed ecologies, and daily marine activities along Taiwan's east coast. Other assessments should also be included, such as the influences of turbines' operation on the flow fields of Kuroshio and the harms of power plant construction and operation on marine ecologies.

References

1. Tang TY, He CR, Wang YH, Jan S, Hsu SK, Wen LS, Yang TY, Song SR, Chen HY, Song GS, Chang TY, Chiao LY (2008–2010) Comprehensive research on the natural resources of the east waters of Taiwan: a precisely topographic, geological, hydrological, and ecological surveys of the waters around Green Island. A research report of the project sponsored by National Science Council

2. Worthington LV, Kawai H (1972) Comparison between deep sections across the Kuroshio and the Florida current and Gulf Stream. In: Stommel H, Yoshida K (eds) Kuroshio -its physical aspects. University of Tokyo Press, Tokyo, pp 371–385

3. Hsin YC, Wu CR, Shaw PT (2008) Spatial and temporal variations of the Kuroshio east of Taiwan, 1982–2005: a numerical study. J Geophys Res 113:C04002. doi:10.1029/2007JC004485

4. Hsin Y-C (2010) Intra-seasonal variation of the Kuroshio southeast of Taiwan and its possible forcing mechanism. J Ocean Dyn 60:1293–1306. doi:10.1007/s10236-010-0294-2

5. Gong GC, Liu KK, Pai SC (1995) Prediction of nitrate concentration from two end member mixing in the East China Sea. Cont Shelf Res 15:827–842. doi:10.1016/0278-4343(94)00039-P

6. Hung JJ, Chan CL (1998) Distribution and enrichment of particulate trace metals in the southern East China Sea. Geochem J 32:189–203

7. Hsiao SH, Hwang JS, Fang TH (2011) Copepod species and their trace metal contents in coastal northern Taiwan. J Mar Syst 88:232–238. doi:10.1016/j.jmarsys.2011.04.009

8. Takahashi M, Kikuchi K, Hara Y (1985) Importance of picocyanobacteria biomass (unicellular, blue-green algae) in the phytoplankton population of the coastal waters off Japan. Mar Biol 89:63–69. doi:10.1007/BF00392878

9. Gong GC, Shiah FK, Liu KK, Wen YH, Liang MH (2000) Spatial and temporal variation of chlorophyll a, primary productivity and chemical hydrography in the southern East China Sea. Cont Shelf Res 20:411–436. doi:10.1016/S0278-4343(99)00079-5

10. Shiah FK, Chen TY, Gong GC, Chen CC, Chiang KP, Hung JJ (2001) Differential coupling of bacterial and primary production in mesotrophic and oligotrophic systems of the East China Sea. Aquat Microb Ecol 23:273–282

11. Chung JL, Shiah FK, Gong GC, Chiang KP (2009) Trophic cascading of medusa on the relationship between copepods and diatoms in a subtropical coastal ecosystem. Terr Atmos Ocean Sci 20:547–556. doi:10.3319/TAO.2008.05.23.01(Oc)

12. Shih CT, Chiu TS (1998) Copepod diversity in the water masses of the southern East China Sea north of Taiwan. J Mar Syst 15:533–542. doi:10.1016/S0924-7963(97)00053-5

13. Lee CY, Liu DC, Su WC (2009) Seasonal spatial variations in the planktonic copepod community of Ilan Bay and adjacent Kuroshio water off northeastern Taiwan. Zool Stud 48:151–161

14. Chen JP, Jan RQ, Kuo JW, Huang CH, Chen CY (2009) Fish fauna around Green Island. J Natl Park 19:23–45

15. Chang KH, Jan RQ, Shao KT (1983) Community ecology of the marine fishes on LuTao Island, Taiwan. Bull Inst Zool, Acad Sinica 22:141–155

16. Juang WS, Chen JC, Jhang JG (2005) The topographic landscapes of vocanic necks in the coastal range, Lutao, and Lanyu, eastern Taiwan (in Chinese). Bull Cent Geol Surv 14:108–148

17. Sinotech Engineering Consultants: metropolitan area and the periphery sloping integrated environmental and geological databases to build a sloping rock engineering survey study (5/5) (2006) The final report of the eastern region of Taiwan (in Chinese). Bull Cent Geol Surv 95–21

18. Bedard R (2005) Survey and characterization tidal in stream energy conversion (TISEC) devices. EPRI-TP-004-NA

19. Hagerman G, Bedard R (2006) Massachusetts tidal in-stream energy conversion (TISEC): survey and characterization of potential project sites. EPRI-TP-003 MA Rev 1

20. Polagye B, Bedard R (2006) Tidal in-stream energy resource assessment for southeast Alaska. EPRI-TP-003 AK

21. Previsic M, Polagye B, Bedard R (2006) System level design, performance, cost and economic assessment – Minas Passage Nova Scotia tidal in-stream power plant. EPRI-TP-006-NS

22. Previsic M, Polagye B, Bedard R (2006) System level design, performance, cost and economic assessment – New Brunswic head harbour passage tidal in-stream power plant. EPRI-TP-006-NS

23. http://en.wikipedia.org/wiki/Feed-in_tariff. Accessed 20 Mar 2013

Appendix A: Catalog of Global Underwater Turbines

This catalog collects data of underwater turbines available online globally. Based on the actuation principle, the turbines are categorized into five groups: (1) horizontal axis turbines, including 29 models, (2) vertical axis turbines, including 17 models, (3) reciprocating turbines, including 3 models, (4) venturi turbines, including 10 models, and (5) others, including 4 models. The five groups consist of 63 models, wherein 324 patents are granted or being filed, and over 28 models had been deployed underwater for a long-term test or operation.

The data collected are shown in the following tables. For each turbine, the data are shown by four aspects: (A) product outline, (B) current status of development, (C) company owned the product, its nationality, and patent number, and (D) the scope of application.
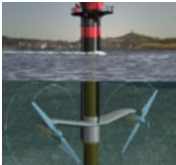
Horizontal Axis Turbines

For the horizontal axis turbines, the rotation axis is parallel to flow direction, and the blades convert current's kinetic energy into electricity via rotating blades and gear sets. This type of turbine, in general having two or three blades, is generally equipped with yaw drives, capable of boosting efficiency by aligning the rotation axis with flow. A three-blade turbine has the advantages of higher conversion efficiency, being easier to maintain stability and less fatigue loading. Whereas a two-blade turbine offers the advantages of being easy to maintain and operate, simpler machine design, and lower cost. The characteristics of energy conversion and mechanical properties for horizontal axis turbines are summarized as follows:

- For per unit power, a horizontal axis turbine has lower solidity blades, indicating a lower cost.
- Due to a more even axis thrust, it is less likely for blades and rotation axes to undergo fatigue damage.
- Higher energy conversion efficiency is achieved because the rotation plane is perpendicular to flow direction.

The representative model, SeaGen & Seaflow (see the product no. A.1 of the following table), developed by Marine Current Turbines (MCT), is anchored to the seabed by a single pile, which is applicable to shallow and stable waters with high strength geology. The turbine, capable of producing electricity with high efficiency during flood and ebb tides, has two 20 m-diameter rotors and a mechanism controlling the pitch angle. The cut-in speed is higher but cannot achieve optimal efficiency in a low-speed flow field. The company MCT, founded in UK, installed a 300 kW single turbine generator called SeaFlow in Lynmouth on the North Devon Coast of UK in May 2003, and a 1.2 MW two-rotor generator called SeaGen in Strangford in Northern Ireland in 2008, which operates 18–20 h/day, and has been connected to the local grid.

Based on the tide data of Dorset and Portland Bill in the southwest UK, Bahaj and coworkers [1–6] investigated the performance of MCT models by conducting a series of research both numerically and experimentally. They concluded that the 16 m diameter MCT turbine can capture 100–174 MWh of energy within a month. Some independent researchers also analyzed MCT models from different aspects [7–12].
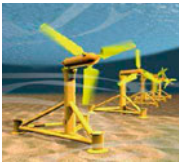
Besides, MCT also cooperated with the local university (Queen's University) in a series of ecological environment research to study the influence of turbine operation on the ecological environment. Two projects are in progress: the construction project for a 10.5 MW power plant in Saint George's Channel between UK and Ireland and the demonstration project for setting up power plants in Nova Scotia and British Columbia, Canada.

Name	Item	Content
1. SeaGen	A	SeaGen: A horizontal axis turbine system, fixed to a seabed by a single pile, can be installed in a sea area with a strong current or a current moving steadily at a considerable speed. The two 14–20-diameter rotors, equipped with a pitch control mechanism, can achieve efficiency of nearly 48 % during flood and ebb tides, and even under a full load, the turbine can come to a complete stop within 3 s
	B	A 300 kW system was installed in Devon, Canada in 2003 A 1.2 MW system was installed in Strangford in spring 2008 A 10.5 MW system, expected to operate in 2012, is in progress
	C	Sea Generation Ltd, UK MCT(marine current turbine) http://www.seageneration.co.uk/ http://www.marineturbines.com/ Patent numbers US2006125242 (A1); US2006244267 (A1); US2008284176 (A1); US2009121487 (A1); US2010183377 (A1); WO2004048774 (A1); WO2004055365 (A1); WO2007083105 (A1); WO2007045853 (A1); GB2425329 (A); GB2431437 (A); GB2434413 (A); CA2637305 (A1); CA2625127 (A1); EP1945939 (A1); EP1984572 (A1); AU2006303120 (A1); AU2007206762 (A1)

(continued)

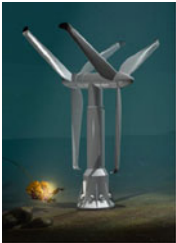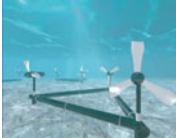| Name	Item	Content
	D	The technology for this system matures, able to achieve high efficiency. However, the system cannot achieve optimal performance in a low-speed flow field because it requires a higher cut-in speed. Besides, redesigning the anchoring system and changing SeaGen to a whole underwater system is required
2. Hammerfest	A	The system is fixed to a seabed by a gravity base connecting to the turbine through a slant support, which aims to reduce flow disturbance. The variable pitch turbine can align the rotation axis with flow direction. The generator, gearbox, and control system is located in the central cabinet
	B	A 300 KW system, still operating currently, is connected to a grid in 2003 A 1 MW system is scheduled to be installed in Scotland in 2012
	C	Hammerfest Strom, Norway http://www.hammerfeststrom.com Patent numbers WO2004022968 (A1); WO2004015264 (A1); CA2438041 (A1); NO316980 (B1); NO320852 (B1); AU2003248520 (A1); AU2003258892 (A1); EP1540172 (A1)
	D	Redesigning the anchoring method is required Reliability of the control system in deep sea requires to be evaluated High efficiency, mature, and low cost technologies
3. Verdant power	A	A whole underwater system, anchored to a seabed directly Down wind turbines; the rotation axes can align with the flow direction The cut-in speed is lower than 1 m/s; higher efficiency can be achieved at 2–6.5m/s Rated power is 35 kW, occurring at 2.1 m/s Installation cost (20 MW and above): $1.5–4 M/MW
	B	In the RITE project, the system is designed to be 5 m in diameter, 6 m in height, and 4 m in length
	C	Verdant Power, USA/Canada http://verdantpower.com/what-systemsint/ Patent numbers WO2009064430 (A1); US2009123283 (A1); US2009041584 (A1); US2008056906 (A1)
	D	The Kuroshio speed falls outside the recommended range; whether a down scale model can solve said problem is to be surveyed The rotation axis can align with the flow direction without a control mechanism
4. Tocardo	A	A mini system anchored through a float, suitable for a water channel, is featured by a 2.8-m rotor, a robust system, and high reliability
	B	A 3.5 kW prototype (2.8 m in diameter) was successfully tested in 2005 A preliminary commercial operation test was completed in The Netherlands in 2008

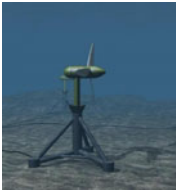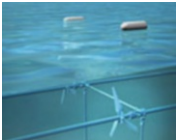| Name	Item	Content
		Currently the 50 kW T50 and 150 kW T150 models are available
	C	Tocardo International BV, Netherlands
		http://www.tocardo.com
		Patent numbers
		WO2009031887 (A1); US2010244452 (A1); EP2195524 (A1); CA2699165 (A1); NL2000840 (C2); KR20100086983 (A)
	D	A low cost mature system that has ever commercially operated. Expanding the application to a large power plant requires a lot of machinery and a redesign of the anchoring system, which not only increases the cost but makes maintenance difficult as well
5. Deep-gen	A	A 3-bladed, horizontal axis, variable pitch, up wind system. The turbine itself can be surfaced by buoyancy to facilitate maintenance. The rotatable turbine body, fixed to a seabed or a gravity base, is totally submerged in water
	B	Currently an EMEC 500 kW system is in operation in Orkney island; a 1 MW system is being planned
		The initial operation cost is about 8–9 p/kWh, which is expected to go down to 5–6 p/kWh after technology becomes more mature
	C	Tidal Generation Limited, UK
		http://www.tidalgeneration.co.uk/
		Patent numbers
		US2010119309 (A1); US2010038911 (A1); WO2008125830 (A1); WO2008032025 (A2); GB2448358 (A); EP2147162 (A1); CA2684068 (A1)
	D	Anchored to a seabed directly, not applicable to the east coast of Taiwan
		Requiring a control system, reliability for which needs assessment
		Large torque; high efficiency
6. Open Centre Turbine	A	The turbine body, installed inside the venturi-shaped shroud, is most characterized by the hole in the turbine center, which can boost efficiency and mitigate the harm to marine creatures
		This PMG-based system, operating at the depth of 25–50 m and having the advantages of robustness and simplification, is fixed to a seabed by piles, the height of which can be adjusted
	B	Currently a full-scale test on a 250 kW model at the depth of 25–50 is completed in the neighborhood of the UK-governed Eday island
		A 1 MW system operating currently was installed in Nova scotia in July 2009
	C	OpenHydro, Ireland
		http://www.openhydro.com
		http://www.emec.org.uk/tidal_site.asp
		Patent numbers

Name	Item	Content
		WO2010118766 (A1); WO2010069569 (A2); WO2010069539 (A1); WO2010069538 (A1); WO2010069537 (A1); WO2009098057 (A1); US2010068037 (A1); US2010232885 (A1); US2010172698 (A1); EP2241749 (A1); EP2209175 (A1); EP2199601 (A1); EP2088311 (A1); EP1980746 (A1); EP1980670 (A1); CA2714182 (A1); AU2009211519 (A1); NO20093300 (A); KR20100016370 (A); JP2010523888 (T)
	D	The problem of no control mechanism in place requires to be rectified, and the anchoring method needs redesigning
		With stability maintained, the system is operable in deep water
7. Atlantis AK, AS, AN series	A	AR series refer to dual rotor, fixed pitch horizontal axis turbines; currently 1 M and 2 MW models are available
		AS series refer to the ducted horizontal axis turbines equipped with one-directional or bi-directional blades. Currently 100 kW, 500 kW, and 1 MW models are available
		AN-400™ refers to Aquafoil-based shallow water turbines, able to withstand debris in water flow
	B	The AK-1000 model is scheduled to be built in summer 2010 and tested in Orkney
		Simulation for the AS-400™ model was completed in August 2008, and the drag test is in progress
		The 6-year-period drag and reliability test for the full-scale AN-400™ model is finished, which has been in pilot run and connected to the Australia grid system
	C	Atlantis Resources Corp, UK
		http://www.atlantisresourcescorporation.com/marine-power/atlantis-technologies.html
		Patent numbers
		WO2009126996 (A1); WO2009126995 (A1)
	D	The ducts of the AS series can enhance the performance in a low speed flow such as Kuroshio. However, a yaw drive is required in that the performance is more sensitive to flow direction
		The AK series outputs more power, but the anchoring system needs improving so as to extend the scope of application to a very deep sea
8. DeltaStream Concept	A	This system, consisting of three horizontal axis turbines connecting to one another by three truss pieces that form a triangle-shaped structure with 30 cm side length, is anchored to a seabed by gravity
		The mass center for the whole system is low, ensuring a high stability. The system reliability is enhanced via existing technology to lower cost
	B	A plan for testing the 2 M model installed in StJustinian's Pembrokeshire took shape in 2009
		The test for said turbines with 12 m diameter rotors is expected to last for 1 year
		The system will be relocated following the test
	C	Tidal Energy Ltd, UK
		http://www.tidalenergyltd.com/news.asp
		Patent numbers

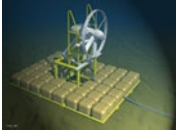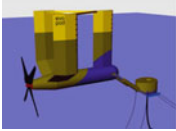| Name	Item	Content
		US2009162144 (A1); WO2009081162 (A2); WO2010007342 (A2); GB2455784 (A); GB2461265 (A); GB2467653 (A); EP2232059 (A2); CA2710399 (A1)
	D	Fixed to a seabed directly; not applicable to the east coast of Taiwan
		A yaw drive is required to align the rotation axis with flow direction
		The cost is lowered by the modular design
		Employing existing technology mostly to achieve higher reliability
9. Neptune	A	This system, consisting of two horizontal axis turbines, capable of operating during flood and ebb tides and expected to achieve efficiency of 45 %, is fixed to a seabed by a single pile, wherein the electromechanical system is exposed above the sea surface
	B	Since 2010, totally a 2.4 MW EMEC system has been tested in Orkney, which costs a total of €2 millions
	C	Neptune renewable energy, UK
		http://www.aquamarinepower.com/
		http://www.engineerlive.com/Power-Engineer/ Engines_Turbines/Major_tidal_turbine_contract/21312/
	D	Neptune is suitable for shallow waters
		The anchoring system needs improving, and the whole system must be put under water to reduce influence of harsh weather conditions for application in the Kuroshio region
10. Morild	A	A floatable, low speed, horizontal axis turbine system, anchored by cables, and consisting of four dual-bladed turbines and four constant speed generators, is capable of operating with high efficiency
		The turbine body can rotate with flow
	B	A full-scale prototype, expected to operate in 2010, was built in Norway, which aims to evaluate reliability and efficiency and to lower lost
	C	Statkraft and Hydra Tidal, Norway
		http://www.hydratidal.com/Morild-Technology
		http://www.statkraft.com/pub/innovation/tidal_power/ MORILD_demonstration_plant/index.asp
		Patent numbers
		US2010074750 (A1); WO2009157778 (A2); WO2008100157 (A1); EP2118482 (A1); NO328410 (B1); NO327567 (B1); AR072384 (A1); KR20090128416 (A); JP2010519446 (T)
	D	The floatable body is likely to be influenced by typhoons
		Test records are unavailable; another evaluation on reliability is required
		Easy to install; easier to move
		It is likely to outperform other similar turbines in efficiency
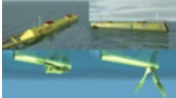
(continued)

Name	Item	Content
11. TiDEL	A	The system, anchored to a seabed by chains, and consisting of two 500-kW generators and two horizontal axis, fixed-pitch, 15 m diameter rotors, can generate 1 MW electricity at 2.3 m/s. The cut-in speed is 0.7 m/s Suitable for floating in a depth of 30 m and above Cost for a 100 MW scale model is approximately $5.75/kWh
	B	A 1/10 scale down prototype was tested A full-scale 1 MW model underwent a 12-month period test
	C	SMD Hydrovision, UK http://www.smd.co.uk/ http://www.reuk.co.uk/TidEl-Tidal-Turbines.htm
	D	The cut-in speed is lower than that for a traditional horizontal axis turbine The efficiency at a low flow speed needs assessment Another problem—how to revise the design to make it operable in deep waters—remains to be overcome
12. Swan turbines	A	The system with a yaw drive, but without a gearbox is supported by a heavy duty bracket fixed to seabed The turbine, featured by the advantages of high reliability, low cost, etc., generates electricity via a variable speed generator The modular design lowers the maintenance cost
	B	A small array consisting of several 1 m diameter turbines is being tested in UK to assess reliability and cost The turbine was successfully put in operation from a huge ship directly to verify the installation technology The commercial operation system is expected to be completed in 2014
	C	Swanturbine, Norway http://www.swanturbines.co.uk Patent numbers WO2010049670 (A2); WO2007125349; GB2437534; GB2437533
	D	The modular design, able to lower the installation cost, is not applicable to Taiwan because the water near the east coast of Taiwan is too deep
13. SeaPower Project	A	The system, an integral power plant design, consists of trusses connecting turbines, floats, and anchoring cables Kinetic energy captured by the horizontal axis turbines is transmitted to the floating PMGs via universal joints The modular design-based system can be applied to the offshore and inshore regions
	B	Currently the prototype laboratory at University of Naples is finished A scale-down model test in Messina strait is finished A test on a full-scale model, expected to produce 500 kW electricity at 2.5 m/s flow speed, is being planned
	C	Fri-El Seapower, Italy ADAG http://www.fri-el.it/en/sea-power/fri-el-sea-power/who-we-are
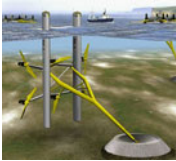
Name	Item	Content
		Patent numbers
		WO2008110915 (A2); US2010045043 (A1); EP2134962 (A2); CN101680420 (A)
	D	The R&D progress for the system can be used as reference for developing an ocean current power plant
		The system, not totally placed under water, is not suitable for Taiwan because of its vulnerability to harsh weather conditions such as typhoon winds
14. Sabella D10	A	The system is most characterized by the anchoring platform, to which a turbine is anchored
		The turbine, capable of rotating slowly (10–15 rpm) to align with flow direction, can reduce environment disturbance
	B	Two modules, D03 and D10, are developed following completion of two 1/3 scale-down model tests
		The D03 model, published in spring 2009, was tested to identify likely problems
		The D10 model, with 10 m diameter rotors, and capable of generating 200–500 kW electricity, is in a design phase
	C	Sabella, France
		http://www.sabella.fr/eng
	D	The anchoring platform design is applicable to Taiwan if a large-scale, high reliable model is developed
15. Evopod	A	A semi-under water system, having an above water platform, and simply as well as high efficiently anchored by cables, can passively rotates with water flow
		A modular design system; easy to take apart and assemble
		Low cost
	B	A 1/10 scale-down model was tested in the northern Ireland during 2008–2009
		A 1/5 scale-down model, expected to generate 22 kW electricity, is being built
	C	Aquamarine Power, UK
		http://www.oceanflowenergy.com/
		http://www.aquamarinepower.com
		Patent numbers
		US2008050993 (A1); WO2006054084 (A1); GB2422878 (A)
	D	The above water platform is likely to be hit by typhoons, and the Max. dive depth for turbines remains unknown
		The system can passively rotate with water flow; no extra control system is required
		Easy to install
16. Sea Snail	A	This system is most characterized by the anchoring method. A 15 m × 12 m anchoring device which uses six hydrofoils-wings that "fly" in the water to generate more than 200 tons of downward force to the seabed
	B	The model is being tested in Orkney, UK
	C	Robert Gordon University, UK
		http://www4.rgu.ac.uk/cree/general/page.cfm?pge=10769
		http://radio-weblogs.com/0105910//2004/04/09.html
		Patent numbers

(continued)
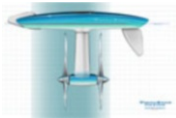
Name	Item	Content
		WO2004022856 (A1); US2008053358 (A1); US2006140724 (A1); US7611307 (B2); US7275891 (B2); ES2329359 (T3)
	D	The anchoring method is innovative, but is not applicable to Taiwan
17. GEM-ocean's kite project	A	This system, in possession of a venturi-shaped shroud, and two sets of turbines, is anchored to a seabed by cables, which has the advantages of high stability, low cost, and ability to passively rotate with flow
		The electromechanical facility is inside the floatable chamber located at the center between the two turbines.
		The buoyancy can balance the cable tension, and if necessary, float the machinery for maintenance
	B	The "dragged by ship" test on a scale-down model is completed
		A full-scale prototype, expected to generate 100 kW electricity at 2.5 knot flow speed, is being built, which will be tested at a very low speed flow field located in the vicinity of Venice
	C	ADAG, Italy
		http://www.dias.unina.it/adag/italian/marine_turbine.html#gem
	D	The system structure is more complicated, raising the entry barrier
		The mechanism stabilizing the system needs to be studied
		If relevant technologies mature, the installation and maintenance cost for the modular design can be lowered
		Lower cut-in speed; high efficiency
18. University of Strathclyde	A	The design concept of contra-rotating rotors makes the system easy to maintain stability without using a base
		The system, anchored to a seabed by cables, is suitable for deep water area, wherein the turbine generator is suspended like a kite
	B	A scale-down test is completed
		The inventor sought sponsorship for designing a large size model with an 8 m diameter rotor
	C	University of Strathclyde, UK
		http://www.strath.ac.uk/features/archive/tidal/
		Patent numbers
		WO2007017629 (A1); US2008226450 (A1); EP1917436 (A1); NO20081135 (A); KR20080033476 (A)
	D	The anchoring method and scope of application for this system are applicable to the east coast of Taiwan
		The system has the advantage of high stability, which is an appropriate option for developing a power plant if a certain level of efficiency is maintained and a large scale test is completed (the inventor is seeking sponsorship)
19. SRTT (Scotrenewables Tidal Turbine)	A	A SRTT system, consisting of two horizontal axis turbines that can be turned on or off depending on the environment, is fixed to a floating device
		The 1.2 MW turbine, having a 12 m diameter rotor, is designed to operate at the depth of 25 m and above where the speed is between 2.5 and 5 m/s
		The turbine can be returned to a harbor for maintenance
		Estimated cost: $0.07–0.12 p/kWh

Name	Item	Content
	B	A scale-down model test was conducted at a laboratory and in ocean areas
	C	Scotrenewables, UK
		http://webarchive.nationalarchives.gov.uk/+/http://www.berr.gov.uk/files/file41865.pdf
		Patent numbers
		WO2006061652 (A1); US2008258465 (A1); RU2007126325 (A); NO20072834 (A); NZ555635 (A); JP2008523302 (T)
	D	The cut-in speed is too high, perhaps not applicable to a low speed current such as Kuroshio
20. SST Semi Submersible Turbine	A	The system is especially suitable for too deep waters, where anchoring the turbine economically by a single pile is impossible
		Initially the system, anchored to a seabed by a semi-floating pile connecting to slender mechanical arms, aims to operate at the depth of 60 m
	B	The project is still at the phase of small-scale laboratory tests A 10 MW power plant is scheduled to be established at the depth of 60 m in Orkney
	C	Tidalstream, UK
		http://www.tidalstream.co.uk/
		Patent numbers
		WO2009004308; GB2450624 (A); GB2348249 (A); GB2441821 (A); GB2441822 (A); GB2434410 (A)
	D	This system is characterized by the anchoring method, which is not necessarily suitable for the east coast of Taiwan, where the water depth is more than 1,000 m
21. Deep Green Energy	A	A system, consisting of hydrofoils and turbines and designed by Minesto based on the concept of a kite, is anchored to a seabed by tethers made of a light special material. The hydrofoil, capable of generating 500 kW electricity, spans about 40 f. in length
	B	Minesto has raised a fund of $2.5 million to conduct offshore tests in the Northern Ireland
	C	Minesto, UK
		http://www.minesto.com
		Patent numbers
		US2009185904 (A1); WO2007101756 (A1); EP1816345 (A1); MX2008009564 (A); KR20080099258 (A); JP2009525427 (T)
	D	Perhaps the anchoring system is applicable to the east coast of Taiwan, which can serve as a reference
		The electricity generation capacity remains obscure (Still in the initial R&D stage; far away from commercial operation)
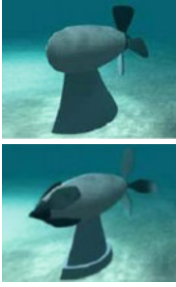
Name	Item	Content
22. Cetus Turbine	A	A Cetus turbine can be applied to a river dam system. The special blades can capture energy from water flow from any direction, and prevent aquatic weed invasions
	B	According to an agreement signed in Feb 2010, a prototype will be built in Rubicon valley in Central Victoria, Australia to verify its applicability
	C	Cetus Energy. Australia http://www.cetusenergy.com.au/technology.php Patent numbers WO9628657 (A1); US5937644 (A); EP0815359 (A1); AU703844 (B2)
	D	Still far away from commercial operation; the method of how to prevent aquatic weed invasions can be used as reference
23. Keys Hydro Power	A	The system, comprised of two sets of turbines, and anchored to a seabed by two piles, can generate 100 kW electricity, the cabinet of which is made of composites
	B	Still in the initial R&D stage; a test report on the prototype is unavailable
	C	Keys Hydro Power, USA http://www.keyshydropower.com http://www.miamiherald.com/multimedia/news/hydro/index.html
	D	Composites, costing more, can extend service life The anchoring method needs revising
24. FAU turbine	A	The system, comprised of a hydrofoil and a double shaft, is anchored to a seabed by cables
	B	To explore marine energy technology, DOE has sponsored $1.2 million to FAU to establish Southeast National Marine Renewable Energy Center
	C	Florida Atlantic University, USA http://blogs.palmbeachpost.com/extracredit/2009/08/31/learn-more-about-fau%E2%80%99s-center-for-ocean-energy-technology-at-audubon-open-house/
	D	The anchoring method is applicable to Taiwan Still far away from commercial operation; the reliability and applicability remain unknown
25. TidalStar	A	The system, comprised of dual rotors, and suspended by buoyancy, can generate up to 50 kW electricity
	B	Still in the initial R&D stage. Bourne Energy will cooperate with China in establishing a 200 MW power plant in the Pohai area
	C	Bourne Energy, USA http://www.bourneenergy.com Patent numbers WO2008051446 (A2); US2008093859 (A1); US7492054 (B2); EP2084396 (A2); CN101568719 (A)
	D	The dual rotors output a large torque, and thus large power, but the anchoring system needs redesigning and testing

Name	Item	Content
26. Gulf Stream Turbine	A	This system, consisting of 2 contra-rotating rotors and a generator, and anchored to a seabed by cables, is suspended in water via the buoyancy force from the float The tail provides a force to balance the turbine body
	B	In the R&D stage; no quantified data are available
	C	Gulf Stream Turbines LLC, USA http://www.gulfstreamturbine.com/ Patent numbers US 6531788 (B2); US7291936 (B1); US2002158472 (A1); WO2007130479 (A2)
	D	The design concept makes sense, but no quantified data to verify its feasibility The design is based on the characteristics of Gulf stream, the feasibility and efficiency of which in Kuroshio is still difficult to assess
27. Voith Hydro	A	A 3-bladed, fixed pitch, horizontal axis turbine, having a nacelle retrieval module, is designed to operate at the depth of 30 m and above The minimum peak current speed is 3 m/s
	B	A 600 MW power plant is being planned
	C	Voith Hydro, Germany http://www.voithhydro.com/media/t331_Ocean_Current_Technologies_72dpi.pdf http://www.voithhydro.com/vh_en_paa_ocean-energy_tidal-current-power-stations.htm
	D	In spite of being applicable to deep waters, the cut-in speed is too high, perhaps disabling the turbine from harnessing energy from Kuroshio
28. Tidevannskraft	A	This system, comprised of four horizontal axis turbines, is balanced at a fixed position by a float platform and steel-made cables, the electromechanical facilities of which are placed under water The system is floatable, facilitating maintenance and lowering cost The system is easy to retrieve; likely to reduce the environment disturbance
	B	In the initial development stage; no operation test is conducted
	C	Statkraft, Norway http://www.statkraft.com
	D	The parts that float above water are likely to be damaged by harsh weather conditions No operation test is conducted; still far away from commercial operation

Name	Item	Content
29. Hydrokinetic Generator, KESC Bowsprit Generator, KESC Tidal Generator	A	N/A
	B	The concept design is in lab test stage
	C	Kinetic Energy Systems, USA
		http://www.kineticenergysystems.com/
		http://www.british-hydro.org/uploads/1072008121933PM.pdf
	D	Unable to evaluate its applicability

Vertical Axis Turbines

The vertical axis turbine has a rotation axis perpendicular to flow direction, can be classified into upright and lying types. The rectangle-shaped swept area of a vertical axis turbine makes it suitable for application in a shallow, long, and narrow water conduit. Generally, a traditional fixed pitch vertical axis turbine, operating with optimal efficiency at a higher tip speed ratio, cannot be actuated without an auxiliary motor. But the problem had been resolved by applying improved variable pitch blades [13–15]. On the other hand, the Gorlov helical turbine is also exempted from the starting problem and claimed to perform better than the traditional Darrieus counterpart.
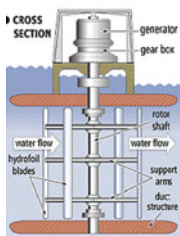
The characteristics of vertical axis turbines are summarized as follows:

- A yaw drive is not required.
- A simple blade geometry and thus a lower manufacturing cost.
- Less likely to induce cavitation.
- A lower cut-in speed.

The representative upright turbine is Blue Energy Ocean Turbine, see the first turbine of the table below, which was derived from the wind turbine patent by the French inventor Georges Darrieus in 1927 and anchored by a gravity base tethered with cables or fixed by being combined into a civil construction. A single turbine of which can generate power up to 10 kW. Currently three major projects are in progress or taking shape. The first one is regarding the 20–25 kW demo power plant in British Columbia, Canada, which aims to generate hydrogen to be used by fuel cell. The second one is the Retrofit Bridge Project, wherein Davis Hydro Turbines was installed under the bridge in Tacoma, Washington. The third one is

the electricity generation project. A 2.2-GW tide power plant will be established in San Bernardino Strait.
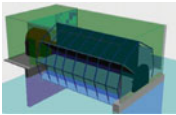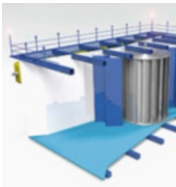
The representative lying type turbine is called OCGen, see appendix no. A-2.14, which was developed by Ocean Renewable Power Company founded in the USA in September 2004. The design and test of the turbine was completed in 2006 and April 2008, respectively. The system may consist of several turbines, the number of which can be manipulated to the advantage of different environmental conditions. This feature expands the application scope of OCGen to river, tidal, and ocean and lowers the manufacturing cost. The module comprised of four turbines can generate 1 MW of electricity in a 3 m/s ocean current. At present, projects are in progress or taking shape in Florida (West Passage), Maine (Cobscook Bay), and Alaska.

Name	Item	Content
1. Blue Energy Ocean Turbine (Davis Hydro Turbine)	A	A vertical axis turbine, centered by Davis Hydro Turbine, having a 1.2 m diameter rotor, and developed by Blue Energy, is equipped with a duct structure to guide the water flow
		The turbine is generally anchored by a gravity base
		The electricity generation capacity of a single turbine is between 5 and 25 kW
		The installation cost, depending on the turbine size, is estimated at $1,200–3,000/kW
	B	In 2009, Blue Energy Co. Ltd joined the World Energy Research project concerning commercial operation of a 200 MW system
		Currently several prototypes are being tested at University of British Columbia
	C	Blue Energy, Canada
		http://www.bluenergy.com/Technology.htm
	D	The system requires no yaw drive, boosting reliability
		The anchoring method needs redesigning to withstand earthquake forces, and the area of the parts floating above water should be reduced to mitigate the damage of typhoons
2. Kobold turbines	A	The vertical axis system, consisting of an above water platform that is anchored to a seabed by cables, is suitable for shallow waters
		The system is equipped with symmetric, variable pitch blades
	B	A full-scale 400 MW model has been operating in Melissa strait
	C	Ponte di Archimede, Italy
		http://www.pontediarchimede.com/Italy
		Patent numbers
		WO2005024226 (A1); AU2003266496 (A1); CN1839258 (A); TR200600993 (T2)
	D	"Easy to install" is the greatest strength for this system
		Can be pulled by a tugboat
		The above water platform is likely to be influenced by typhoons
		Unable to capture deep sea current energy
		The horizontal wing surface is vulnerable to cavitation damage

(continued)

Name	Item	Content
3. Gorlov Turbine	A	A vertical axis system, comprised of turbines having helical blades, is able to operate independently of wind direction. The cut-in speed can be as low as 2 ft/s
		It can produce a uniform torque and is less likely to induce cavitation at a high speed
	B	The system was tested in the Uldolmok Strait, Korea in 2002, wherein a total of 15 modules generated 1,000 kW electricity for the neighboring islands
		The Korea government is expected to construct 3.6 GW power plants (equivalent to the capacity of four thermal power plants) therein
	C	GCK Technology, USA
		http://gcktechnology.com/GCK/pg2.html
		Patent numbers
		WO2005061173 (A1); AU2003291807 (A1); WO0148374 (A2)
	D	With more complicated geometries, the helical blades cost more. How to select an appropriate blade material and lower manufacturing cost is the key to whether the gorlov system can be popularized
4. DHV Turbine	A	The vertical axis DHV turbine, equipped with a venturi-shaped shroud, and capable of boosting efficiency by 384 %, can be dependently anchored by a single pile, suspended via a tugboat, or floated via a buoyancy device
		Currently a multinational patent is being filed
	B	A test on a full-scale model is completed in 2005
		The company, Tidal Energy Pty Ltd, will cooperate with Europe, South America, Nigeria, Pakistan and Taiwan for commercial operation
	C	Tidal Energy Pty Ltd, Australia
		http://tidalenergy.net.au
		http://peswiki.com/index.php/Directory:Davidson_Hill_Venturi_by_Tidal_Energy_Pty_Ltd
		Patent numbers
		AU2003213510 (A1); WO0028210 (A1); EP1180213 (A1); JP2002544419 (T); CA2350752 (A1)
	D	A DHV turbine costs more, but enables higher efficiency, the mechanical features of which suit Kuroshio
		The cut-in speed is lower
		The casing design makes it easy to install
		Cost needs lowering, and the problem of creature invasion on the nonmoving parts needs solving
5. Atlantisstrom	A	With a relatively simple structure, a horizontal cross flow turbine system suiting deep waters, and fixed to a seabed or piles by cables, is shippable
		The blades, moving at a lower speed than ocean current, and thus less affecting the marine ecology, is proclaimed to have a service life of 20 years
	B	The simulation was conducted in 2002
		A scale-down model was tested in Dwinger in 2008
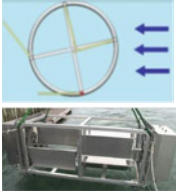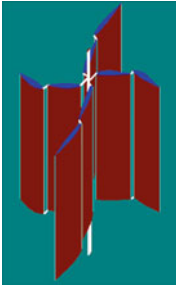
Name	Item	Content
		A model with a diameter of 8 m and a length of 20 m was tested at a speed of approximately 2 m/s in Berlin in 2009
	C	Atlantisstrom, Germany
		http://www.atlantisstrom.de/index_english.html
		Patent numbers
		WO2005108780 (A1); US20080014089 (A1); EP1747374 (A1); DE102004022844 (A1); NO20064759 (A); JP2008523286 (T)
	D	The system, anchored to a seabed directly, is not applicable to the east coast of Taiwan
		The simple and durable structure can lower the cost
		Efficiency of the system is low at a low speed flow field
		The horizontal wing surface, likely to induce cavitation, is expected to shorten the service life
6. WWTurbine	A	The water wall turbine(WWT), a cylinder-shaped structure with half of its volume submerged in water, is fixed by suspension or driving piles
		The cut-in speed is 1.5 m/s
		The cost for commercial operation is about $1,000–2,000/kW
		The electricity generation cost is estimated at $0.05/kW
	B	The 100–2,500 kW systems are scheduled to be tested
	C	Water Wall Turbine, Canada
		http://www.wwturbine.com/
		Patent numbers
		WO2007022549 (A2); US2007122279 (A1); CA2546897 (A1); ZA200709738 (A)
	D	The design is not applicable to deep waters. The area of the parts floating above water is large, likely to be damaged by harsh weather conditions
7. Neptune Proteus	A	The Proteus turbine, consisting of a vertical axis, crossflow rotor with curved blades, is mounted in a 6 m × 6 m venture diffuser duct, whose weight is balanced by buoyancy force and cable tension force
		The electromechanical facilities are installed in the buoyancy chamber
		A computer-controlled shutter within a duct, located in front of the rotor, assists the rotor in maintaining optimal power output, which, along with the venturi tube effect, greatly boosts the efficiency to 45 %
	B	Tests on the 1/10, 1/40, 1/100 scale-down models have been finished, the efficiency of which can be up to 45 %
		A full-scale prototype test has been planned since July 2010, which is expected to operate in Humber UK during 2011–2012
	C	Neptune renewable energy, UK
		http://www.neptunerenewableenergy.com/tidal_technology.php
		Patent numbers
		US2009322091 (A1); WO2008050149 (A1); EP2076671 (A1); CA2667530 (A1); AU2007310569 (A1)
	D	The proteus turbine can achieve very high efficiency. However, reliability for the computer-controlled shutter and the full-scale operation needs assessment

(continued)
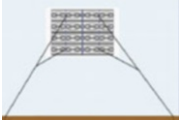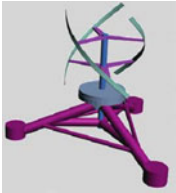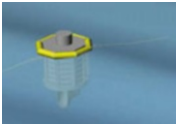
Name	Item	Content
		The design may exert a greater negative influence on marine creatures
		Typhoons are perhaps unfavorable to the floating facilities
8. EnCurrent Vertical Axis Hydro Turbine	A	The vertical axis turbine, modified from the Darrieus one and equipped with a 5 kW, 10 kW, or 25 kW permanent magnet generator, is anchored by a floating structure
		The cut-in speed is about 1.5 m/s, at which the rotational speed is 90 rpm
		The price is estimated at about $5,000/kW
	B	A 5 kW model was installed in Alaska in 2008; another 25 kW model was installed in Pointe Du Bois Manitoba, Canada
	C	New Energy Corp., Canada
		http://www.newenergycorp.ca
		Patent numbers
		WO2010006431 (A1); US2010176595 (A1)
	D	The turbine system, having been fully developed and tested, is undersized, each module of which produces a small amount of power
		Installing a numerous modules is required to achieve the desired power for a Kuroshio power plant, which increases cost and the degree of difficulty
9. OSPREY	A	A vertical axis turbine system, consisting of a platform and capable of generating electricity independently or as part of a larger system, can be anchored to a seabed directly or be fixed at the position where the buoyancy force (from the fluid acting on the float) and the cable tension force balance
		The system, benefiting from the modular design concept, can generate power ranging from 1 kW to 5 MW
		The system is proclaimed to less affect the environment
	B	A down-scale model test is finished; the test for a full-scale model, expected to generate electricity up to 10 MW, started in fall 2007
		Following the full-scale test, a series of smaller modules will be tested
	C	FreeFlow 69, UK
		http://www.freeflow69.com/
		http://pesn.com/2007/08/17/9500490_FreeFlow69/
	D	The floating platform is disadvantageous to survival in hurricanes
		Low installation cost
		The modular design is flexible
10. Hales Tidal Turbine	A	The system consists of four rotatable blades that operate via being pushed side by side by water, and are hinged on shafts, whereby the efficiency is boosted
	B	The patent is being filed
		Hales Energy Ltd. will cooperate with Kingston University, London in conducting a test and R&D
		A special 81,500 L water tank is being prepared for conducting tests exclusively on prototype turbines and generators
	C	Hales Energy Ltd, UK
		http://www.hales-turbine.co.uk
		Patent numbers
		GB2452484 (A); GB2435908 (A)

(continued)

Name	Item	Content
	D	The system, able to operate independently of wind direction, will be an appropriate option if the service life and efficiency are improved
11. HydroVolts	A	A horizontal crossflow turbine system, mainly anchored by cables, and characterized by the fact that the blades can rotate with water flow to reduce drag, can generate power of 1–25 kW
	B	An operation test on the 25 kW model is conducted in January 2010, wherein the current was generated by a large ship engine A one-day duration test was conducted in Roza Canal, verifying that the installation can be finished within 1 h
	C	HydroVolts, USA http://www.hydrovolts.com/ Patent numbers WO2010111259 (A2); US2010237626 (A1)
	D	No large-scale model is available Cost tends to increase in that this model is likely to be influenced by marine debris and creatures
12. Tideng	A	The system, resembling a traditional waterwheel, consists of 6 blades that can expand and contract radially to increase the efficiency The system is anchored by a concrete gravity base
	B	The patent is Europe is granted Test data are not available
	C	Tideng, Denmark http://www.tideng.com Patent numbers WO03029646 (A1); EP1478847 (A1); ES2309234 (T3); AT398729 (T)
	D	The addition of a control system increases the long-term operation risk, which, in comparison with others, is not suitable for commercial operation unless it can perform with particularly high efficiency
13. Neo-Aerodynamic	A	The vertical axis turbine, operable in air or water, and capable of effectively overcoming the turbulence problem, can be installed on the roof or in the backyard of a general house to satisfy the household electricity demand The patented blade design can increase the efficiency and lower the cut-in speed
	B	The patent is being filed, among which a prototype wind turbine has been tested outdoors, and a scale-down water turbine is at the test phase Neo-Aerodynamic Ltd Company is seeking sponsorship for the next stage test
	C	Neo-Aerodynamic Ltd Company, USA http://www.neo-aerodynamic.com/default.html Patent numbers WO2009068950 (A2); US2008159873 (A1)

(continued)

Name	Item	Content
	D	The system, having the advantage of low cut-in speed, is particularly suitable for a low speed flow field
		Reliability of the more complicated blade structure needs assessment to avoid blade damage and to control manufacturing and maintenance cost
14. OCGen	A	A horizontal crossflow turbine system, possibly comprised of a TGU, is fixed to a seabed
		A module consisting of 4 TGUs can generate power up to 1,000 kW in a 6 knot current
	B	The DOE (USA) sponsored a project in Sep. 2010 for a commercial scale operation test in Cobscook Bay to verify the operation reliability at the depth of 150 ft
		Operation projects are in progress in Tanana River, Alaska, Gulf Stream (Florida), Bay of Fundy, Maine, etc.
	C	Ocean Renewable Power Company, USA
		http://www.oceanrenewablepower.com
		Patent numbers
		WO2010114794 (A1); WO2009067210 (A1); WO2008051455 (A2); WO2009067209 (A1); US2010140947 (A1); US2009129928 (A1); US2009126544 (A1); US2009309365 (A1); EP2222548 (A1); EP2086830 (A2); CA2706192 (A1); CA2667134 (A1); AU2008326738 (A1); JP2010507043 (T)
15. The Pulsus Turbine	A	This system, enabling a higher rotational speed, is improved from the Darrieus turbine
		The location for deploying this turbine is flexible, depending on water depth and flow speed
	B	Norwegian Ocean Power, founded in 2009, is conducting simulation studies. The prototype is expected to come out in 2011
	C	Norwegian Ocean Power, Norway
		http://www.norwegianoceanpower.com
		Patent numbers
		WO2010107316 (A1)
	D	The turbine, anchored to a seabed by a gravity base, is not applicable to the east coast of Taiwan, along which the waters are deep
		The system has not undergone a real test, the advantages of which are not revealed
16. Water turbine	A	The vertical axis floating system is made up of several modules, the size of which is adjustable to form a power plant with a desired capacity
		It is still in the initial development stage
	B	In the lab stage
		Updated data are not available
	C	Ing Arvid Nesheim, Norway
		http://www.anwsite.com/
		Patent numbers
		WO2010077150 (A1); NO328433 (B1); NO319964 (B1)
	D	No detailed data; it is estimated to be far away from actual operation
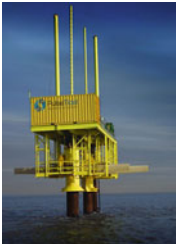
Name	Item	Content
17. Coastal Hydropower	A	A vertical axis turbine, with a venturi-shaped shroud proving to increase electricity generation by 250 %, has helical or straight blades
	B	In a lab R&D stage. The actual test status remains obscure
	C	Coastal Hydropower Corp., Canada http://coastalhydropower.com/
	D	Fluid flows toward foil sections of the helical blade at every possible angle of attack to achieve high stability of operation, and to extend the service life, an advantage for establishing a power plant, which, together with a venturi-shaped shroud, can enable the turbine to generate a large amount of electricity at a low speed current

Reciprocating Turbines

A reciprocating turbine converts the kinetic energy of the current into electricity by using an oscillating hydrofoil. The Stingray, for example, has an oscillating hydrofoil moving up and down to create change of lift and drag force, thus driving the oscillation of the hydrofoil and the hydraulic pump via the connecting rod. The pump pressurizes the working fluid to drive the generator. This type of turbine is typically suitable for shallow waters. However, the wide range of oscillations may exert a negative influence on shipping, fisheries, or ecology.

The representative model is the Stingray, see the third turbine of the table below, which was developed by The Engineering Business Limited, a UK-based branch of IHC Holland Merwede Group (Netherland). The machine controls the angle of attack of the hydrofoil to create the reciprocating movement of the connecting rod; both are driven by a hydraulic system. The design was originated in 1997 and ended up with a 150 kW prototype built in 2002 and tested in Yell Sound-Shetland in 2003. The machine can be anchored by a gravity base or by piling. The efficiency of Stingray, greatly influenced by ocean current speed, can reach 25 % to 30 % at low speed currents during flood tides.

Name	Item	Content
1. Pulse Generators	A	The turbine produces electricity by controlling angle of attack via an oil hydraulic system, as well as by making the airfoil like blade moves up and down, which overcomes the problem that a traditional large scale turbine is unable to operate in shallow waters
		An even larger blade is applicable to this system, which is mainly anchored by a fixed pile, and proclaimed to be capable of producing three times the electricity generated by a traditional turbine
	B	A 100 kW system is installed in the vicinity of the Humber estuary, UK
		A 1 MW system is scheduled to operate in 2012
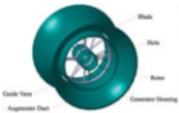
Name	Item	Content
	C	Pulse Generation, UK
		http://www.pulsegeneration.co.uk
		Patent numbers
		WO2005108781 (A1); US2006275109 (A1); US7455503 (B2); GB2426794 (A); GB2413785 (A)
	D	The system, especially designed for the shallow waters, cannot give scope to its advantage in deep waters
		The anchoring system as well as the electromechanical system needs redesigning to prevent seismic damage or influences of harsh weather conditions
2. bioStream	A	The system consists of reciprocating hydrofoils, the shape of which resembles the caudal fin of fishes such as sharks
		Taking advantage of the flow energy, the caudal fin moves side to side to generate electricity
		The single axis turbine, able to align with the flow, is applicable to any flow direction
	B	Simulations on the 250 kW, 500 kW, and 1,000 kW systems are completed; lab tests on the scale-down models were done
		Biopower Systems Ltd. signed a MOU with Hydro Tasmania (Australia) in May 2008, based on which a full-scale pilot power plant in the vicinity of the Tasmania island will be established
	C	BioPower Systems Pty Ltd, Australia
		http://www.biopowersystems.com
		Patent numbers
		US2010140933 (A1); WO2007019607 (A1); JP2008261342 (A); KR20080034477 (A); AU2006281967 (A1)
	D	"Simple structure" and "applicable to any flow direction" are the greatest advantages for this system; the efficiency needs assessment
3. Stingray	A	The turbine, anchored to a seabed by a single pile or a gravity base, controls the hydrofoil angle of attack through a simple mechanism. The hydrofoils move up and down to activate the oil hydraulic pump, whereby the generator produces electricity
	B	The project is set aside
		A 150 kW prototype is available now. Establishment of the originally scheduled 500 kW power plant is suspended due to capital shortfall
	C	The Engineering Business, UK
		http://www.engb.com
		http://www.energyvcfair.com/download_03/presentation_engb.pdf
	D	The power generation model and facilities are analogous to those for the Pulse Generators, which, however, are fully submerged in waters, thus less likely to be influenced by harsh weather conditions
		The anchoring system needs redesigning

Venturi Turbines

The venturi turbine can be categorized into two different types. One is the turbine with a venturi-shaped shroud to prevents the invasion of foreign bodies into the machine, to rectify the ocean current making it flow through the turbine more uniformly, and to accelerate the ocean current through the nozzle-type venturi to enhance the efficiency. The other type is also equipped with a venturi-shaped shroud, which takes advantage of the pressure difference induced by the accelerated fluid to introduce a secondary flow that enhances the kinetic energy of the current. This type of turbine is not required to be placed underwater and thus the installation and maintenance cost can be lowered significantly.
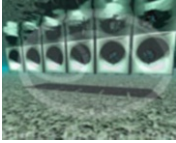
The representative model is the Clean Current Tidal Turbine, see the first turbine of the table below, developed by Clean Current Power Systems Incorporated, a Canada-based company. The design originated in 2001 and was verified in 2004. The turbine, installed inside a venturi-shaped shroud, connects to a variable speed permanent magnet generator. Each blade is connected to a permanent magnet, and the coils are installed inside the shroud. The modular model, anchored with a single pile foundation, was designed to operate at a water depth of 15 m, being capable of aligning its rotation axis with flow direction. This turbine has a 14 m-diameter rotor and can achieve an efficiency up to 50 %. The model was also installed in Race Rock, Canada in 2006, and was scheduled to operate for demonstration in Bay of Fundy in 2009, which nevertheless has never achieved successfully.

Name	Item	Content
1. Clean Current Tidal Turbine	A	The system, anchored to a seabed by a single pile or a gravity base, and equipped with a 16.8 m diameter rotor, is designed to operate in bidirectional flows at the depth of 15 m
		The magnets, connected to the blades, drive the variable speed permanent magnet generator
		Cut-in speed is about 1 m/s
		The rated power is 2.2 MW, occurring at 4.1 m/s flow
		The installation cost is about $2,500–3,000/kW
		The estimated power generation cost is $0.12–0.23/kWh
	B	The installation was finished in Race Rock in 2006; a commercial demo power plan was planned in 2009
	C	Clean Current Power Systems, Canada
		http://www.cleancurrent.com/technology
		Patent numbers
		CA2460479 (A1); WO2006029496; WO03025385 (A2)(A3); US2007284884 (A1); US20050285407 (A1); NO20071909 (A); NO20080819 (A); JP2008513650 (T); EP1789676 (A1); EP1430220 (A2); KR20070058620 (A)
	D	The structure is simple, and the electro-mechanical facilities are combined into the turbine casing, which eliminates the unnecessarily projecting parts, and makes the system more robust

Name	Item	Content
		The anchoring system needs improving to prevent damages caused by earthquakes, etc.
2. Hydro-gen	A	The semi-underwater turbine is installed inside a venturi-shape shroud, capable of augmenting water current to boost the turbine efficiency and preventing marine creature invasions as well as typhoon damage to the above-water parts
	B	A 10 kW prototype was tested in 2006 A 20 kW prototype was tested in 2008 Currently a system with rotors 14 m in diameter and 16 m in width can generate 1,000 kW electricity at the flow speed of 2 m/s The MW scale model is expected to be tested in 2010
	C	Hydro-Gen, France http://www.hydro-gen.fr/index.php?option=com_content&task=view&id=2&Itemid=3&lang=en Patent numbers GB2448393 (A); FR2913070 (A1)
	D	The semi-floating system design, able to greatly lower the installation and maintenance cost, is not applicable to the waters along east coast of Taiwan where it is frequently hit by typhoons and the sea is rough The semi-floating system is unable to effectively capture the energy of Kuroshio current located in the deep sea
3. Underwater electric kite	A	An underwater, variable pitch system, allowing to be comprised of modules of different sizes, is equipped with a "guard grating" The cut-in speed for the module with a 2 m diameter rotor is 0.2 m/s
	B	A commercial operation test was conducted in the Atlantic Ocean coast, Canada in 2006 (in cooperation with ATEC)
	C	UEK corp., Canada http://www.uekus.com/ Patent numbers WO0227151 (A1); WO0077393 (A1); WO0071890 (A1); US2002088222 (A1); US6406251 (B1); US6168373 (B1); US4205943 (A); US6139255 (A); EP1268983 (A1); ES2313913 (T3); GB2026620 (A); CA2370980 (A1); CA1099190 (A1); AU5160200 (A); AU5123500 (A); JP54160934 (A)
	D	This system, requiring high stability in current direction, can be installed in a low speed flow field, which is applicable to the waters along the east coast of Taiwan This system is proclaimed to less affect marine creatures
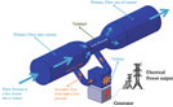
(continued)

Name	Item	Content
4. Hydrokinetic turbine	A	The system, equipped with a 3.5 m diameter rotor, installed on a floating platform, and anchored to seabed by cables, is suitable for the shallow waters The cut-in speed is below 1 m/s
	B	Two full-scale models were tested in Hasting City in 2009, the influence of which on environment is being evaluated
	C	Hydro Green Energy, USA http://www.hgenergy.com Patent numbers US2006266038 (A1); WO2007143021 (A2); RU2008137926 (A); NO20084112 (A); MX2008012361 (A); AU2004320413 (A1)
	D	The floating platform is vulnerable to harsh weather conditions The modular design is the advantage for establishing a power plant if the system can effectively capture deep sea current energy
5. Rotech Tidal Turbine (RTT)	A	The turbine, installed in a venturi-shaped shroud capable of increasing the efficiency, is operable at the water depth of 40 m and above The turbine body, supported by a heavy duty bracket, sinks to a seabed through gravity, which reduces the anchoring cost The rotor is separable from the bracket and shroud to facilitate maintenance
	B	A 1 MW prototype was tested onshore in May 2009 A commercial operation test on an 8 MW EMEC model is expected to proceed in 2010 Korea plans to satisfy the electricity needs of 200,000 households using this system by 2015
	C	Lunar Energy Power Ltd., UK http://www.lunarenergy.co.uk/ Patent numbers WO03029645 (A1); US2010148513 (A1); US2009179425 (A1); US2008265583 (A1); US2005001432 (A1); US7768145 (B2); GB2447514 (A); GB2426295 (A); GB2408294 (A); NO20075941 (A); NO20041465 (A); NZ532286 (A); MX2009009872 (A); KR20100038078 (A); KR20080018184 (A); JP2008540928 (T)
	D	This system, capable of generating a large amount of electricity with high efficiency, is applicable to deep sea environment The installation and maintenance cost for this system is lower, but the anchoring method needs redesigning due to the over deep waters along the east coast of Taiwan

Name	Item	Content
6. Hydroventuri	A	The system, especially suitable for a long and narrow water channel, is designed based on the Bernoulli's principle Driven by the pressure difference, fluid inside the venturi diffuser is accelerated, whereby the efficiency is increased
	B	A demo power plant was established in River Derwent in Derby, UK, and a suitable site in Canada, Scotland, New Zealand, etc., is sought for building a power plant
	C	Hydroventuri, UK http://www.hydroventuri.com Patent numbers US2005081517 (A1); US7150149 (B2); WO03081029 (A1); PT1488101 (E); NZ535961 (A); JP2005520984 (T)
	D	This system aims at what DHV does; the possible advantage of Hydroventuri is the low cost The large system has not come out, the applicability of which remains uncertain
7. SmarTurbine Generator	A	This system generates approximately 10 kW and 40 kW at the flow speeds of 2.25 m/s and 3 m/s, respectively No certain design method is specified. Generally the system is suspended in water
	B	Free Flow Power Ltd. is planning to test the turbine in Mississippi river
	C	Free Flow Power Corporation, USA http://www.free-flow-power.com/Technology.html
	D	The system is preliminarily designed to operate in rivers, the anchoring method of which needs improving for the deep sea Kuroshio current
8. University of Southampton	A	A The horizontal axis turbine system, installed in a shroud that is used to rectify flow direction, is operable independently of flow current in any direction The number of moving parts are greatly reduced to lower cost and to reduce risk of parts failure
	B	Currently only a small-scale prototype is being tested The inventor plans to make a commercial model come out within 5 years
	C	University of Southampton, UK http://pesn.com/2006/06/13/9500281_Southampton_Tidal_Generator/
	D	Only small-sized models are being tested; whether the large-sized counterpart can operate well remains to be experimented

Name	Item	Content
9. Spectral Marine Energy Convertor	A	The system, coming in a variety of sizes and applicable to river, tidal, and ocean currents, is designed based on the Bernoulli's principle
		A pressure difference is created when fluid flows through a venturi tube, wherein a secondary flow induced will pass the turbine to generate electricity
	B	R&D is in progress at Severn Estuary (at laboratory)
	C	Verderg, UK
		http://www.verderg.com
		http://www.verderg.com/attachments/-01_SMEC_Doc_Oct%2009.pdf
		Patent numbers
		WO2008015047 (A1); US2010207393 (A1); EP2064441 (A1); GB2443195 (A); GB2443195 (B8); CA2659578 (A1); KR20090038923 (A); JP2009545692 (T)
	D	Electricity is generated in an innovative way
		The pipe may be clogged with silt, likely to lower efficiency, which should be avoided
		Installation cost needs to be cautiously taken into account
10. Gentec Venturi	A	A 2-stage water turbine. Design data are unavailable
	B	The inventor is planning a 250 kW pilot model
	C	Greenheat Systems Ltd, UK
		http://www.macharsoft.co.uk/rmp/gentec.html
	D	The electricity generation model is not applicable to the Kuroshio current; still far away from commercial operation

Others

There are many other different types of turbines, designed with similar power generation principles but ended up with new inventions obviously different from those of the aforementioned four categories. Totally 4 items fall into this category, which are listed as follows:

名稱	項目	内容
1. Tidalsails	A	This system, capable of being anchored to a seabed by cables and having generators and anchoring mechanism in place on the two endpoints, harnesses ocean current energy in a different way
		A series of sails, pulled by current, are affixed to wires, pulled by said sails, on a triangle-shaped structure; the pulled wires pull sheaves that turn generators

名稱	項目	內容
	B	A 1/40 scale-down model was tested in 2006 (at laboratory) A larger model was tested in 2008 in Lukksundet A 200–250 m long prototype system will be tested in river currents A 1 km long full-scale model will be installed in Kvalsudent
	C	Tidalsails, Norway http://www.tidalsails.com
	D	The system, unable to react to the change in flow direction, will achieve lower efficiency (as flow direction changes) An innovative design, featured by fewer moving parts, can lower the cost for installation and maintenance No large scale test is conducted
2. HydroCoil	A	This system is suitable for being installed downstream a dam or in a water conduit where the water level difference is about a single-story height The small turbine system has blades with unequal pitch, aiming to increase efficiency; water flows in from the wider pitch side, and flow out from the narrower pitch side A single turbine generates approximately 1.5 kW electricity
	B	The US patent is granted; a scale-down model is being tested Sponsorship is sought to conduct full-scale tests at several location, which costs $350,000
	C	HydroCoil Power, Inc., USA http://www.hydrocoilpower.com/1summaryhomepage.html Patent numbers US6357997 (B1); US6626638 (B2); US2002062644 (A1)
	D	Whether a larger counterpart can operate is a problem. The blade geometry is complicated, increasing the cost
3. VIVACE (Vortex Induced Vibrations Aquatic Clean Energy)	A	Vortex Hydro Energy Ltd is authorized the patent by University of Michigan, wherein the lateral vibration of approximately 1 Hz, induced by vortex flows in the wake of a cylinder, is used as the driving force to generate electricity, which proves not to impose a great influence on marine creatures The system, able to operate at the flow speed of 2–4 knots, at which a traditional turbine, whose cut-in speed is about 4 knots, cannot be absolutely activated
	B	A four cylinder prototype was made in 2010, which was field-tested in the St. Clair River at Port Huron in spring 2010
	C	Vortex Hydro Energy, USA http://www.vortexhydroenergy.com/ Patent numbers WO2006055393 (A2); US2008295509 (A1); US7493759 (B2); EP1812709 (A2)
	D	The cut-in speed is low, meeting the requirement, but the gross power output remains unknown, which should be taken into account

(continued)

名稱	項目	內容
4. Flumill Power Tower	A	The system, consisting of four key elements: buoyancy, a robust turbine, a permanent magnet synchronous generator, and a simple 4 point foundation, can generate 4 MW electricity at 3 m/s flow speed
	B	In laboratory simulation stage; no test data
	C	Flumill, UK http://www.flumill.co.uk/power-tower Patent numbers US2010266406 (A1); WO2009093909 (A1); NO327873 (B1); CA2709527 (A1); AU2009206829 (A1)

References

[1] Myers LE, Bahaj AS (2012) An experimental investigation simulating flow effects in first generation marine current energy converter arrays. Renew Energy 37(1):28–36. doi:10.1016/j.renene.2011.03.043

[2] Batten WMJ, Bahaj AS, Molland AF, Chaplin JR (2008) The prediction of the hydrodynamic performance of marine current turbines. Renew Energy 33(5): 1085–1096. doi:10.1016/j.renene.2007.05.043

[3] Bahaj AS, Batten WMJ, McCann G (2007) Experimental verifications of numerical predictions for the hydrodynamic performance of horizontal axis marine current turbines. Renew Energy 32(15):2479–2490. doi:10.1016/j.renene. 2007.10.001

[4] Bahaj AS, Molland AF, Chaplin JR (2007) Power and thrust measurements of marine current turbines under various hydrodynamic flow conditions in a cavitation tunnel and a towing tank. Renew Energy 32:407–426. doi:10.1016/j.renene.2006.01.012

[5] Batten WMJ, Bahaj AS, Molland AF, Chaplin JR (2007) Experimentally validated numerical method for the hydrodynamic design of horizontal axis tidal turbines. Ocean Eng 34(7):1013–1020. doi:10.1016/j.oceaneng. 2006.04.008

[6] Batten WMJ, Bahaj AS, Molland AF, Chaplin JR (2006) Hydrodynamics of marine current turbines. Renew Energy 31(2):249–256. doi:10.1016/j.renene. 2005.08.020

[7] Zanette J, Imbault D, Tourabi A (2010) A design methodology for cross flow water turbines. Renew Energy 35:997–1009. doi:10.1016/j.renene. 2009.09.014

[8] Goundar JN, Ahmed MR, Lee Y-H (2011) Numerical and experimental studies on hydrofoils for marine current turbines. Renew Energy 42:173–179. doi:10.1016/j.renene.2011.07.048

[9] VanZwieten J, Driscoll FR, Leonessa A, Deane G (2006) Design of a prototype ocean current turbine—part I: mathematical modeling and dynamics simulation. Ocean Eng 33:1485–1521. doi:10.1016/j.oceaneng.2005.10.005

[10] VanZwieten J, Driscoll FR, Leonessa A, Deane G (2006) Design of a prototype ocean current turbine—part II: flight control system. Ocean Eng 33:1522–1551. doi:10.1016/j.oceaneng.2005.10.006

[11] Myers L, Bahaj AS (2006) Power output performance characteristics of a horizontal axis marine current turbine. Renew Energy 31(2):197–208. doi:10.1016/j.renene.2005.08.022

[12] Molland AF, Bahaj AS, Chaplin JR, Batten WMJ (2004) Measurements and predictions of forces, pressures and cavitation on 2-D sections suitable for marine current turbines. In: Shenoi RA (ed) Proceedings of the Institution of Mechanical Engineers, Part M: Journal of Engineering for the Maritime Environment. University of Southampton, UK, pp 127–138. doi:10.1243/1475090041651412

[13] Antheaume S, Maıtre T, Achard JL (2008) Hydraulic Darrieus turbines efficiency for free fluid flow conditions versus power farms conditions. Renew Energy 33:2186–2198. doi:10.1016/j.renene.2007.12.022

[14] (2006) Variable pitch foil vertical axis tidal turbine. Edinburgh Designs Ltd
[15] Coiro DP, Nicolosi F, De Marco A, Melone S, Montella F (2005) Dynamic behavior of novel vertical axis tidal current turbine: numerical and experimental investigations. In: Chung JS, Hong SW, Koo J, Komai T, Koterayama W (eds) The proceedings of 15th international offshore and polar engineering conference, Seoul, Korea, 19–24 June 2005

Appendix B: Design Characteristics of the Gulf Stream Turbine

The Gulf Stream Turbine (or GST) has a triangle-shaped structure (see Fig. 2.2) and is composed of two contra-rotating three-bladed rotors and a major float. The generator is accommodated in the watertight nacelle and serves as a ballast to stabilize the turbine body by being placed at the bottom of the GST.

The main float, located above the center of the turbine, is equipped with a tail to maintain the body orientation. The design of the volume and shape of rods between the main float and watertight nacelle shall be designed with a streamline shape to minimize the influence the wake on the rotor performance. Under the triangle-shaped turbine body is a rotatable anchor bearing with which the turbine is anchored on the relay platform.

The turbine has four mechanical stability mechanisms. The first mechanism is the tail stabilizer, consisting of a vertical and a horizontal stabilizer. The former ensures alignment between the rotation axes and flow direction. The latter stabilizes the turbine body by providing a restoring torque and makes the turbine operate at the designed depth.

The second mechanism is that the center of drag is located behind the anchoring bearing. When the turbine body pitches or yaws, the drag force and anchoring force will generate an opposing torque, returning the turbine body to an equilibrium position.

The third mechanism is that the mass center is located below the center of buoyancy. When the turbine pitches or rolls, the torque generated by buoyancy and gravity will move the turbine back to the equilibrium position.

The fourth mechanism is that, once the turbine body yaws, an opposing torque generated by the bilateral symmetry of the turbine body, including the contra-rotating rotors, helps the turbine body return to the equilibrium position.

In May 2011 John H. Robson was granted two patents, numbered US 6531788 and US 7291936. The data of these patents are shown as follows:

Patent (1)
- Number: US 7531788
- Year: 2003
- Inventor: John H. Robson
- Brief description

This patent describes the structure and controlling mechanism, the two major concepts to be protected, for said horizontal axis underwater turbines, which claims 98 items illustrated by 32 diagrams. The important disclosures are as follows:

- Carbon fiber composite materials are used as the base to reduce the maintenance cost.
- The turbine mass center is below the buoyancy center to increase stability.
- The turbine body is equipped with a vertical stabilizer, including the analogous facilities above and below said body, to boost directional stability.
- The horizontal stabilizer at the tail is to keep the turbine body at the desired depth.
- The depth of the turbine body that possesses several controlling valves and compartments can be remotely controlled by manipulating the amount of water injected, whereby the position of mass center and pitch angle are shifted.
- A turbine equipped with two carbon fiber-based contra-rotating rotors.

Patent (2)
- Number: US 7291936
- Year: 200.
- Inventor: John H. Robson
- Brief descriptions

This patent, investigating the turbine depth control system in details, supplements the patent numbered US 6531788, which claims 6 items, illustrated by 16 diagrams, as follows:

The pitch angle of a turbine, the operation depth of which is detected via a pressure monitor system, can be manipulated by activating the pump system to control the water amount injected to the two compartments to the front and the rear of the main float so as to make the turbine ascend or descend.

Prior to surfacing of the turbine, the grid and anchoring cables will be cut, and the ballast water will be drained using the pressurized ballast water purging system, wherein the front cabinet drains water faster than the rear one, making the turbine nose side face up to creates more buoyancy.

Appendix C: Shape Functions, Stiffness and Mass Matrices of Platform Elements

In Chap. 4 we show the derivation of force balance equation of the relay platform, in which the shape functions, stiffness matrices, and mass matrices of pipes and cables are shown in the following.

(a) Shape functions of the line (cable) and pipe (tube) elements [1, 2]:

$$
{}_{cable}\mathbf{N} = \begin{bmatrix} 1 - \frac{x}{l_c} & 0 & 0 & \frac{x}{l_c} & 0 & 0 \\ 0 & 1 - \frac{x}{l_c} & 0 & 0 & \frac{x}{l_c} & 0 \\ 0 & 0 & 1 - \frac{x}{l_c} & 0 & 0 & \frac{x}{l_c} \end{bmatrix},
\tag{C.1}
$$

$$
{}_{pipe}\mathbf{N} = \begin{bmatrix}
N_1 & 0 & 0 & 0 & 0 & 0 & N_2 & 0 & 0 & 0 & 0 & 0 \\
0 & N_3 & 0 & 0 & 0 & N_4 & 0 & N_5 & 0 & 0 & 0 & N_6 \\
0 & 0 & N_3 & 0 & -N_4 & 0 & 0 & 0 & N_5 & 0 & -N_6 & 0 \\
0 & 0 & 0 & N_1 & 0 & 0 & 0 & 0 & 0 & N_2 & 0 & 0 \\
0 & 0 & \frac{-\partial N_3}{\partial x} & 0 & \frac{\partial N_4}{\partial x} & 0 & 0 & 0 & \frac{-\partial N_5}{\partial x} & 0 & \frac{\partial N_6}{\partial x} & 0 \\
0 & \frac{\partial N_3}{\partial x} & 0 & 0 & 0 & \frac{\partial N_4}{\partial x} & 0 & \frac{\partial N_5}{\partial x} & 0 & 0 & 0 & \frac{\partial N_6}{\partial x}
\end{bmatrix},
$$

$$
\tag{C.2}
$$

where $N_1 = 1 - \xi, N_2 = \xi, N_3 = 2\xi^3 - 3\xi^2 + 1, N_4 = l_p\left(\xi^3 - 2\xi^2 + \xi\right), N_5 = -2\xi^3 + 3\xi^2, N_6 = l_p\left(\xi^3 - \xi^2\right), \xi = \frac{x}{l_p}, l_c$ and l_p are the lengths of the line and pipe elements.

(b) Stiffness matrices of the line (cable) and pipe (tube) elements [1, 3]:

$$
_{cable}\mathbf{K}^e =
\begin{bmatrix}
E_c A_c/l_c & & & & & \\
0 & 0 & & & symm. & \\
0 & 0 & 0 & & & \\
-E_c A_c/l_c & 0 & 0 & E_c A_c/l_c & & \\
0 & 0 & 0 & 0 & 0 & \\
0 & 0 & 0 & 0 & 0 & 0
\end{bmatrix},
\tag{C.3}
$$

$$
_{pipe}\mathbf{K}^e =
\begin{bmatrix}
E_p A_p/l_p & & & & & & & & & & & \\
0 & a_1 & & & & & & & & & & \\
0 & 0 & a_1 & & & & & & & & & \\
0 & 0 & 0 & GJ/l_p & & & symm. & & & & & \\
0 & 0 & -a_2 & 0 & a_3 & & & & & & & \\
0 & a_2 & 0 & 0 & 0 & a_3 & & & & & & \\
-E_p A_p/l_p & 0 & 0 & 0 & 0 & 0 & E_p A_p/l_p & & & & & \\
0 & -a_1 & 0 & 0 & 0 & -a_2 & 0 & a_1 & & & & \\
0 & 0 & -a_1 & 0 & a_2 & 0 & 0 & 0 & a_1 & & & \\
0 & 0 & 0 & -GJ/l_p & 0 & 0 & 0 & 0 & 0 & GJ/l_p & & \\
0 & 0 & -a_2 & 0 & a_4 & 0 & 0 & 0 & a_2 & 0 & a_3 & \\
0 & a_2 & 0 & 0 & 0 & a_4 & 0 & -a_2 & 0 & 0 & 0 & a_3
\end{bmatrix},
\tag{C.4}
$$

where E_c and E_p are the elastic coefficients of the line and pipe elements, G is the shear modulus of the pipe element, $A_c = \frac{\pi}{4}D_c^2$ and $A_p = \frac{\pi}{4}\left(D_o^2 - D_i^2\right)$ are the cross-sectional areas of the line and pipe elements, D_c is the diameter of the cable element, D_o and D_i are the outer and inner diameters of the pipe element, $J = 2I = \frac{\pi}{32}\left(D_o^4 - D_i^4\right)$, $a_1 = \frac{12E_pI}{l_p^3(1+\phi)}$, $a_2 = \frac{6E_pI}{l_p^2(1+\phi)}$, $a_3 = \frac{(4+\phi)E_pI}{l_p(1+\phi)}$, $a_4 = \frac{(2-\phi)E_pI}{l_p(1+\phi)}$, and $\phi = \frac{24E_pI}{GA_pl_p^2}$.

(c) Mass matrices of the line (cable) and pipe (tube) elements [1, 3]:

$$
_{cable}\mathbf{M}^e = \rho_c A_c l_c
\begin{bmatrix}
(1/3)\frac{m_w}{m_w+m_{add}} & & & & & \\
0 & 1/3 & & & symm. & \\
0 & 0 & 1/3 & & & \\
(1/6)\frac{m_w}{m_w+m_{add}} & 0 & 0 & (1/3)\frac{m_w}{m_w+m_{add}} & & \\
0 & 1/6 & 0 & 0 & 1/3 & \\
0 & 0 & 1/6 & 0 & 0 & 1/3
\end{bmatrix},
\tag{C.5}
$$

$$_{pipe}\mathbf{M}^e = \rho_p A_p l_p \begin{bmatrix} \frac{M_w}{3(M_w+M_{add})} & & & & & & & & & & & \\ 0 & A_1 & & & & & & & & & & \\ 0 & 0 & A_1 & & & & & & & & & \\ 0 & 0 & 0 & \frac{M_w J}{3(M_w+M_{add})A_p} & & & \text{symm.} & & & & & \\ 0 & 0 & -A_3 & 0 & A_5 & & & & & & & \\ 0 & A_3 & 0 & 0 & 0 & A_5 & & & & & & \\ \frac{M_w}{6(M_w+M_{add})} & 0 & 0 & 0 & 0 & 0 & \frac{M_w}{3(M_w+M_{add})} & & & & & \\ 0 & A_2 & 0 & 0 & 0 & A_4 & 0 & A_1 & & & & \\ 0 & 0 & A_2 & 0 & -A_4 & 0 & 0 & 0 & A_1 & & & \\ 0 & 0 & 0 & \frac{M_w J}{6(M_w+M_{add})A_p} & 0 & 0 & 0 & 0 & 0 & \frac{M_w J}{3(M_w+M_{add})A_p} & & \\ 0 & 0 & A_4 & 0 & A_6 & 0 & 0 & 0 & A_3 & 0 & A_5 & \\ 0 & -A_4 & 0 & 0 & 0 & A_6 & 0 & -A_3 & 0 & 0 & 0 & A_5 \end{bmatrix},$$

$$(C.6)$$

where $m_w = \rho_c A_c l_c$, $m_{add} = C_I \rho_w A_c l_c$, C_I is the added mass coefficient, $M_w = \rho_p A_p l_p$,
$M_{add} = C_I \rho_w A_p l_p$, $A_1 = \left[(13/35) + (7\phi/10) + \left(\phi^2/3\right) + \left(6I \big/ 5A_p l_p^2\right) \right] \big/ (1+\phi)^2$,
$A_2 = \left[(9/70) + (3\phi/10) + \left(\phi^2/6\right) - \left(6I \big/ 5A_p l_p^2\right) \right] \big/ (1+\phi)^2$, $A_3 = \{(11/210) + (11\phi/120) + \left(\phi^2/24\right) + [(1/10) - (\phi/2)] \left(I \big/ A_p l_p^2\right)\} l_p \big/ (1+\phi)^2$,
$A_4 = \left\{ (13/420) + (3\phi/40) + \left(\phi^2/24\right) - [(1/10) - (\phi/2)] \left(I \big/ A_p l_p^2\right) \right\}$
$l_p \big/ (1+\phi)^2$, $A_5 = \left\{ (1/105) + (\phi/60) + \left(\phi^2/120\right) + [(2/15) + (\phi/6) + \left(\phi^2/3\right)] \left(I \big/ A_p l_p^2\right) \right\} l_p^2 \big/ (1+\phi)^2$, $A_6 = \left\{ (1/140) + (\phi/60) + \left(\phi^2/120\right) + [(1/30) + (\phi/6) - \left(\phi^2/6\right)] \left(I \big/ A_p l_p^2\right) \right\} l_p^2 \big/ (1+\phi)^2$.

References

[1] ANSYS@Theory reference for the mechanical APDL and mechanical applications, release 12.1, Help System, ANSYS Inc.
[2] Luo Y (2008) An efficient 3D timoshenko beam element with consistent shape functions. Adv Theor Appl Mech 1:95–106
[3] Przemieniecki JS (1968) Theory of matrix structural analysis. McGraw-Hill, New York
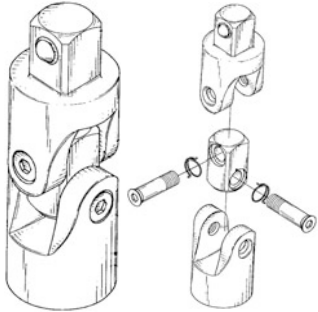
Appendix D: Options of Universal Joint, Cable, and Anchor for Relay Platform

The options for the three main components of the relay platform are listed in this appendix section. Among these options, only a universal joint type which is similar to that applied to the proposed relay platform could be found in the literature. However, many other universal joint types may be developed based on the design principles described by Seherr-Thoss et al. [1]. Besides, the options for the cable are according to their material properties. Thus the synthesis fiber rope that provides light weighted and high strength characteristics is more suitable for the undersea structures than the heavy steel wire rope. The rope construction type is one of the important factors determining its mechanical properties, which will be described later. Finally, several anchoring methods are surveyed, providing the suggestions of the permanent anchor under the andesite strata along the eastern sea area of Taiwan. The options for the three components are described respectively as follows:

Universal Joint

A typical universal joint (Hooke joint) has an identical translation and axial rotation between its two ends, and the non-axial degrees of freedom can rotate freely. For the relay platform, the non-axial degrees of freedom should be restricted to certain range to maintain the platform stability, thus the torsion springs are put in the universal joint to absorb the non-axial bending moments. The torsion springs help recover the joint's relative rotations while the active load varies or disappears (Table D.1).

Table D.1 The option of the universal joint for the relay platform

Title	Automatic recovered universal joint (Taiwan patent no. 468734)
Sketch	
Author	Zhen-Cai Zhang [2]
Characteristics	Torsion springs are inserted into the pivot of the joint, resulting in reaction moments to recover the rotations under the action of bending forces. The degrees of bending can be controlled by the torsional stiffness of the spring

Cable

The conventional rope materials for ocean engineering can be categorized by steel wire and synthesis fiber. Due to the high strength, steel wires are usually applied to the anchor chain. Nevertheless, it does not suitable for the undersea relay platform since the high density is adverse to the buoyancy especially for the deep-sea structure and thus the additional pontoons may be used to float the platform. In addition, the unfavorable steel corrosion increases the maintenance cost. All the above disadvantages prompted engineers to use the substitute material, the synthesis fiber rope, for ocean engineering. Synthesis fiber ropes do not corrode with the seawater, have high tensile strength, and the rope performance depends on the types of rope construction. The strength performance can be improved by using a particular construction method and the wired diameter. Table D.2 presents the general properties of fibers used in the production of ropes as well as steel wire [3].
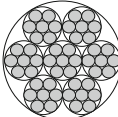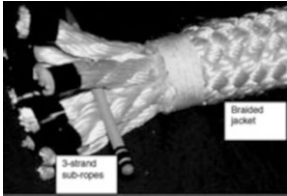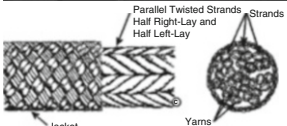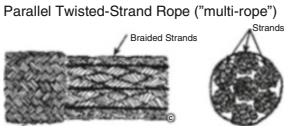
Table D.2 General fiber properties [3]

Fiber	Characteristics
Steel	• Heavier than water • High strength • Corrodes
Nylon (Polyamide)	• Lighter than water • 10−15 % wet strength loss • Poor wet internal abrasion resistance • Moderate creep
PET (Polyester)	• Slight heavier than water • Good wet internal abrasion resistance • Low creep
PP (Polypropylene)	• Lighter than water • Low strength • Moderate creep

The proposed relay platform can be categorized as a taut leg mooring system. The cable's weight which is slight heavier than water can be balanced with the mooring system to support a floating structure and to reduce the exerted force on the cable. Many are the advantages in using the mooring design taut leg for polyester fibers, namely [3]: (1) low creep and good creep rupture resistance; (2) good fatigue performance; (3) low sensitivity to alternate tension compression; (4) low hysteresis; (5) elasticity of synthetic line provides the restoring force, i.e., there is a favorable force vector to restore the platform to its neutral position; (6) reduction of mooring line weight hence better vessel payload; (7) more efficient system allowing a smaller footprint in the ocean; (8) lower cost; (9) due to its lower tensile stiffness an extreme reduction is visible/verified in line dynamic tension; (10) very low rate of hydrolysis; (11) corrosion resistance; (12) easy handling and subsequent simpler and better installation techniques; (13) in most cases lower vessel offset.

According to the analysis results, the maximum cable force exerted by the relay platform with turbines is about 1.8 MN. The options of the cable with its construction method and diameter for the relay platform are presented in Table D.3.

Table D.3 The options of the cable for the relay platform

Construction type	Diameter (strength)	Figure	Characteristics
7 strand jacketed wire rope [4]	96 mm (2.7 MN) 160 mm (6.86 MN)	(cross-section)	The 7 strand jacketed wire rope is one of the common construction methods, which is six strands helically wound around a center strand (6 around 1). The cross-sectional diameter can be determined by the strand diameter
Parallel strand jacketed wire rope [4]	96 mm (2.773 MN) 160 mm (6 MN)	[4] [5] Parallel Twisted-Strand Rope ("multi-rope") [5] Parallel Braided-Strand Rope ("multi rope")	The cores of the parallel strand ropes are usually constructed in one of the following ways [4]: "1. Three-strand laid ropes with a long ray length, half S and half Z lay. 2. Braided ropes with a long braid pitch. 3. Multiple ply, twisted yarns, half S and half Z twist." Parallel strand ropes provide excellent strength conversion from fiber strength to rope strength in large sizes if all the elements are tensioned equally and termination is efficient

Anchor

The relay platform is exerted by great buoyancy and turbine forces. Cables connected with the relay platform should be anchored to the rock formation under the seabed. To increase the drag for the anchor, the screw-type anchor can be applied and drilled into the seabed. The drilling method, the anchor positioning, and the cable connecting are also important problems under construction. Table D.4 presents two optional patents for the anchor system under construction.

Table D.4 The options of the anchor method for the relay platform

Title	Method and system for anchoring a buoy via a screw-type anchor [6]
Drawing	
Procedure	(1) Dropping a buoy drilling anchoring system, where the anchoring drilling device and the supported cable are equipped with buoys; releasing the buoy with the cable after settling down the drilling device to mark a predetermined location
	(2) Activating the retrievable buoy anchoring drilling device after a predetermined delay
	(3) Drilling and anchoring the penetrable anchor means into the earth's surface
	(4) Retrieving the retrievable buoy anchoring drilling device; disconnecting retrievable buoy anchoring drilling device from anchorable marker buoy via a quick disconnect coupler; automatically deploying floatation buoy member to a top surface of water from underwater
Characteristics	This patent provides a concept to mark the anchoring location via the buoy releasing during the anchoring procedure. The marker buoy connected with the cable directly supports the following works for the relay platform

Title	Mooring system [7]
Drawing	
Procedure	(1) Settling down the drilling device with its supporting frame with the right angle on the seabed
	(2) Drilling the anchor point into the seabed to a particular depth using the coiled tubing and a motor driving drill bit driven by a rotating shaft inside the coiled tubing

Table D.4 (continued)

Title	Mooring system [7]
	(3) When the mooring apparatus has been lowered to the required depth, the securement member opens to its pyramidal form to ensure that it is difficult to drag through the seabed material. Once at the required depth setting material such as cement can be pumped down the tubing and the anchor set permanently into the seabed
	(4) When the mooring point is no longer required and the mooring apparatus is to be retrieved, the securement member can be detached from the mooring post
Characteristics	This patent is designed for several mooring apparatus (one type is mentioned above), where the securement member can open to a pyramidal form to provide better anchoring performance. The mooring apparatus can be retrieved but the securement member will be left under the seabed if it opens

References

[1] Seherr-Thoss HC, Schmelz F, Aucktor E (2006) Universal joints and driveshafts – analysis, design, applications. Springer, Berlin
[2] Zhang ZC. Automatic recovered universal joint (in Chinese). Taiwan Patent 468734, 11 Dec 200.
[3] Deopura BL, Alagirusamy R, Joshi M, Gupta B (eds) (2008) Polyester and polyamides. CRC, Boca Raton, FL
[4] McKenna HA, Hearle JWS, O'Hear N (2004) Handbook of fibre rope technology. Woodhead Publishing, Cambridge, GBR
[5] (1999) ABS guidance notes on the application of synthetic ropes for offshore mooring. American Bureau of Shipping
[6] Brown JD. Method and system for anchoring a buoy via a screw-type anchor. US Patent 6066015, 23 May 200.
[7] Head P. Mooring system. US Patent 6223671, 1 May 200.

Appendix E: Cost Comparison of the Tidal and Kuroshio Power Plants

Since 2003, the Electric Power Research Institute (or EPRI) of the USA has conducted a series of marine energy assessments (known as the Tidal In-Stream Energy Conservation (TISEC) program), including seven potentially feasible tidal power plant sites in North America. The locations of the seven sites are shown in Fig. E.1, with four in the northeastern USA and three on the Pacific coast. Their locations in natural bays or estuaries at high latitudes ensure a large tidal range for potentially high-quality tidal power.

Fig. E.1 Locations of seven TISEC tidal power plants

Construction Data

Table E.1 summarizes the engineering data for the seven tidal power plants, showing that the Nova Scotia (NS) plant has the highest energy density at 4.5 kW/m^2, while that in Massachusetts (MA) has the lowest at 0.95 kW/m^2. These sites also have the highest and lowest power reserves. While the New Brunswick (NB) plant has developable energy reserves of 20 %, the level is about 15 % for the other sites. Each site has an average depth ranging from 25 to 65 m, with seabed geology consisting of layers of sandy sediments, gravel sands, rocks, sediments, and gravel. The Nova Scotia site features the largest number of turbines (250), while Massachusetts has the fewest (9).

Table E.1 Engineering data for the seven tidal plants

Item	Site						
	AK	WA	CA	MA	ME	NB	NS
Power density (kw/m^2)	1.6	1.7	3.2	0.95	2.9	0.94	4.5
Cross section (1,000 m^2)	72.5	62.6	74.7	14	36	60	225
Power Available (MW)	116	106	237	13.3	104	56.4	1,013
Extractable (MW)	17.4	16	35.5	2.0	15.6	12	152
Depth (ave/est) (m)	29/59	42/68	54/96	25/45	47/105	60/100	65/100
Seabed composition	Sand	Gravel sand	Rock sedi	Sedi	Rock	Rock sedi	Rock gravel
# of Turbines	66	68	40	9	12	66	250

Construction Costs

Figure E.2 presents the construction costs for the seven plants (pilot plant vs. commercial plant). The cost analyses are elucidated as follows:

- The construction cost for the pilot plant is 2.5–3.5 times that of the commercial plant, where an average multiple of 3 is considered reasonable. The relatively high cost of the pilot plant is due to the high cost of testing, and the small scale of the pilot plant results in a high per-unit production cost.
- The cost structure is closely tied to the site selection. Massachusetts (MA) is the most expensive site due to its small scale and low energy density, whereas Nova Scotia's (NS) large scale and high energy density makes it the lowest cost site. Visible scale size and energy density are the key factors to determine construction costs.
- For plants with comparatively reasonable costs (e.g., AK, WA, CA, ME, and NS), the two main elements in the cost structure are the turbine and anchorage structure, on average accounting for 60 to 80 % of total construction costs, or as much as 90 % when turbine installation is included.
- The MA and NB plants are situated further offshore, resulting in increased complexity and higher costs for cable and turbine installation.
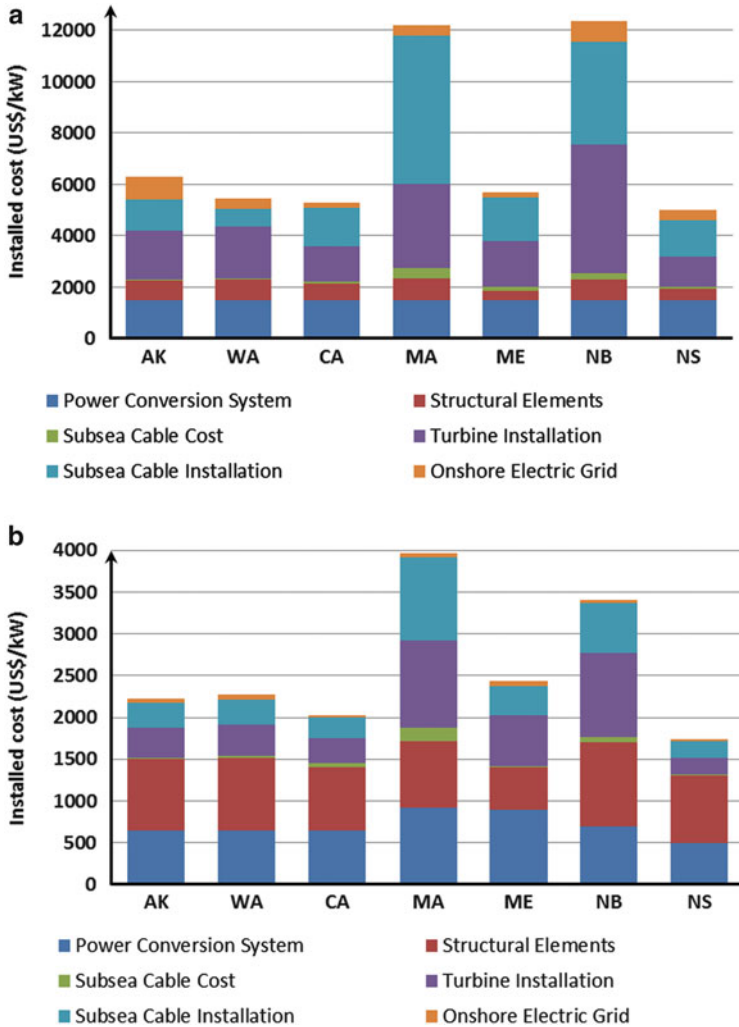
Fig. E.2 Construction cost structures for the seven plants. *AK* Alaska, *WA* Washington, *CA* California, *MA* Massachusetts, *ME* Maine, *NB* New Brunswick, *NS* Nova Scotia. (**a**) Pilot plant, (**b**) Commercial plant

Power Generation Costs

Figure E.3 summarizes the power generation cost data for the seven power plants. NS has the greatest generating capacity of 1,140 GWh due to its greatest number of turbines (250 units). With installation costs reaching USD486m, operating and maintenance costs could reach USD18m. MA has the smallest capacity with only nine turbines generating 1.5 GWh annually from an installation cost of USD17m and operating and maintenance costs of USD600,000.

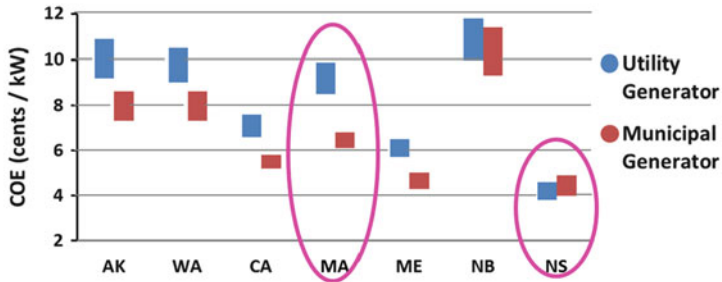| Item Site	AK	WA	CA	MA	ME	NB	NS
# of Turbines	66	68	40	9	12	66	250
Annual Energy (GWh)	128	121	129	1.5	40	64	1140
Installed Cost (M$)	110	103	90	17	24	68	486
Annual O&M Cost (M$)	4.1	3.8	3.6	0.6	1	2.3	18

Fig. E.3 Generating costs for the seven planned TISEC tidal power plants. (*Above*) Plant installed capacity, generating capacity, construction costs, operating and maintenance costs. (*Below*) Generating costs for each plant, divided into generating costs and end-user prices

Figure E.3 shows the relationship between each plant's generating costs and scale. For example, generating costs at NS are close to end-user costs at about USD0.042/kWh due to the short distance between the plant and the end user. The generating cost for NB is higher than the average end-user costs due to the poor seabed geology conditions requiring stronger anchorages and increasing the complexity of the engineering involved. These factors raise overall costs, thus pushing up generating costs.

Generally speaking, the average generating cost paid by end user is higher than the plant's generating cost because varying degrees of wear and tear in the process of power transmission result in higher costs. However, shorter distances between the plant and the end user (as in NS and NB) will reduce these costs. On average, the cost of electricity from the seven tidal power plants ranged from USD0.04 to USD0.08/kWh, while the cost to the end user ranged from USD0.06 to USD0.11/kWh. In NTD, the end-user cost ranges from NTD1.8/kWh to NTD3.3/kWh.

Estimated Generating Costs for Commercial Kuroshio Power Plants

Unlike the aforementioned tidal power plants, which are built in shallow water only several tens of meters deep, Kuroshio power plants are built in seas several hundred meters deep, entailing different construction and maintenance cost

structures, which affect the cost of power generation. The differences include the following:

- Tidal turbines require a sturdy, strong, and rigid anchorage structure, pushing up costs; Kuroshio turbines are anchored by a single cable to the relay platform, thus reducing overall costs for the anchorage structure.
- Kuroshio power plants are situated in deep seas, entailing marine engineering which is significantly more expensive than for shallow-water tidal power plants.
- The power feed from the Kuroshio power plant does not lie on the seabed, but rather runs from the relay platform to the transmission and distribution power station onshore, thus entailing lower cable construction costs than for tidal power plants.
- Aside from these differences, the turbine and cable costs should be similar for both types of power plant.

Due to the novelty of the Kuroshio power plant, many cost details are still unknowable. In addition, the cost comparison provided above shows the relative disparity between costs for Kuroshio and tidal power plants, but the extent of that disparity is still impossible to be determined accurately. Therefore, we use the average cost for the seven tidal power plants as a benchmark for cost estimates for the Kuroshio power plant. That is to say, the construction cost is USD2,000/kW (about NTD60,000), while the generation cost is USD0.08/kWh (about NTD2.4/kWh). Here, USD1 equivalents to NTD30.

These standards are used to estimate the construction costs of a 100 MW Kuroshio power plant at about NTD6b. The detailed operating costs are estimated as follows:

- Annual power generation: $100 \times 1,000$ kW $\times$ 365 days/year $\times$ 24 h/day $\times$ $0.7 = 613.2$ m kWh/year (assuming a capacity factor of 0.7).
- Annual power generation income: 613.2 m kWh/year $\times$ NTD2.8/kWh = NTD1.717b/year (this assumes prices of NTD2.8/kWh, which are stipulated for offshore wind power under the provisions of the National Renewable Energy Development Act).
- Annual income from selling carbon credits: 613.2 m kWh/year $\times$ 0.8 kg/kWh $\times$ USD20/ton $\times$ NTD30/USD1 = NTD294m/year. Assuming that each kWh is matched by a 0.8 Kg carbon credit and that each ton of carbon is worth USD20 (2008 European futures market price).
- Power plant operations costs: NTD200m/year, including maintenance (no maintenance during the first 5 years), loans and interest, payroll and general expenses (this figure requires careful evaluation).
- Annual net income = 1,717 + 314 − 2 = NTD1,831m.
- Recovery period: 65/18.31 = 3.55 years.
- Assuming the plant has a 10-year life span, the cost of each generated kWh equals NTD6b (10 years $\times$ 613.2 m kWh/year) = NTD0.98/kWh, which is certainly competitive with the USD0.08/KWh (NTD2.4/kWh) cost for tidal power plants.

Cost Uncertainties in Kuroshio Plant Construction

Dr. Chia-Hao Ko of the Houston Marine Engineering Corp. provided a detailed description of the cost calculation uncertainties inherent in the construction of a Kuroshio power plant. His findings are summarized as follows:

- A significant part of construction costs is determined by the number of working days and type of construction rig. The specifications of the installation vessel are determined by the complexity of the engineering design, along with the difficulty of sea or environmental conditions. For example, in terms of seabed soil, the depth and size of the base piles; the weight and size of the platform plus the sea turbine determine the carrying capacity of the installation crane; and the anchoring method used determines the functional requirements of underwater vehicles. Therefore, lack of clarity for these conditions makes it difficult to estimate installation costs.
- Leasing a large installation vessel with a carrying capacity of 300 t and underwater construction capacity costs USD25,000/day. Therefore, when in designing the turbine relay platform, it's important to control the number and sizes of the anchor cables while also reducing the structural weight as much as possible. This can contribute to reducing the specification requirements for the installation vessel and also reduce the number of work days required.
- In addition, the risks inherent in sea-based installation require that engineers be sufficiently familiar with the installation technology. At the same time, a bad installation concept design can result in millions of dollars of cost overruns.
- Taiwan lacks experience in deep water engineering. Expertise in construction specifications, design analysis, and other relevant engineering techniques are far below what would be necessary to implement a Kuroshio power plant installation. At the same time, Taiwan lacks experience in managing such large and complex projects. The market for deep water construction engineers is currently controlled by several European countries along with the USA and Japan.
- During construction, it is recommended first creating a preliminary turbine design for analysis of weight, dimensions, and current force impact (covered in Chap. 3), followed by sea bed drilling (covered in Chap. 6) to determine the anchoring method or size and depth of the foundation piles. Once this is complete, consider the construction site in regard to the required installation vessel and underwater vehicle requirements. By this process, one can calculate the overall installation cost.
- Globally, few companies have the capacity to conduct deep sea installations. The websites of a few such firms are listed below for reference. Such deep sea installation engineering is not inexpensive, and costs are related to the scale of the overall plan.

  - http://www.helixesg.com/
  - http://www.akersolutions.com/internet/default.htm
  - http://www.saipem.it/
  - http://www.technip.com/english/index.html

Dr. Ko's expert suggestions are genuine and pertinent. Aside from the above-mentioned engineering uncertainties, we're aware that engineering schedules are subject to risk from natural disasters along with political, financial, regulatory, and social factors. As noted in Chap. 6, for example Sects. 6.7 and 6.8, these factors can have a significant impact on construction costs.

Kuroshio power plants are a completely new type of engineering. Although the technology involved is based on mature commercialized products, many unforeseeable problems can arise during assembly. Therefore, even with the government's upfront investment and full policy support, measures must be taken to prevent these types of risks, which are also the responsibilities should be taken by a mighty and capable government.

References

[1] Bedard R (2005) Survey and characterization tidal in stream energy conversion (TISEC) devices, Colorado. EPRI-TP-004 NA

[2] Hagerman G, Bedard R (2006) Massachusetts tidal in-stream energy conversion (TISEC): survey and characterization of potential project sites, Colorado. EPRI-TP-003 MA Rev 1

[3] Polagye B, Bedard R (2006) Tidal in-stream energy resource assessment for southeast Alaska, Colorado. EPRI-TP-003 AK

[4] Previsic M, Polagye B, Bedard R (2006) System level design, performance, cost and economic assessment – Minas Passage Nova Scotia tidal in-stream power plant, Colorado. EPRI-TP-006-NS

[5] Previsic M, Polagye B, Bedard R (2006) System level design, performance, cost and economic assessment – New Brunswick Head Harbour Passage tidal in-stream power plant, Colorado. EPRI-TP-006-NB